Synthesis and Characterisation of Monodispersed Ferrite Nanoparticles

A thesis submitted to the University of Manchester for the Degree of Doctor of Philosophy in the Faculty of Engineering and Physical Sciences

2013

Khadijat Olabisi Abdulwahab

School of Chemistry, The University of Manchester, Oxford Road Manchester,

M13 9PL

Table of Contents

Words: 40,421

Characters (no spaces): 213,939

Characters (with spaces): 254,168

List of Figures

List of Tables

Abbreviations

ca	Circa
EDAX	Energy Dispersive X-rayAnalysis
emu/g	Electromagnetic unit/ gram
EPMA	Electron Probe Micro Analysis
et al	Et alia
eV	Electron Volt
FC	Field Cooled
FHWM	Full Width Half Maxima
g	grams
HRTEM	High Resolution Transmission Electron Microscopy
ICDD	International Centre for Diffraction Data
ICP-OES	Inductively Coupled Plasma- Optical Emission
K	Kelvin
mL	millilitres
mmol	millimole
Oe	Oersted
O_h	Octahedral
p-XRD	Powder X-ray Diffraction
RT	Room Temperature
SAED	Selected Area Electron Diffraction
	Spectroscopy
SQUID	Superconducting Quantum Interference Device

T	Tesla
T_d	Tetrahedral
TEM	Transmission Electron Microscopy
TGA	Thermogravimetric Analysis
XAS	X-ray Absorption Spectroscopy
XMCD	X-ray Magnetic Circular Dichroism
ZFC	Zero Field Cooled

Abstract

The work presented in this thesis reports the use of a series of iron pivalate clusters as single source precursors for the synthesis of colloidal iron oxides, ternary ferrites and quaternary ferrite nanoparticles. The iron pivalate clusters $[Fe_3O(O_2C^tBu)_6(H_2O)_3](O_2C^tBu).HO_2C^tBu$**,** $Fe_8(OH)_4(O_2C^tBu)_{12}(OC_6H_4C_6H_5)_8]$ and $[Fe_3O(O_2C^tBu)_6(C_5H_5N)_3]$ were used to synthesise iron oxide nanoparticles by the hot injection thermolysis method. The effect of reaction time was studied for $[Fe_3O(O_2C^tBu)_6(H_2O)_3](O_2C^tBu).HO_2C^tBu$ at 260 °C gave a mixture of maghemite-C (Fe_2O_3) and magnetite (Fe_3O_4) for the aliquots withdrawn for reaction times of less than 30 minutes whilst only magnetite was obtained after one hour. The diameters of the nanoparticles increase in the higher boiling point solvent; 4.3 ± 0.4 and 4.9 ± 0.5 nm were produced at 260 °C and 289 °C respectively.

Heterometallic pivalate clusters of $[Fe_2CoO(O_2C^tBu)_6(HO_2C^tBu)_3]$, $[Co_4Fe_2O_2(O_2C^tBu)_{10}]$**,** $[Fe_2MnO(O_2C^tBu)_6(HO_2C^tBu)_3]$, $[Zn_4Fe_2O_2(O_2C^tBu)_{10}]$ and $[Fe_2NiO(O_2C^tBu)_6(HO_2C^tBu)_3]$ were used to synthesise cobalt, manganese, zinc and nickel ferrites respectively. Quaternary ferrite was synthesised from the thermolysis of $[CrCoFeO(O_2C^tBu)_6(HO_2C^tBu)_3]$. TEM showed that highly monodispersed spherical ferrite nanoparticles were obtained using 0.50 mmol precursor concentrations at 260 °C in all cases except for $[Co_4Fe_2O_2(O_2C^tBu)_{10}]$ for which a nearly monodispersed nanoparticles were produced. The decomposition of precursors at 0.25 mmol at different temperatures revealed that larger ferrites nanoparticles were obtained at higher temperature whilst for cobalt ferrite from $[Co_4Fe_2O_2(O_2C^tBu)_{10}]$, smaller nanoparticles appeared. In all cases, reaction times of less than 1 hour contain traces of iron oxide whilst only pure binary/quartenary ferrite was obtained after one hour.

Magnetic measurements revealed that all the iron oxide and ferrite particles are superparamagnetic at room temperature with high saturation magnetisation values. X-ray Magnetic Circular Dichroism (XMCD) analysis confirmed that in cobalt and nickel ferrite particles, most of the nickel and cobalt cations are in the octahedral site. Water-dispersible magnetite and ferrite (MFe_2O_4 where M = Co, Ni, Zn, Mn) nanoparticles were synthesised from the iron based pivalate clusters. All the ferrites nanoparticles produced are monodispersed without a further size selection process.

Declaration

I hereby declare that no portion of the work referred in this thesis has been submitted in support of an application for any degree or qualification of the University of Manchester or any other University/Institute of Learning.

……………………..

Khadijat Olabisi Abdulwahab

Copyright

1. The author of this thesis (including any appendices and/or schedules to this thesis) owns certain copyright or related rights in it (the “Copyright”) and she has given The University of Manchester certain rights to use such Copyright, including for administrative purposes.

2. Copies of this thesis, either in full or in extracts and whether in hard or electronic copy, may be made only in accordance with the Copyright, Designs and Patents Act 1988 (as amended) and regulations issued under it or, where appropriate, in accordance with licensing agreements which the University has from time to time. This page must form part of any such copies made.

3. The ownership of certain Copyright, patents, designs, trademarks and other intellectual property (the “Intellectual Property”) and any reproductions of copyright works in the thesis, for example graphs and tables (“Reproductions”), which may be described in this thesis, may not be owned by the author and may be owned by third parties. Such Intellectual Property and Reproductions cannot and must not be made available for use without the prior written permission of the owner(s) of the relevant Intellectual Property and/or Reproductions.

4. Further information on the conditions under which disclosure, publication and commercialisation of this thesis, the Copyright and any Intellectual Property and/or Reproductions described in it may take place is available in the University IP Policy (see http://documents.manchester.ac.uk/DocuInfo.aspx?DocID=487), in any relevant Thesis restriction declarations deposited in the University Library, The University Library’s regulations (see http://www.manchester.ac.uk/library/aboutus/regulations) and in The University’s policy on Presentation of Theses.

Dedication

This thesis is dedicated to Allah (SWT) and my entire family.

Acknowledgments

All praise, thanks and adoration are due to Allah for His Mercies and Whose Grace has made it possible to come this far. Alhamdulillah!

My profound gratitude goes to my supervisor Prof. Paul O'Brien for his immense guidance, precious help, encouragement and support throughout the programme. I would also like to thank Dr. Azad Malik for his assistance and constructive comments while drafting papers and thesis. I gratefully acknowledge the financial support from the Islamic Development Bank (IDB), Saudi Arabia. I also wish to thank all the new post docs in the POB group (Dave, Nick and Paul) and also other members past and present especially; Dr. Kuvi Govender, Dr. Ahmed Abdelhady, Dr. Dayo Oyetunde, Dr. Karthik Ramasamy, Dr. Masood Akhtar, Emmanuel Ezenwa and Nathaniel. It's been a great pleasure knowing you all.

I cannot but remember the staffs (past and present) in the School of Materials: Ms Judith Shackleton, Mr Garry, Dr. Chris Wilkins, Dr. Alan Harvey, Dr. Uschi Banguet and Dr. Sarah Haigh for their unalloyed assistance on the XRD, SEM and TEM instrumentation and analysis.

My special thanks to Prof Richard Winpenny and Dr. Gregore Timco for the pivalate clusters used in this thesis. A big thank you to Dr. Floriana Tuna for the magnetic measurements. I appreciatively acknowledge Prof Richard Pattrick and Dr. Vicky Coker (School of Environmental Sciences) for their work on the XMCD measurements, analysis and interpretation.

My thanks to the administrative staff in the school of chemistry: Lorraine Onabanjo, Angela Dermody and Christine Taylor. I would also like to appreciate the support received from Dr Paul's Christian group during my first year. Also a big shout to friends in the OMIC group especially Mohammed and Hosna.

I am very glad to acknowledge the support from my teachers and lecturers in Nigeria especially Mr. Adebayo, Dr. Olayinka, Prof. Osibanjo for motivating my interest in chemistry. The support from Dr. Adekoya is also greatly appreciated.

During my stay in Manchester I have met some wonderful people and made many friends. In no particular order, I thank Mrs Kehinde Bayo, Mrs. Wunmi Aina,

Bolaji Okelola, Nana (hulme), Kemi Jaji and Julie Obi. I would also like to thank my colleagues and teachers at the Tajweed Foundation course, my neighbours for being great and also for the sumptuous iftar during Ramadhan. Special thanks to all well-wishers especially The Salau’s, The Makarfi’s, Hanan Alchaghouri and Sarah El-tarhuni.

My heartfelt gratitude goes to my parents (Mr. and Mrs. Adio), siblings (Mariam, Rasheedat and Qudus) and nephew (Fareed) for their unflinching love, support, encouragement and prayers. I would also like to thank my in-laws; Mr. Aliyy Wahab (Senator!) and the entire Abdulwahab-Alwajud family for their support and prayers.

Words are not enough to express my feelings and sincere thanks to my loving husband (Idris Abdulwahab) for his understanding and being there always! Last but by no means least my beautiful daughter (Nabeelah Opeyemi Abdulwahab) whose presence has been a source of inspiration to keep going during the hard time. I love you all!

Chapter 1

Introduction

Nanoparticles are often defined as materials that have one or more dimensions less than 100 nm and as a result, generally have novel properties different from their bulk counterparts or atomic / molecular constituents.[1] The history of nanoparticles can be traced back to early cultures in Egypt, Iran and Rome, where colloidal gold was used for decorative ornamentation.[2] The most famous example of this kind is the Lycurgus Cup from the 4th Century, currently owned by the British Museum. Its scientific evaluation however began in 1857 when Michael Faraday prepared red gold sols by reducing gold in solution with white phosphorus.[3] He called them divided metals and established that these metal sols were thermodynamically unstable, hence must be stabilised against aggregation. The 20th century witnessed a lot of advances in methods of synthesising colloidal gold.[4] Bredig used an electrochemical method,[5] Zsigmondy discovered the seeding method[6] and he later won a nobel prize in 1925. This was followed by the landmark works of Turkevich with citrate-stabilised sols[7] and the work of Brust and Schiffrin with monolayer-protected clusters.[8] In recent times, there has been ongoing research into nanoparticulate materials because of their small size and subsequently high surface to volume ratio. This in turn has translates into novel properties such as superparamagnetism, morphology tuneable optical properties, photostable luminescence.[9] The field of nanoscience has experienced exponential growth year-on-year due to emerging synthetic routes as well as the availability of new tools for characterisation.[10] Nanomaterials have found applications in different fields including electronic devices, storage devices, computer modelling, catalysis, solar system, biological labelling, environmental remediation, drug delivery.

1.1 Properties of nanoparticles

When the size of a crystal is decreased to the nanometer range, the electronic structure is changed from continuous bands to discrete or quantized electronic levels. Consequently, the continuous optical transitions in the molecule become quantized and therefore their properties become size controlled.[11] This in turn leads to changes in chemical features such as electronic, structural, spectroscopic, magnetic and thermodynamic.[10] The size of quantum dots determines their properties such as their electronic absorption as well as their melting points. In magnetic materials, size effect has brought about a new phenomenon known as superparamagnetism. In metals, very small sized particles of about 1-2 nm in diameter exhibit unexpected catalytic activity as observed in gold nanoparticles.[10]

1.1.1 Magnetic properties of nanoparticles

The magnetic properties of nanoparticles are influenced by many parameters including their size, shape, chemical composition**,** crystal structure and interparticle interactions.[12]

Magnetic materials are found everywhere: in soils, plants, animals and even human brain. In bulk/giant magnetic materials, their intrinsic magnetic properties including saturation magnetization, coercive force and Curie temperature depend only on their chemical and crystallographic structure but in nanoparticles these properties become influenced by the finite size and surface effects. The evolution of nanoparticles has provided the opportunity to study magnetic properties from the bulk to the atomic scale.

Hence novel properties including superparamagnetism, high magnetic coercivity and quantum tunnelling are sometimes exhibited by these magnetic nanoparticles.

Magnetism is as a result of magnetic moments associated with individual electrons. Magnetic moments originate from two main sources: orbital motion and electron spin. The net magnetic moment is the sum of these moments from all electrons.

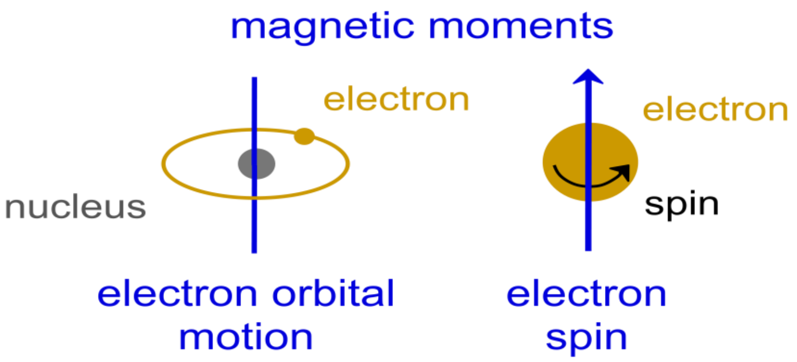

Fig. 1.1 Magnetic moments arising from electron orbital motion(left) and electron spin(right).[13]

The magnetic property of a material depends on the response of electron and magnetic dipoles to an applied magnetic field and these are classified into diamagnetic, paramagnetic, antiferromagnetic, ferrimagnetic and ferromagnetic materials.

Diamagnetism is a very weak form of magnetism and only persists when an external field is applied. The induced magnetic moment is as a result of change in the orbital motion of electrons which creates an opposite field to that of the applied magnetic field.

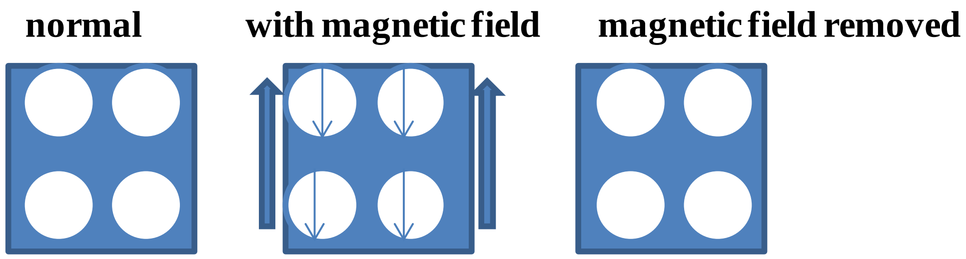

Fig. 1.2 The atomic dipole of a diamagnetic material.

Paramagnetism is as a result of random movement of the spins and therefore there is zero magnetisation in the absence of a magnetic field. It is as a result of incomplete cancellation of electron spin and or orbital magnetic moments.

Ferromagnetic materials possess permanent magnetic moment even in the absence of an external magnetic field. These are characteristics of the transition metals such as iron, cobalt and nickel. They have high magnetic susceptibility due to unpaired electron/ uncancelled electron spin as a result of their electronic structure.

Antiferromagnetic materials have their spins aligned in opposite directions thereby cancelling each other and no net magnetic moment in the absence of an external magnetic field. Zinc ferrite is a good example of an antiferromagnetic material.

In ferrimagnetic materials, the spin magnitude is greater in one direction leading to a net permanent magnetisation but their saturation magnetisation is not as high as ferromagnets. Magnetite and some other ferrites exhibit this type of magnetic property.

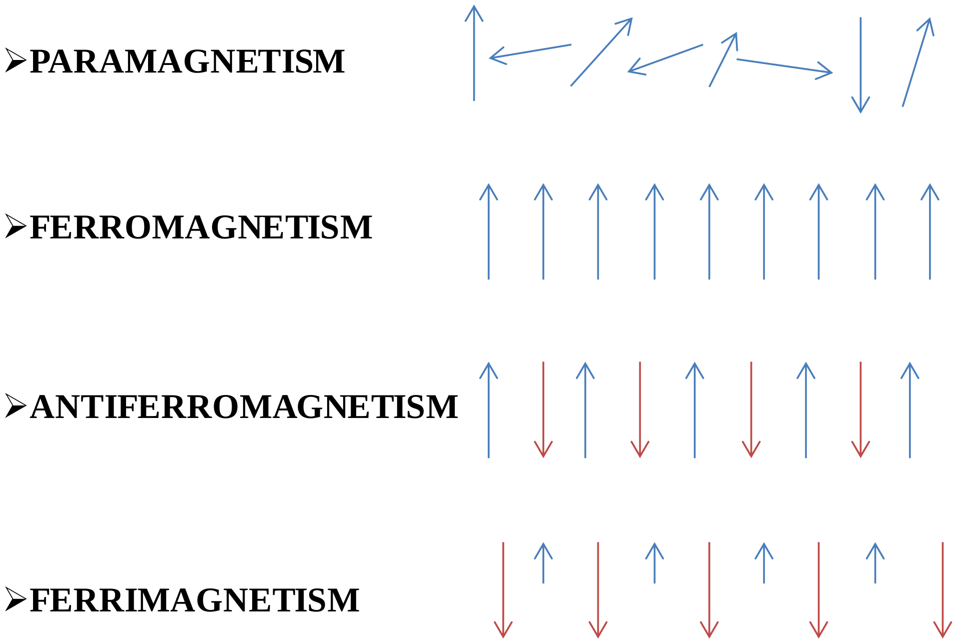

Fig. 1.3 Illustration of the different types of magnetism.

The size dependent magnetic properties are usually observed in the range of a few microns to a few nanometers. In bigger particles, there exists a multi domain structure where regions of uniform magnetization are separated by domain walls and whose magnetization can be reversed by the shift or movement of the domain walls. As the size of the particles decreases, these walls become energetically unfavourable leading to the formation of just one single domain state in which all spins are aligned in the same direction. This is usually observed in a few tens of nanometers and is called the critical diameter, D_c.[4]

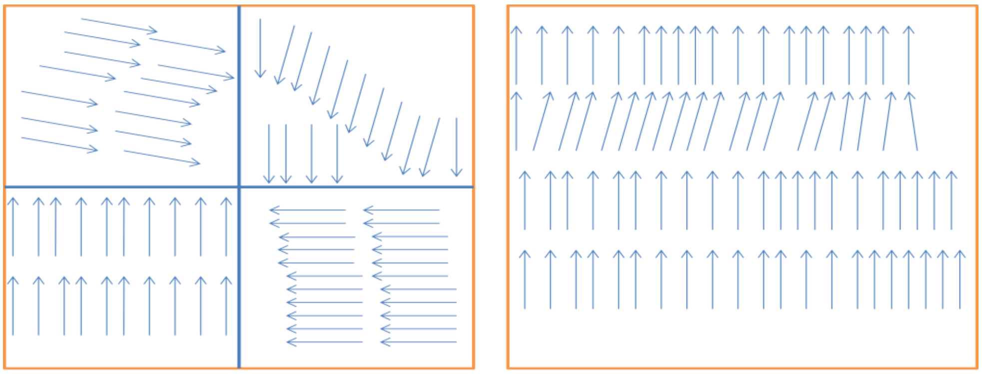
(a) **(b)**

Fig. 1.4 The different domain states that can exist in a particle. (a) multi domain separated by domain walls and (b) single domain.

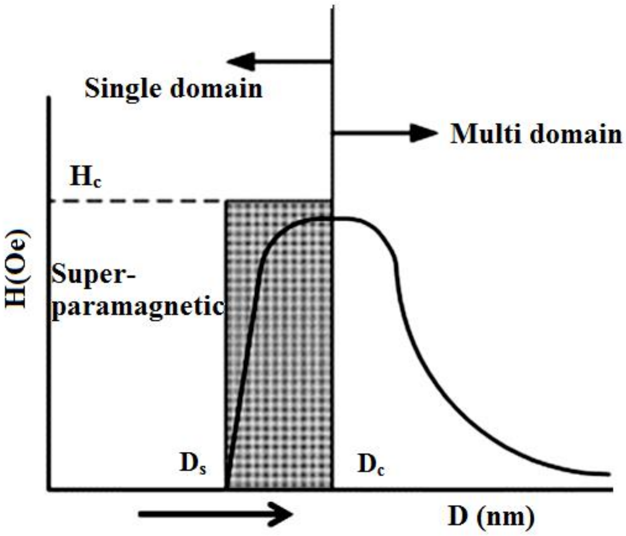

Fig. 1.5 Illustration of variation in coercivity of a particle with diameter.[14]

The coercivity of a material which is defined as the magnetic field needed for the magnetisation to return to zero after saturation is size-dependent. Initially the coercivity increases with decrease in particle until a critical diameter is reached. This is due to the fact that change in magnetisation cannot be achieved by the motion of domain wall which normally requires a weak magnetic field. However, below the critical diameter, coercivity tends to decrease due to thermal effects and follows the equation below:

$$H_C = g- h/D^{1.5} \qquad (1.0)$$

where g and h are constants.[15] Hence below the critical diameter $D_{s,}$ the coercivity becomes zero because thermal energy is sufficent to radomnise the magnetic moments in the particle. This phenomenon is known as superparamagnetism.[16] Superparamagnetic particles often exhibit the magnetic properties of their bulk counterparts at low temperatures. A typical hysteresis loop of the different types magnetism is shown in Fig.1.6 below. Superparamagentic materials have little or no coercivity at high temperatures whilst ferromagnetic materials have a high coercivity.

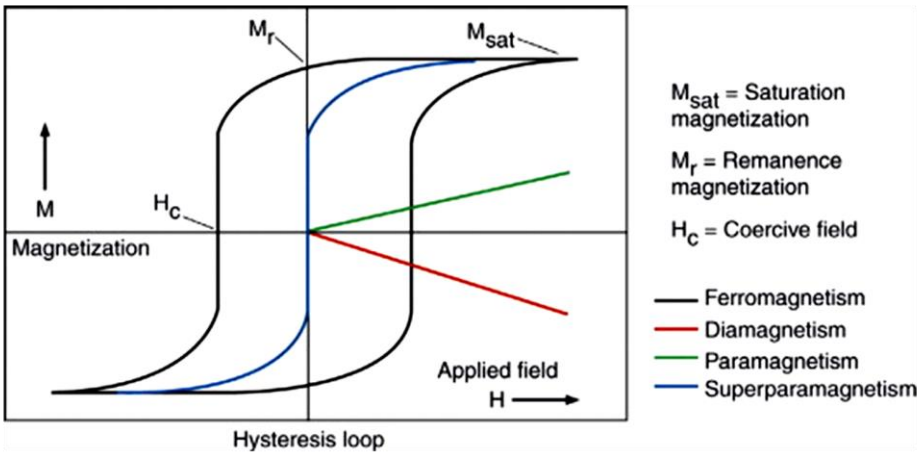

Fig. 1.6 Hysteresis loops for the different types of magnetic materials.[17]

Nanoparticles are said to be in a state of superparamagnetism when the magnetization of the nanoparticles is a single giant magnetic moment in each particle instead of individual atomic moment.[16] This behaviour can be explained in terms of magnetic anisotropy which is defined as the dependence of magnetic properties on a preferred direction. Because of the nanoparticle's magnetic anisotropy, the magnetic moment has usually only two stable orientations separated by an energy barrier. At a particular temperature, it is possible for magnetization to flip and change its orientation.[16] The time between two flips is called the Néel Relaxation time and is given by the equation below:

$$\tau = \tau_0 \exp\left(KV/k_B T\right) \qquad (1.1)$$

where τ is relaxation time, τ_0 is characteristic of the material called the attempt time and its typical value is 10^{-9} to 10^{-10} second, K is magnetic anisotropy constant, V is volume, k_B is Boltzmann constant and T is temperature.[16]

In the equation, it can be seen that τ is an exponential function of volume and thus give a probable reason why large particles do not exhibit superparamagnetism. If the magnetization of a nanoparticle is measured (τ_m) and the value is less than τ, it means there will be no flip and it is said to be in a blocked state. On the other hand if τ_m is greater than τ, then magnetization will flip many times and the particle is said to be superparamagnetic.[16] The transition between these two states depends on temperature and the temperature at which $\tau = \tau_m$ is called the blocking temperature.

Superparamagnetic materials have a high saturation magnetization but zero coercivity and remanence. This unique property makes it possible for controlling their movement when placed in an external magnetic field. Thus they find numerous applications in biomedicine.[18]

1.1.2 Electronic Properties of Nanoparticles

Bulk solid materials can be generally classified into conductors, semiconductors or insulators depending on their ability to conduct electrical charge. In conductors, (typical of metals), the ability to conduct electrons is due to overlapping valence and conduction bands giving rise to free movement of electrons. In bulk semiconductors, the valence bands are fully filled and the conduction is empty and they are by a small energy gap (band gap). Movement from valence to conduction is possible by thermal or optical excitation.

In insulators, the valence bands are completely filled and the empty conduction bands are separated by a large band gap making impossible the movement of electrons.

On the scale of nanometre, the continuous band in the metal breaks down and thus the samples becomes insulating. In case of semiconductor nanoparticles, the energy levels at the band edge become discrete with interlevel spacing similar to metals and thus increasing their band gap.[4] These changes are referred to as quantum size effects and they are observed in some physico- chemical properties including optical and thermal properties. Size dependent changes have been observed in the absorption spectra of some semiconducting nanocrystals. For instance, CdS, a yellow solid, exhibits an excitonic absorption around 520 nm which undergoes a hypsochromic shift when the particle diameter is decreased below 10 nm.

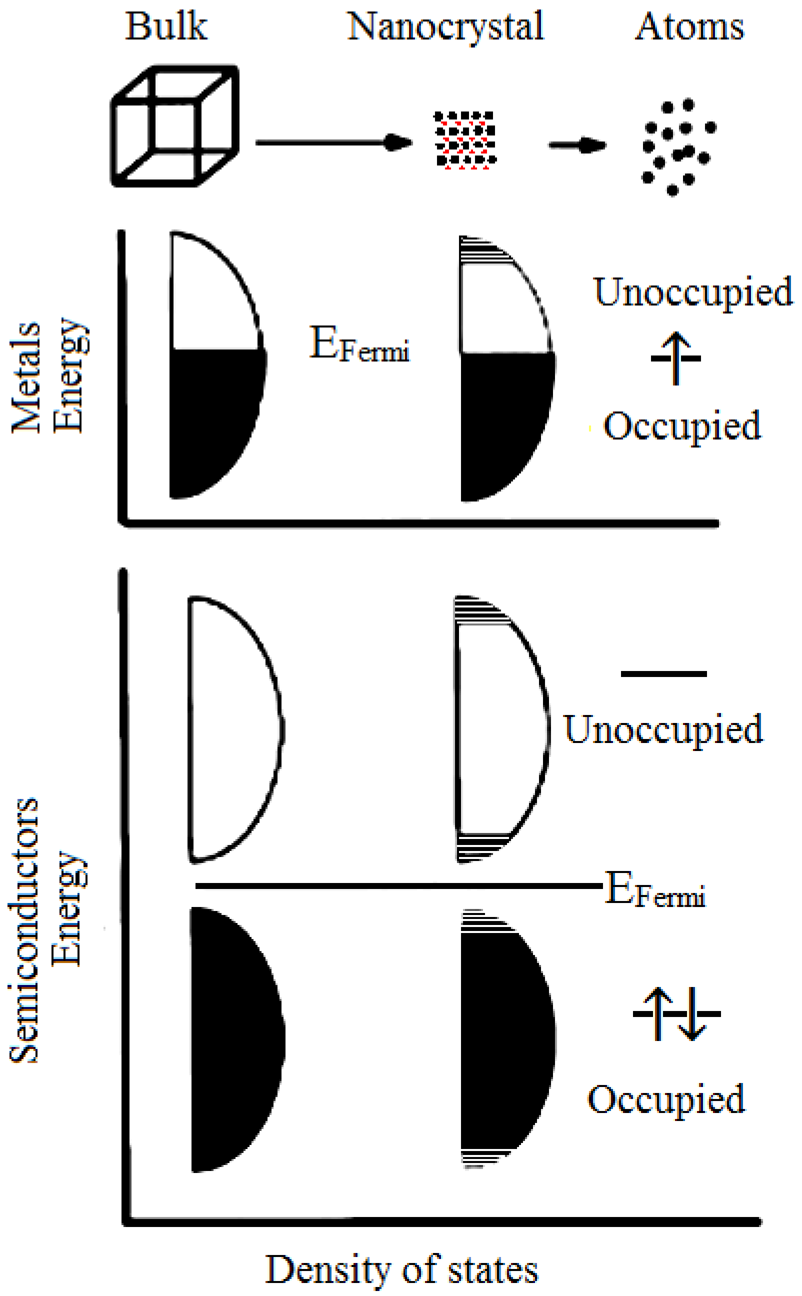

Fig. 1.7 Illustration of the variation in electronic structure of metals and semiconductors as a result of size effects.[4]

1.2 Preparation of Nanoparticles

There are two main methods for the preparation of nanoparticles: top - down and bottom- up. The top down involves breaking down the bulk matter into nanoparticles whist the bottom-up methods involve building nanoparticles from molecules or their constituent atoms. The top-down synthesis can be achieved through physical methods such as lithographic techniques or etching.[9] Although these methods have advantage of producing nanoparticles in large quantities but size control is usually very difficult.[19] The bottom-up approach is considered as a chemical method of synthesising nanoparticles and is a more convenient and reliable method of producing high purity, crystalline monodispersed nanoparticles.[19]

1.2.1 Formation Mechanism of Nanoparticles

A good understanding of the theory behind the formation of nanoparticles helps in controlling the size and shape of nanoparticles. This is important because most often applications of nanotechnology require very monodispersed nanoparticles. The formation mechanism involves two main steps: nucleation and growth.

1.2.1.1 Nucleation

Nucleation occurs when the solute in a particular solvent becomes supersaturated thereby leading to the formation of new nuclei and then followed by a growth process. To prepare a highly monodispersed nanoparticles, it is necessary to adopt a "burst nucleation" process.[19] This strategy involves simultaneous or a single nucleation process which prevents a further nucleation during the subsequent growth process. The generation of many nuclei at the same time during a burst nucleation makes it possible for controlling their growth, which means they grow at nearly the same pace thus giving rise to monodispersity.

Nucleation can be either homogenous or heterogeneous. In homogenous nucleation, nuclei are formed without aid from any external material such as dust, bubbles or solid surfaces whilst heterogeneous nucleation involves the use of seeds or external materials.[9,19,20]

Homogenous nucleation is driven by thermodynamics force as a result of instability of the supersaturated solution. The overall free energy change, ΔG, is the sum of the free energy due to the formation of a new volume and the free energy due to new surface created. Thus:

$$\Delta G = 4\prod r^2 \gamma + 4/3 \prod r^3 \Delta G_V \qquad (1.2)$$

Where γ is the surface free energy per unit area or interfacial tension, r is the radius and ΔG_V is the free energy change between the monomers in the solution and unit volume of bulk crystal.[19,21] ΔG_V is always negative whilst γ is always positive as long as the solution is supersaturated. As nucleation begins in a supersaturated solution, there exists a critical radius, r^*, which a nucleus must attain before it can be stable. If the radius is lower than r^*, the nuclei redissolves whilst those higher than r^* grow. From equation (1.2), r^* can be obtained by setting $\Delta G/dr = 0$,

$$\Delta G/\mathrm{dr} = 8\prod r\gamma + 4\prod r^2\ \Delta G_V \qquad (1.3)$$

At $\Delta G/dr = 0$, r^* becomes:

$$r^* = -\ 2\gamma/\ \Delta G_V \qquad (1.4)$$

It therefore means that ΔG^* is the minimum required energy for r^* to be formed and it can be obtained by combining equation 1.2 and 1.4 and we have:

$$\Delta G^* = 16\prod\gamma^3 /\ 3(\Delta G_V)^2 \qquad (1.5)$$

The change in Gibb's free energy value is maximum at ΔG^* as seen in Fig. 1.8 and corresponds to the energy required to form a stable nuclei.[19- 21]

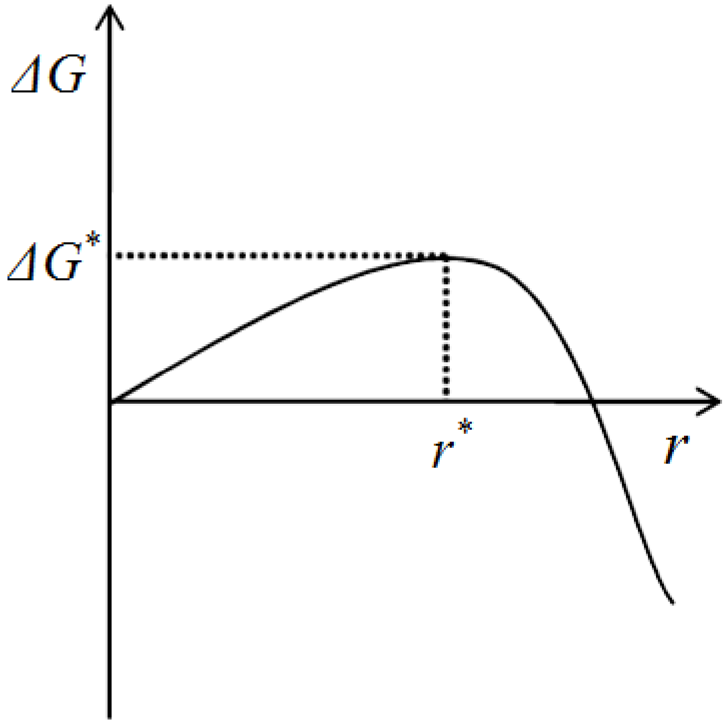

Fig. 1.8 Graph of free energy versus the radius of colloidal particles.

1.2.1.2 Growth

In homogenous nucleation, monodispersed nanoparticles are usually achieved through a burst of nucleation wherein all the nuclei are generated at the same time and then followed the growth process.[9] There are two growth modes: focusing or defocusing. Focusing brings about a narrow size distribution whilst defocusing or Ostwald ripening leads to a broad size distribution. At higher monomer concentrations, smaller particles grow more rapidly than the larger ones and this is due to the diffusion controlled growth when only mass transport processes are considered. [20] This growth is termed focusing and continues until the monomer concentration is lower than the solubilities of the particles in solution. After this, an Ostwald ripening or defocusing takes place wherein the larger particles grow at the expense of the smaller ones. This can be explained in terms of reaction kinetics. Smaller particles are less stable because of their higher chemical potential and so their growth is difficult; hence they dissolve.[20]

In the case of a heterogeneous nucleation using seeds, additional nuclei formation are suppressed by introduction of preformed nuclei into the reaction and the monomers in solution are subsequently added on the existing nuclei, thus separating nucleation from growth.[19,22] However, the seed particles need to be uniform in order to obtain a narrow size distribution.

1.2.2 Stabilisation of Nanoparticles

One of the novel properties of nanoparticles is their high surface area-to-volume ratio. This in turn has led to an enormous surface energy which makes them agglomerate in solution. Once they agglomerate, it becomes very difficult to disperse them and hence lose some of their properties. It is therefore important to reduce their surface energy to stabilise them and this can be achieved by two main methods: steric and electrostatic stabilisation.

1.2.2.1 Electrostatic Stabilisation

This is also known as charge stabilisation. It works by creating a stern layer. This consists of a charged surface with surrounded by counter ions and some solvent molecules which are tightly held by the surface of the particle. Because the surfaces have like charges, they repel each other according to Coulomb's law thereby providing a barrier or separation between particles.[23] One of the advantages of charged or electrostatic stabilised particles is their dispersibility in aqueous medium. A major disadvantage however is that their stability is usually affected by change in ionic concentration. An increase in ionic concentration causes shielding of charges leading to agglomeration. Also an exchange of ions might occur at the surface of the charge which often results to precipitation and eventual agglomeration of particles.[23] Precipitation or agglomeration can also arise when the pH of the solution is altered; often this causes a change or loss of charge on the surface of the nanoparticles.

1.2.2.2 Steric Stabilisation

This type of stabilisation involves the use of surfactants or capping agents that have a strong affinity for the solvent. Stabilisation is achieved by the attachment of long chain molecules to the surface of the particle.

They are usually long chain molecules which could be polymers or long molecule with a polar head or anchor point. The anchoring group ensures that the capping agents are bound to the particle whilst the affinity of the long chain for the solvent provides stabilisation of the dispersion. Unlike charge stabilisation method, steric stabilisation is not sensitive to change in ionic concentration. Common capping agents are polymers, alkyl amines such as hexadecyl amine (HDA), oleylamine (OLAm), alkanoic acids such as oleic acid, lauric acid, thiols such as dodecanethiol (DDT). Some polymers are amphiphilic in nature; hence nanoparticles capped by such polymers can be dispersed in a variety of solvents. Examples of such polymers are polyethylene glycol (PEG), polyvinyl pyrrolidone (PVP).

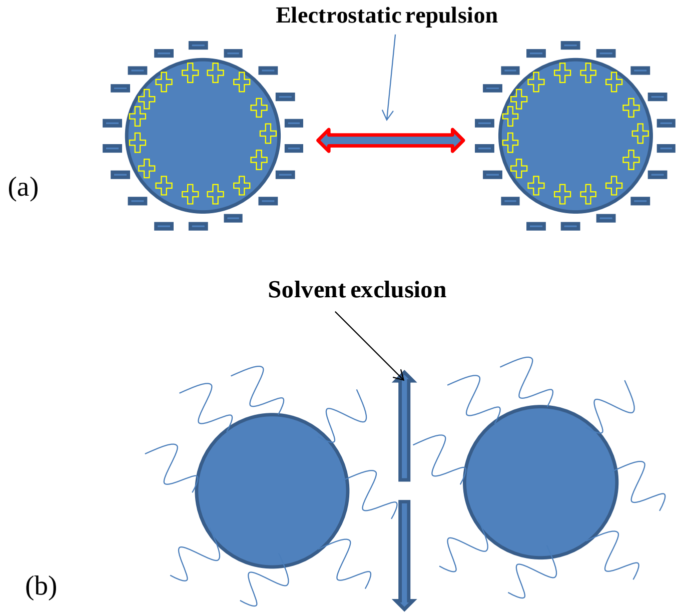

Fig. 1.9 A representation of stabilisation of nanoparticles with (a) charge and (b) steric methods.

1.3 Magnetic Ferrite Nanoparticles

Recently, attention has been focused on synthesis, characterisation and improving the applications of magnetic nanoparticles in different fields. This is because magnetic nanoparticles usually exhibit novel properties that differ from those of their bulk counterpart. Two important parameters control the magnetic properties of nanoparticles: the size and surface effects.

Size effects impart two important phenomena: single magnetic domain and superparamagnetism. Single magnetic domain arises at a critical diameter below which the formation of domain wall becomes energetically unfavourable. This results in a large magnetic moment per unit volume and a large magnetic anisotropy.[15] Magnetic anisotropy can be seen as an energy barrier which is responsible for holding the magnetic moments in a certain direction. With decreasing particle size, the thermal energy exceeds the energy barrier and therefore flips at random. This phenomenon is called superparamagnetism.[16]

Other special properties include the high surface-to-volume ratio and also surface particle coating. Because a large percentage of the atoms in nanoparticles are on the surface, it can bring about some changes including crystal lattice vacancies, short range magnetic order and enhanced magnetic anisotropy. [13,14] Surface effects can also lead to a decrease in magnetisation value with respect to the bulk and this has been associated with the existence of a magnetically dead layer on the surface of the particle.[24]

Spinel ferrites nanoparticles are of great interest in fundamental science especially for addressing the relationships between magnetic properties and their crystal chemistry. Crystal chemistry shows how the chemical formula, internal structure and physical properties are linked together. Ferrites nanoparticles have the general formula MFe_2O_4 (where M is a divalent cation and could be Fe, Co, Mn, Zn, Ni, Cr). By varying the composition of the divalent cation, their electrical and magnetic properties differs and as such they find applications in different areas including biomedical, environmental remediation, storage systems, transformers, medical and diagnostics. These numerous applications have prompted the development of many synthetic methods and characterisations of these nanoparticles.

1.3.1 Iron oxide Nanoparticles

Iron oxides are chemical compounds composed of iron and oxygen. There are about sixteen known iron oxides and hydroxides. They are widespread in nature and have myriad applications. The two most common iron oxide nanoparticles are magnetite (Fe_3O_4) and maghemite (γ-Fe_2O_3).

1.3.1.1Magnetite (Fe_3O_4)

Magnetite is a naturally occurring black mineral in sedimentary rock and it is also known as ferrous-ferric oxide. It is the only mineral that exhibits strong magnetism. A chunk of crystallised magnetite is called lodestone. Crystals of magnetite have also been found in some organisms such as bacteria, bees, birds and even the brain of humans. Its structure is an inverse spinel with a cubic close packed oxygen and iron in both tetrahedral and octahedral sites. The spins on both sites are antiparallel to each other giving rise to ferrimagnetism. Magnetite has received much attention because of its unusual magnetic properties arising from the exchange interactions between iron spins in the tetrahedral and octahedral sites. Bulk magnetite has a very high Curie temperature and hence has found applications in magnetoelectronic devices. In the nanoparticle form, however, size effects sets in leading to a phenomenon called superparamagnetism. This unique property coupled with its biocompatibility has led to its various applications in biomedicine.

1.3.1.2 Maghemite (γ-Fe_2O_3)

Maghemite (γ- Fe_2O_3) is naturally occurring in terrestrial sediments, soils and is the second most stable form of iron oxide. It occurs as a result of oxidation of iron (II) containing spinels like magnetite. Maghemite like magnetite has a spinel crystal structure but with all the cations as Fe^{3+}. Each cell contains 32 O^{2-} ions, $21^{1}/_{3}$ Fe^{3+} and $2^{2}/_{3}$ vacancies. These vacancies are responsible for the neutrality of the cells. The unit cell can be represented as $(Fe)_8[Fe_{13.3}\blacksquare_{2.67}]O_{32}$ (where$\blacksquare$ =vacant sites, the parentheses ( ) and [ ] denotes tetrahedral and octahedral respectively), which conforms with the space group Fd3m.[25] It therefore means that eight ions are in the tetrahedral states while the rest of the ions and the vacant sites are distributed over the octahedral sites. Maghemite just like magnetite has found numerous applications in biological field.

1.3.2 Structure of Ferrite Nanoparticles

Ferrites (MFe_2O_4) are structurally classified as spinels and can be described as a cubic close-packed arrangement of oxygen atoms with divalent cation (M^{2+}) and trivalent cation (Fe^{3+}) at two different crystallographic sites. These sites are named tetrahedral (A) and octahedral (B) sites with respect to the positions of oxygen ions within the unit cell and in total amounts to 24 sites (8-A and 16-B sites). In a normal spinel structure, the divalent cations (M^{2+}) occupy the tetrahedral holes whilst the octahedral sites are occupied by the trivalent cations (Fe^{3+}). A common example of normal ferrites is zinc ferrite. However, the structure becomes an inverse spinel if all A-sites are occupied by the Fe^{3+} whilst the B-sites are now occupied by both M^{2+} and Fe^{3+}. Magnetite and Nickel ferrites are examples of inverse spinels. In some cases, there could be a redistribution of cations wherein in each site; both cations are present giving rise to a mixed spinel structure.

The preferred site occupancy of transition metal cations can be explained by the theory of Crystal Field Stabilisation Energy (CFSE). The cation with more CFSE in octahedral geometry as compared to its value in tetrahedral geometry tends to occupy the octahedral sites. The difference in these values is called

Octahedral Site Preference Energies (OSPE). Hence, if the trivalent cation has more CFSE value in octahedral site than that of the divalent cation, a normal spinel is expected. An inverse spinel is formed when the divalent cation has more CFSE value in octahedral geometry than the trivalent cation.

In the case of ferrites, because the oxide anion is a weak ligand, high spin systems are expected. The trivalent cation, Fe^{3+} has a d^5 configuration and therefore has zero CFSE value. If the divalent cation is Fe, Co and Ni with configurations d^6, d^7 and d^8 respectively, their CFSE value are higher than that of Fe^{3+} and hence inverse spinel structures are formed.

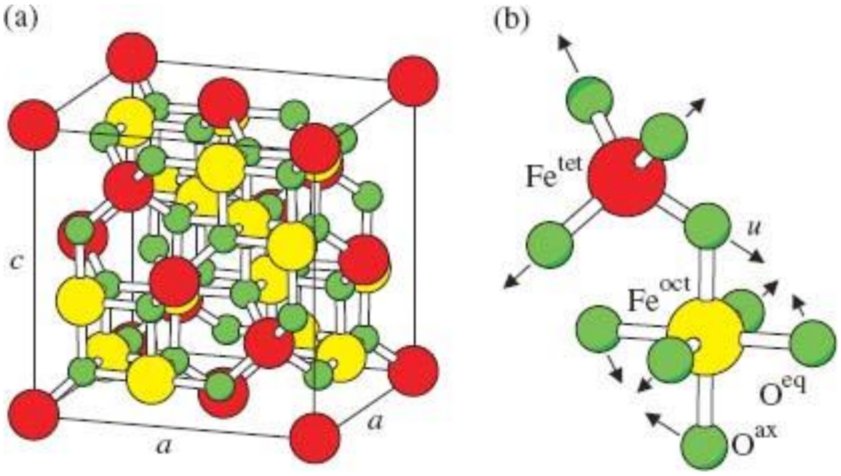

Fig. 1.10 (a) Face-centred cubic spinel structure of magnetite, (b) Magnification of one tetrahedron and an adjacent octahedron. Fe^{tet} (red colour) and Fe^{oct} (yellow colour) reperesent iron atoms on tetrahedrally and octahedrally coordinated sublattices respectively whilst oxygen atoms are labelled green, a is the lattice parameter in the (001) plane and c is perpendicular to a.[26]

Table 1.1 Illustration of the different possible combinations in spinel structure.

A^{2+}	B^{3+}	Structure	Example
d^0, d^5, d^{10}	d^1, $d^{2,}$ d^3, d^4, d^6, $d^{7,}$ $d^{8,}$ d^9	Spinel	Mn_3O_4
d^1, $d^{2,}$ d^3,d^4, d^6,$d^{7,}$ d^8, d^9	d^0, $d^{5,}$ d^{10}	Inverse Spinel	Fe_3O_4, $NiFe_2O_4$
Transition metal with lower CFSE value	Transition metal with higher CFSE value	Spinel	$FeCr_2O_4$

1.3.3 Synthesis of ferrite nanoparticles

Magnetic nanoparticles have been synthesised in different compositions and phases including iron oxides (magnetite or maghemite), cobalt ferrite, zinc ferrite, nickel ferrite, chromium ferrite and manganese ferrite. Many methods have been used for the synthesis of these ferrite nanoparticles including co-precipitation, micro-emulsion, thermal decomposition, hydrothermal/solvothermal, and also by biological methods.

1.3.3.1 Co- precipitation

This method is a simple and convenient way of synthesising ferrite nanoparticles from aqueous salts of Fe^{3+} and the corresponding divalent cation salt by the addition of a base either at room temperature or at elevated temperature. The factors affecting the composition, size and shape of the nanoparticles are: the ratio of Fe^{3+}/M^{2+}, temperature, type of salts used, pH and the addition of surfactants. A typical equation of reaction for the formation of ferrite nanoparticles (MFe_2O_4) by co-precipitation is given below:

$$2Fe^{3+} + M^{2+} + 8OH^{-} \rightarrow MFe_2O_4 + 4H_2O \qquad (1.6)$$

Highly alkaline media tend to produce goethite (α FeOOH) as impurities alongside magnetite (Fe_3O_4),[27] whilst high concentrations and temperatures usually favours the formation of spherical nanoparticles because the direction of crystallographic growth is less selective.[28] Different morphologies of ferrite nanoparticles including spheres,[28–32] cubes,[28, 33,] platelets[28,34] and rods[35] have been synthesised using this method. Although this method can produce nanoparticles on a large scale, a major disadvantage is that the particles tend to have broad size distributions.

1.3.3.2 Hydrothermal/solvothermal methods

A hydrothermal system involves the use of water at a temperature beyond its boiling point (100 °C) under a high pressure in a sealed autoclave vessel. Similar to hydrothermal methods, solvothermal synthesis employs the same technique but with a non-aqueous solvent. The use of high temperature and pressure increases the solubility and reactivity of the precursors thereby leading to the production of very crystalline nanoparticles. Indeed, this method has been used to synthesise different ferrite nanoparticles including magnetite (Fe_3O_4),[36–38]cobalt ferrite ($CoFe_2O_4$)[39,40] and nickel ferrite ($NiFe_2O_4$).[41–48]

1.3.3.3 Micro emulsion methods

A microemulsion consists of a mixture of two immiscible liquids that is stabilised by an interfacial film of surface active agents.[49] Microemulsions are classified into: normal micelles and reverse micelles. In normal micelles, also known as oil-in-water (o/w), the oil is dispersed as microdroplets surrounded by a layer of surfactant molecules in the dispersing water phase, the opposite is the case for reverse micelles or water-in-oil (w/o). These micelles serve as a template for synthesising nanoparticles and their shapes/ sizes are influenced by some factors including concentrations of surfactant and precursors, also the ratio of water-to-oil is crucial.[14] Spinel ferrites including iron oxide,[50,51] manganese ferrite,[52] cobalt ferrite[53,54] and zinc ferrite[55] have been synthesised using this approach.

1.3.3.4 Biological methods

This method involves the use of microbes to synthesise nanoparticles. The mode of synthesis could be by intracellular (biologically controlled) or extracellular (biologically induced) means. In intracellular approach, the production of nanoparticles is within the cells of the organism and is enzymatically controlled. Magnetotatic bacteria are good examples of organisms that produce nanoparticles by intracellular means. These bacteria were discovered by Blakemore in 1975 when he observed that they arrange themselves pointing to the North Pole.[56] Magnetotatic bacteria form magnetosomes chains which give rise to compartmentalisation.[57] This in turn has made it possible to control the factors affecting the biochemical production of nanoparticles. Hence the production of monodispersed nanoparticles has been achieved intracellularly. Examples of magnetotatic bacteria are *Magnetospirillum magnetotacticum* and *Magnetospirillum gryphiswaldense.*[58]

The extracellular approach involves synthesis of the nanoparticles on the surface of the microbe. The mechanism of producing nanoparticles is as a metabolite. For instance, iron reducing bacteria that live in the anaerobic environment conserve energy for growth by the oxidation of organic matter, the electrons generated are then used for the reduction of Fe(III)- oxyhydroxides to form magnetite.[58–60]The process has been be extended to synthesise transition metal doped magnetite by an electrochemical process.[61] Although this approach could be exploited for industrial scale, the success of getting monodispersed nanoparticles depends on environmental parameters such as temperature, redox potential and pH.[58] Examples of bacteria that can produce extracellularly are: *Geobacter sps., Shewanella sps.,* and *Thermoanaerobacter ethanolicus.*

Biological methods been used to synthesise ferrite nanoparticles including magnetite,[62–72] cobalt ferrite,[59,61,73] zinc ferrite,[73,74] nickel ferrite[61,73] and manganese ferrite.[73]

1.3.3.5 Thermal decomposition method

This method involves heating precursors in a high boiling point organic solvent in the presence of capping agents. This method has been used to synthesise different nanoparticles and has proven to produce monodispersed nanoparticles with a very narrow size distribution and good crystallinity. The process can involve either a progressive heating of the reactants in a suitable media to the desired temperature or alternatively a more rapid process termed hot injection. In the former, the reaction medium containing the precursor, solvent and the capping agent is progressively heated from low (often ambient) temperature to a higher predefined reaction temperature. The latter involves rapid injection of the precursor solution into a hot medium containing capping agent. Both processes can be used to produce monodispersed nanoparticles because there is a separation of nucleation from growth. For instance, in hot injection approach, a highly supersaturated solution is formed by the rapid injection of the precursor solution that leads to a burst of nucleation. This in turn leads to the depletion of monomers in solution and the sudden drop in temperature prevents a further nucleation process. Thus, nucleation is separated from the growth process leading to the growth of monodispersed nanoparticles. In the progressive approach, the reaction of the precursor proceeds slowly *via* the formation of intermediates which eventually acts as monomers. The monomers build up until a the supersaturation limit is reached where rapid nucleation takes place, followed by growth.[20,75,76]

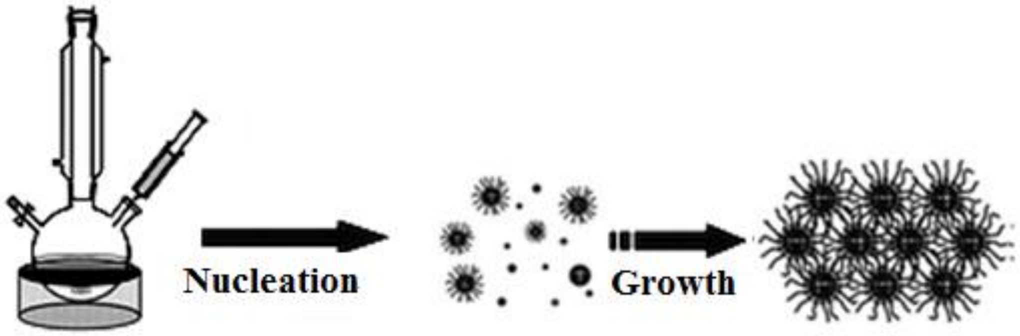

Fig. 1.11 Hot injection method[19]

The size and shape of the nanoparticles are affected by the concentration of precursors, reaction time, temperature, heating rate, and capping agent.

Generally, size of nanoparticles increases with increasing growth temperature because kinetically, the rate of addition of nuclei to the existing ones increases. However, more often, thermolysis in a higher boiling point solvent gives a larger diameter than a lower boiling point solvent. This can be explained by the higher reactivity of the precursors in higher boiling point solvents.[76,77] Also there are several reports which have shown that shorter reaction time gives smaller particles compared to longer reaction times,[9] due to focusing or defocusing in size.

The shape of ferrite nanoparticles can be directed by controlling the heating rate and temperature. Spherical nanoparticles are usually obtained when the heating rate is high leading to a rapid nucleation and depletion of monomer concentration, hence non-selective crystal growth takes place and the thermodynamically favoured spheres are formed. However, with a slower heating rate, a limited number of nuclei are formed, leaving a high monomer concentration in solution. The remaining monomers are thus added slowly on the few existing nuclei which then to grow in a particular direction leading to the evolution of different shapes such as cubes and stars.[78–80]

The concentration of precursor also plays a crucial role in the size of the ferrite nanoparticles. Higher precursor concentration usually leads to the formation of smaller nanoparticles because at higher concentration, more nuclei are generated as compared to that of the lower concentration, hence more the nuclei slows down the growth and smaller size of the nanoparticles are formed.[81,82]

Capping agents constrain the growth of nanoparticles by providing a steric barrier between them and thus prevent them from aggregation. The use of long-chain alkyl groups provides better steric hindrance compared to short-chain variants.[83] The nanoparticles synthesised are isolated from the reaction mixture by the addition of a suitable polar solvent followed by centrifugation. The nanoparticles obtained after centrifugation can then be redispersed in a variety of non-polar solvent. The size distribution of the nanoparticles can be made narrower by the gradual addition of an anti-solvent such as methanol, this leads to the flocculation of the heavier/larger particles whilst the smaller particles remained dispersed in the supernatant. Common capping agents for ferrite nanoparticles are: oleylamine, oleic acid and HDA.

Thermal decomposition methods have been used to successfully synthesise ferrite nanoparticles of different sizes and shapes including iron oxide[75,76,84–94]cobalt ferrite,[79,80,82,92,95–100] nickel ferrite,[92,99] manganese ferrite[92,100,95]and zinc ferrite.[101,102]

1.3.4 Single Molecular Precursors for Ferrite Nanoparticles

A single source precursor (SSP) is a molecular compound containing all the elements required to form the ferrite nanoparticles. There are a number of organometallic compounds that have been used as SSPs for the synthesis of iron oxide nanoparticles. Alivisatos *et al* in 1999 first developed the thermal decomposition method for producing monodispersed iron oxide nanoparticles by the thermolysis of cupferron complexes in octyl amine.[103] In 2001, Hyeon *et al* further developed the process by thermolysing iron pentacarbonyl ($Fe(CO)_5$) in a mixture of oleic acid and octyl ether. They obtained monodispersed iron oxide nanoparticles without a size selection process.[104] Similarly using the same ($Fe(CO)_5$), different shapes and sizes of iron oxide have been obtained.[76,85,89,94,105,106] The synthesis of monodispersed magnetite of diameter less than 20 nm by the thermolysis of iron(III) acetylacetonate, [$Fe(acac)_3$], was first reported by Sun in 2002. A host of other researchers have used the same [$Fe(acac)_3$] to produce monodispersed magnetite nanoparticles with size ranging from 3 to 20 nm.[76,84,90,91,93,107] Recently, a less toxic iron oleate complex[75–77,87,108] has been used to synthesise iron oxide nanoparticles. However only very few SSPs have been used for ternary ferrite nanoparticles. Moriya and co-workers synthesised various morphologies of cobalt, nickel and manganese ferrite nanoparticles by the thermolysis of heterometallic acetate complexes with benzilic acid as the capping agent.[100] The shape obtained was dependent on the molar ratio between the complex and the benzilic acid. A very high ratio of complex to benzilic acid produced spherical nanoparticles whilst cubes were obtained with a very low ratio. Similarly, using the same complex, Naidek *et al.* synthesised cubic magnetite, cobalt ferrite and nickel ferrite nanoparticles but with oleylamine and oleic acid as capping agents.[99] A hydrothermal approach was used by Chen and co-workers to synthesise ferrite nanoparticles with the same complex without any capping agents, obtaining spherical nanoparticles of zinc, cobalt and nickel and manganese ferrite.[45] Also mixed metal oleate complexes have been used to grow different shapes of ferrite nanoparticles including spherical, cubic and star-like.[78,79,92]

1.4. Functionalisation of magnetic nanoparticles

Magnetic nanoparticles exhibit unique properties including superparamagnetism and quantum tunnelling due to their small size and high surface to volume ratio. Superparamagnetic nanoparticles have attracted a lot of attention particularly in the field of biomedicine, biology and environment. These applications usually require monodispersed nanoparticles of high saturation magnetisation, colloidal stability in biological environment, non-toxic and controlled interaction or specificity. Although thermal decomposition method has been proven to produce monodispersed nanoparticles, the ferrofluids obtained are usually hydrophobic. More often, biological applications require water soluble nanoparticles, it therefore means there is need to transfer or change the capping agents for hydrophobic nanoparticles. A commonly used method for transferring hydrophobic ferrite nanoparticles to a water soluble one is by modifying the surface or overcoating with a water soluble polymer. Li *et al*. synthesised iron oxide nanoparticles capped with hexadecylamine (HDA) and then modified the surface by overcoating with amine modified Poly Acrylic Acid (PAA) to make them dispersible in water.[84] Other surface modifications to make ferrite nanoparticles hydrophilic include using glucosamic acid,[94] modified polyethylene glycol,[93] alkyl phosphanate modified with fatty acid,[96] modified polymaleic anhydride,[109,110] methyl catechol.[111]

Alternatively, the nanoparticles could be prepared by thermal decomposition as a one pot water soluble nanoparticles using amphiphilic polymers or strong polar solvents as capping agents.[107, 112,113]

In order to make these nanoparticles target specific, surface reactive molecules such as carboxylic acid, amine or thiol group must be present which can be further conjugated or coupled via amide or ester bonds to antibodies, proteins or other specific ligands.[114] FT-IR is an important spectroscopic tool for studying the ligand attachment on the surface of nanoparticles.

1.5 Characterisation techniques

In recent years, the invention of powerful analytical tools in recent years like the Transmission Electron Microscope (TEM) has made the study of nanoparticles more versatile and interesting. In addition, there are other characterisation techniques that were used to characterise the ferrite nanoparticles and will be discussed below:

1.5.1 Powder X-ray diffraction (p-XRD)

The p-XRD is used for the identification, purity and phase of a crystalline material. It is a rapid, non-destructive method and it is based on constructive interference of X-rays and a sample. The X-rays generated by a cathode ray tube are filtered and directed to the sample. Diffracted X-rays are produced when Bragg's Law is satisfied ($n\lambda=2d \sin \theta$).Where λ is the wavelength of x-ray, n is the order, d is the spacing between two crystal planes and θ the diffraction angle. The identification is achieved by processing the diffracted rays. These diffracted rays (2θ) are converted to *d*-spacings which are then matched with standard reference patterns stored in the ICDD (International Centre for Diffraction Data) database. An X-ray diffractometer is comprised principally of an X-ray tube, a sample holder and an X-ray detector/monitor. In the X-ray tube, lies a cathode ray tube which generates electrons; these are accelerated towards a metal anode target by applying a potential difference. Incident electrons with sufficient energy remove inner shell electrons of the metal atoms in the anode and therefore X-rays are emitted which are then directed towards the sample. Typical anode materials include Cu (most common), Co, Mo, Fe and Cr.

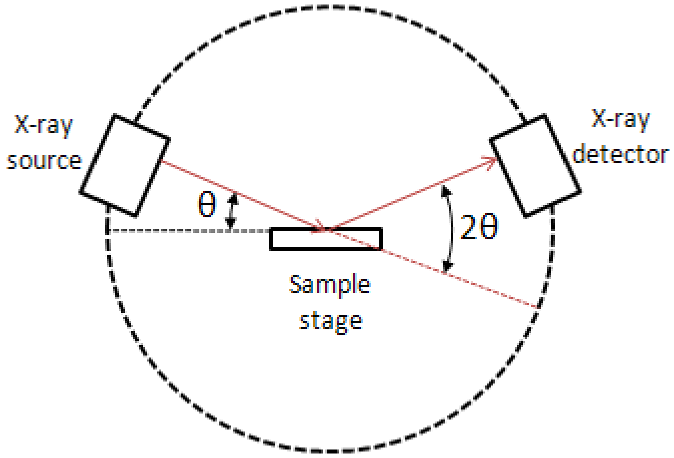

Fig. 1.12 Schematic of X-ray diffractometer[115]

Another application of XRD is in the determination of crystallite size. This can be done by evaluating the broadness of the peak using the Scherrer equation:

$$D = k\lambda/\beta\cos\theta \qquad (1.7)$$

Where D is the particle diameter, K is Scherrer constant, λ is the wavelength, θ is the angle of diffraction and β is the Full width at half maximum (FWHM) of a reflection.

1.5.2 Transmission electron microscopy (TEM)

A microscope is an instrument that provides visual images of samples and has three main functions:

1. Resolution: The ability to provide the finest detail of the sample in its image.
2. Magnification: To make the sample big enough to be seen and resolved by the eye.
3. Contrast: To differentiate between the features of the image be seen and its immediate environment.

However, the ability of the microscope to perform these functions depends on the wavelength of the imaging radiation. The wavelength of light used in the conventional light/optical microscopes is about 0.4 µm (400 nm) thereby inherently limiting resolution. With the advent of the transmission electron microscope, a potential 100, 000 fold resolution can be attained and this is because the wavelength of the electron is very small (0.005 nm). Hence TEM is a very important analytical tool in visualising the shapes and sizes of nanoparticles. However, the resolving power of TEM is limited by some factors such as spherical and chromatic aberrations which are as a result of imperfection in lenses. TEM operates by passing a high voltage electron beam through a very thin sample. The electron beam is produced by an electron gun and then accelerated by an anode usually between 100-400 kV. The electron beam is then focused by the electromagnetic lenses. It is then passed through a very thin sample where some are scattered, lost or transmitted. The transmitted one then passes through the objective lens where the information about the structure of the sample is magnified. The image is then projected onto a fluorescent screen or the image can be recorded on a special photographic film.

High resolution Transmission electron microscopy (HRTEM) provides atomic resolution in images of nanoparticles. These are seen as lattice fringes in the image and indicate that the sample is crystalline. The *d*- spacing can be calculated from the lattice fringe which can then be compared with crystallographic data to determine the plane of growth. Information about the crystal structure can also be obtained using selected area electron diffraction (SAED). SAED is similar to X-ray diffraction but the Bragg's angle is very small. SAED of a single crystal is can be seen as an array of regular spots but in multicrystals, continuous ring is observed.

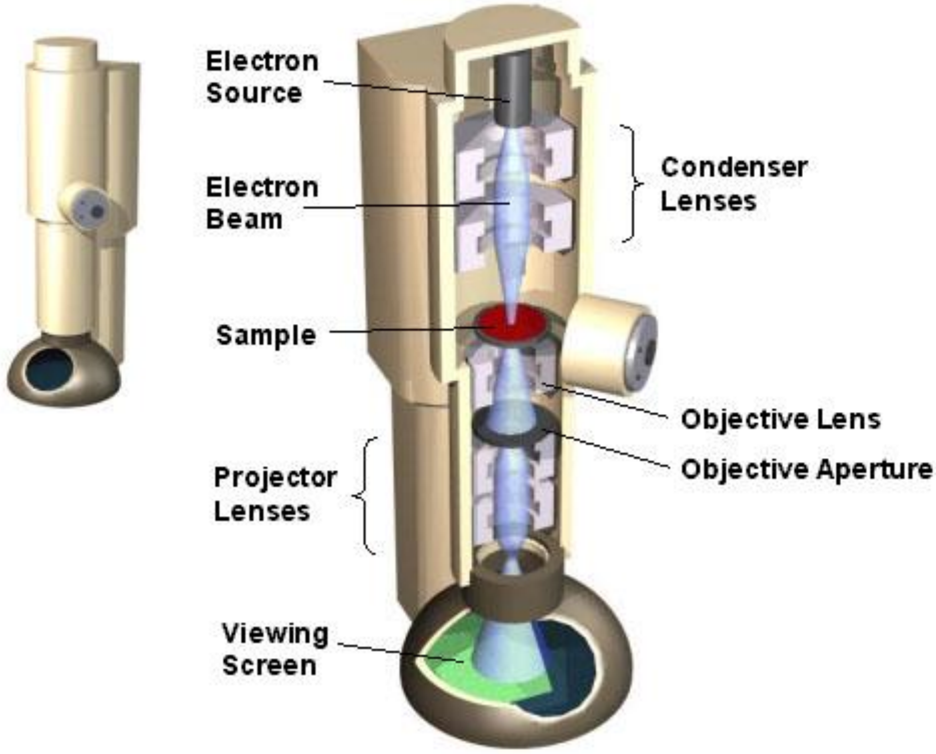

Fig. 1.13 Schematic of a TEM.[116]

1.5.3 Energy dispersive X-ray spectroscopy (EDX)

EDX is an analytical tool which is used to determine the elemental composition of a sample in a TEM or Scanning electron microscope (SEM). It works on the principle that each element has a unique electronic structure which gives rise to a unique pattern of peaks when it interacts with electromagnetic radiations.

EDX is done by focusing a high energy electron beam on a sample; this beam removes an electron from the inner shell thereby creating a hole. This hole is then filled by an electron from a higher energy shell and the difference in energy may be released in the form of X-ray fluorescence which is then measured by the spectrometer. EDX is used qualitatively by assigning the energies of X-rays emitted to corresponding elements present.

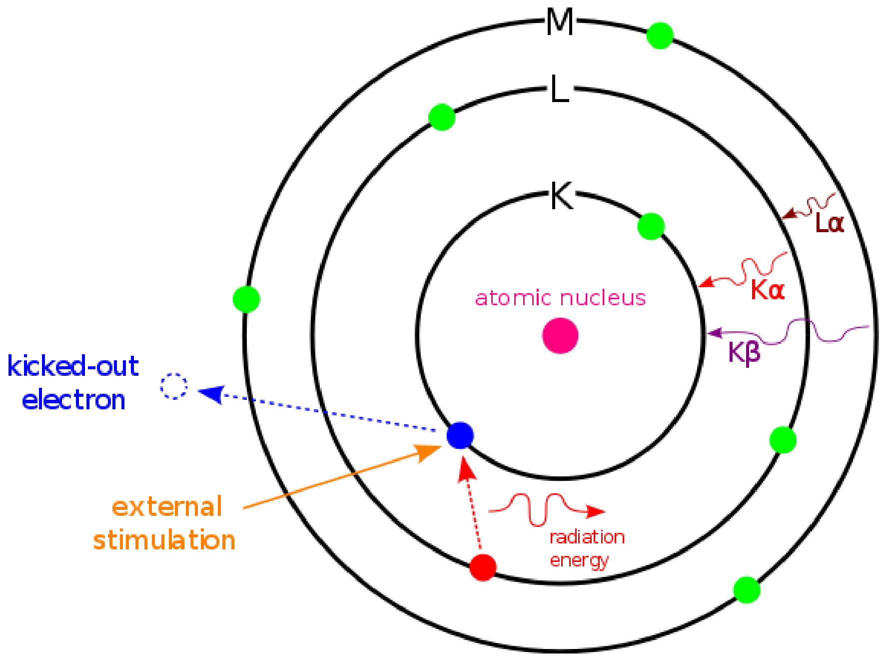

Fig. 1.14 Principle of EDX.[117]

1.5.4 Inductively coupled plasma-optical emission spectroscopy (ICP-OES).

ICP/OES is a very powerful analytical tool for the determination of trace elements. The technique is based on characteristic emission from excited atoms and ions in the plasma. Liquid sample is nebulised into plasma where the temperature is sufficiently high (10,000 K) to liberate the element into free gaseous atoms. These free gaseous atoms are further energised within the plasma promoting them from the ground to the excited state. On relaxation, they emit radiation at wavelength characteristic of the element present and thus can be used for qualitative analysis. The intensity of the radiation is directly proportional to the concentration of the element present in the sample and so can be used quantitatively. In this work, ICP-OES was used to determine the stoichiometry of ternary and quaternary ferrite nanoparticles.

ICP has the following advantages:

1. High temperature (up to 10000 K) hence appreciable degree of ionisation for many elements including refractory elements.
2. Very stable resulting in high accuracy and precision.

3. Very low detection limits. (ICP-MS - Inductively coupled plasma Mass spectrometry can measure as low as parts per trillion (ppt) concentrations).
4. Cost effective.

1.5.5 Superconducting Quantum Interference Device (SQUID) Magnetometry

Magnetic measurements based on SQUID technology are currently the most sensitive because they are capable of measuring magnetic moments in the order of 10^{-7} emu.[118] When certain materials are cooled below a certain critical temperature, they become superconductors; the resistance to the flow of electricity becomes zero. If a line of magnetic flux is threaded through a ring made of a superconducting material, it induces a current which can continue to flow unless disturbed. The magnitude of this current is proportional to the flux density; the measurement of magnetic flux together with Josephson junction forms the operation of SQUID. A Josephson junction consists of a very thin layer of insulator between two superconductors where the layer is thin enough to allow the flow of supercurrent. In the SQUID coil, two Josephson junctions are used. When a magnetic material is moved through the coil, the magnetic moment of the sample induces an electric current which leads to changes in phase at the two Josephson junctions. Because the current passing through the superconductors has been quantized, the change in current can be evaluated and correlated to the magnetic flux of the sample.[118]

Magnetic measurements using the SQUID can either be field dependent or temperature dependent. The field dependent measurement of a magnetic sample is carried out at a constant temperature to get the saturation magnetisation (Ms). Temperature dependent measurements are performed under a constant field- zero field cooled (ZFC) and field cooled (FC). In ZFC measurements, the sample is cooled from room temperature to 2 or 5 K, in a zero dc-field. Then a small magnetic field of ca. 100 Oe is applied and the magnetization is recorded on warming whilst in FC measurements, the sample is cooled from room temperature under an applied magnetic field. In this thesis, magnetic measurements were performed on a Quantum Design MPMS-XL SQUID magnetometer equipped with a 7 T magnet.

1.6 Applications

Ferrite nanoparticles have found applications in various fields including biomedical, environmental remediation, information storage and gas sensors. Some of these applications will be discussed below.

1.6.1 Magnetic resonance imaging (MRI) contrast agents

Magnetic resonance imaging (MRI) was invented in the 1970's and it is a powerful clinical diagnostic tool for imaging of human internal organs. It has advantage over the use of X-rays based imaging method because it doesn't infiltrate or penetrate into healthy tissues. It is based on the relaxation signals of hydrogen spins within the human when excited by pulses of radio waves in a strong magnetic field. The human body is composed of fat and water both having protons/ hydrogen atoms. In the presence of magnetic field, the protons spin and align in the direction of the external field. The spinning protons precess about the axis of the applied magnetic field at its resonance or Larmor frequency. If an electromagnetic radio frequency (RF) is introduced at this Larmor frequency, the protons will absorb this energy and become excited.[119] When the RF is turned off, two things happen at the same time.

First, the protons relax to its original orientation and the time taken to achieve this called the recovery rate (T1) is constant and unique for every tissue. This is also called longitudinal relaxation. Secondly, the absorbed energy is retransmitted and finally, the excited spins that were initially in phase begin to de-phase, this is a transverse relaxation known as T2 and is also unique for every tissue.

The uniqueness of T1 and T2 is the basis for the MRI differentiation of tissues in the body. In order to enhance the contrast between a diseased and a healthy tissue, an MRI contrast agent is introduced to reduce the T1 and T2 relaxation times of surrounding protons thereby giving rise to a positive/ sharp contrast. Superparamagnetic ferrite nanoparticles can produce spin-spin relaxation effects and so are used as contrast agents. There are a number of commercially available iron oxide contrast agents such as Abdoscan, GastroMARK, Resovist, Feridex.[112]

1.6.2 Drug delivery and Hyperthermia

Hyperthermia treatment of cancerous cells is a supplementary treatment to chemotherapy or radiotherapy. It works on the principle that when magnetic nanoparticles are exposed to an alternating field, they generate heat which can be used to destroy the cancerous cells.[16] The nanoparticles can be made to target only the tumour cells by functionalisation with an appropriate antibody.[120]

Magnetite nanoparticles have been used to achieve localised drug delivery by functionalisation with bioactive agents. It works on the principle that when the functionalised ferrite nanoparticles are injected, they are guided under the influence of external magnetic field to a specific location and held there until the therapy is over and they are removed.[16] Superparamagnetic ferrite nanoparticles are very promising for this application because once the external field is removed, they do not aggregate.

1.6.3 Remediation of water

Water resources are continuously being contaminated as a result of human, industrial and agricultural activities. These contaminants could be in form of toxic metals including arsenics As(V), As(III), chromium (Cr(VI) and uranium all of which are carcinogenic. Many dyes from the textile industries are toxic and mutagenic and affect the aesthetics of water if discharged directly into the water body.

The removal of these contaminants is therefore a major concern. Although various physical and chemical methods have been employed but there is still need to develop efficient and environmental friendly approach for the removal of these contaminants. In view of this, iron oxide nanoparticles have been functionalised in various ways to serve as an adsorbent and subsequent removal of some of these contaminants. For example iron oxides functionalised with oleic acids have been employed for the removal of arsenic in aqueous solution.[120] Similarly, iron oxides functionalised with calixerenes have been used to remove arsenate and chromate ions by liquid/liquid extraction.[121] In other ways, ferrite nanoparticles have been functionalised and used as magnetic separator to isolate microorganisms needed for the remediation of dye polluted water in textile industries and also in biodesulfurisation in the oil company.[122,123]

Ferrite nanoparticles can also be combined with mesoporous materials to build a magnetic mesoporous nanocomposites which have potential applications in water treatment and industrial sorbents.[124]

1.6.4 Catalysis

Ferrite nanoparticles can be coupled with some catalysts and thus provide a wider surface area for reaction to take place due to their small size. These catalysts could also be recovered by magnetic decantation and can be reused for up to ten times without loss of activity. For example, magnetite nanoparticles were coupled to a chiral catalyst used in the hydrogenation of aromatic alkenes by Hu *et al*.[125] The recycling of catalyst by magnetic separation is an economical way of recovering expensive ligands or catalyst and is easier than using other methods such as flow filtration or centrifugation.[16]

Lu *et al*. developed a high surface magnetically separable catalyst by coating cobalt nanoparticles with carbon and the resulting superparamagnetic pore system was functionalised with palladium and used in the hydrogenation process. The catalyst showed a very high activity and could easily be recovered by magnetic separation.[126] The same principles in theory could be extended to other ferrite nanoparticles.

1.6.5 Electronics

Ferrites can be classified into soft and hard depending on their ability to be magnetised and demagnetised. While soft ferrites are easily magnetised, have low coercivity, hard ferrites on the other hand are not easily magnetised and have a high coercivity; hence do not lose their magnetism easily. Soft ferrite and has found applications in heads, ac motors and generators.[41] Hard ferrites have been used in data storage and magnetic recording media.[14] Cobalt ferrite is known to have a high coercivity and thus find application in information storage.

1.7 Aims and scope of present study

In the continued search for other single source precursors that could be used in the synthesis of these important ferrite nanoparticles, iron based pivalate clusters have been used for the first time as single source precursors for the synthesis of hydrophobic magnetite, ternary ferrite of cobalt, nickel, zinc, manganese and quaternary iron cobalt chromium ferrite. Furthermore, the same set of precursors was used to synthesise water soluble ferrite by the thermal decomposition method. In order to establish the cation site occupancies of these ferrite nanoparticles, analysis have been performed using X-ray Magnetic Circular Dichroism (XMCD).

1.8 References

1. J. R. Lead and K. J. Wilkinson, *Environ. Chem.*, 2006, **3**, 159.
2. J. Pérez-Arantegui, J. Molera, A. Larrea, T. Pradell, M. Vendrell-Saz, I. Borgia, B. G. Brunetti, F. Cariati, P. Fermo, M. Mellini, A. Sgamellotti, and C. Viti, *J. Am. Ceram. Soc.*, 2004, **84**, 442.
3. M. Faraday, *Phil. Trans. R. Soc. London*, 1857, **147**, 145.
4. P. J. Thomas and G. U. Kulkarni, *Nanocrystals: Synthesis, Properties and Applications (Google eBook)*, Springer, 2007.
5. G. Bredig, *Z . Angew. Chem.*, 1898, **11**, 951.
6. R. Zsigmondy, *Z. Phys. Chem.*, 1906, **56**, 65.
7. J. Turkevich, P. C. Stevenson, and J. Hillier, *Discuss. Faraday Soc.*, 1951, **11**, 55.
8. M. Brust, M. Walker, D. Bethell, D. J. Schiffrin, and R. Whyman, *Chem. Commun.*, 1994, 801.
9. C. Burda, X. Chen, R. Narayanan, and M. A. El-Sayed, *Chem. Rev.*, 2005, **105**, 1025.
10. C.N.R. Rao, A. Muller, and A. K. Cheetham, *The Chemistry of Nanomaterials, Synthesis, Properties and Applications Vol. 1*, WILEY-VCH, 2004.
11. C. Altavilla and E. Ciliberto, *Inorganic Nanoparticles: Synthesis, Applications, and Perspectives (Google eBook)*, CRC Press, 2010, vol. 2010.
12. S. P. Gubin, *Magnetic Nanoparticles*, WILEY-VCH, 2009.
13. D.C. William and D.G. Rethwisch, *Wiley: Fundamentals of Materials Science and Engineering, 4th Edition SI Version*, 2012.
14. D. S. Mathew and R.-S. Juang, *Chem. Eng. J.*, 2007, **129**, 51.
15. R. J. Pankhurst, Q.A., Pollard, *J. Phys. Condens. Matter*, 1993, **5**, 8487.
16. A. H. Lu, E. L. Salabas, and F. Schüth, *Angew. Chem. Int. Ed.*, 2007, **46**, 1222.
17. M. Arruebo, R. Fernández-pacheco, M. R. Ibarra, and J. Santamaría, *Nanotoday*, 2007, **2**, 22.
18. N. K. Devaraj, B. H. Ong, and M. Matsumoto, *Syn. React. Inorg. Met.Org. Nano-Met. Chem.*, 2008, **38**, 208.
19. J. Park, J. Joo, S. G. Kwon, Y. Jang, and T. Hyeon, *Angew. Chem. Int. Ed.*, 2007, **46**, 4630.
20. S. G. Kwon and T. Hyeon, *Small*, 2011, **7**, 2685.
21. S. Kumar and T. Nann, *Small*, 2006, **2**, 316.
22. D. V Talapin, J.-S. Lee, M. V Kovalenko, and E. V Shevchenko, *Chem. Rev.*, 2010, **110**, 389.

23. P. Christian, F. Von der Kammer, M. Baalousha, and T. Hofmann, *Ecotoxicology* 2008, **17**, 326.
24. R. H. Kodama, *J. Magn. Magn. Mater.*, 1999, **200**, 359.
25. R.M. Cornell and U. Schwertmann, *The Iron Oxides: Structure, Properties, Reactions, Occurences and Uses.*, Wiley VCH, 2nd Edition., 2003.
26. M. Friák, A. Schindlmayr, and M. Scheffler, *New J. Phys.*, 2007, **9**, 5.
27. T. Sugimoto and E. Matijevic, *J. Colloid Interface Sci.*, 1980, **74**, 227.
28. R. T. Olsson, G. Salazar-Alvarez, M. S. Hedenqvist, U. W. Gedde, F. Lindberg, and S. J. Savage, *Chem. Mater.*, 2005, **17**, 5109.
29. P. Sivakumar, R. Ramesh, A. Ramanand, S. Ponnusamy, and C. Muthamizhchelvan, *J. Mater. Sci- Mater. Electron.*, 2011, **23**, 1041.
30. I. Martínez-Mera, M. E. Espinosa-Pesqueira, R. Pérez-Hernández, and J. Arenas-Alatorre, *Mater. Lett.*, 2007, **61**, 4447.
31. J. Mürbe, A. Rechtenbach, and J. Töpfer, *Mater. Chem. Phys.*, 2008, **110**, 426.
32. K. Maaz, A. Mumtaz, S. K. Hasanain, and A. Ceylan, *J. Magn. Magn. Mater.*, 2007, **308**, 289.
33. F. Dang, N. Enomoto, J. Hojo, and K. Enpuku, *J. Cryst. Growth*, 2010, **312**, 1736.
34. Y. Qi, Y. Yang, X. Zhao, X. Liu, P. Wu, F. Zhang, and S. Xu, *Particuology*, 2010, **8**, 207.
35. C. Yang and H. Yan, *Mater. Lett.*, 2012, **73**, 129.
36. Y. Tian, B. Yu, X. Li, and K. Li, *J. Mater. Chem.*, 2011, **21**, 2476.
37. J. Wang, M. Yao, G. Xu, P. Cui, and J. Zhao, *Mater. Chem. Phys.*, 2009, **113**, 6.
38. X. Jia, D. Chen, X. Jiao, and S. Zhai, *Chem. Commun.*, 2009, 968.
39. L. J. Cote, A. S. Teja, A. P. Wilkinson, and Z. J. Zhang, *Fluid Phase Equilib.*, 2003, **210**, 307.
40. L. Zhao, H. Zhang, Y. Xing, S. Song, S. Yu, W. Shi, X. Guo, J. Yang, Y. Lei, and F. Cao, *J. Solid State Chem.*, 2008, **181**, 245.
41. K. Nejati and R. Zabihi, *Chem. Cent. J.*, 2012, **6**, 23.
42. S. Yáñez-Vilar, M. Sánchez-Andújar, C. Gómez-Aguirre, J. Mira, M. A. Señarís-Rodríguez, and S. Castro-García, *J. Solid State Chem.*, 2009, **182**, 2685.
43. X. Li, G. Tan, W. Chen, B. Zhou, D. Xue, Y. Peng, F. Li, and N. J. Mellors, *J. Nanopart. Res.*, 2012, **14**, 751.
44. J. Wang, *Mater. Sci. Eng., B*, 2006, **127**, 81.
45. L. Chen, Y. Shen, and J. Bai, *Mater. Lett.*, 2009, **63**, 1099.
46. J. Huo and M. Wei, *Mater. Lett.*, 2009, **63**, 1183.

47. Y. Cheng, Y. Zheng, Y. Wang, F. Bao, and Y. Qin, *J. Solid State Chem.*, 2005, **178**, 2394.
48. W. Cheng, K. Tang, and J. Sheng, *Chem. Eur. J.*, 2010, **16**, 3608.
49. D. Lagevin, *Annu. Rev. Phys. Chem.*, 1992, **43**, 341.
50. K. Woo, H. J. Lee, J.-P. Ahn, and Y. S. Park, *Adv. Mater.*, 2003, **15**, 1761.
51. Y. Lee, J. Lee, C. J. Bae, J.-G. Park, H.-J. Noh, J.-H. Park, and T. Hyeon, *Adv. Funct. Mater.*, 2005, **15**, 503.
52. C. Liu, B. Zou, A. J. Rondinone, and Z. J. Zhang, *J. Phys. Chem. B*, 2000, **104**, 1141.
53. N. Moumen and M. P. Pileni, *J. Phys. Chem.*, 1996, **100**, 1867.
54. O. Döker, E. Bayraktar, Ü. Mehmetoðlu, and A. Çalimli, *Rev. Adv. Mater. Sci.*, 2003, **5**, 498.
55. F. Grasset, N. Labhsetwar, D. Li, D. C. Park, N. Saito, H. Haneda, O. Cador, T. Roisnel, S. Mornet, E. Duguet, J. Portier, and J. Etourneau, *Langmuir*, 2002, **18**, 8209.
56. R. P. Blakemore, *Science*, 1975, **190**, 377.
57. D. Schüler, *J. Mol Micro. Biotech.*, 1999, **1**, 79.
58. Abhilash, K. Revati, and B. D. Pandey, *Bull. Mater. Sci.*, 2011, **34**, 191.
59. V. S. Coker, N. D. Telling, G. van der Laan, R. A. D. Pattrick, C. I. Pearce, E. Arenholz, F. Tuna, R. E. P. Winpenny, and J. R. Lloyd, *ACS Nano*, 2009, **3**, 1922.
60. K. B. Narayanan and N. Sakthivel, *Adv. Colloid Interface Sci.*, 2010, **156**, 1.
61. Y. Roh, R. J. Lauf, A. D. McMillan, C. Zhang, C. J. Rawn, J. Bai, and T. J. Phelps, *Solid State Commun.*, 2001, **118**, 529.
62. W. Li, L. Yu, P. Zhou, and M. Zhu, *World J. Microbiol. Biotechnol.*, 2007, **23**, 1489.
63. C. T. Lefèvre, F. Abreu, M. L. Schmidt, U. Lins, R. B. Frankel, B. P. Hedlund, and D. A. Bazylinski, *Appl. Environ. Microbiol.*, 2010, **76**, 3740.
64. W. Zhou, W. He, S. Zhong, Y. Wang, H. Zhao, Z. Li, and S. Yan, *J. Magn. Magn. Mater.*, 2009, **321**, 1025.
65. T. Perez-Gonzalez, C. Jimenez-Lopez, A. L. Neal, F. Rull-Perez, A. Rodriguez-Navarro, A. Fernandez-Vivas, and E. Iañez-Pareja, *Geochim. Cosmochim. Acta*, 2010, **74**, 967.
66. Y. Amemiya, A. Arakaki, S. S. Staniland, T. Tanaka, and T. Matsunaga, *Biomaterials*, 2007, **28**, 5381.
67. L. W. Yeary, L. J. Love, J. R. Thompson, C. J. Rawn, and T. J. Phelps, *IEEE Trans. Magn.*, 2005, **41**, 4384.

68. A. Bharde, D. Rautaray, V. Bansal, A. Ahmad, I. Sarkar, S. M. Yusuf, M. Sanyal, and M. Sastry, *Small*, 2006, **2**, 135.
69. V. S. Coker, C. I. Pearce, C. Lang, G. van der Laan, R. A. D. Pattrick, N. D. Telling, D. Schüler, E. Arenholz, and J. R. Lloyd, *Eur. J. Mineral.*, 2007, **19**, 707.
70. A. P. Philipse and D. Maas, *Langmuir*, 2002, **18**, 9977.
71. D. A. Bazylinski, R. B. Frankel, and H. W. Jannasch, *Nature*, 1988, **334**, 518.
72. V. S. Coker, J. A. Bennett, N. D. Telling, T. Henkel, J. M. Charnock, G. van der Laan, R. A. D. Pattrick, C. I. Pearce, R. S. Cutting, I. J. Shannon, J. Wood, E. Arenholz, I. C. Lyon, and J. R. Lloyd, *ACS Nano*, 2010, **4**, 2577.
73. J. W. Moon, Y. Roh, R. J. Lauf, H. Vali, L. W. Yeary, and T. J. Phelps, *J. Microbiol. Methods*, 2007, **70**, 150.
74. L. W. Yeary, J. W. Moon, C. J. Rawn, L. J. Love, A. J. Rondinone, J. R. Thompson, B. C. Chakoumakos, and T. J. Phelps, *J. Magn. Magn. Mater.*, 2011, **323**, 3043.
75. S. G. Kwon, Y. Piao, J. Park, S. Angappane, Y. Jo, N.-M. Hwang, J.-G. Park, and T. Hyeon, *J. Am. Chem. Soc.*, 2007, **129**, 12571.
76. A. G. Roca, M. P. Morales, and C. J. Serna, *IEEE Trans. Magn.*, 2006, **42**, 3025.
77. J. Park, K. An, Y. Hwang, J.-G. Park, H.-J. Noh, J.-Y. Kim, J.-H. Park, N.-M. Hwang, and T. Hyeon, *Nat. Mater.*, 2004, **3**, 891.
78. N. Bao, L. Shen, W. An, P. Padhan, C. Heath Turner, and A. Gupta, *Chem. Mater.*, 2009, **21**, 3458.
79. N. Bao, L. Shen, P. Padhan, and A. Gupta, *Appl. Phys. Lett.*, 2008, **92**, 173101.
80. Q. Song and Z. J. Zhang, *J. Am. Chem. Soc.*, 2004, **126**, 6164.
81. E. V Shevchenko, D. V Talapin, H. Schnablegger, A. Kornowski, O. Festin, P. Svedlindh, M. Haase, and H. Weller, *J. Am. Chem. Soc.*, 2003, **125**, 9090.
82. C. A. Crouse and A. R. Barron, *J. Mater. Chem.*, 2008, **18**, 4146.
83. C. B. Murray, D. J. Norris, and M. G. Bawendi, *J. Am. Chem. Soc.*, 1993, 8706.
84. Y. Li, M. Afzaal, and P. O’Brien, *J. Mater. Chem.*, 2006, **16**, 2175.
85. M. F. Casula, Y. Jun, D. J. Zaziski, E. M. Chan, A. Corrias, A. P. Alivisatos, M. Science, and L. Berkeley, *J. Am. Chem. Soc.*, 2006, **128**, 1675.
86. A. G. Roca, M. P. Morales, K. O’Grady, and C. J. Serna, *Nanotechnology*, 2006, **17**, 2783.
87. A. Shavel and L. M. Liz-Marzán, *Phys. Chem. Chem. Phys.*, 2009, **11**, 3762.
88. S. Sun and H. Zeng, *J. Am. Chem. Soc.*, 2002, **124**, 8204.
89. K. Woo, J. Hong, S. Choi, H. Lee, J. Ahn, C. S. Kim, and S. W. Lee, *Chem. Mater.*, 2004, **16**, 2814.

90. V. Yathindranath, L. Rebbouh, D. F. Moore, D. W. Miller, J. van Lierop, and T. Hegmann, *Adv. Funct. Mater.*, 2011, **21**, 1457.
91. E. Umut, F. Pineider, P. Arosio, C. Sangregorio, M. Corti, F. Tabak, A. Lascialfari, and P. Ghigna, *J. Magn. Magn. Mater.*, 2012, **324**, 2373.
92. N. Bao, L. Shen, Y. Wang, P. Padhan, and A. Gupta, *J. Am. Chem. Soc.*, 2007, **129**, 12374.
93. T. Kikuchi, R. Kasuya, S. Endo, A. Nakamura, T. Takai, N. Metzler-Nolte, K. Tohji, and J. Balachandran, *J. Magn. Magn. Mater.*, 2011, **323**, 1216.
94. C. Yu, J. Zhao, Y. Guo, C. Lu, X. Ma, and Z. Gu, *J. Biomed. Mater. Res.*, 2008, **87**, 364.
95. S. Sun, H. Zeng, D. B. Robinson, S. Raoux, P. M. Rice, S. X. Wang, and G. Li, *J. Am. Chem. Soc.*, 2004, **126**, 273.
96. D. B. Robinson, H. H. J. Persson, H. Zeng, G. Li, N. Pourmand, S. Sun, and S. X. Wang, *Langmuir*, 2005, **21**, 3096.
97. T. Hyeon, Y. Chung, J. Park, S. S. Lee, Y.-W. Kim, and B. H. Park, *J. Phys. Chem. B*, 2002, **106**, 6831.
98. S. Verma and D. Pravarthana, *Langmuir*, 2011, **27**, 13189.
99. K. P. Naidek, F. Bianconi, T. C. R. da Rocha, D. Zanchet, J. A. Bonacin, M. A. Novak, M. D. G. F. Vaz, and H. Winnischofer, *J. Colloid Interface Sci.*, 2011, **358**, 39.
100. M. Moriya, M. Ito, W. Sakamoto, and T. Yogo, *Cryst. Growth Des.*, 2009, **9**, 1889.
101. C. Bárcena, A. K. Sra, G. S. Chaubey, C. Khemtong, J. P. Liu, and J. Gao, *Chem. Commun.*, 2008, 2224.
102. J. Wan, X. Jiang, H. Li, and K. Chen, *J. Mater. Chem.*, 2012, **22**, 13500.
103. E. C. Scher and A. P. Alivisatos, *J. Am. Chem. Soc.*, 1999, **121**, 11595.
104. T. Hyeon, S. S. Lee, J. Park, Y. Chung, and H. B. Na, *J. Am. Chem. Soc.*, 2001, **123**, 12798.
105. J. Cheon, N.J. Kang, S.M. Lee, J.-H. Lee, J.H. Yoon, and S. J. Oh, *J. Am. Chem. Soc.*, 2004, **126**, 1950.
106. X. Teng and H. Yang, *J. Mater. Chem.*, 2004, **14**, 774.
107. Z. Li, H. Chen, H. Bao, and M. Gao, *Chem. Mater.*, 2004, **16**, 1391.
108. N. R. Jana, Y. Chen, and X. Peng, *Chem. Mater.*, 2004, **16**, 3931.
109. T. Pellegrino, L. Manna, S. Kudera, T. Liedl, D. Koktysh, A. L. Rogach, S. Keller, J. Ra, G. Natile, and W. J. Parak, *Nano Lett.*, 2004, **4**, 703.
110. W. W. Yu, E. Chang, C. M. Sayes, R. Drezek, and V. L. Colvin, *Nanotechnology*, 2006, **17**, 4483.

111. J. Xie, K. Chen, H. Y. Lee, C. Xu, A. R. Hsu, S. Peng, X. Chen, and S. Sun, *J. Am. Chem. Soc.*, 2008, **130**, 7542.
112. R. Qiao, C. Yang, and M. Gao, *J. Mater. Chem.*, 2009, **19**, 6274.
113. Z. Li, L. Wei, M. Y. Gao, and H. Lei, *Adv. Mater.*, 2005, **17**, 1001.
114. R. Mout, D. F. Moyano, S. Rana, and V. M. Rotello, *Chem. Soc. Rev.*, 2012, **41**, 2539.
115. http:// www.tulane.edu/~sanelson/eens211/x-ray.htm Accessed on 17/02/13.
116. http://barett-group.mcgill.ca/tutorials/nanotechnology/nano02.htm Accessed on 13/02/13.
117. http://en.wikipedia.org/wiki/energy-dispersive_X-ray_spectroscopy Accessed on 13/02/13.
118. J. E. Lenz, in *Proceedings of the IEEE*, 1990, vol. 78, p. 973.
119. http://www.simplyphysics.com/page2_11.html Accessed on 17/02/13.
120. P. Majewski and B. Thierry, *Crit. Rev. Solid State Mater. Sci.*, 2007, **32**, 203.
121. S. Sayin, M. Yilmaz, and M. Tavasli, *Tetrahedron*, 2011, **67**, 3743.
122. Y. G. Li, H. S. Gao, W. L. Li, J. M. Xing, and H. Z. Liu, *Bioresour. Technol.*, 2009, **100**, 5092.
123. I. Safarik, L. F. T. Rego, M. Borovska, E. Mosiniewicz-Szablewska, F. Weyda, and M. Safarikova, *Enzyme Microb. Technol.*, 2007, **40**, 1551.
124. Y. Zhang, S. Xu, Y. Luo, S. Pan, H. Ding, and G. Li, *J. Mater. Chem.*, 2011, **21**, 3664.
125. A. Hu, G. T. Yee, and W. Lin, *J. Am. Chem. Soc.*, 2005, **127**, 12486.
126. A. H. Lu, W. C. Li, A. Kiefer, W. Schmidt, E. Bill, G. Fink, and F. Schüth, *J. Am. Chem. Soc.*, 2004, **126**, 8616.

Chapter 2

Iron Oxide Nanoparticles

2.1 Summary

The iron pivalate clusters $[Fe_3O(O_2C^tBu)_6(H_2O)_3](O_2C^tBu).HO_2C^tBu$**(1),** $[Fe_8(OH)_4(O_2C^tBu)_{12}(OC_6H_4C_6H_5)_8]$ **(2)** and $[Fe_3O(O_2C^tBu)_6(C_5H_5N)_3]$ **(3)** were used as single source precursors to synthesise iron oxide nanoparticles. A hot injection thermal decomposition method in hexadecanol, oleylamine/oleic acid with dodecanol (boiling point 260 °C) or octyl ether (boiling point 289 °C) as solvent. The effect of different reaction parameters such as temperature, reaction time and varying capping agents on the phase and morphology was studied. The reaction time was studied for **(1)** by withdrawing aliquots at selected time intervals. The results obtained showed that a mixture of maghemite-C (Fe_2O_3) and magnetite (Fe_3O_4) were obtained from the aliquots withdrawn for reaction times of less than 30 minutes whilst only magnetite was obtained after one hour. The diameters of the nanoparticles increase with higher boiling point solvent; 4.3 ± 0.4 and 4.9 ± 0.5 nm were produced at 260 °C and 289 °C respectively from **(1)**.

The effect of hexadecanol investigated on **(1)** revealed that it assisted in a fast nucleation process thereby leading to the formation of monodispersed magnetite nanoparticles. The thermolysis of the three different iron pivalate clusters under identical reaction conditions produced monodispersed magnetite nanoparticles. Magnetic measurements revealed that all the particles are superparamagnetic at room temperature with high saturation values.

2.2 Introduction

The development of synthetic routes to iron oxide nanoparticles possessing specific, chemical and/or physical properties has been a focus of much recent research.[1] Magnetite (Fe_3O_4) is of particular interest due to its unique magnetic properties. It has an inverse spinel structure and electrons can hop between the two cations in the octahedral sites.[2] Studies have shown that magnetite nanoparticles with diameters in the range of 5-20 nm are usually superparamagnetic.[3,4] These particles have been used in: biomedical imaging, hyperthermia treatment, bioseparations, information technology, environmental remediation and electronics.[5–8] Most often the applications usually require monodispersed magnetite nanoparticles.

To date, many different routes have been used for the synthesis of such particles, including: co-precipitation, solvothermal, microbial, flow injection and thermal decomposition methods. The co-precipitation methods have been used to synthesise crystals with different morphologies including spherical,[9–13] cubic,[13,14] octahedron[15] and nanorods.[12,16] Using solvothermal methods, nanocrystals of iron oxide have been grown as spheres,[17,18] hexagons[19] and platelets[20]. The microbial synthesis of iron oxides is often considered as an eco-friendly method but the factors affecting the quality of nanoparticles are often difficult to control. Different morphologies of iron oxide crystals have been obtained by biological approaches including polyhedral,[21–25] nearly spherical[26,27] bullet shaped[28] and parallel piped.[29]

Flow injection technique involves the continuous or periodic injection of reagents into a liquid carrier, followed by mixing which leads to the formation of the product. Salazar-Alvarez *et al.* have synthesized spherical magnetite nanoparticles in the size range of 2-7 nm using a flow injection method.[30] Thermal decomposition of organometallic precursors has produced monodispersed nanoparticles of iron oxide with a narrow size distribution and good crystallinity.[31] The process can involve either a progressive heating of the reactants in a suitable media to the desired temperature or alternatively a more rapid process termed hot injection. In the former, the reaction medium containing the precursor solution and the capping agent is progressively heated from low (often ambient) temperature to a higher predefined reaction temperature. The latter involves rapid injection of the precursor solution into a hot reaction medium containing capping agent.[32]

Previously, the O'Brien group has prepared magnetite nanoparticles by a progressive heating approach using [Fe(acac)$_3$] as the precursor with hexadecylamine as both the solvent and capping agent.[33] Nearly monodispersed nanocrystals were obtained which were further reacted with amine-modified poly(acrylic acid) to obtain water soluble particles suitable for biomedical applications. A host of other research groups have reported the synthesis of iron oxide nanoparticles using different precursors including iron pentacarbonyl,[31,34–38] cupferron complexes,[39] iron acetylacetonate[40,3,41–44] and iron carboxylates.[32,34,45–47]

In comparison to the progressive heating approach, the hot injection method can often yield a narrower size distribution due to the initial high supersaturation as a result of rapid injection that leads to a burst of nucleation thereby separating nucleation from the growth process.[48]

Alivisatos and Scher first developed the thermal decomposition method for producing iron oxide nanoparticles by hot injection thermolysis of iron cupferron in octylamine, obtaining a nearly monodispersed nanoparticles and a further size selection process was carried out to get a more monodispersed nanoparticles.[39] This was followed by the work of Hyeon and his co-workers who further developed the process by employing oleic acid and octyl ether as the capping agent/solvent.[31]

Casula *et al.* described the synthesis of iron oxide nanocrystals by co-injecting iron pentacarbonyl and *m*-chloroperoxybenzoic acid into hot octyl ether and tridecanoic acid was used as the capping agent.[49] These workers studied the effect of growth temperature and time on the diameter of crystals obtained and changes in the phase of the products. Crystalline nanodisks of iron oxide were prepared whose size increased with time. Raman spectroscopy provided evidence that crystals obtained following long growth times were magnetite.[49] Verma *et al.* synthesised spherical magnetite nanoparticles using the hot injection thermolysis of iron acetylacetonate in *N*-methyl 2-pyrrolidone as the solvent and a mixture of oleic acid and oleyl amine as capping agents.[50]

In this chapter, we explore the use of iron pivalate clusters as novel single source precursors for the synthesis of monodispersed iron oxide nanoparticles by a hot injection approach in a mixture of oleic acid and oleylamine using dodecanol or octyl ether as the solvent. The effect of temperature, capping agents and reaction time on the morphology or the phase of the particles formed is described. The particles were characterized by powder X-ray diffraction (p-XRD), high resolution transmission electron microscopy (HRTEM) and the magnetic properties were investigated using a superconducting quantum interference device (SQUID).

2.3 Experimental

2.3.1 Precursor synthesis

All the clusters were synthesised and characterised by Prof. Winpenny group of the School of Chemistry. A brief outlines of the syntheses is now presented.

2.3.1.1 $[Fe_3O(O_2C^tBu)_6(H_2O)_3](O_2C^tBu). HO_2C^tBu$ (1) [51]

Iron nitrate nonahydrate ($Fe(NO_3)_3.9H_2O$, 10.0 g, 24.8 mmol) and pivalic acid (30.0 g, 294 mmol) were heated at 160 °C with stirring until evolution of NO_2 was complete (approximately 4 hours). The flask was cooled to 80 °C before ethanol (100 mL) was added; the solution was diluted with water (30 mL) and cooled to room temperature. A red-brown crystalline product was obtained, which was filtered, washed with toluene and hexane before being dried in vacuum. Elemental analysis: Found (%): C, 45.91; H, 7.68; Fe, 16.02. Calc. (%) for $C_{40}H_{79}Fe_3O_{20}$: C, 45.86; H, 7.60; Fe, 15.99.

2.3.1.2 $[Fe_8(OH)_4(O_2C^tBu)_{12}(OC_6H_4C_6H_5)_8]$ (2) [52]

4-Phenylphenol ($C_6H_5C_6H_4OH$, 0.8 g, 4.7 mmol) and compound **(1)** (1.4 g, 1.34 mmol) were stirred in trichloroethylene (30 mL) at room temperature for 1 hour. The obtained solution was left to stand undisturbed at room temperature for two weeks in a sealed flask. The dark violet-brown crystals obtained were washed with a large quantity of acetone and dried in vacuum. Elemental analysis: Found (%): C, 60.18; H, 6.03; Fe, 14.41. Calc. (%) for $C_{156}H_{184}Fe_8O_{36}$: C, 60.80; H, 6.02; Fe, 14.50.

2.3.1.3 $[Fe_3O(O_2C^tBu)_6(C_5H_5N)_3]$ (3) [53]

2 g of iron was dispersed in pivalic acid (30 mL) and was heated at 155-160 °C in air to evoke complete dissolution of iron. The resulting solution was cooled to room temperature; the precipitate obtained was dissolved by refluxing in diethyl ether. A

dark brown solution was obtained which was cooled to 10 °C. The crystallized products were filtered after 24 hours in an inert atmosphere and then washed with cooled diethyl ether and acetonitrile to get $[Fe_3O(O_2C^tBu)_6(HO_2C^tBu)_3]$. 4 g (3.65 mmol) of this compound was dissolved in pyridine (10 mL) by heating under an inert atmosphere. The solution was filtered hot and then slowly cooled and left for 48 hours at room temperature. A black precipitate was formed which was collected, washed with cooled pyridine and acetonitrile then left to dry at room temperature. Elemental analysis: Found (%): C, 52.74; H, 6.66; N, 4.13; Fe, 16.18. Calc. (%) for $C_{45}H_{69}Fe_3N_3O_{13}$: C, 52.60; H, 6.77; N 4.09; Fe, 16.30.

2.3.2 Synthesis of nanoparticles

Table 2.1 below shows the summary of the reaction conditions used in the synthesis of iron oxide nanoparticles. In a typical synthesis, a mixture of oleic acid (OLA) (18 mmol), oleylamine (OLAm) (18 mmol), hexadecanol (10 mmol) and dodecanol (15 mL) was dispensed into a three-neck flask and heated to 100 °C under vacuum for 1 hour. The temperature was then increased to 260 °C under nitrogen and a solution of **(1)** (0.275g, 0.25 mmol) in 15 mL dodecanol was injected. The temperature was maintained at 230 °C for 2 hours. The mixture was allowed to cool and on addition of excess methanol resulted in a black precipitate which was isolated by centrifugation. The black residue was washed with methanol three times and redispersed in toluene or hexane for further characterisations. The kinetics of the reaction was investigated on **(1)** by withdrawing aliquots at selected time intervals.

Table 2.1 Summary of the reaction conditions used in synthesis of iron oxide nanoparticles by a hot injection method.

Cluster	Conc. mmol	OLAm mmol	OLA mmol	Solvent 30ml	Hexadecanol mmol	Injection Temp (°C)
(1)	0.25	18	18	Dodecanol	10	260
(1)	0.25	18	18	Dioctyl ether	10	260
(1)	0.25	18	18	Dioctyl ether	10	289
(1)	0.25	36	0	Dodecanol	10	260
(1)	0.25	0	36	Dodecanol	10	260
(1)	0.25	18	18	Dodecanol	0	260
(2)	0.25	18	18	Dodecanol	10	260
(3)	0.25	18	18	Dodecanol	10	260

2.4 Results and Discussion

2.4.1 Thermogravimetric analysis (TGA)

TGA of the three iron clusters shows multiple-step decomposition with rapid weight losses between 260-317 °C, 215-340 °C and 263-397 °C for complexes **(1)**, **(2)** and **(3)** respectively (Fig. 2.1). The solid residue remaining amounts to 17% for **(1)** which is lower than the calculated value of 23% for Fe_2O_3. For **(2)**, solid residue remaining amounts to 22% which is slightly higher than the calculated value of 20% for Fe_2O_3. For **(3)** a 10% residue was obtained which is lower than the calculated value of 23% for Fe_2O_3. The lower values obtained for these complexes can be attributed to sublimation process which takes place before the complex is fully decomposed. For **(2)**, the residual value was higher than the calculated value; this may be as a result of incomplete decomposition due to the phenol groups.

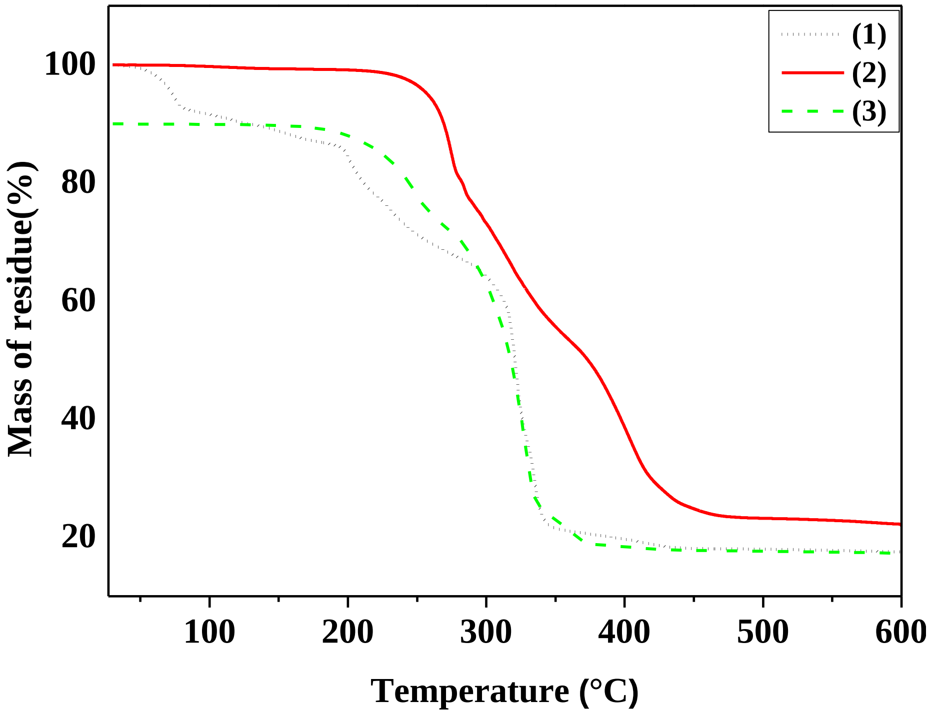

Fig. 2.1 Thermogravimetric analysis of **(1), (2)** and **(3).**

2.4.2 Monodispersed magnetite nanoparticles

The hot injection thermolysis of $[Fe_3O(O_2C^tBu)_6(H_2O)_3](O_2C^tBu).HO_2C^tBu$ **(1)** in a mixture of OLA, OLAm, hexadecanol and dodecanol at 260 °C produced monodispersed nanoparticles as shown in the TEM images (Fig. 2.2). The p-XRD peaks correspond to cubic magnetite (Fe_3O_4) (ICDD Card No: 00-019-0629) (Fig. 2.3). The peaks are broad, indicative of small particles with an average diameter of 4.5 nm estimated by the Scherrer equation. TEM images revealed that the magnetite nanoparticles are spherical with an average diameter of 4.3 ± 0.4 nm which is in good agreement with the p-XRD result. The particles are very crystalline as observed in the well resolved lattice fringes (Fig. 2.2 (d)) with a *d*-spacing of 2.58 Å, a measurement that is very close to the (311) reflection plane of magnetite (ICDD card No: 00-19-0629).

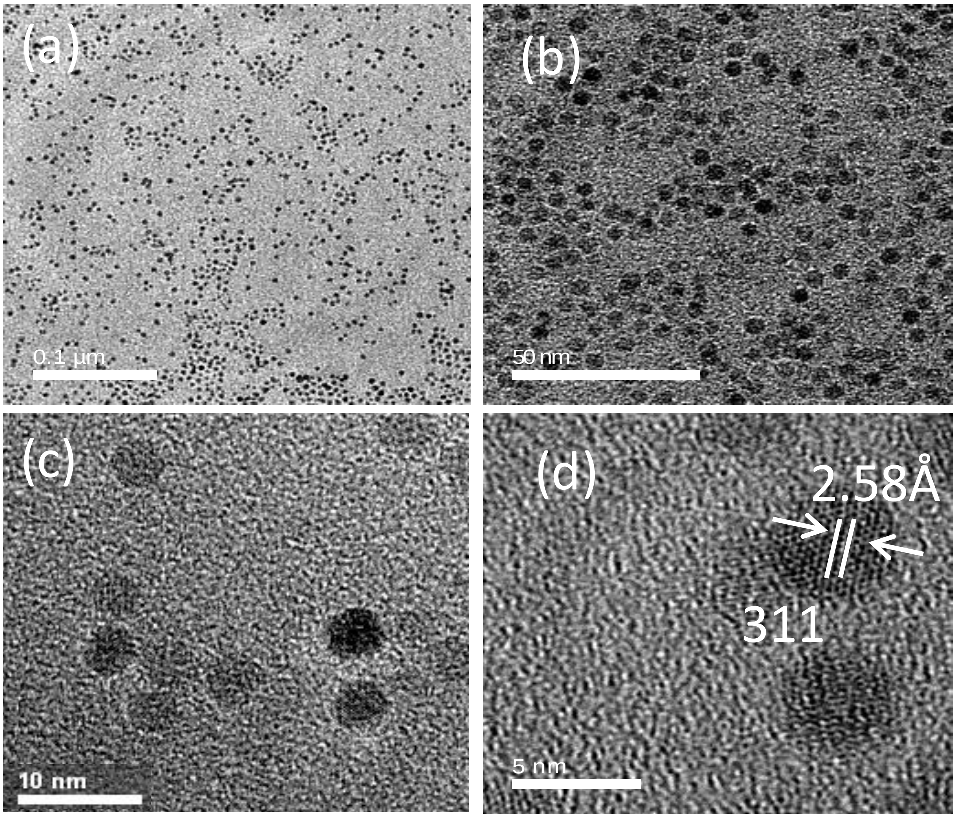

Fig. 2.2 (a)-(c) TEM images of monodispersed magnetite particles obtained from **(1)** at different magnifications, (d) HRTEM showing *d*-spacing.

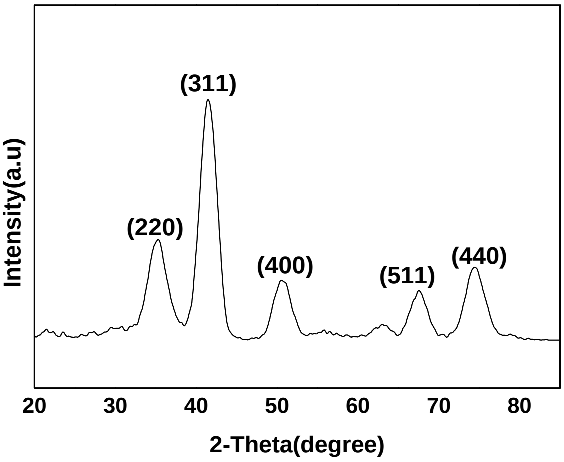

Fig. 2.3 The p-XRD pattern for monodispersed magnetite nanoparticles obtained by the thermolysis of 0.25 mmol solution of **(1)** in a mixture of oleylamine, oleic acid, hexadecanol and dodecanol at 260 ºC.

2.4.3 Effect of Injection Temperature

The effect of injection temperature was studied for complex **(1)** with two different solvents- dioctyl ether (b.p. 289 °C) and dodecanol (b.p. 260 °C). Three different syntheses were carried out. In one, the precursor solution was injected at the boiling point of dodecanol at 260 ºC; whilst for dioctyl ether two temperatures were used: 260 ºC and its boiling point (289 ºC). The p-XRD pattern obtained for the particles in all three syntheses (Fig. 2.4) were matched with magnetite (ICDD card No: 19-0629). The average particle diameter estimated by the Scherrer equation is 4.5 nm with dodecanol, 5.0 nm with dioctyl ether at 289 ºC and 9.5 nm at 260 ºC.

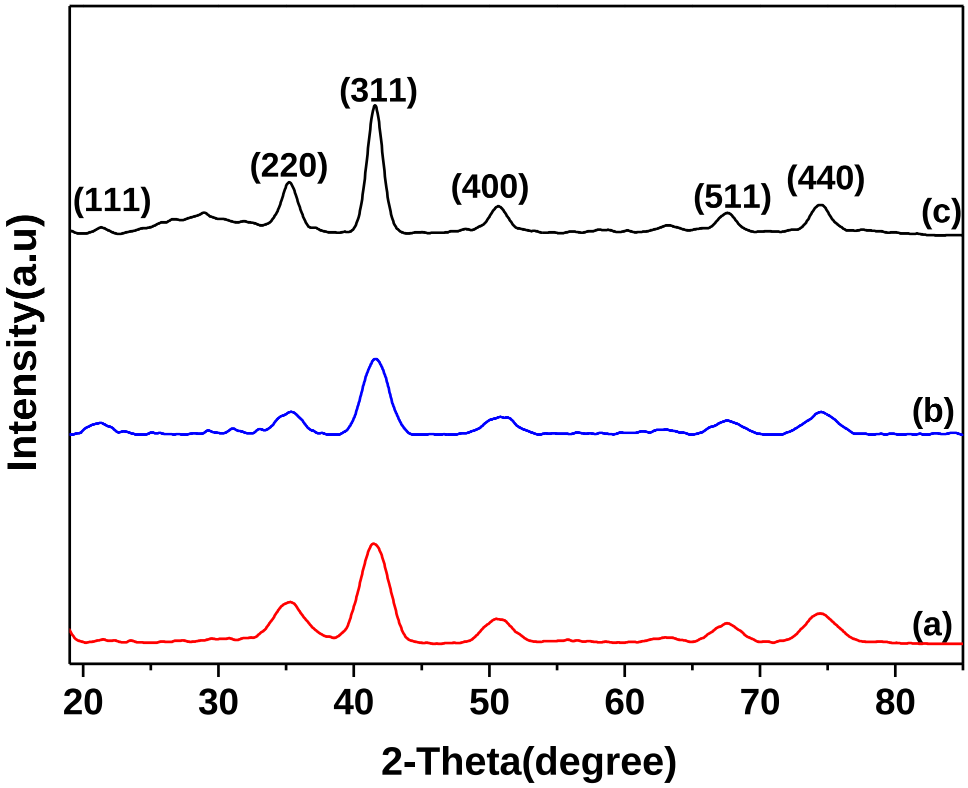

Fig. 2.4 The p-XRD pattern for magnetite nanoparticles from **(1)** thermolysed in different solvents at their boiling points (a) dodecanol at 260 °C, (b) dioctyl ether at 289 °C and (c) dioctyl ether at 260 °C.

The average diameter calculated from TEM are 4.3 ± 0.4 nm with dodecanol at 260 ºC, 8 ± 1.5 nm and 4.9 ± 0.5 nm at 260 ºC and 289 ºC respectively with dioctyl ether (Fig. 2.5). The TEM results showed that the diameter of the nanoparticles increases with higher boiling point solvents. A similar observation has been reported by some research groups.[34,45]

All the results from the TEM are in good agreement with those calculated value from p-XRD. The size distribution appears to improve as the injection temperature is increased close to the boiling point of the solvent. This result is in agreement with what has been reported in literature.[49]

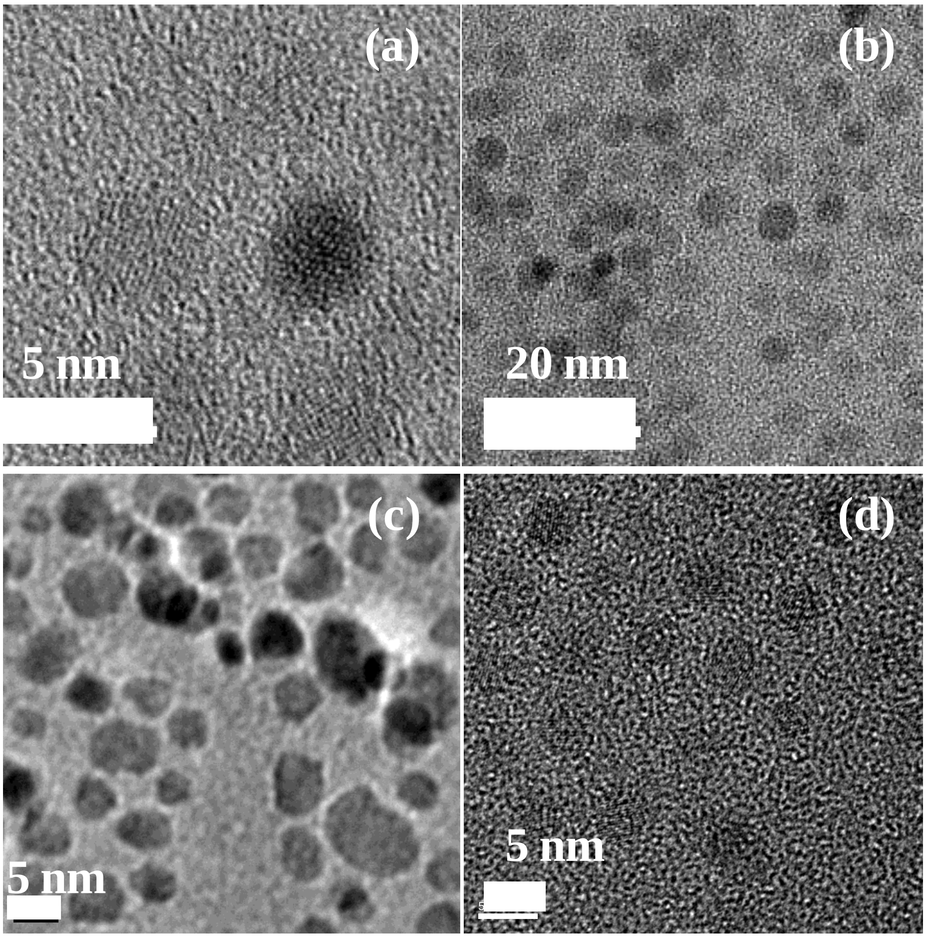

Fig. 2.5 TEM images obtained for magnetite particles from **(1)** thermolysed in different solvents (a) - (b) dodecanol at 260 °C, (c) octyl ether at 260 °C and (d) octyl ether at 289 °C.

2.4.4 The effect of reaction time

The effect of reaction time was studied for **(1)** by withdrawing aliquots at 5 minutes, 15 minutes, 30 minutes, 1 hour and at 2 hours. The p-XRD (Fig. 2.6) showed that nanoparticles produced at 5 minutes, 15 minutes and 30 minutes were a mixture of maghemite-C (Fe_2O_3) (ICDD Card No: 024-0081) and magnetite (Fe_3O_4) (ICDD Card No: 19-0629). However, the samples withdrawn at 1 hour and 2 hours are of only magnetite (ICDD Card No: 19-0629).

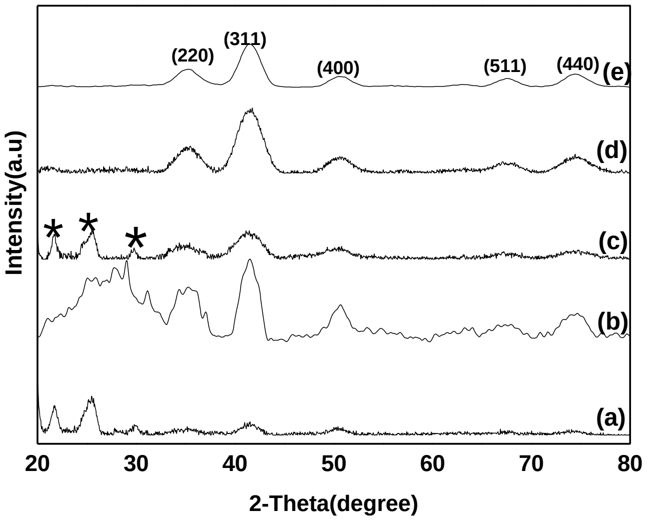

Fig. 2.6 The p-XRD pattern for iron oxide nanoparticles by thermolysis of **(1)** in a mixture of oleylamine, dodecanol, oleic acid and hexadecanol at 260 °C. The pattern showed for aliquots withdrawn at (a) 5 minutes, (b) 15 minutes, (c) 30 minutes, (d) 1 hour and (e) 2 hours. *corresponds to the maghemite-C (Fe_2O_3) peaks assigned to aliqouts at 5 minutes, 15 minutes and 30 minutes. All other peaks are assigned to magnetite (Fe_3O_4).

At the beginning of the reaction, the predominant phase appear to be maghemite-C (Fe_2O_3) which then reacts with the reducing agents (oleylamine, dodecanol, hexadecanol) present in the reaction medium to obtain a final phase of magnetite (Fe_3O_4). TEM images taken for these samples revealed an increase in diameter at longer reaction times as shown in samples withdrawn at 30 minutes (3.5 ±0.6 nm), 1 hour (3.7 ± 0.6 nm) and 2 hours (4.3 ± 0.4 nm) (Fig. 2.7). This observation can be attributed to Ostwald ripening/growth which take place during aging.[54,55]

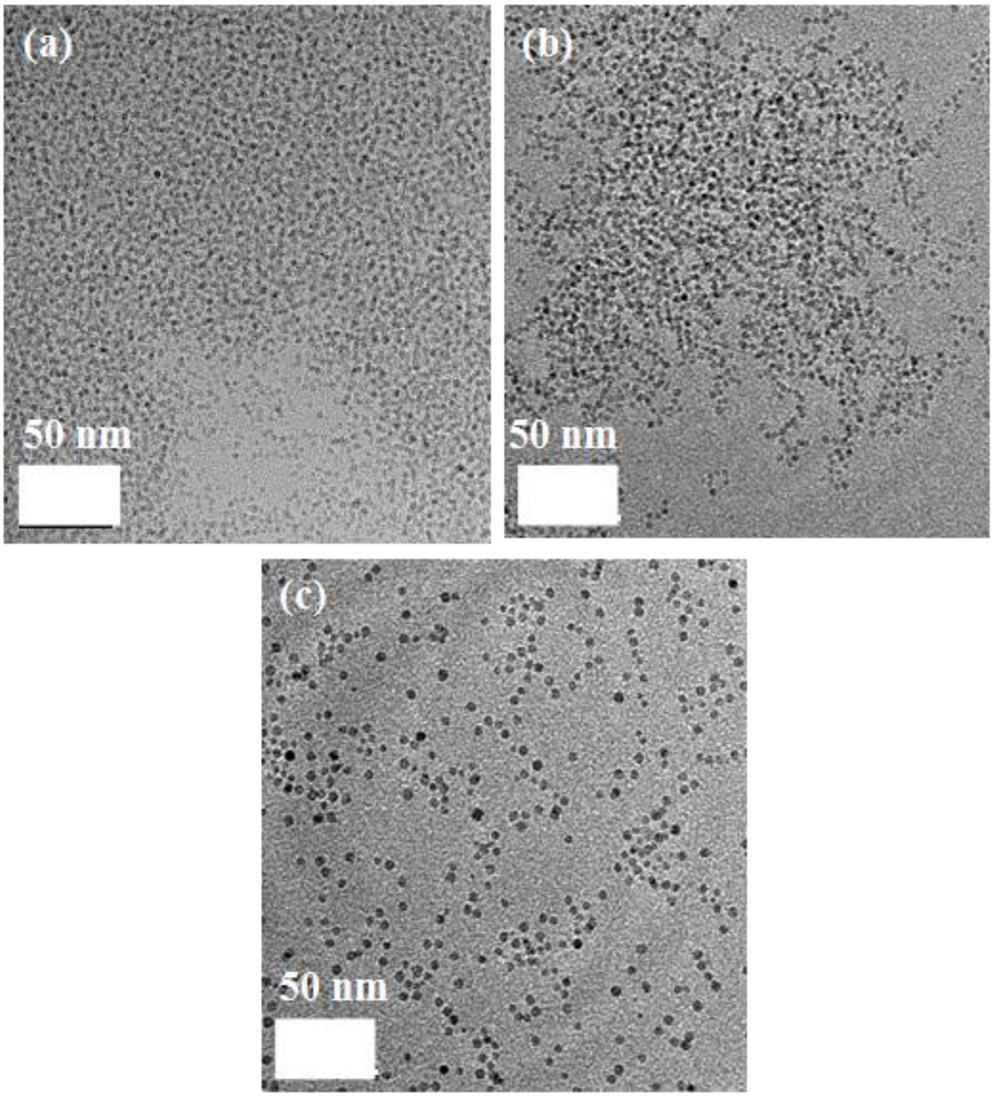

Fig. 2.7 TEM images of iron oxide nanoparticles obtained from thermolysis of **(1)** at different reaction times (a) 30 minutes, (b) 1 hour and (c) 2 hours.

2.4.5 Nanoparticles obtained from different precursors

The three different precursors were thermally decomposed using the hot injection method employing identical reaction conditions and the same concentration of precursor. The p-XRD data indicated that all three precursors produced magnetite (Fig. 2.8). The average diameter of the particles estimated using the Scherrer formula are 4.5 nm for Fe_3O_4 obtained from **(1)** and **(2)** whilst 5 nm was obtained from **(3)**.

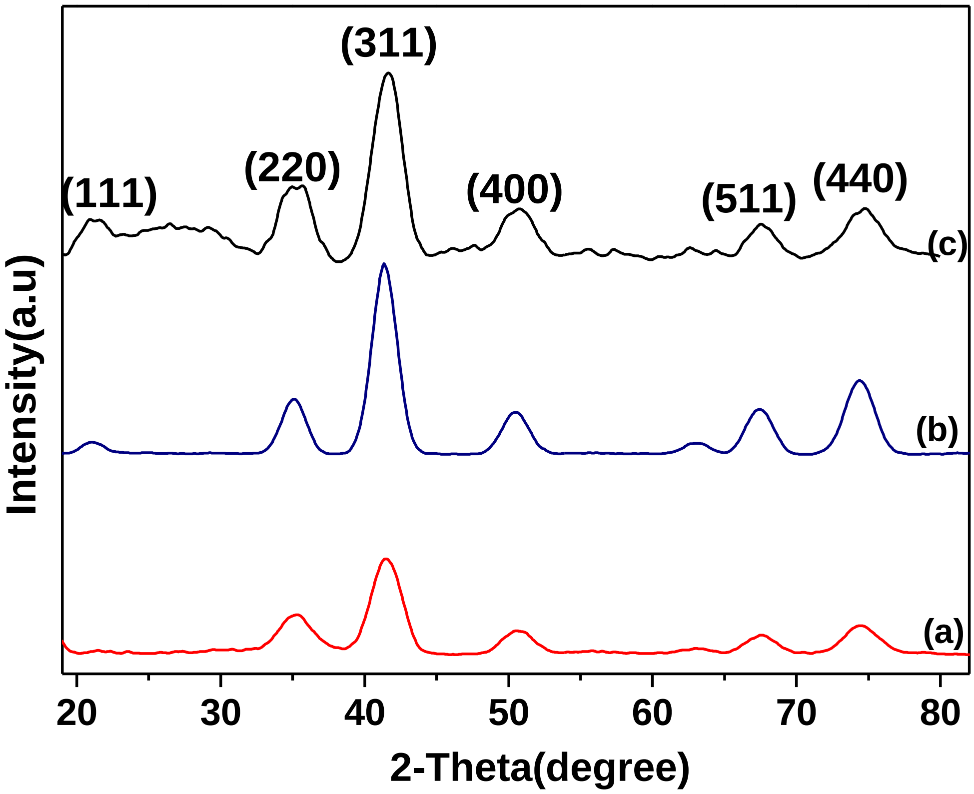

Fig. 2.8 The p-XRD pattern of magnetite (Fe_3O_4) nanoparticles obtained from three different precursors by injecting 0.25 mmol solution of precursor into a mixture of oleylamine, oleic acid, hexadecanol and dodecanol at 260 °C (a) Fe_3O_4 from **(1),** (b) Fe_3O_4 from **(2)** and (c) Fe_3O_4 from **(3).**

TEM images of the nanoparticles obtained from **(1)** and **(2)** were monodispersed whilst **(3)** showed nearly monodispersed particles (Fig. 2.9). Their average diameters calculated from the TEM images in nm were 4.3 ± 0.4 nm, 5.0 ± 0.8 nm and 5.9 ± 1.2 nm for **(1)** **(2)** and **(3)** respectively.

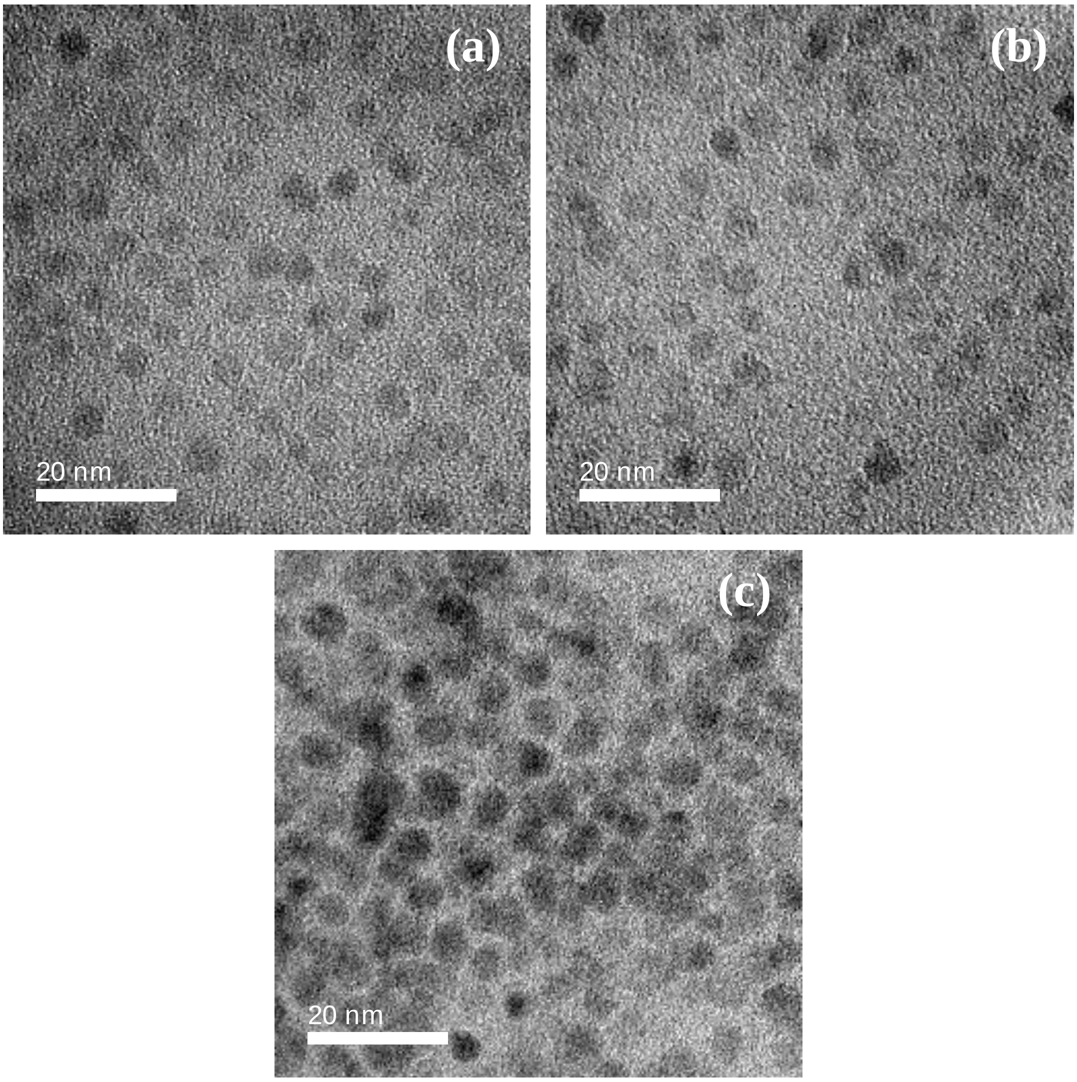

Fig. 2.9 TEM images of magnetite nanoparticles obtained from thermolysis of three different precursors (a) from **(1)**, (b) from **(2)** and (c) from **(3).**

2.4.6 The effect of hexadecanol

The effect of addition of hexadecanol was studied for **(1)**. In one experiment, dodecanol was used as the solvent and hexadecanol as the reducing agent while in the other; dodecanol was used both as the solvent and as the reducing agent. Although the p-XRD pattern of the nanoparticles produced in the absence of hexadecanol shows predominantly Fe_3O_4 [ICDD Card No: 19-0629], there is still a weak reflection at 57.2° which was assigned to Fe_2O_3 [ICDD Card No: 00-056-1302] (Fig. 2.10 (a)). The nanoparticles produced with a mixture of hexadecanol and dodecanol revealed reflections consistent with only magnetite [ICDD card No: 19-0629] (Fig. 2.10 (b)).

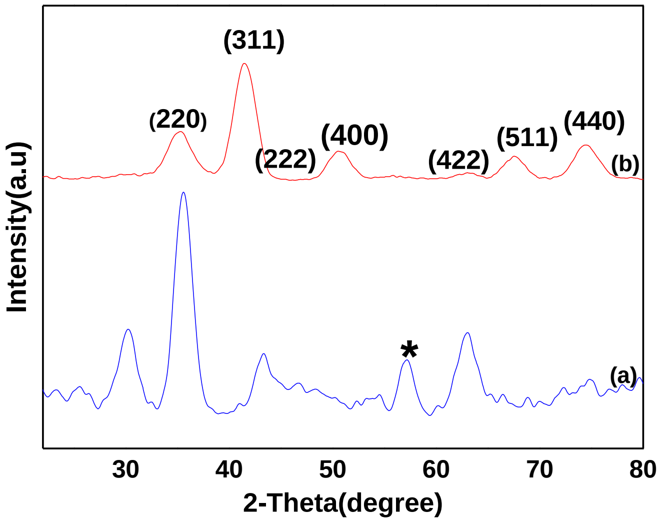

Fig. 2.10 The p- XRD pattern of Fe_3O_4 (magnetite) nanoparticles from thermolysis of **(1)** in (a) dodecanol, oleylamine and oleic acid (b) hexadecanol dodecanol, oleic acid and oleylamine. *Shows the traces of Fe_2O_3 when thermolysis was carried out in absence of hexadecanol.

Their average diameters were estimated by the Scherrer equation, were found to be 4.5 nm with the mixture and 5 nm with only dodecanol. TEM images revealed that particles obtained with a mixture of dodecanol and hexadecanol are monodispersed (Fig. 2.11(a)); particles obtained with only dodecanol are not monodispersed and in fact aggregated (Fig. 2.11(b)). This aggregation was also observed in the sample 48 hours after preparation as precipitates were formed, but the sample prepared in the presence of hexadecanol was stable for months. The average diameter calculated from the TEM images are 4.3 ± 0.4 and 5.5 ± 1.0 nm for nanoparticles obtained with and without hexadecanol respectively. These results may therefore suggest that hexadecanol promotes a rapid nucleation process because it is a faster reducing agent and thus leading to the production of monodispersed particles. The use of long chain alcohol in addition with capping agents to get monodispersed ferrite nanoparticles has been reported in the literature.[34,40,56–58]

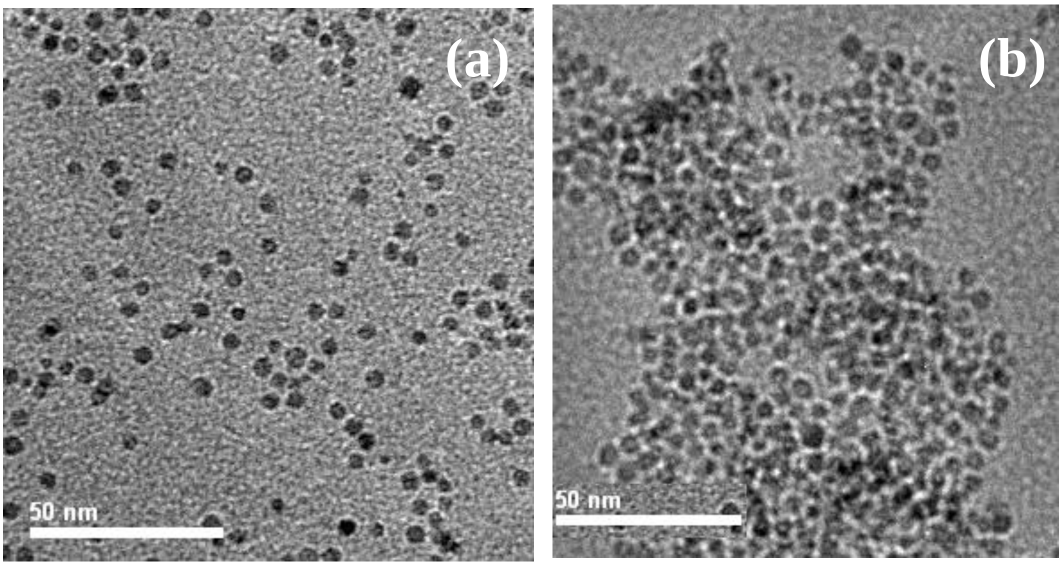

Fig. 2.11 TEM images for magnetite nanoparticles obtained by the thermolysis of **(1)** in (a) in the presence of hexadecanol (b) in the absence of hexadecanol.

2.4.7 The effect of capping agents

The effect of capping agents on the morphology of nanoparticles obtained from **(1)** was studied. Three experiments were carried out: in one experiment only oleylamine was used, in the second only oleic acid was used and in the third a mixture of oleylamine and oleic acid were used (Table 2.1). The p-XRD patterns recorded from the nanoparticles from all three experiments were consistent with magnetite (Fig. 2.12). The size of the nanoparticles were estimated by the Scherrer equation and the results obtained are 5.0, 6.0 and 4.5 nm with oleylamine, oleic acid and the mixture of the two respectively. The average diameter calculated from the TEM images are 5.0 ± 0.7 nm with oleylamine, 6.0 ± 0.9 nm with oleic acid and 4.3 ± 0.4 nm with the mixture.

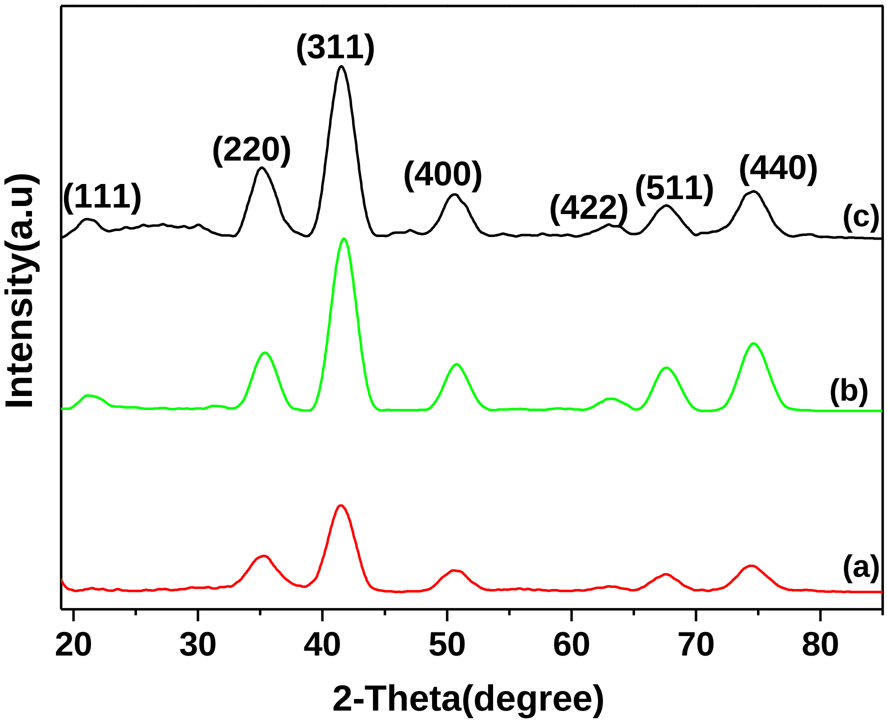

Fig. 2.12 The p-XRD pattern for magnetite nanoparticles obtained by thermolysis of **(1)** in different capping agents (a) mixture of oleylamine and oleic acid (b) oleic acid (c) oleylamine.

The TEM images obtained for the nanoparticles showed that a very narrow size distribution is obtained from the mixture of oleylamine and oleic acid (4.3 ± 0.4 nm), followed by oleylamine (5.0 ± 0.7 nm) whilst oleic acid capped nanoparticles have the broadest size distribution (6.0 ± 0.9 nm) (Fig. 2.13). These results are similar to what has been reported by Crouse *et al.*[59]

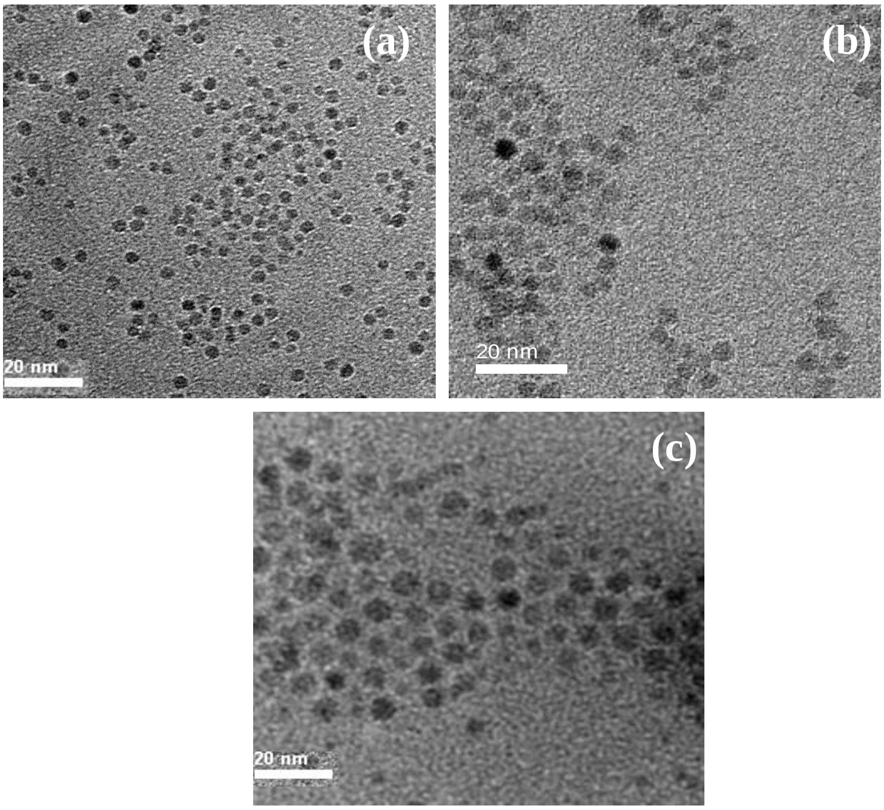

Fig. 2.13 TEM images obtained for magnetite nanoparticles obtained from thermolysis of **(1)** in different capping agents (a) mixture of oleylamine and oleic acid (b) oleylamine only (c) oleic acid only.

2.4.8 Magnetic Properties

Changes in magnetization of the magnetite nanoparticles as a function of temperature and applied magnetic field were measured by SQUID magnetometry. In general, small nanoparticles have their magnetic properties governed by their anisotropy energy, which normally constrains the nanoparticle magnetization to align along a specific direction known as the easy axis. Since the maximum anisotropy energy of a given nanoparticle depends on the product of its volume, V, and the anisotropy constant, K, most magnetite nanoparticles with diameters below ~30 nm become superparamagnetic above a certain temperature, known as their blocking temperature (T_B).[60] This important property is vital for their applications in biological imaging, bioseparations and hyperthermia treatment.[1] At temperatures above T_B, the thermal energy is sufficient to surmount the anisotropy energy barrier and the nanoparticle magnetization freely aligns in arbitrary directions. Thus, for an assembly of such nanoparticles, the net magnetization measured in the absence of an applied dc field average out to zero and the particles are said to be in the superparamagnetic state.[61]

All the particles reported in this chapter here have an average diameter (4.3 - 6 nm) well below the threshold of ~30 nm, and their hysteresis loops at room temperature (Figs. 2.14 and 2.15) display the characteristic features of superparamagnetism, such as negligible coercivity and zero magnetic resonance.

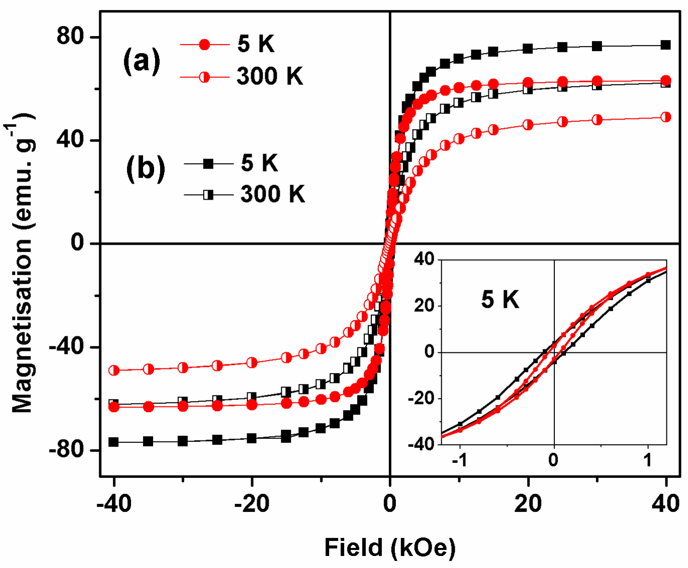

Fig. 2.14 The hysteresis loops measured at 5 and 300 K for magnetite (Fe_3O_4) nanoparticles obtained from **(1)** by thermolysis in hexadecanol with dodecanol at 260 °C and (a) a mixture of oleylamine and oleic acid (diameter 4.3 ± 0.4 nm) (b) oleic acid (diameter 6.0 ± 0.9 nm).

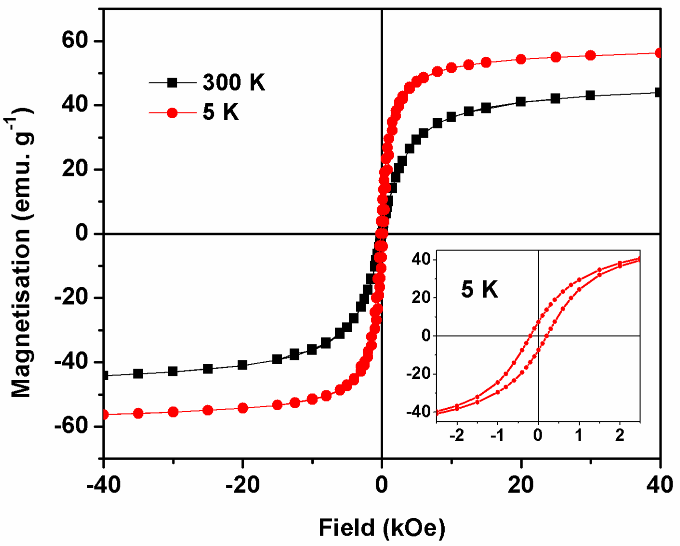

Fig. 2.15 The hysteresis loops measured at 5 and 300 K for magnetite (Fe_3O_4) nanoparticles of average diameter 5.0 ± 0.8 nm, obtained from **(2)** by thermolysis in a mixture of oleylamine, oleic acid, hexadecanol and dodecanol at 260 °C.

An estimation of the blocking temperature of the nanoparticles can be easily obtained from dc magnetometry measurements, in which a zero-field cooled (ZFC) – field-cooled (FC) procedure is employed.[1,62] In a ZFC measurement, the sample is cooled from room temperature to 2 or 5 K, in a zero dc-field. Then a small magnetic field of *ca.* 100 Oe is applied and the magnetization is recorded on warming. As the temperature increases, the thermal energy disturbs the system and more moments acquire enough energy to be able to align with the external field direction. The number of unblocked, aligned moments reaches a maximum at T_B. Above the blocking temperature the thermal energy is strong enough to randomize the magnetic moments causing a decrease in magnetization.

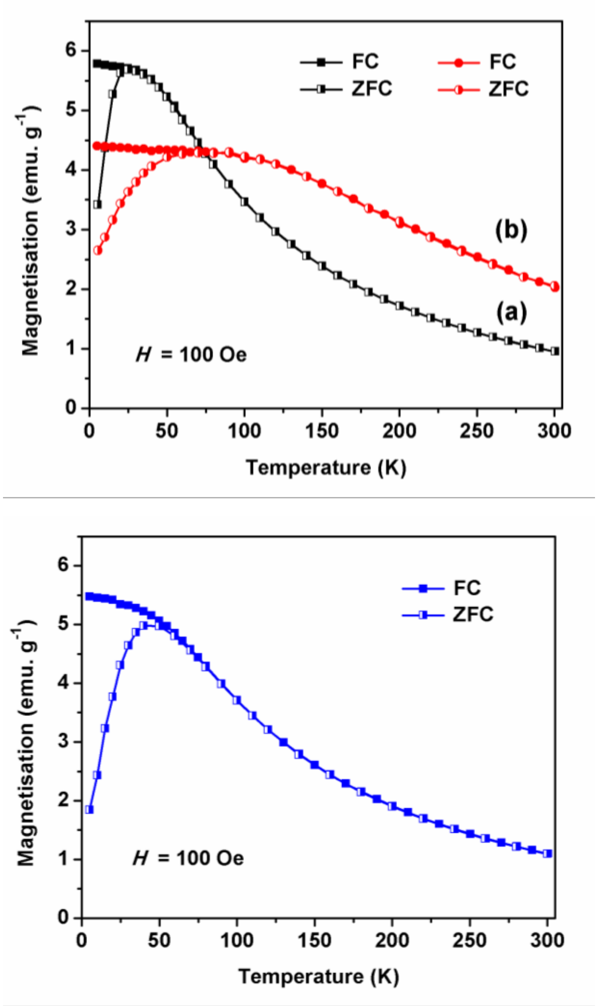

Fig. 2.16 Top: Zero field cooled (ZFC) and Field-cooled (FC) magnetisation curves for magnetite nanoparticles of average diameter (a) 4.3 ± 0.4 nm and (b) 6.0 ± 0.9 nm, obtained from **(1)** by thermolysis in (a) oleylamine/oleic acid at 260 °C (b) oleic acid at 260 °C. Bottom: ZFC and FC magnetisation curves for magnetite nanoparticles with average diameter 5.0 ± 0.8 nm, obtained from **(2)** by thermolysis in oleylamine, oleic acid at 260 °C.

Cooling the sample in applied magnetic field (for example, in a FC magnetization measurement) allows such magnetic moments to remain aligned with the external field direction, and the magnetization value recorded below T_B is higher than that obtained through a ZFC procedure. In practice, T_B is graphically determined to be the point at which the gradient of the ZFC curve approaches zero.[60] As seen in Fig. 2.16, T_B decreases with decreasing particle size, ranging from ~ 25 K for magnetite nanoparticles obtained from **(1)** with the average diameter of 4.3 nm, to 45 K for particles obtained from **(2)** with average diameter of 5 nm and to 70 K for nanoparticles obtained from **(1)** with average diameter of 6 nm. The blocking temperature for the smallest nanoparticles (4.3 ± 0.4 nm) is well defined, indicating a very narrow distribution of the particle diameter. In contrast, the largest particles (6.0 ± 0.9 nm) obtained from **(1)** show a broader distribution of the blocking temperature, consistent with the greater distribution of the particle diameters.

Field dependence of the magnetization was recorded for all these nanoparticles at 5 and 300 K. Representative hysteresis curves are given in Figs. 2.14 and 2.15. Comparison between nanoparticles generated from **(1)** indicates that, irrespective of temperature, the saturation of the magnetization increases with average particle diameter, from M_s = 49.0 (at 300 K) and 63.2 emu. g^{-1} (at 5 K) (4.3 ± 0.4 nm) to M_s = 62.2 (at 300 K) and 76.8 emu/ g (at 5 K) (6.0 ± 0.9 nm). The saturation magnetization of the nanoparticles generated from **(2)** is 43.9 emu.g^{-1} at 300 K and 56.2 emu.g^{-1} at 5 K (Fig. 2.15). Bulk magnetite is reported to have M_S = 92 emu.g^{-1} at 300 K, [63] which is much larger than that observed for our nanoparticles. Some studies suggests that surface effects can lead to a decrease of the magnetization of small oxide nanoparticles with respect to the bulk value.[1] This reduction has been associated with different mechanisms, such as the existence of a magnetically dead layer on the particle's surface, the existence of canted spins, or the existence of a spin-glass-like behaviour of the surface spins.

Another surface-driven effect is the enhancement of the magnetic anisotropy, K_{eff}, with decreasing particle size. In a very simple approximation, the anisotropy energy of a spherical particle with diameter D, surface area S, and volume V, may be described by one contribution from the bulk and another from the surface: $K_{eff} = K_V + 6/DK_S$, where K_V and K_S are the bulk and surface anisotropy energy constants, respectively. It has been found that K_{eff} changes when the surface is modified, which explains the contribution of the surface anisotropy to K_{eff}. The coercive force for all the samples is about 180-200 G at 5 K, while the coercivity at room temperature is almost negligible, which is a common characteristic of superparamagnetic materials. Our investigation suggests that all samples are of good magnetic quality which makes them suitable for potential biological and other medical applications.

Table 2.2 Summary of the various sizes of nanoparticles obtained at different reaction conditions from precursors **(1)**, **(2)** and **(3).**

Precursor	**Time (min)**	**Solvent**	**OLA (mmol)**	**OLAm (mmol)**	**Injection temp (°C)**	**p-XRD (nm)**	**TEM (nm)**
$[Fe_3O(O_2C^tBu)_6(H_2O)_3](O_2C^tBu).HO_2C^tBu$ **(1)**	30	dodecanol	18	18	260	-	3.5 ± 0.6
(1)	60	dodecanol	18	18	260	-	3.7 ± 0.6
(1)	120	dodecanol	18	18	260	4.5	4.3 ± 0.4
(1)	120	dodecanol	0	36	260	5.0	5.0 ± 0.7
(1)	120	dodecanol	36	0	260	6.0	6.0 ± 0.9
(1)	120	dioctyl ether	18	18	260	9.5	8.0 ± 1.5
(1)	120	dioctyl ether	18	18	289	5.0	4.9 ± 0.5
$[Fe_8(OH)_4(O_2C^tBu)_{12}(OC_6H_4C_6H_5)_8]$ **(2)**	120	dodecanol	18	18	260	4.5	5.0 ± 0.8
$[Fe_3O(O_2C^tBu)_6(C_5H_5N)_3]$ **(3)**	120	dodecanol	18	18	260	5.0	5.9 ± 1.2

2.5 Conclusion

Iron oxide nanoparticles have been synthesized by a hot injection thermal decomposition of $[Fe_3O(O_2C^tBu)_6(H_2O)_3](O_2C^tBu).HO_2C^tBu$**(1),** $[Fe_8(OH)_4(O_2C^tBu)_{12}(OC_6H_4C_6H_5)_8]$ **(2)** and $[Fe_3O(O_2C^tBu)_6(C_5H_5N)_3]$ **(3)** in oleic acid and or oleylamine(capping agents), hexadecanol with either dodecanol or octyl ether as solvent. The thermolysis of **(1)** in different boiling point solvents at different temperatures showed that larger nanoparticles were obtained at higher temperature. The presence of hexadecanol enhanced the nucleation process leading to the production of monodispersed nanoparticles whilst aggregated nanoparticles were obtained in the absence of hexadecanol. It has been demonstrated that an equimolar mixture of oleylamine and oleic acid resulted in a monodispersed magnetite nanoparticles with a very narrow size distribution as compared to using either oleic acid or oleylamine alone. Monodispersed magnetite nanoparticles were produced directly without a further size selection process when the precursor was injected in a mixture of the capping agents at the boiling point of the solvent used. The effect of reaction time was studied for **(1)** and the results showed that shorter reaction times of less than 30 minutes produced a mixture of maghemite-C (Fe_2O_3) and magnetite (Fe_3O_4) whilst only magnetite was obtained after one hour. Magnetic studies showed that the particles are superparamagnetic at room temperature with high saturation magnetisation.

2.6 References

1. A. H. Lu, E. L. Salabas, and F. Schüth, *Angew. Chem. Int. Ed.*, 2007, **46**, 1222.
2. Abhilash, K. Revati, and B. D. Pandey, *Bull. Mater. Sci.*, 2011, **34**, 191.
3. P. Guardia, A. Labarta, and X. Batlle, *J. Phys. Chem. C*, 2011, **115**, 390.
4. J. Santoyo Salazar, L. Perez, O. de Abril, L. Truong Phuoc, D. Ihiawakrim, M. Vazquez, J.-M. Greneche, S. Begin-Colin, and G. Pourroy, *Chem. Mater.*, 2011, **23**, 1379.
5. M. Zhao, D. A. Beauregard, L. Loizou, B. Davletov, and K. M. Brindle, *Nat. Med.*, 2001, **7**, 1241.
6. M. Sugimoto, *J. Am. Ceram. Soc.*, 1999, **82**, 269.
7. C. T. Yavuz, J. T. Mayo, W. W. Yu, A. Prakash, J. C. Falkner, S. Yean, L. Cong, H. J. Shipley, A. Kan, M. Tomson, D. Natelson, and V. L. Colvin, *Science* , 2006, **314**, 964.
8. S.-H. Huang, M.-H. Liao, and D.-H. Chen, *Biotechnol. Progr.*, 2003, **19**, 1095.
9. J. Mürbe, A. Rechtenbach, and J. Töpfer, *Mater. Chem. Phys.*, 2008, **110**, 426.
10. I. Martínez-Mera, M. E. Espinosa-Pesqueira, R. Pérez-Hernández, and J. Arenas-Alatorre, *Mater. Lett.*, 2007, **61**, 4447.
11. S. Qu, H. Yang, D. Ren, S. Kan, G. Zou, D. Li, and M. Li, *J. Colloid Interface Sci.*, 1999, **215**, 190.
12. R. F. Fakhrullin, J. García-Alonso, and V. N. Paunov, *Soft Matter*, 2010, **6**, 391.
13. M. M. Lin, S. Li, H. H. Kim, H. Kim, H. B. Lee, M. Muhammed, and D. K. Kim, *J. Mater. Chem.*, 2010, **20**, 444.
14. F. Dang, N. Enomoto, J. Hojo, and K. Enpuku, *J. Cryst. Growth*, 2010, **312**, 1736.
15. I. Nyirő-Kósa, D. Csákberé Nyinagy, and M. Pósfai, *Eur. J. Mineral.*, 2009, **21**, 293.
16. C. Yang and H. Yan, *Mater. Lett.*, 2012, **73**, 129.
17. Y. Tian, B. Yu, X. Li, and K. Li, *J. Mater. Chem.*, 2011, **21**, 2476.
18. X. Jia, D. Chen, X. Jiao, and S. Zhai, *Chem. Commun.*, 2009, 968.

19. J. Wang, M. Yao, G. Xu, P. Cui, and J. Zhao, *Mater. Chem. Phys.*, 2009, **113**, 6.
20. X.-M. Liu and J.-K. Kim, *Mater. Lett.*, 2009, **15**, 428.
21. A. P. Philipse and D. Maas, *Langmuir*, 2002, **18**, 9977.
22. H. Lee, A. M. Purdon, V. Chu, and R. M. Westervelt, *Nano Lett.*, 2004, **4**, 995.
23. C. Zhang, H. Vali, C. S. Romanek, T.J. Phelps, and S.V Liu, *Am. Mineral.*, 1998, **83**, 1409.
24. T. Perez-Gonzalez, C. Jimenez-Lopez, A. L. Neal, F. Rull-Perez, A. Rodriguez-Navarro, A. Fernandez-Vivas, and E. Iañez-Pareja, *Geochim. Cosmochim. Acta*, 2010, **74**, 967.
25. Y. Amemiya, A. Arakaki, S. S. Staniland, T. Tanaka, and T. Matsunaga, *Biomaterials*, 2007, **28**, 5381.
26. A. Bharde, A. Wani, Y. Shouche, P. A. Joy, B. L. V Prasad, and M. Sastry, *J. Am. Chem. Soc.*, 2005, **127**, 9326.
27. V. S. Coker, J. A. Bennett, N. D. Telling, T. Henkel, J. M. Charnock, G. van der Laan, R. A. D. Pattrick, C. I. Pearce, R. S. Cutting, I. J. Shannon, J. Wood, E. Arenholz, I. C. Lyon, and J. R. Lloyd, *ACS Nano*, 2010, **4**, 2577.
28. C. T. Lefèvre, F. Abreu, M. L. Schmidt, U. Lins, R. B. Frankel, B. P. Hedlund, and D. A. Bazylinski, *Appl. Environ. Microbiol.*, 2010, **76**, 3740.
29. D. A. Bazylinski, R. B. Frankel, and H. W. Jannasch, *Nature*, 1988, **334**, 518.
30. G. Salazar-Alvarez, M. Muhammed, and A. A. Zagorodni, *Chem. Eng. Sci.*, 2006, **61**, 4625.
31. T. Hyeon, S. S. Lee, J. Park, Y. Chung, and H. B. Na, *J. Am. Chem. Soc.*, 2001, **123**, 12798.
32. S. G. Kwon, Y. Piao, J. Park, S. Angappane, Y. Jo, N.-M. Hwang, J.-G. Park, and T. Hyeon, *J. Am. Chem. Soc.*, 2007, **129**, 12571.
33. Y. Li, M. Afzaal, and P. O’Brien, *J. Mater. Chem.*, 2006, **16**, 2175.
34. A. G. Roca, M. P. Morales, and C. J. Serna, *IEEE Trans. Magn.*, 2006, **42**, 3025.
35. K. Woo, J. Hong, S. Choi, H. Lee, J. Ahn, C. S. Kim, and S. W. Lee, *Chem. Mater.*, 2004, **16**, 2814.

36. C. Yu, J. Zhao, Y. Guo, C. Lu, X. Ma, and Z. Gu, *J.Biomed. Mater. Res.*, 2008, **87**, 364.
37. J. Cheon, N.-J. Kang, S.-M. Lee, J.-H. Lee, J.-H. Yoon, and S. J. Oh, *J. Am. Chem. Soc.*, 2004, **126**, 1950.
38. X. Teng and H. Yang, *J. Mater. Chem.*, 2004, **14**, 774.
39. E. C. Scher and A. P. Alivisatos, *J. Am. Chem. Soc.*, 1999, **121**, 11595.
40. S. Sun and H. Zeng, *J. Am. Chem. Soc.*, 2002, **124**, 8204.
41. V. Yathindranath, L. Rebbouh, D. F. Moore, D. W. Miller, J. van Lierop, and T. Hegmann, *Adv. Funct. Mater.*, 2011, **21**, 1457.
42. E. Umut, F. Pineider, P. Arosio, C. Sangregorio, M. Corti, F. Tabak, A. Lascialfari, and P. Ghigna, *J. Magn. Magn. Mater.*, 2012, **324**, 2373.
43. T. Kikuchi, R. Kasuya, S. Endo, A. Nakamura, T. Takai, N. Metzler-Nolte, K. Tohji, and J. Balachandran, *J. Magn. Magn. Mater.*, 2011, **323**, 1216.
44. Z. Li, H. Chen, H. Bao, and M. Gao, *Chem. Mater.*, 2004, **16**, 1391.
45. J. Park, K. An, Y. Hwang, J.-G. Park, H.-J. Noh, J.-Y. Kim, J.-H. Park, N.-M. Hwang, and T. Hyeon, *Nat. Mater.*, 2004, **3**, 891.
46. A. Shavel and L. M. Liz-Marzán, *Phys. Chem. Chem. Phys.*, 2009, **11**, 3762.
47. N. R. Jana, Y. Chen, and X. Peng, *Chem. Mater.*, 2004, **16**, 3931.
48. C. B. Murray, D. J. Noms, and M. G. Bawendi, *J. Am. Chem. Soc.*, 1993, 8706.
49. M. F. Casula, Y. Jun, D. J. Zaziski, E. M. Chan, A. Corrias, A. P. Alivisatos, M. Science, and L. Berkeley, *J. Am. Chem. Soc.*, 2006, **128**, 1675.
50. S. Verma and D. Pravarthana, *Langmuir*, 2011, **27**, 13189.
51. A. S. Batsanov, Y. T. Struchkov, and G. A. Timko, *Koord. Khim.*, 1988, **14**, 266.
52. K. Abdulwahab, M. A. Malik, P. O’Brien, K. Govender, C. A. Muryn, G. A. Timco, F. Tuna, and R. E. P. Winpenny, *Dalton Trans.*, 2013, **42**, 196.
53. C. Wilson, B. B. Iversen, J. Overgaard, F. K. Larsen, G. Wu, S. P. Palii, G. A. Timco, and N. V. Gerbeleu, *J. Am. Chem. Soc.*, 2000, **122**, 11370.
54. C. Burda, X. Chen, R. Narayanan, and M. A. El-Sayed, *Chem. Rev.*, 2005, **105**, 1025.
55. S. G. Kwon and T. Hyeon, *Small*, 2011, **7,** 2685.

56. S. Sun, H. Zeng, D. B. Robinson, S. Raoux, P. M. Rice, S. X. Wang, and G. Li, *J. Am. Chem. Soc.*, 2004, **126**, 273.
57. H. Zeng, P. M. Rice, S. X. Wang, and S. Sun, *J. Am. Chem. Soc.*, 2004, **126**, 11458.
58. A.G. Roca, M. P. Morales, K. O’Grady, and C. J. Serna, *Nanotechnology*, 2006, **17**, 2783.
59. C. A. Crouse and A. R. Barron, *J. Mater. Chem.*, 2008, **18**, 4146.
60. J. M. Byrne, N. D. Telling, V. S. Coker, R. A. D. Pattrick, G. van der Laan, E. Arenholz, F. Tuna, and J. R. Lloyd, *Nanotechnology*, 2011, **22**, 455709.
61. V. S. Coker, N. D. Telling, G. van der Laan, R. A. D. Pattrick, C. I. Pearce, E. Arenholz, F. Tuna, R. E. P. Winpenny, and J. R. Lloyd, *ACS Nano*, 2009, **3**, 1922.
62. S. Si, C. Li, X. Wang, D. Yu, Q. Peng, and Y. Li, *Cryst. Growth Des.*, 2005, **5**, 391.
63. I. S. Jacobs, *J. Phys. Chem. Solids*, 1959, **11**, 1.

Chapter 3

Ternary and Quaternary Ferrite Nanoparticles

3.1 Summary

This chapter describes the synthesis of ternary ferrites of cobalt, manganese, zinc, nickel and quartenary- chromium cobalt ferrite nanoparticles using heterometallic pivalate clusters of $[Fe_2CoO(O_2C^tBu)_6(HO_2C^tBu)_3]$ **(1)**, $[Co_4Fe_2O_2(O_2C^tBu)_{10}]$ **(2),** $[Fe_2MnO(O_2C^tBu)_6(HO_2C^tBu)_3]$ **(3)**, $[Zn_4Fe_2O_2(O_2C^tBu)_{10}]$ **(4),** $[Fe_2NiO(O_2C^tBu)_6(HO_2C^tBu)_3]$ **(5)** and $[CrCoFeO(O_2C^tBu)_6(HO_2C^tBu)_3]$ **(6)** respectively as single source precursors. The precursors were thermolysed with oleylamine and oleic acid (capping agents) in either diphenyl ether or dibenzyl ether as solvent at their respective boiling points of 260 and 300 °C. The effect of reaction time, temperature and concentration (0.25 or 0.50 mmol) on the stoichiometry, phases or morphology of the nanoparticles were studied. TEM showed that highly monodispersed spherical ferrite nanoparticles were obtained using 0.50 mmol precursor concentrations at 260 °C in all cases except from **(2)** where a nearly monodispersed nanoparticles was produced.

The decomposition of precursors (0.25 mmol) investigated at different temperatures revealed that larger ferrites nanoparticles were obtained from **(1)** - **(5)** at higher temperature (300 °C) whilst the opposite was observed for cobalt ferrite from **(2)** as smaller nanoparticles appeared. The reaction time was investigated for all the precursors (0.25 mmol) at 260 °C by withdrawing at selected time intervals. The results obtained showed that aliquots withdrawn at reaction times of less than 1 hour contain traces of iron oxide whilst only pure ternary/quaternary ferrite was obtained after one hour. Magnetic measurements revealed that all the ferrite particles are superparamagnetic at room temperature with high saturation magnetisation values. XMCD confirmed that in cobalt and nickel ferrite particles, most of the nickel and cobalt cations are in the octahedral site. The site occupancy in cobalt ferrite is evident in their magnetic measurements having a large hysteresis (> 1T) at 5 K.

3.2 Introduction

Monodisperse magnetic nanoparticles have recently become significant in science and technology due to their unique properties. This is especially true for the spinel nanoparticles because their studies have brought about establishing a relationship between their magnetic properties and their basic chemical structure. These properties depend on the nature of the ions, their valency and their cation distribution between octahedral and tetrahedral sites.[1,2] Ferrite nanoparticles of general formula MFe_2O_4 (M= Fe, Co, Cr, Ni, Mn, Zn) are of interest because by varying the chemical identity of the M^{2+} ion, their electrical and magnetic properties can be fine-tuned for different applications.

Iron cobalt oxide (Fe_2CoO_4) has been reported to have a high magnetic anisotropy[3,4] whilst manganese ferrites ($MnFe_2O_4$) are characterised by low blocking temperatures and high saturation magnetisation.[5] Such ferrite nanoparticles find applications in electronic devices,[6] high density magnetic recording,[2] contrast agents in medical resonance imaging (MRI)[7,8] and gas sensors.[9] The numerous applications of such nanoparticles have prompted the development of different synthetic methods. Using co-precipitation methods, spherical[10] platey[11,12] or cubic[12] cobalt ferrite nanoparticles have been produced. Manganese and cobalt ferrite nanocrystals of different morphologies such as cubes,[3,13–17] spheres,[15–22] stars,[16] polyhedra[13,17] have been reported by thermal decomposition approaches.

Hydrothermal methods have also been used to grow cubic[23] or spherical[23,24] cobalt ferrite crystals. Manova *et al.* employed both co-precipitation and mechanical ball milling methods to synthesise cobalt ferrite nanoparticles and produced pseudo-spherical nanoparticles whose size increases with increase in milling time.[25] Zhang *et al.* synthesised $MnFe_2O_4$ nanoparticles by the formation of water-in-toluene reverse micelles using sodium dodecylbenzenesulfonate as the surfactant to obtain superparamagnetic nanoparticles whose size can be controlled by adjusting the ratio of water and toluene.[26] Similarly, Zhang *et al.* employed a reverse micelle microemulsion system to prepare silica coated magnetic nanoparticles of cobalt and manganese ferrites.[27] The magnetic measurements of these nanoparticles show a reduction in saturation magnetisation which was attributed to reduced quantity of magnetic material per gram of the ferrite-silica composite nanoparticles. Coker *et al.* synthesised cobalt ferrite nanoparticles extracellularly by using the iron(III) reducing bacterium (*Geobacter sulfurreducens*).[28] They obtained a high yield of nanoparticles with a narrow size distribution as indicated by the magnetisation measurements. A flow reactor synthesis of cobalt ferrite nanoparticles by a hydrothermal method has also been reported by several groups. Polyhedra[29] pseudo-spheres[30,31] or cubes[31] were prepared by this method.

Nickel ferrites are one of the important materials as its inverse spinel structures give rise to typical ferromagnetic properties, high electrical resistivity, moderate saturation magnetisation, and are readily available.[32,33] These properties find applications in various fields such as in recording tapes,[34] thermal therapy,[35] MRI,[36] gas sensors,[37] magnetic fluids,[1] electrodes,[38] catalysis[39] and transformers.[33] A number of synthetic routes have been developed for nickel ferrite nanoparticles including: co-precipitation[40,41] hydrothermal,[42,24,34,43–47] pulsed wire discharge,[1] sol-gel method,[48,49] flow reactor[30] and thermal decomposition.[19,14,50,17] Despite the numerous methods of synthetic routes, research on synthesising monodispersed nickel ferrites is still ongoing.

Zinc ferrite nanoparticles show significant differences in magnetic properties compared to the bulk material. Bulk zinc ferrite has a normal spinel structure with the nonmagnetic Zn^{2+} ions in the tetrahedral sites and Fe^{3+} ions in the octahedral sites leading to an antiferromagnetic interactions at about 10 K but in the zinc ferrite nanoparticles, there is a rearrangement of iron and zinc ions due to the high surface area of nanoparticles. This rearrangement of ions in turn creates a ferrimagnetic exchange interactions leading to a higher saturation magnetisation.[51–53] Zinc ferrite nanoparticles have potential applications in MRI,[54] gas sensors,[55] absorbent material in gas desulphurization,[56] and photocatalysts.[57] These applications have prompted the development of different synthetic methods including co-precipitation,[58,59] sol-gel,[60] biological,[61,62] micro-emulsion[63] and thermal decomposition.[24,28,32,41]

Quaternary ferrite nanoparticles could be prepared by the incorporation of another metal into ternary ferrites. Amongst the ternary ferrite nanoparticles, cobalt ferrite

($CoFe_2O_4$) has been a focus of research due to its excellent chemical stability, high coercivity, moderate saturation magnetisation, mechanical hardness and high magnetoristriction.[65–69] The doping of other metals into its structure affects cation distributions thereby resulting in a change in the magnetic and electrical properties which can be fine –tuned for different applications.[65,67,68,70–72]

The effect of chromium doped cobalt ferrite nanocrystals on their electrical and magnetic properties has been studied by some researchers and their investigation revealed that electrical resistivity increases whilst the blocking temperature, saturation magnetisation and coercivity decrease with increase in chromium concentration.[65,67,68,70,73–75] Paulsen *et al*. studied the effects of magnetic and magnetochemical properties of manganese doped cobalt ferrite by a ball milling process and observed that the Curie temperature and magnetorestriction decreased with increase in manganese contents.[76] Such ferrites have potential applications in stress sensor and high temperature materials.[69,73,75,76]

To date, very few reports are available on the use of single source precursor for the synthesis of nickel and zinc ferrite nanoparticles.[24,14,17] To the best of our knowledge, there have been no reports on the use of single source precursor to synthesise chromium doped and chromium cobalt ferrite nanoparticles.

In this chapter, we explore the use of heterometallic pivalate clusters as novel single source precursors for the synthesis of ternary ferrite (M = Co, Mn, Ni and Zn) and quaternary ferrite of chromium cobalt iron oxide nanoparticles.

3.3 Experimental

3.3.1 Synthesis of precursors

The clusters were synthesized and characterised by Prof. Winpenny group and the procedures followed are described below.

3.3.1.1 $[Fe_2CoO(O_2C^tBu)_6(HO_2C^tBu)_3]$ (1)

An excess of pivalic acid (30.0 g, 294 mmol) and potassium hydroxide (6.0g, 107 mmol) were stirred in water (25 mL) at 50 °C until a clear solution was formed (~10-15 minutes). To the solution was added a pre-heated (50 °C) iron nitrate nonahydrate (10.0 g, 24.8 mmol) and cobalt nitrate hexahydrate (5.0 g, 17.2 mmol) solution in water (25 mL). The mixture was stirred for 15 minutes during this time two layers formed, a brown organic layer and a clear pink aqueous solution. The flask was cooled in ice water, which results in solidification of the organic layer. The water layer was removed by decantation and the solid was washed with cold water followed by dissolution in petroleum ether (200 mL) The petroleum ether solution was filtered and the residue extracted with further petroleum ether (100 mL) to complete extraction. The two petroleum ether solutions were combined and the solvent was removed under reduced pressure. Acetonitrile (50 mL) was added to the residue obtained with stirring. After 15 minutes, the reddish-brown crystalline product was collected by filtration, washed with cold acetonitrile (3 x 10 mL) and dried in air. Elemental analysis: Found (%): C, 48.73; H, 7.49; Fe, 10.30; Co 5.22. Calc. (%) for $C_{45}H_{84}CoFe_2O_{19}$: C, 49.15; H, 7.70; Fe, 10.16; Co 5.36.

3.3.1.2 $[Co_4Fe_2O_2(O_2C^tBu)_{10}]$ (2)

Iron nitrate nonahydrate (10.0 g, 24.8 mmol), pivalic acid (70.0 g, 685 mmol) were heated while stirring at 160 °C (~ 3 hours), until the elimination of NO_2 has finished. The flask was then cooled to 100 °C and then cobalt(II) acetate tetrahydrate (12.45 g, 50 mmol) and toluene (75 mL) were added under a slow flow of nitrogen. After 1 hour, the temperature was increased to 165 °C in order to remove the toluene and the reaction mixture is kept at this temperature for 7 hours. The flask was then cooled to 60 - 70 °C and acetonitrile (50 mL) was added in small portion after which the temperature was increased to 175 °C and pivalic acid was removed by distillation in a flow of N_2. The brown-green powder was cooled to room temperature then tetrahydrofuran (100 mL) and toluene (50 mL) were added followed by refluxing with stirring for 5 hours. The solvent was removed and acetonitrile (150 mL) added to the residue and the mixture stirred for 1 hour at R.T. The solid formed was then collected by filtration and extracted with diethyl ether (200 mL). The diethyl ether solution was filtered and acetonitrile (300 mL) was added to the filtrate in small portions with stirring. During this time a microcrystalline brown-green product started to precipitate. Next day the product was filtered, washed copiously with acetonitrile and dried in air. Elemental analysis: Found (%): C, 42.88; H, 6.48; Fe, 7.89; Co 16.76. Calc. (%) for $C_{50}H_{90}Co_4Fe_2O_{22}$: C, 43.18; H, 6.52; Fe, 8.03; Co 16.95.

3.3.1.3 [$Fe_2MnO(O_2C^tBu)_6(HO_2C^tBu)_3$] (3)

The same method as for **(1)** but using manganese(II) nitrate tetrahydrate (5g, 19.9 mmol) in place of cobalt nitrate hexahydrate. Elemental analysis: Found (%): C, 49.29; H, 7.79; Fe, 10.30; Mn, 4.55. Calc. (%) for $C_{45}H_{84}Fe_2MnO_{19}$: C, 49.33; H, 7.73; Fe, 10.19; Mn, 5.01.

3.3.1.4 [$Zn_4Fe_2O_2(O_2C^tBu)_{10}$] (4)

The same method as for **(2)** but using zinc acetate dihydrate (11.0 g, 50 mmol). A pale yellow product was obtained. Elemental analysis: Found (%): C, 42.63; H, 6.36; Fe 7.79; Zn 18.47. Calc. (%) for $C_{50}H_{90}Fe_2Zn_4O_{22}$: C, 42.40; H, 6.40; Fe 7.89; Zn 18.46.

3.3.1.5 [$Fe_2NiO(O_2C^tBu)_6(HO_2C^tBu)_3$] (5)

The same method as for **(1)** but using nickel nitrate hexahydrate (5.0 g, 17.2 mmol). Experimental analysis: Found (%): C, 49.29; H, 8.06; Fe, 9.87; Ni, 5.03. Calc. (%) for $C_{45}H_{84}NiFe_2O_{19}$: C, 49.16; H, 7.70; Fe, 10.16; Ni, 5.34.

3.3.1.6 [$CrCoFeO(O_2C^tBu)_6(HO_2C^tBu)_3$] (6)

Iron nitrate nonahydrate (5.0 g, 12.4 mmol), chromium nitrate nonahydrate (5.0 g, 12.4 mmol) and pivalic acid (60.0 g, 588 mmol) were heated while stirring at 160-165 °C until the elimination of NO_2 has finished (about 5 hours). The flask was then cooled to 100 °C and cobalt(II) acetate tetrahydrate (3.60 g, 12.4 mmol) was added under a slow flow of nitrogen. This was followed by the addition of toluene (25 mL). After 1 hour, the temperature of oil bath was increased to 165 °C in order to remove the toluene and the reaction mixture is kept at this temperature for 32 hours. The flask was then cooled to 40 °C and acetonitrile (50 mL) was added in small portion while stirring. After 1 hour, the product was filtered, washed with acetonitrile (4 x 15 mL) and dried in air. Elemental analysis: Found (%): C, 49.46; H, 8.08; Fe, 5.36; Cr, 4.57; Co, 5.39. Calc. (%) for $C_{45}H_{84}CoCrFeO_{19}$: C, 49.32; H, 7.73; Fe, 5.1; Cr, 4.74; Co, 5.38.

3.3.2 Synthesis of nanoparticles

Nanoparticles were synthesized by thermolysis of the single source precursor. In a typical experiment, a mixture of oleylamine (OLAm) (27 mmol), oleic acid (OLA) (27 mmol), diphenyl ether or dibenzyl ether (20 mL) was degassed at 100 ºC in vacuo for 30 minutes and then heated to the boiling point of the solvent nitrogen. The required concentration of the precursor was dissolved in the appropriate solvent (10 mL) and injected into the solution of the hot mixture. The reaction was maintained at 230 ºC for 2 hours. The dark mixture was allowed to cool and methanol was added in excess to precipitate the nanoparticles which were then isolated by centrifugation. The residue was washed with methanol several times then redispersed in toluene.

3.3.2.1 Cobalt, manganese, zinc and nickel ferrite nanoparticles

The effect of temperature, concentration and reaction time on the phase, stoichiometry and morphology of the ferrite nanoparticles was investigated for each precursor. The concentration effect was studied at 260 °C with 0.25 mmol and 0.50 mmol precursor concentrations. Two different boiling point solvents (diphenyl ether at 260 °C, dibenzyl ether at 300 °C) were used to investigate the effect of decomposition temperature at a fixed precursor concentration of 0.25 mmol. The reaction time was studied at 260 °C using 0.25 mmol precursor concentrations by withdrawing aliquots at selected time intervals.

3.3.2.2 Quaternary ferrite ($FeCrCoO_4$) nanoparticles

The effect of precursor concentration was studied for $[CrCoFeO(O_2C^tBu)_6(HO_2C^tBu)_3]$ **(6)** at 260 °C with 0.25 mmol and 0.50 mmol concentrations. The effect of solvent system was investigated by thermolysis of 0.25 mmol precursor using diphenyl ether or dibenzyl ether or octadecene as the solvent. The reaction time was studied at 260 °C using 0.25 mmol precursor concentrations by withdrawing aliquots at selected time intervals.

3.4 Results and discussion

3.4.1 Thermogravimetric analysis

TGA of the precursors gave an insight into their decomposition pathway and volatility. Complex **(1)** indicated a multi-step decomposition with a rapid weight loss between 203 and 290 °C whilst (**2)** showed single step decomposition with a rapid weight loss between 226 and 418 °C (Fig. 3.1). For **(1)** and **(2),** the amount of solid remaining are 12 % and 9 % which are lower than their calculated value of 17 % and 21 %, respectively, for their ternary oxide ($CoFe_2O_4$). Interestingly complex **(1)** showed a decomposition pathway at about 335 °C with a percentage residue of about 22 % which is close to the calculated value of 21 % for $CoFe_2O_4$.

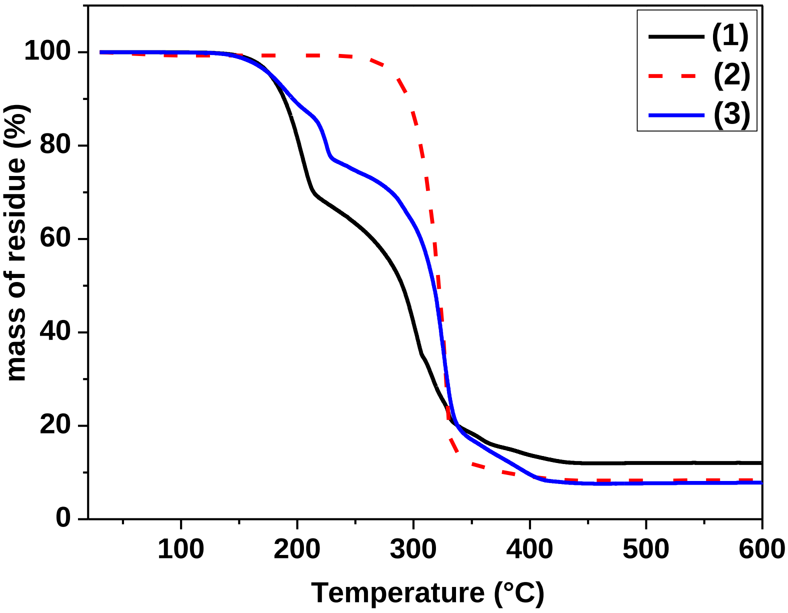

Fig. 3.1 TGA of precursors $[Fe_2CoO(O_2C^tBu)_6(HO_2C^tBu)_3]$ **(1),** $[Co_4Fe_2O_2(O_2C^tBu)_{10}]$ **(2)** and $[Fe_2MnO(O_2C^tBu)_6(HO_2C^tBu)_3]$ **(3).**

The manganese cluster **(3)** indicated a multistep decomposition with a rapid weight loss between 227 and 420 °C with a final residue of 8 %, lower than the calculated value of 21 % for $MnFe_2O_4$. (Fig. 3.1) Cluster **(3)** showed a similar pathway to **(1)** also at about 337 °C, a solid residue of about 20 % was found which is very close to the calculated value of 21 % for $MnFe_2O_4$.

The zinc-iron precursor **(4)** also exhibited similar features with cobalt-iron cluster **(2)** with a single step decomposition and rapid weight loss (Fig. 3.2). **(4)**

decomposed between 250 – 310 °C with a final solid residue of 10 % which is lower than the calculated value of 17 % for $ZnFe_2O_4$ but matches fairly with the calculated residue of Fe_2O_3 (11 %).

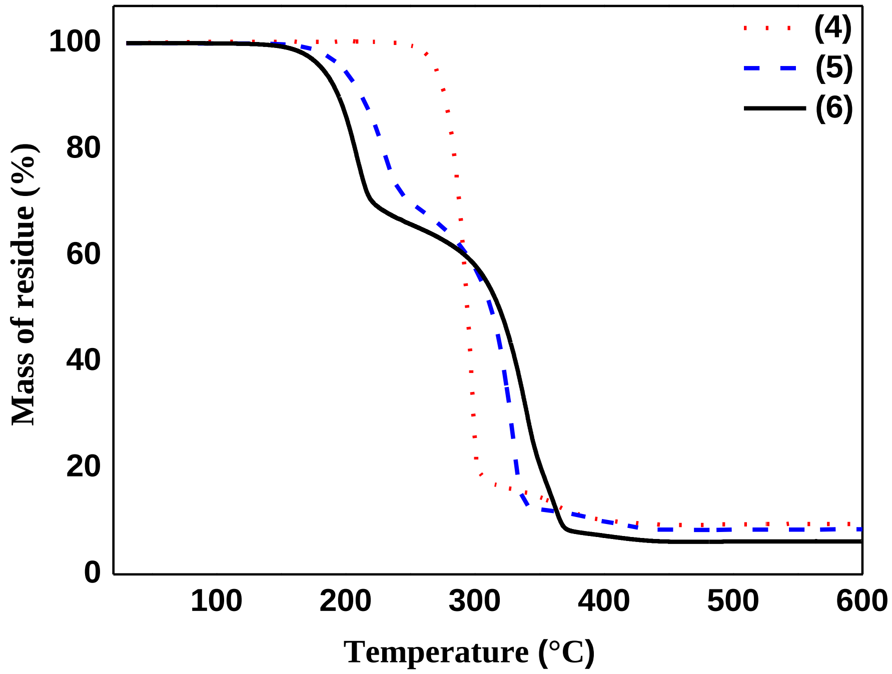

Fig. 3.2 TGA of precursors $[Zn_4Fe_2O_2(O_2C^tBu)_{10}]$ **(4),** $[Fe_2NiO(O_2C^tBu)_6(HO_2C^tBu)_3]$ **(5)** and $[CrCoFeO(O_2C^tBu)_6(HO_2C^tBu)_3]$ **(6).**

The nickel iron cluster **(5)** and the quaternary cluster **(6)** both indicated a multi-step decomposition with a rapid weight loss between 240- 335 °C **(5)** and 275- 370 **(6).** The solid residue remaining is 9 % for **(5)** which is lower than the calculated value of 21 % for $NiFe_2O_4$. For **(6)**, a final residue of 6 % was obtained which is less than the calculated value of 21 % for their quaternary oxide ($CrCoFeO_4$). For the nickel-iron cluster **(5)**, a weight loss was observed at about 339 °C with a percentage residue of 14% which is the same as calculated value for Fe_2O_3.

Pivalate clusters sublime and are thus volatile; hence the lower percentage of residue obtained are as expected.

3.4.2 Cobalt and manganese ferrite nanoparticles

The ferrite nanoparticles obtained from precursors **(1), (2)** and **(3)** were analysed by powder X-ray diffraction (p-XRD), TEM, ICP, EPMA, XMCD and SQUID. The effect of reaction time, temperature and concentration on the morphology and phase of the nanoparticles is described as follows.

3.4.2.1 Cobalt and manganese ferrite nanoparticles obtained at different reaction times.

The effect of reaction time was studied at 260 °C with 0.25 mmol precursor concentration.

The p-XRD pattern obtained from **(1)** showed that the intensity of the peaks increases with reaction time. The nanoparticles produced at reaction times less than 30 minutes were predominantly tetragonal iron oxide ($Fe_{1.996}O_{2.963}$) (ICDD card No. 01-089-5894) whilst those withdrawn at 1 hour and 2 hours were cubic spinel iron cobalt oxide Fe_2CoO_4 (ICDD card No. 04-005-7078) (Fig. 3.3(a)). The presence of iron oxide at 30 minutes suggests that the production of the mixed oxide is still in progress. TEM images showed that the crystallinity and diameter increases over time as observed in images obtained at 30 minutes (3.8± 1 nm), 1 hour (4.3± 0.7 nm) and at 2 hours (5.3± 1 nm) (Fig. 3.3 (b)-(d)).

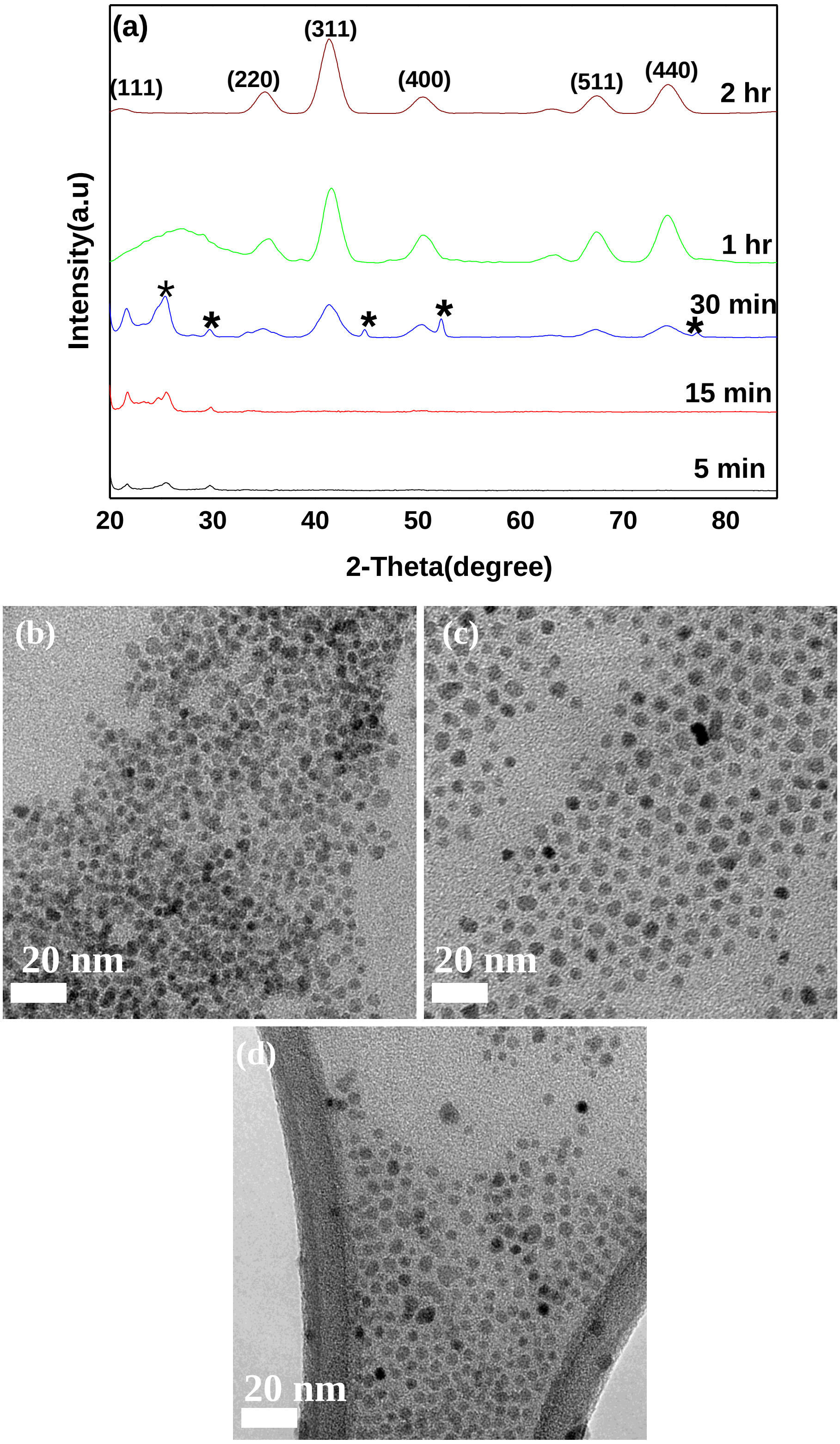

Fig. 3.3 (a) A series of p-XRD pattern for Fe_2CoO_4 nanoparticles from **(1)** at different times.*corresponds to the $Fe_{1.966}O_{2.963}$ peaks. (b)- (d): TEM images of Fe_2CoO_4 obtained from **(1)** at 30 minutes, 1 hour and 2 hours respectively.

The nanoparticles obtained from **(2)** showed similar behaviour with those obtained from **(1)** as the intensity of the peaks and average diameters increase over time. For reaction times less than 30 minutes, the peaks contained traces of tetragonal iron oxide (ICDD card No. 01-089-5894). At over one hour, the patterns obtained correspond to cubic spinel iron cobalt oxide (Fe_2CoO_4) with ICDD card No. 00-022-1086 (Fig. 3.4(a)). The average diameters calculated from TEM images are 4.4 ± 0.6, 5.5 ± 0.6 and 6.7 ± 1 nm at 30 minutes, 1 hour and at 2 hours respectively (Fig. 3.4(b)-(d)).

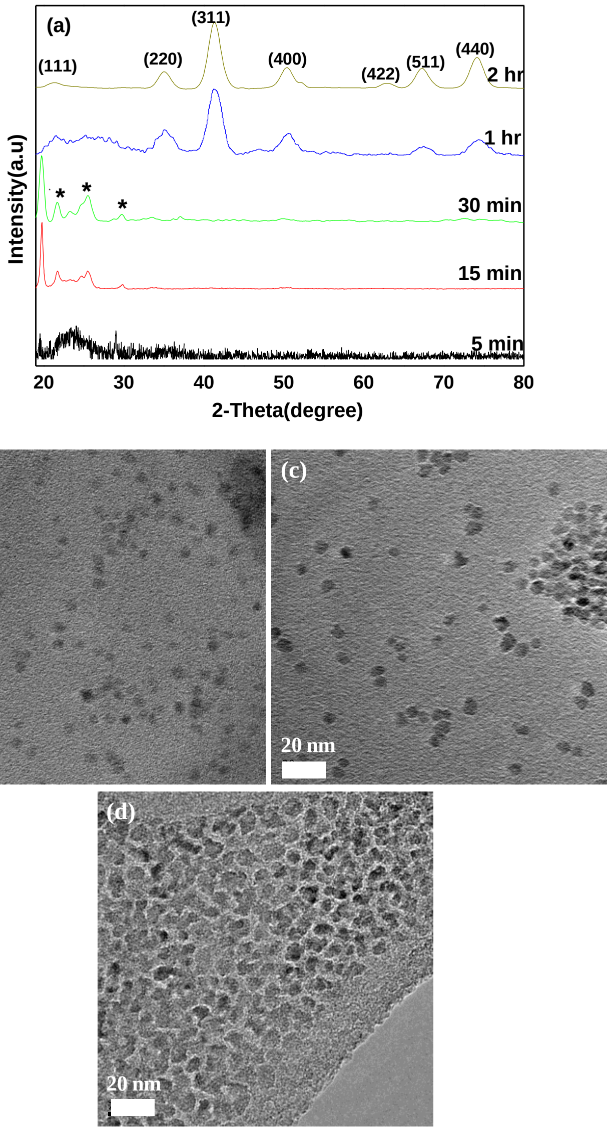

Fig. 3.4 (a) A series of p-XRD pattern for Fe_2CoO_4 nanoparticles from **(2)** at different times.*corresponds to the $Fe_{1.966}O_{2.963}$ peaks. (b)- (d): TEM images of Fe_2CoO_4 obtained from **(2)** at 30 minutes, 1 hour and 2 hours respectively.

The p-XRD pattern for nanoparticles obtained from **(3)** showed no peaks for aliquots withdrawn for reaction times of less than 15 minutes. At 15 minutes there were distinct but broad peaks indicating the growth of cubic magnetite (Fe_3O_4) (ICDD card No.01-079- 0416), these peaks become more intense after 30 minutes. After 1 hour of reaction, p-XRD patterns correspond to the cubic phase of manganese iron oxide nanoparticles ($Mn_{0.43}Fe_{2.57}O_4$) (ICDD card No. 01-089-280(Fig. 3.5(a)). The average diameters of the manganese ferrite nanoparticles calculated from the TEM are: 3.1 ± 0.7, 3.7 ± 0.5 and 4.8 ± 1 nm at 30 minutes, 1 hour and 2 hours respectively (Fig. 3.5(b)-(d). These results are consistent with those obtained from the other two precursors as their average diameters increased with time.

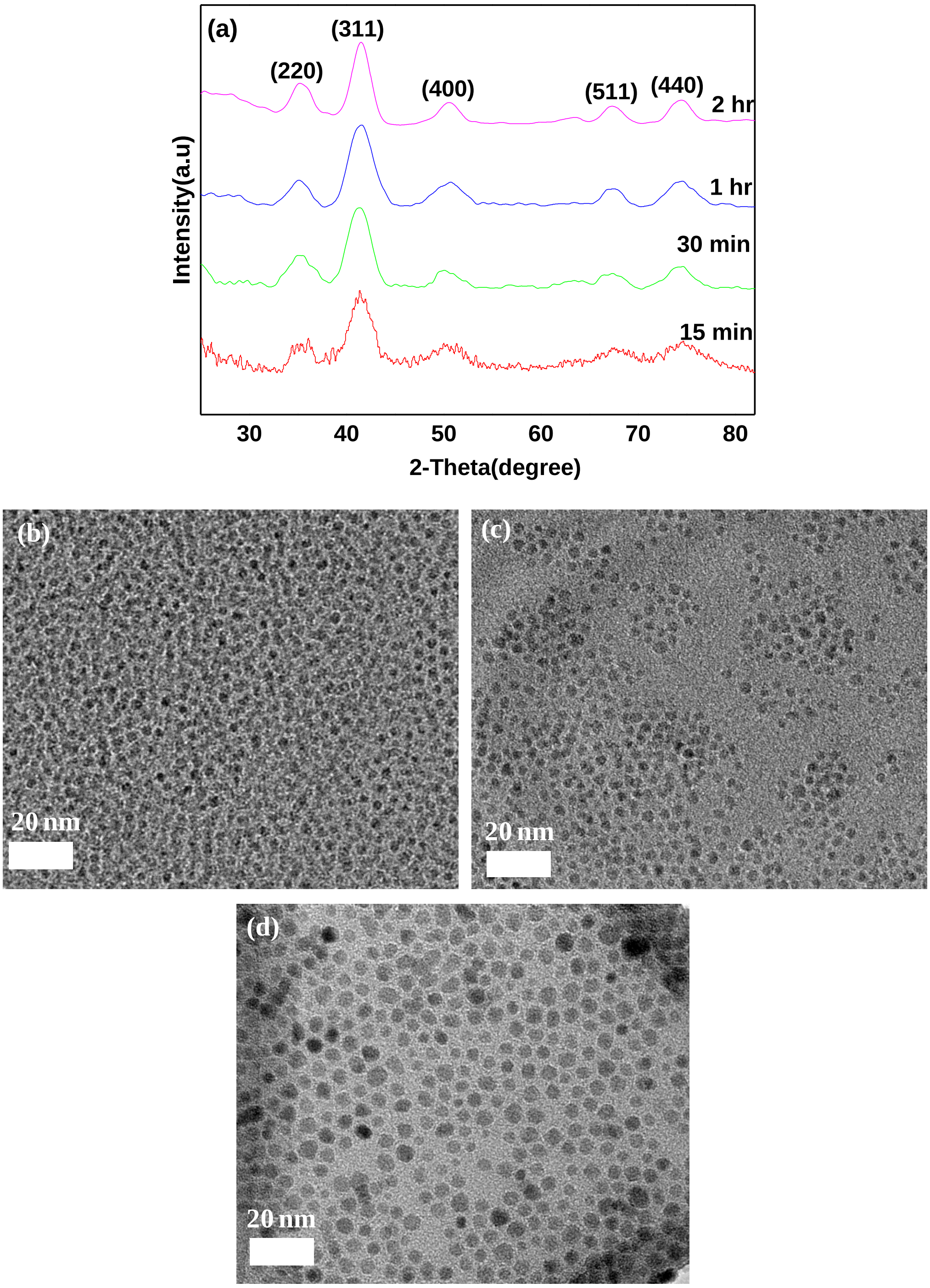

Fig. 3.5 (a) A series of p-XRD pattern for $Mn_{0.43}Fe_{2.57}O_4$ nanoparticles from **(3)** at different times.*represents cubic Fe_3O_4 peaks. (b)- (d): TEM images of $Mn_{0.43}Fe_{2.57}O_4$ obtained from **(3)** at 30 minutes, 1 hour and 2 hours respectively.

An increase in the nanoparticle’s diameter over time was observed in all three cases (Fig. 3.6). At the onset of the reaction, smaller sizes were obtained which are energetically unfavourable and a focusing in size occurs in which small particles grow bigger.[77,78,79] After this stage, Ostwald ripening or defocusing starts in which larger particles grow at the expense of the smaller ones thereby leading to an initial broader size distribution until about 2 hours when a nearly monodispersed distribution was achieved.

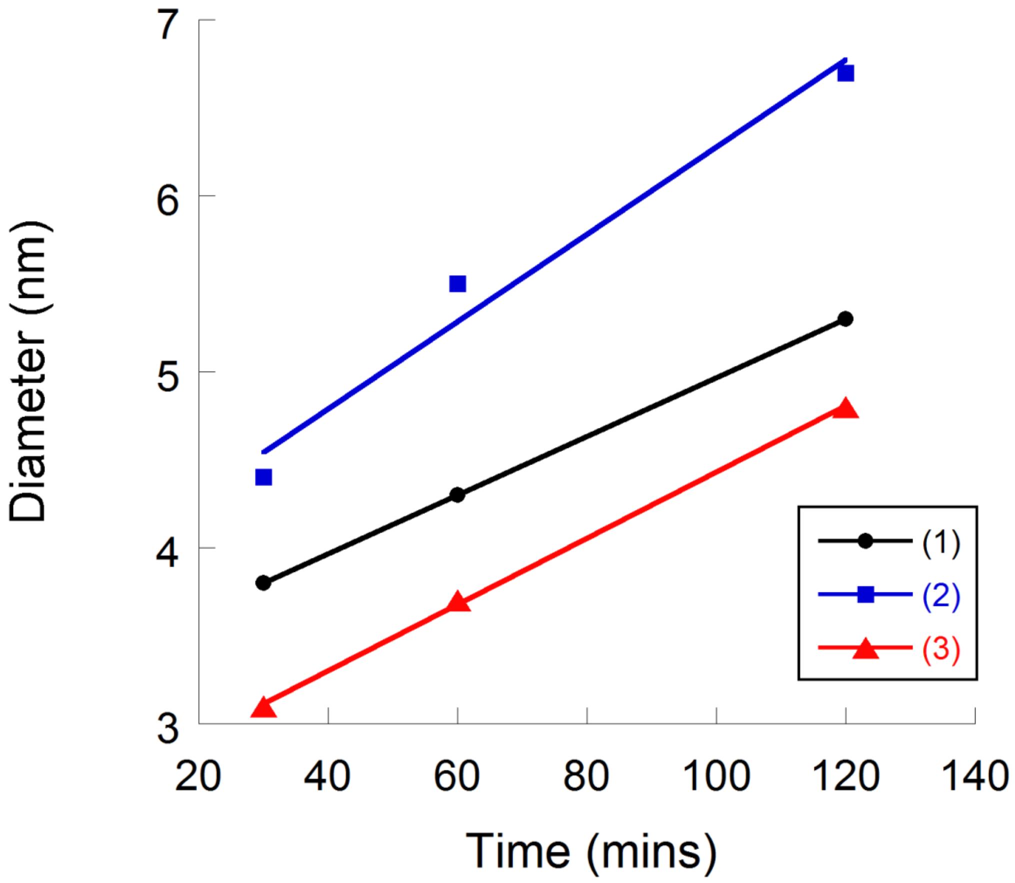

Fig. 3.6 A graph showing a summary of the variation of average nanoparticles' diameters obtained from precursors $[Fe_2CoO(O_2C^tBu)_6(HO_2C^tBu)_3]$ **(1),** $[Co_4Fe_2O_2(O_2C^tBu)_{10}(MeCN)_2]$ **(2)** and $[Fe_2MnO(O_2C^tBu)_6(HO_2C^tBu)_3]$ **(3)** over time**.**

3.4.2.2 Cobalt and manganese ferrite nanoparticles obtained at different temperatures

The effect of decomposition / injection temperature was studied for precursors **(1), (2)** and **(3)** at the boiling point of two different solvents (diphenyl ether at 260 ºC or dibenzyl ether at 300 °C) at a fixed precursor concentration (0.25 mmol).

The p-XRD pattern of nanoparticles obtained from **(1)** at 260 and 300 °C both correspond to cubic iron cobalt oxide (Fe_2CoO_4) (ICDD card No. 04-005-7078).

(Fig. 3.7(a)). The average particle diameter estimated by the Scherrer equation is 5nm for particles obtained at 260 ºC and 6.5 nm for those obtained at 300 ºC.

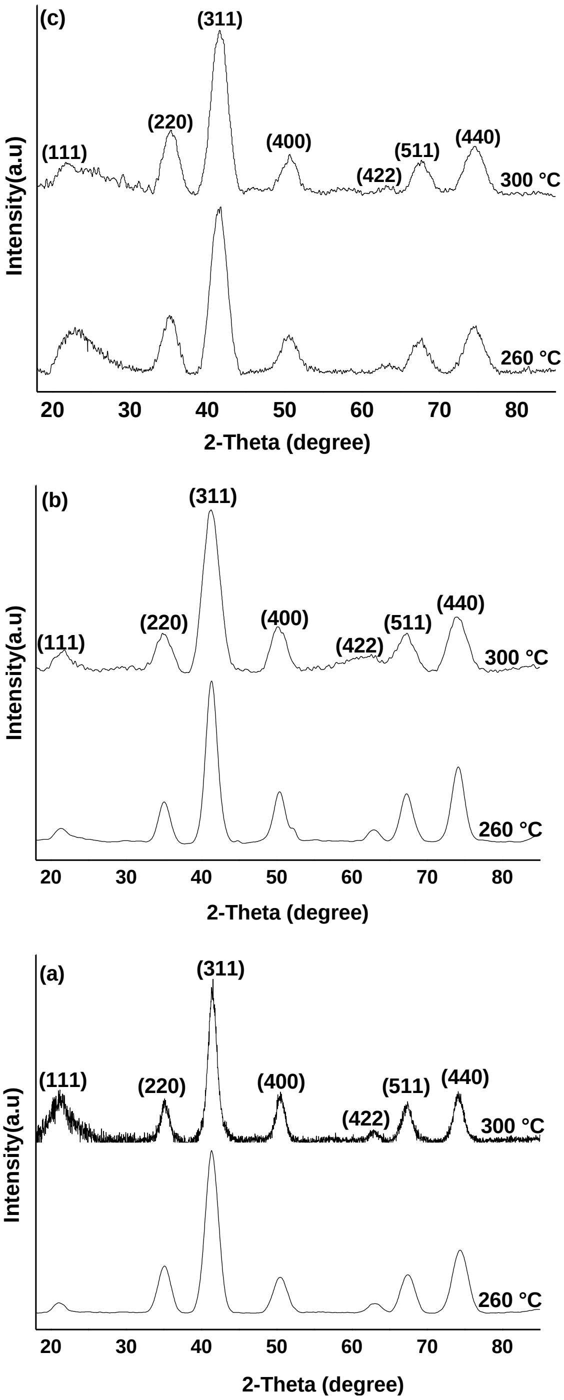

Fig. 3.7 The p-XRD pattern for nanoparticles obtained from the thermolysis of the precursors (0.25 mmol) in different boiling point solvents of either diphenyl ether (260 °C) or dibenzyl ether (300 °C). (a) cubic Fe_2CoO_4 from **(1)** (b**)** cubic Fe_2CoO_4 from **(2)** and (c) cubic $Mn_{0.43}Fe_{2.57}O_4$ from **(3)**.

The nanoparticles obtained from **(2)** at 260 and 300°C were of cubic cobalt iron oxide nanoparticles (Fe_2CoO_4) (ICDD card No. 00-22-1086) (Fig. 3.7(b)). Scherrer equation was used to estimate the particle diameters which correspond to 6 and 3.7 nm at 260 and 300 °C respectively.

The thermolysis of (**3)** at both 260 and 300 °C resulted in cubic iron manganese oxide ($Mn_{0.43}Fe_{2.57}O_4$) (ICDD card No. 01-089-2807) (Fig.3.7(c)). The particle sizes estimated by the Scherrer equation are: 4.5 and 5.0 nm for nanoparticles obtained at 260 and 300 ºC respectively.

The average diameter calculated from the TEM images for nanoparticles obtained at 260 °C and 300 °C are 5.3 ± 1 and 7 ± 0.6 nm for cobalt ferrite from **(1),** 4.6 ± 0.4 and 6.7 ± 1 nm for cobalt ferrite from **(2),** 4.8 ± 1 and 5.3 ± 0.7 nm for manganese ferrite from **(3)** respectively (Fig. 3.8).

In all the cases, more monodispersed nanoparticles were obtained at higher temperature.

The results obtained for nanoparticles from **(1)** and **(3)** at different temperatures are in good agreement to what has been reported by us and other researchers.[16,77,80,81,82,83] This has been explained that higher decomposition temperatures facilitate the formation of bigger particles because the reactivity of the precursors is increased in higher boiling point solvent. Nanoparticles obtained from **(2)** gave smaller particles at higher temperature in contrast to those of **(1)** and **(3)**. This observation could be due to decomposition in single step decomposition as compared to precursors **(1)** and **(3)** which showed multi-step decomposition (Fig. 3.1). At higher temperature, single step decomposition pathway is more favourable to a burst of nucleation than the multi-step. Another possibility is that $[Co_4Fe_2O_2(O_2C^tBu)_{10}]$ (2) gave a high concentration of Co and Fe ions which favour a high initial supersaturation. For a given concentration of solute, a larger number of nuclei translate into smaller sized nanoparticles. The rate of nucleation per unit volume is proportional to the number of particles in solution.[78,79]

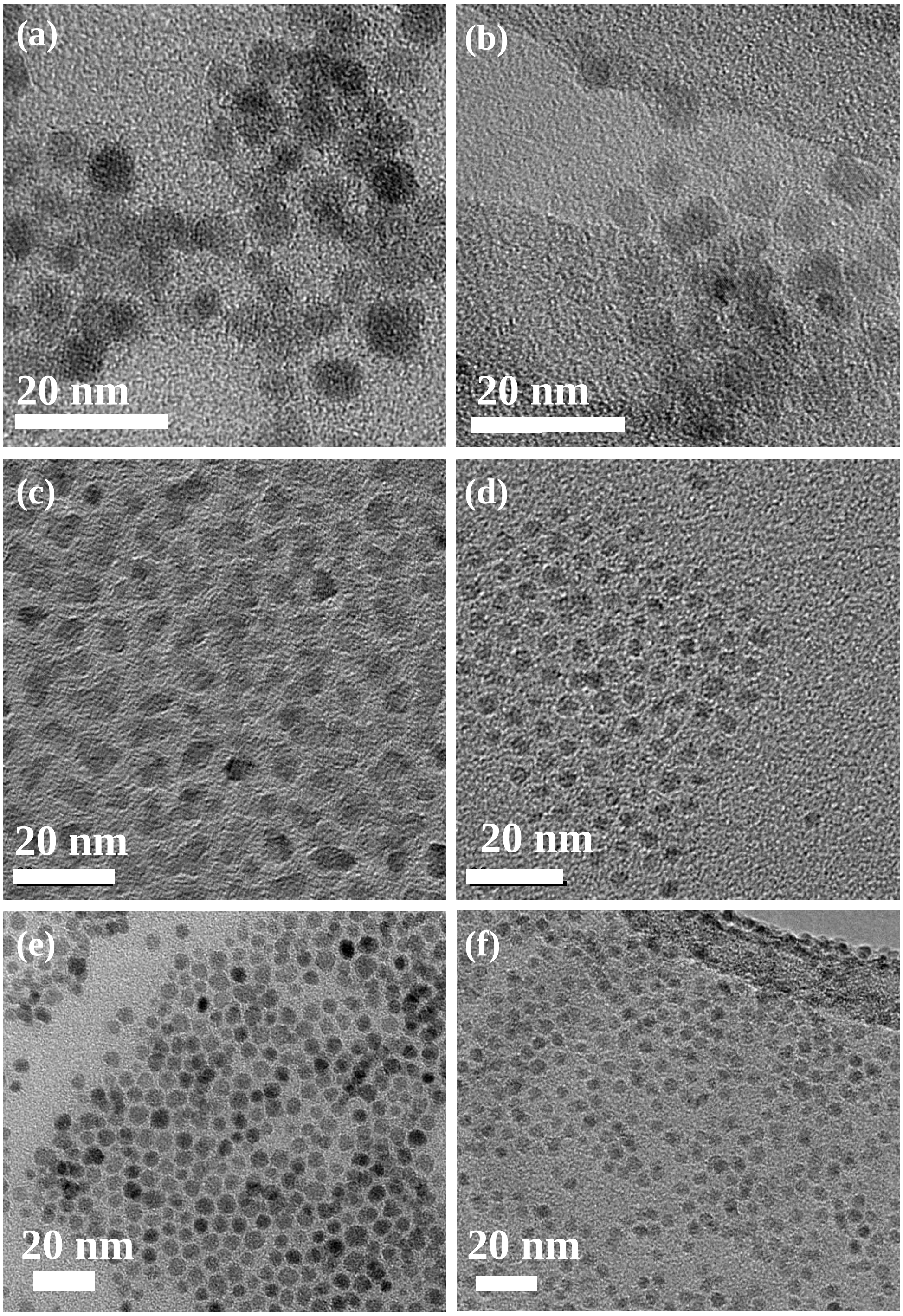

Fig. 3.8 (a) - (b) TEM images of Fe_2CoO_4 from **(1)** at 260 °C and 300 °C.(c) - (d) TEM of Fe_2CoO_4 from **(2)** at 260 and 300 °C respectively. (e) - (f) TEM of $Mn_{0.43}Fe_{2.57}O_4$ from **(3)** at 260 °C and 300 °C.

Table 3.1 Size of the ferrite nanoparticles obtained by thermolysis of **(1), (2) and (3)** at different temperatures.

Precursor	Temp.(°C)	TEM (nm)	p-XRD(nm)
(1)	260	5.3 ± 1.0	5.0
(1)	300	7.0 ± 0.6	6.5
(2)	260	6.7 ± 1.0	6.0
(2)	300	4.6 ± 0.4	3.7
(3)	260	4.8 ± 1.0	4.5
(3)	300	5.3 ± 0.7	5.0

3.4.2.3 Cobalt ferrite nanoparticles obtained from (1) at different concentrations

The effect of precursor concentrations (0.25 or 0.50 mmol) was investigated at 260 °C.

The p-XRD patterns of nanoparticles obtained from **(1)** at the two concentrations (0.25 and 0.50 mmol) matched with cubic spinel Fe_2CoO_4 (ICDD card No. 04-005-7078) (Fig. 3.9). The average crystallite sizes estimated by Scherrer equation were 3.0 nm and 5.0 nm with 0.50 and 0.25 mmol concentrations respectively. TEM images showed that particles obtained with 0.50 mmol concentration (S2) showed a highly monodispersed spherical nanoparticles with an average diameter of 3.6 ± 0.2 nm whilst a nearly monodispersed particles were obtained with 0.25 mmol concentration (S1) with an average diameter of 5.3 ± 1.0 nm (Fig. 3.9(a)).

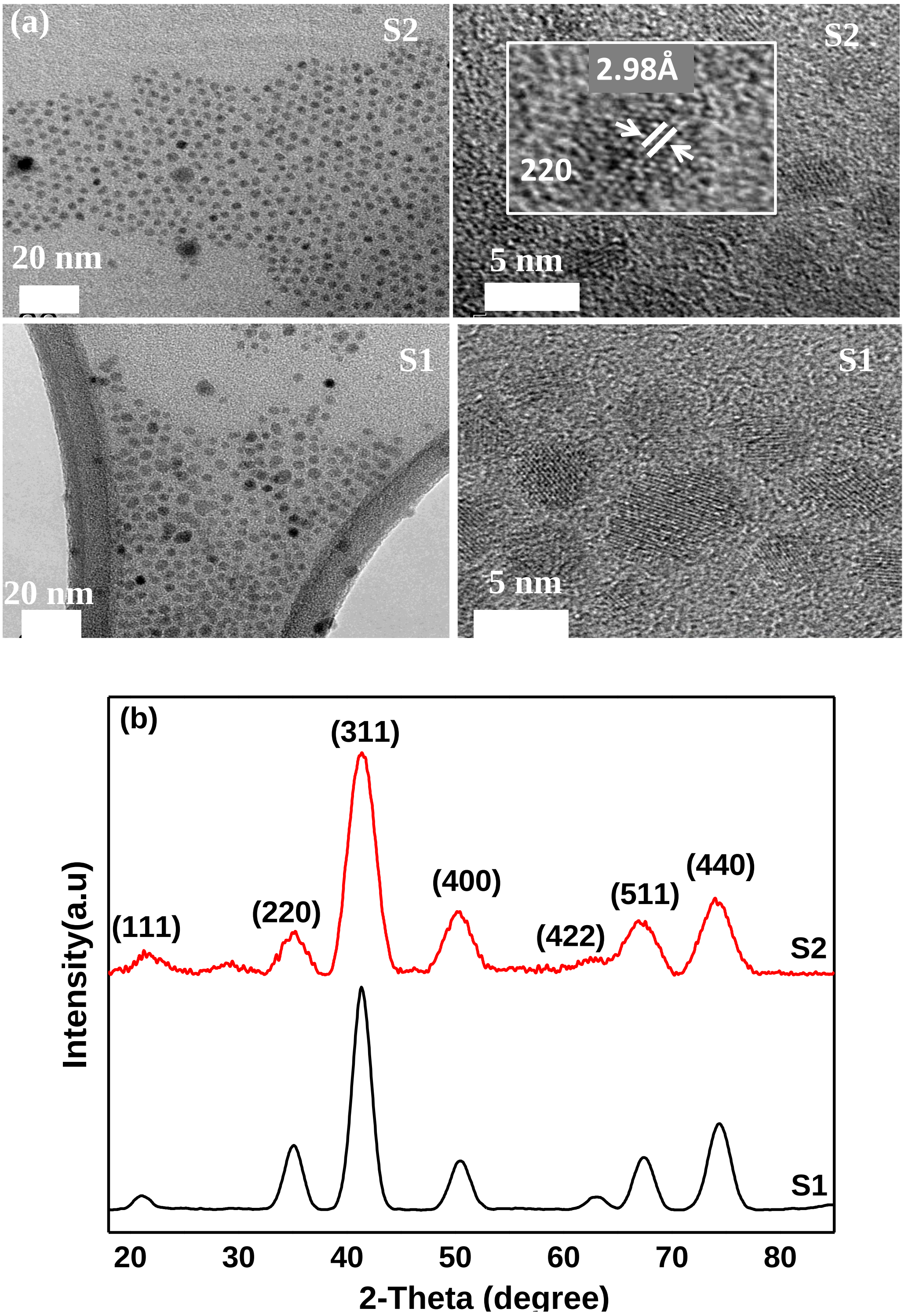

Fig. 3.9 (a) TEM and HRTEM images of Fe_2CoO_4 obtained from **(1)** at different concentrations. S1 and S2 correspond to Fe_2CoO_4 obtained from 0.25 mmol and 0.50 mmol precursor concentrations respectively. (b) The p-XRD patterns of cubic spinel Fe_2CoO_4 obtained from **(1)** at different precursor concentrations.

The particles are crystalline as seen in the lattice fringes (Fig. 3.9(a)) with a *d*-spacing of 2.98 Å which is very close to the (220) reflection of iron cobalt oxide (ICDD card No: 04-005-7078).

The smaller size of nanoparticles obtained from higher concentrations of precursors is in agreement with those reported by other researchers as explained by nucleation plus growth process.[16,84,85,86] The higher concentration of precursor generates more nuclei per unit volume as compared to that of the lower concentration, hence the more nanoparticles but with smaller size.

3.4.2.4 Magnetic properties of Fe_2CoO_4 nanoparticles from (1)

Magnetic measurements of Fe_2CoO_4 obtained from **(1)** revealed that the nanoparticles display superparamagnetic behaviour at room temperature, that is, the orientation of their magnetic moments responds freely to thermal fluctuations. This property is important for biomedical applications. An estimate for the blocking temperature (T_B) of the samples is obtained through examination of the field-cooled (FC) and zero-field-cooled (ZFC) magnetisation curves collected at 100 Oe magnetic field (Fig. 3.10(a)). This blocking temperature defines the crossover between ferri/ferromagnetism and superparamagnetism, and is graphically determined to be the point at which the gradient of the ZFC curve approaches zero.[87] The data show that T_B increases with increasing particle diameter, ranging from 67 K for cobalt iron oxide (Fe_2CoO_4) particles obtained from **(1)** at 0.50 mmol (S2) having an average diameter of 3.6 nm to 90 K for particles produced at 0.25 mmol (S1) with an average diameter of 5.3 nm. The blocking temperature for particles of average diameter 3.6 ± 0.2 nm is well defined, indicating a very narrow distribution of particle diameter whilst the blocking temperature for particles of average diameter 5.3 ± 1 nm is not well defined, indicating a wider distribution of the particle diameters.

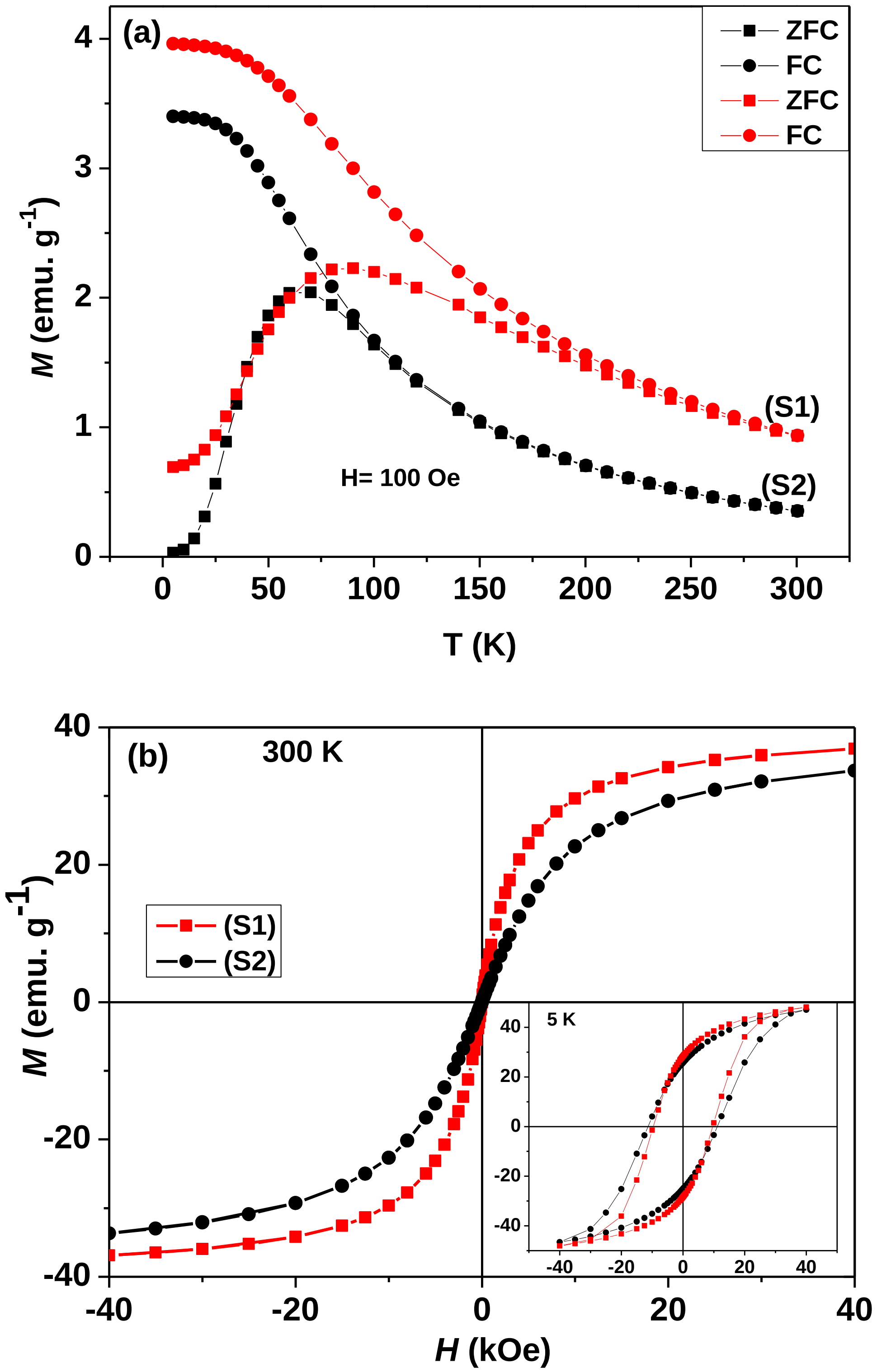

Fig. 3.10 (a) ZFC and FC magnetisation curves for S1 and S2 (Fe_2CoO_4) nanoparticles obtained from **(1)** of average diameter 5.3 ± 1 nm and 3.6 ± 0.2 nm respectively. (b) The hysteresis loops measured at 5 and 300 K for S1 and S2 nanoparticles**.**

Above the blocking temperature, the thermal energy is enough to overcome the anisotropy energy barrier of the particles, thus the remanent magnetisation tend towards zero and the particles are said to exhibit superparamagnetism.[28]

Field dependent magnetisation studies performed at temperatures of 5 and 300 K on Fe_2CoO_4 nanoparticles obtained from **(1)** have showed that the saturation magnetisation (M_s) increases with the average particle diameter at both temperatures (Fig. 3.10(b)).

Cobalt iron oxide nanoparticles of average diameter 3.6 nm are characterised by M_s values of 47 (5 K) and 33 emu.g^{-1} (300 K) whilst those with average diameter of 5.3 nm exhibit M_S values of 48 (5 K) and 37 emu.g^{-1} (300 K). Bulk cobalt iron oxide was reported to have M_S = 80 emu.g^{-1} at room temperature which is greater than that observed for our cobalt iron oxide nanoparticles.[21] Such a difference is often observed with the nanoparticles and is most likely attributed to the existence of organic coating agents, and intrinsic spin disorder, at the surface of such small nanoparticles.[88–91]

Remarkably, the magnetisation *versus* field measurements at 5 K have revealed the presence of a large hysteresis loop with values of the coercive field (H_c) (*i.e.* the magnetic field needed for the magnetisation to return to zero) and remanent magnetisation (M_R) (*i.e.* the magnetisation retained by nanoparticles when the magnetic field is switched off) of *ca.* 11.3 kOe and 25.6 emu/g for cobalt iron oxide nanoparticles of average diameter 3.6 nm, and 10.0 kOe and 28.4 emu.g^{-1} for those with average diameter 5.3 nm. Such a behaviour is directly correlated with the large magnetic anisotropy of the cobalt iron oxide nanoparticles.[92] In addition, the slightly higher Co content of the nanoparticles with average diameter 3.6 nm as compared to those with diameter 5.3 nm is likely to justify their lower M_s and M_R values. Indeed CoO has a low magnetisation (15 emu.g^{-1} at 1.7 K for 4.5 nm sized nanoparticles)[93] which can decrease the overall magnetisation of the cobalt iron oxide nanoparticles.

3.4.2.5 ICP-OES, EPMA and XMCD analysis of Fe_2CoO_4 nanoparticles from (1)

ICP-OES was used to determine the ratio of [Fe]: [Co] which found the ratio is approximately 2.00: 1.00 for Fe_2CoO_4 particles obtained at 0.50 mmol precursor concentration (S2) whilst the ratio 2.30: 0.65 was obtained for particles at 0.25 mmol precursor concentration (S1). In addition, the cation (Fe, Co) ratios of the nanoparticles were determined using EPMA, a ratio of 2.07: 0.93 was found for S2 whist for S1, the ratio was 2.34: 0.66 (Table 3.2).

The ICP results are consistent with the EPMA analysis and also revealed that stoichiometric Fe_2CoO_4 was obtained only at a higher precursor concentration even though in both cases the ratio of [Fe] : [Co] in the precursor is the same (2:1).

XMCD is dependent upon the magnetic moments of the Fe in the two sub-lattices in the ferrite structure, (spin up and spin down), valence state (via the number of *d* electrons) and site symmetry (crystal field).[94] Thus the distribution of Fe cations within the magnetite structure can be determined by comparison of the XMCD to atomic multiplet calculations.[94,95] Atomic multiplet calculations involve fitting experimental spectra by means of a non-linear least square analysis using calculated spectra for each of the Fe sites.[94] The technique has been used successfully to determine site occupancies in ferrite spinels[96,97] and nanoparticulate bio-ferrites.[28,98] The Fe $L_{2,3}$ XAS of the S1 and S2(Fe_2CoO_4) nanoparticles (Fig. 3.11(a)) show consistent spectral shapes with both spectra containing two absorption intensities at 707.6 and 709.0eV.

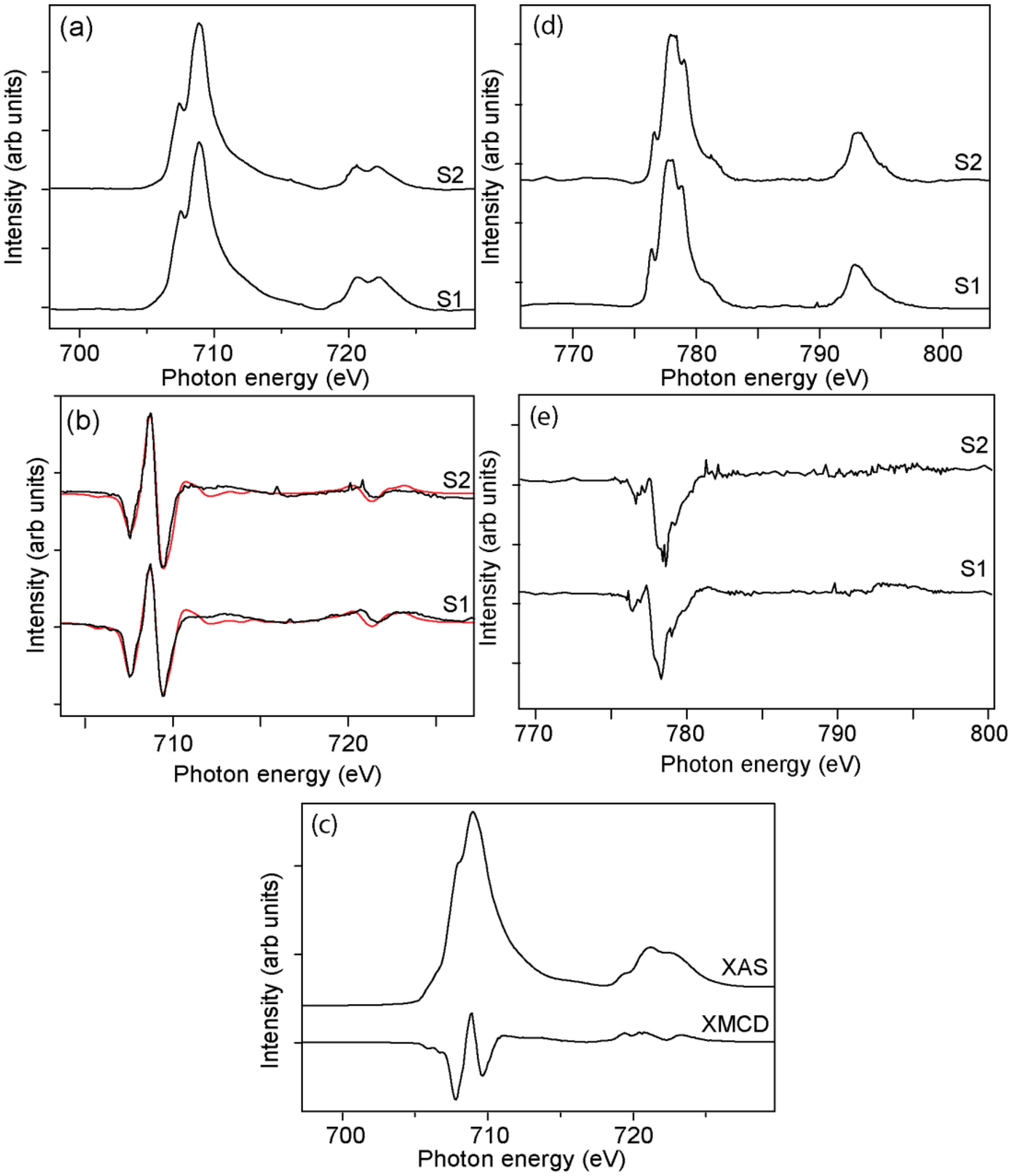

Fig. 3.11 (a) Fe $L_{3,2}$ XAS spectra of Co-ferrite nanoparticles, showing the enhanced peak at 707.6eV, indicating a decrease in Fe(II) concentration compared to magnetite, (b) Fe $L_{3,2}$ XMCD spectra of Co-ferrite nanoparticles, showing the low intensity of the relatively lowest energy contribution, compared to Fe_3O_4 (Fig. 3.11c) Experimental data in black; fits using atomic multiplet calculations in red,; (c) Fe $L_{3,2}$ XAS and XMCD spectrum of stoichiometric magnetite. The three peaks in the XMCD spectrum relate to (from lower to higher energy) $Fe^{2+}O_h$, $Fe^{3+}T_d$ and $Fe^{3+}O_h$ (XMCD x3). (d) Co $L_{3,2}$ XAS of Co ferrite nanoparticles showing the predominance of Co^{2+} O_h with an additional high energy component representing Co^{3+} T_d, (e) Co $L_{3,2}$ XMCD spectra of Co-ferrite nanoparticles. (S1 and S2 correspond to Co-ferrite nanoparticles obtained from **(1)** at 0.25 and 0.50 mmol).

Compared to Fe $L_{3,.2}$ XAS spectra of stoichiometric magnetite $Fe^{2+}(Fe^{3+})_2O_4$ (Fig. 3.11(c)) the peak at lower energy is relatively enhanced, and the spectral shape indicates an additional Fe(III) component. This is to be expected as stoichiometric Co-ferrite contains a greater proportion of Fe(III) as the Fe(II) in magnetite is substituted with Co(II).[99] In the XMCD spectra of stoichiometric Fe_3O_4 (Fig. 3.11(c)) each of the three peaks derived from the L_3 absorption edge corresponds primarily to a different site in the magnetite structure; the lowest energy, negative peak corresponds to octahedral Fe^{2+}[B], the positive peak to tetrahedral Fe^{3+}(A) and the highest energy, negative peak, to Fe^{3+}[B].[97] In the Fe $L_{2,3}$-edge XMCD spectra of the Co-ferrite nanoparticles (Fig. 3.11(b)), the octahedral Fe^{2+} peak is greatly reduced demonstrating the replacement of the Fe in this site by Co. Using atomic multiplet calculations the contributions to the spectra from the three sites and thus the Fe occupancy can be calculated[97] (using Program Q-fit, Neil Telling unpublished).

Combined with the electron microprobe determination of the [Co]: [Fe] cation ratios, these site occupancies can be quantified and are presented in Table 3.2 The EPMA results confirm that the sample with a higher starting concentration of precursor (S2) is close in structure to stoichiometric $CoFe_2O_4$, and the Fe $L_{2,3}$-edge XMCD show that the Co mainly displaces the $Fe^{2+}O_h$ (80% of the site), although a significant amount of Co could be present in tetrahedral coordination (14% of the Fe displaced). This distribution is to be expected for Co-ferrites.[97,99] The sample with a reduced amount of precursor (S1) also has a majority of the Co in the $Fe^{2+}O_h$ site and the Co occupancy of the $Fe^{3+}T_d$ (16%) site is similar. Co^{2+} cations occupying octahedral sites is also supported by magnetic measurements (Fig. 3.10(b)) which show large hysteresis loops at 5 K ($H_c > 10$ kOe) directly correlated with the enhancement in magnetic anisotropy due to the inclusion of octahedral Co^{2+} in the spinel structure.[28]

Additional information can be derived from the Co $L_{2,3}$ XAS and XMCD spectra (Figs. 3.11(d) and (e)). These spectra are characteristic of $Co^{2+}O_h$ in ferrite spinels[94,99] but the increased intensity at the higher energies in the XAS and XMCD compared to calculated $Co^{2+}O_h$ spectrum[97] indicates an additional contribution from either $Co^{2+}T_d$ or Co^{3+}. Charge balance requirements and the evidence of the displacement of Fe^{3+} in the Fe $L_{2,3}$-edge XMCD suggest this to be Co^{3+}, and therefore all samples contain significant Co^{3+} T_d.

3.4.2.6 Cobalt ferrite nanoparticles obtained from (2) at different concentrations

The p-XRD patterns of nanoparticles obtained from **(2)** at both 0.25 and 0.50 mmol concentrations matched with cubic iron cobalt oxide (ICDD card No. 00-022-1086) (Fig. 3.12). The average diameters were estimated by Scherrer equation and the values obtained correspond to 6 nm in both cases.

However, the TEM images showed nearly monodispersed nanoparticles in both cases, with average diameters of 6.7 ± 1 and 7 ± 1 nm at 0.25 mmol (S3) and 0.50 mmol (S4) precursor concentrations respectively. Highly crystalline nanoparticles were obtained from **(2)** as observed in the lattice fringes (Fig. 3.12(a)) with a *d*-spacing of 2.98 Å which is very close to the (220) reflection of iron cobalt oxide (ICDD card No: 00-022-1086).

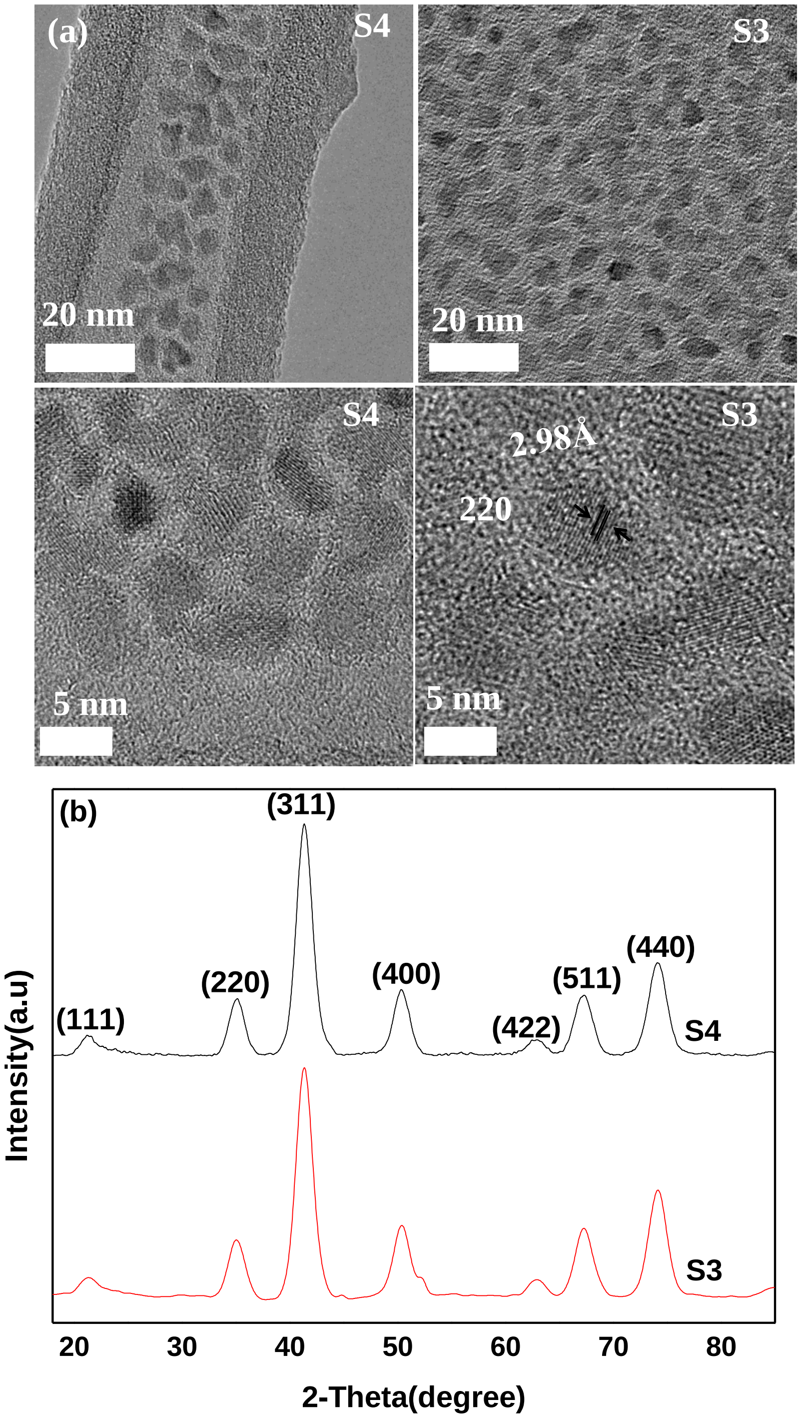

Fig. 3.12 (a) TEM and HRTEM images of Fe_2CoO_4 obtained from **(2)** at different concentrations. S3 and S4 correspond to Fe_2CoO_4 obtained from 0.25 mmol and 0.50 mmol precursor concentrations respectively. (b) The p-XRD patterns of cubic spinel Fe_2CoO_4 obtained from **(2)** at different precursor concentrations.

Magnetic measurements were performed on Fe_2CoO_4 nanoparticles obtained from **(2)** at 0.50 mmol with average diameter 7 ± 1 nm (S4) and the results showed similar behaviour to those particles obtained from **(1)**. The blocking temperature of these nanoparticles is about 180 K and it is not well defined indicating a wider distribution of particle diameters (Fig. 3.13(a)). Above the blocking temperature, the magnetisation orientations average to zero and the nanoparticles become superparamagnetic.

Their superparamagnetism is confirmed by the M (H) data at 300 K which show negligible hysteresis. However, data collected at 5 K show a large hysteresis loop characterised by H_c = 9.8 kOe, M_R = 38.2 emu.g^{-1} and M_S = 61.4 emu.g^{-1} (the inset of Fig 3.13(b)). The saturation magnetisation at room temperature is 46.9 emu.g^{-1} which is larger than that of the nanoparticles obtained from (**1**) sized 3.6 and 5.3 nm.

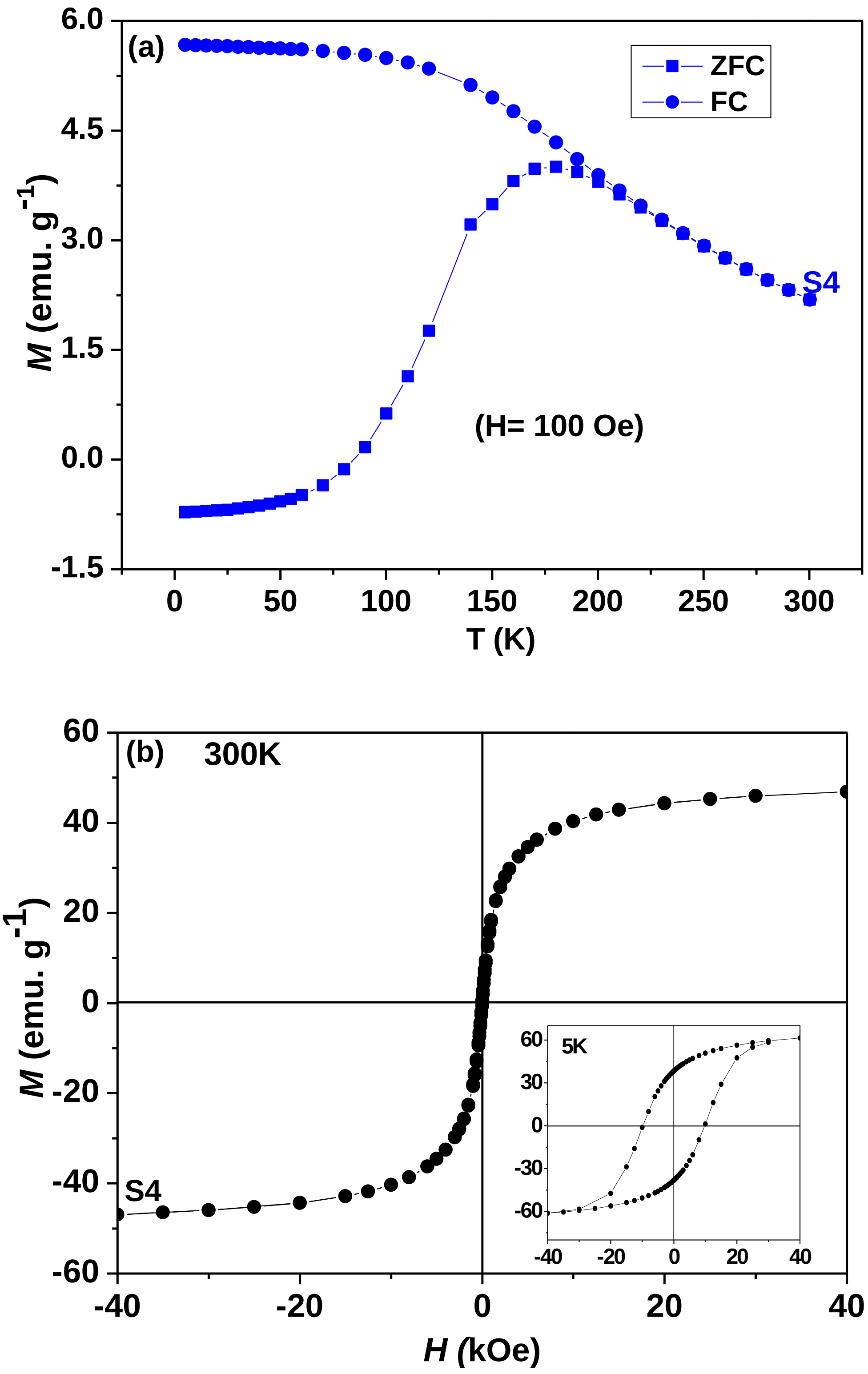

Fig. 3.13 (a) ZFC and FC magnetisation curves for S4 (Fe_2CoO_4) nanoparticles of average diameter 7 ± 1 nm obtained from **(2)** at 0.50 mmol. (b)The hysteresis loops measured at 5 and 300 K for S4.

3.4.2.7 ICP-OES, EPMA and XMCD analysis of Fe_2CoO_4 nanoparticles from (2)

ICP-OES measurement was done for the Fe_2CoO_4 sample obtained at higher precursor concentration (S4) and the results revealed that the ratio between Fe and Co is 1.5:1. EPMA however showed a ratio of 1.99:1.01. The XMCD results for the Fe_2CoO_4 particles obtained from **(2)** show similar behaviour with those particles obtained from **(1)**, particularly near stoichiometric (S2), as discussed earlier. The Co is mainly occupying the $Fe^{2+}O_h$ site, although in (S3) there is a higher occupancy of the $Fe^{3+}T_d$ site (37% of the Fe is displaced) and in (S4) there is a significant displacement of the iron in the $Fe^{3+}O_h$ (Fig 3.14).

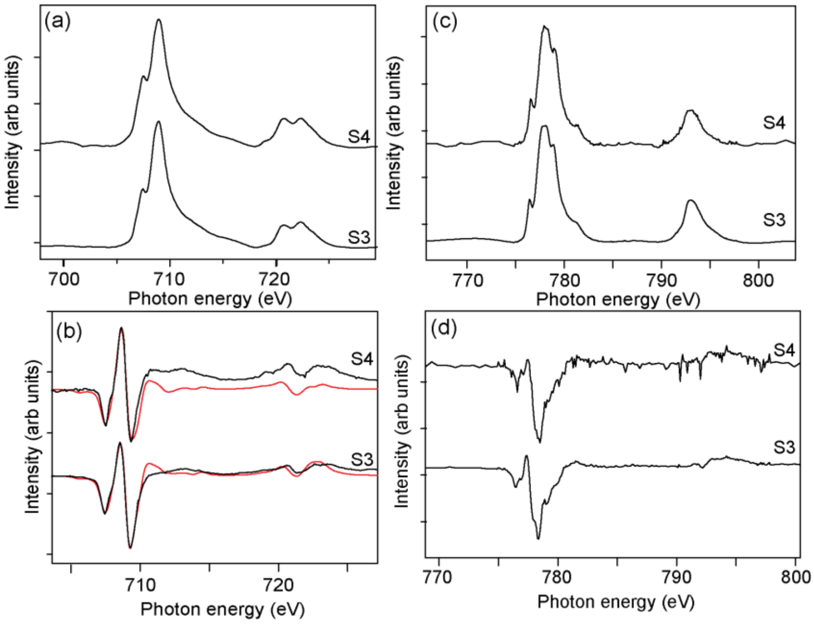

Fig. 3.14 (a) Fe $L_{3,2}$ XAS spectra of Co-ferrite nanoparticles, showing the enhanced peak at 707.6eV, indicating a decrease in Fe(II) concentration compared to magnetite, (b) Fe $L_{3,2}$ XMCD spectra of Co-ferrite nanoparticles, showing the low $Fe^{2+}O_h$ contribution. Experimental data in black; fits using atomic multiplet calculations in red, (c) Co $L_{3,2}$ XAS of Co ferrite nanoparticles showing the predominance of Co^{2+} O_h with an additional high energy component representing Co^{3+} $T_{d,}$ (d) Co $L_{3,2}$ XMCD spectra of Co-ferrite nanoparticles. (S3 and S4 correspond to Co-ferrite nanoparticles obtained from **(2)** at 0.25 and 0.50 mmol).

3.4.2.8 Manganese ferrite nanoparticles obtained from (3) at different concentrations

The p-XRD pattern of nanoparticles obtained from **(3)** at the two concentrations (0.25 and 0.50 mmol) were of cubic $Mn_{0.43}Fe_{2.57}O_4$ (ICDD card No. 01-089-2807) (Fig. 3.15). The average particle diameters estimated by the Scherrer equation are 4.5 and 3 nm for particles obtained with 0.25 mmol and 0.50 mmol concentrations respectively. TEM images showed similar behaviour to those obtained from **(1)**. Smaller and more monodispersed spherical nanoparticles of an average diameter 3.5 ± 0.2 nm were obtained with 0.50 mmol concentration whilst a nearly monodispersed particles (4.8 ± 1 nm) were obtained with 0.25 mmol concentration.

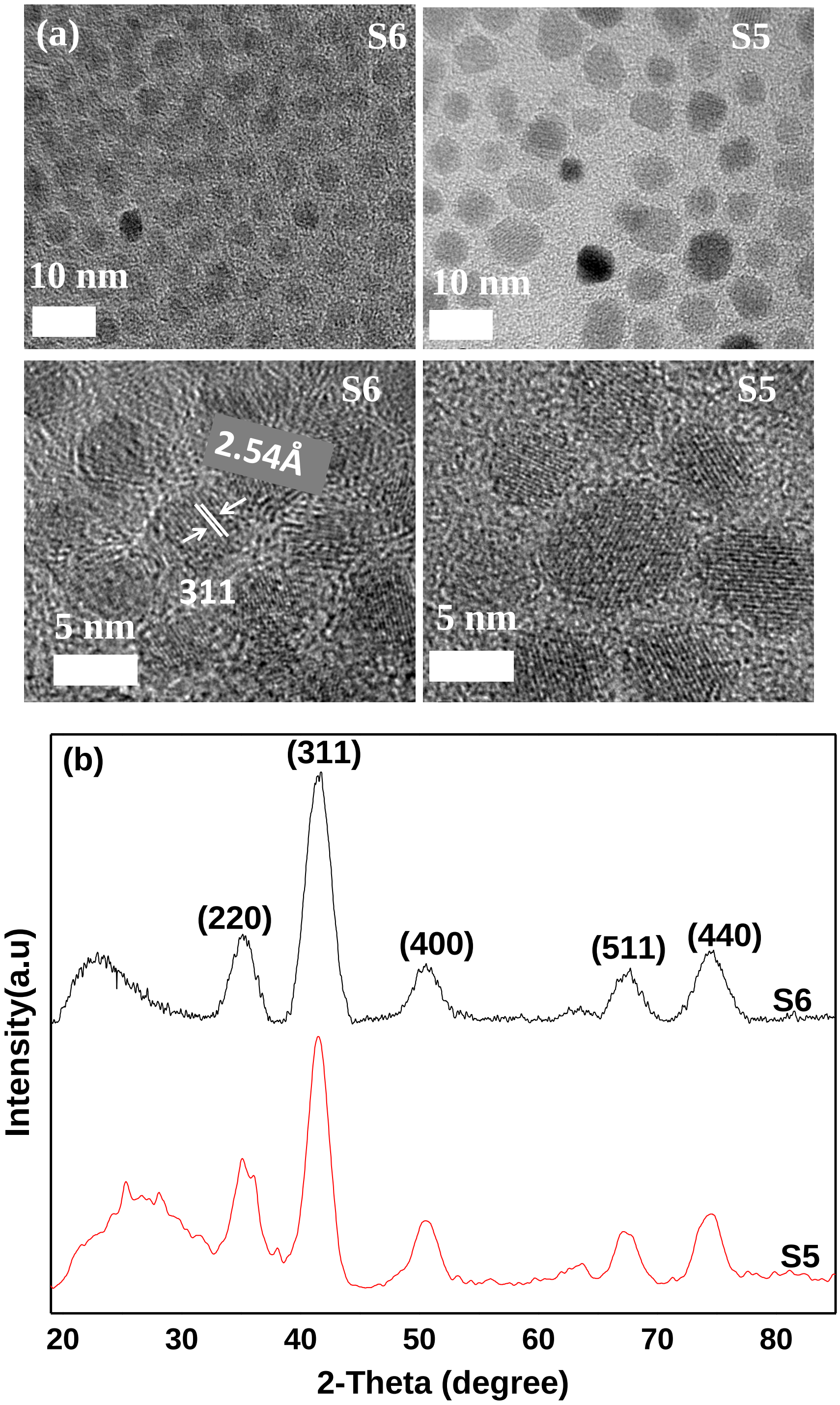

Fig. 3.15 (a) TEM and HRTEM images of $Mn_{0.43}Fe_{2.57}O_4$ obtained from **(3)** at different concentrations. S5 and S6 correspond to $Mn_{0.43}Fe_{2.57}O_4$ obtained at 0.25 mmol and 0.50 mmol precursor concentrations respectively. (b) The p-XRD patterns of cubic spinel $Mn_{0.43}Fe_{2.57}O_4$ obtained from **(3)** at different precursor concentrations.

Magnetic measurements of the $Mn_{0.43}Fe_{2.57}O_4$ nanoparticles produced at 0.50 mmol concentration (S6) revealed that they are superparamagnetic with a very low blocking temperature (~ 9 K) (Fig. 3.16(a)). The blocking temperature is well defined indicating a narrow distribution of particle diameter (3.5 ± 0.2 nm). Saturation magnetisation values of 54 emu.g^{-1} at 5 K and 40 emu.g^{-1} at 300 K were recorded (Fig. 3.16(b)). These values are lower than that associated to the bulk manganese iron oxide of 80 emu.g^{-1} (300 K).[56] The $M(H)$ curve recorded at 5 K shows a weak hysteresis loop characterised by H_c = 0.02 kOe and M_R = 1.2 emu.g^{-1} (inset of Fig. 3.16(b)).

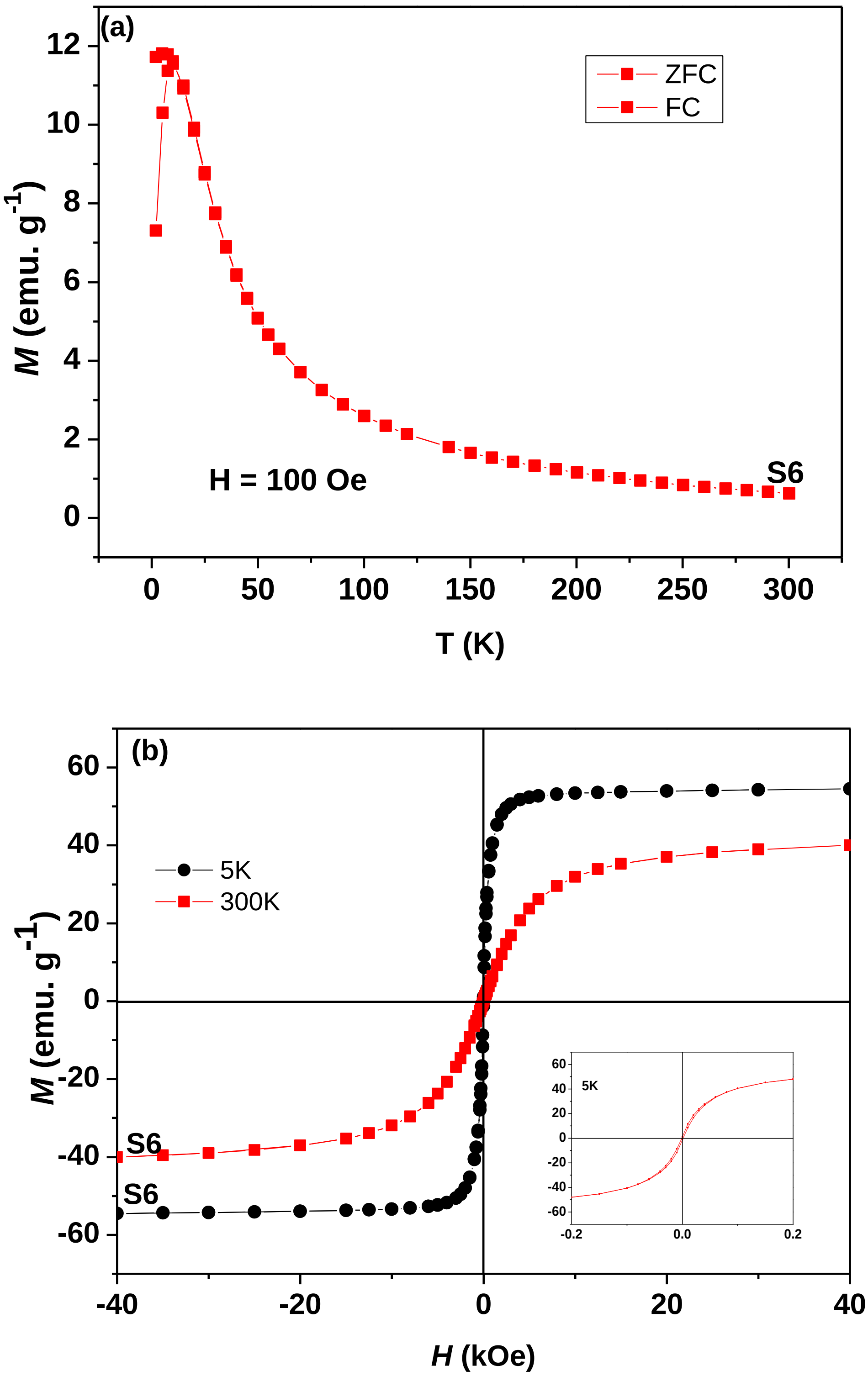

Fig. 3.16 (a) ZFC and FC magnetisation curves for S6 ($Mn_{0.43}Fe_{2.57}O_4$) nanoparticles of average diameter 3.5 ± 0.2 nm obtained from **(3)** at 0.50 mmol. (b) The hysteresis loops measured at 5 and 300 K for S6.

3.4.2.9 ICP, EPMA and XMCD analysis of $Mn_{0.43}Fe_{2.57}O_4$ nanoparticles from (3)

ICP-OES measurements of $Mn_{0.43}Fe_{2.57}O_4$ obtained at 0.50 mmol precursor concentration (S6) revealed that the [Fe]: [Mn] is 7: 1 which is higher than their initial ratio in the precursor (2:1). The ratio obtained from the EPMA results (2.78:0.22) is consistent with the ICP results. Also the p-XRD pattern ($Mn_{0.43}Fe_{2.57}O_4$) shows that Mn is depleted. The Fe $L_{3,2}$ XAS spectrum of the $Mn_{0.43}Fe_{2.57}O_4$ particles again has a peak on the low energy side of the L_3 edge suggesting that, as with the Co-ferrites, there is a less Fe(II) in the structure compared to stoichiometric magnetite and giving an indication of the placement of the Mn cations (Fig. 3.17(a)). Calculation of the site occupancies from the XMCD spectrum (Table 3.2; Fig. 3.17(a)) shows Fe depleted in both the $Fe^{2+}O_h$ and $Fe^{3+}T_d$ sites and a large excess of $Fe^{3+}O_h$. The Mn L_3 XAS data (Fig. 3.17(b)) shows spectral characteristics[98] of Mn^{2+} T_d, and there is no evidence of Mn^{3+}. If Mn^{2+} is displacing the $Fe^{3+}T_d$ then charge balance requirements require additional Fe^{3+}. The evidence here is that this is achieved by 'oxidation' of $Fe^{2+}O_h$ resulting in a much larger $Fe^{3+}O_h$ contribution.

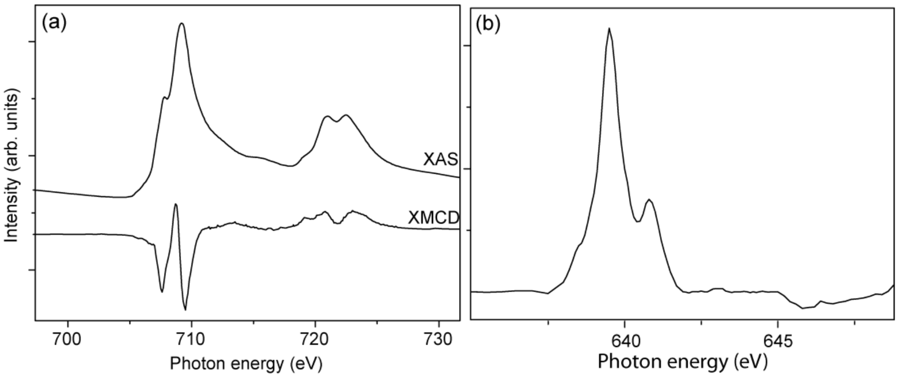

Fig. 3.17 (a) Fe $L_{3,2}$ XAS and XMCD of the $Mn_{0.43}Fe_{2.57}O_4$ nanoparticles (S6), showing a depletion in Fe(II) compared to stoichiometric magnetite and a large quantity of the $Fe^{3+}O_h$ component in the XMCD spectra (XMCD x5), (b) Mn L_3 XAS spectra of the $Mn_{0.43}Fe_{2.57}O_4$ nanoparticles (S6), characteristic of $Mn^{2+}T_d$.[49] (S6 correspond to $Mn_{0.43}Fe_{2.57}O_4$ nanoparticles obtained from **(3)** at 0.50 mmol)

Table 3.2 Fe site occupancies in Co and Mn nanoparticles determined using Fe+Co cation ratios, XMCD spectra and crystal field atomic multiplet calculations**.**

Precursor	**conc.(mmol)**	**Phase**	**Fe+Co = 3 (EPMA)**		**Ratios**		**Fe site occupancies**			**Sample**
		CUBIC	**Fe**	**Co**	**Fe^{2+}/Fe^{3+}**	**T_d/O_h**	**Fe^{2+} O_h**	**Fe^{3+} T_d**	**Fe^{3+} O_h**	
$[Fe_2CoO(O_2C^tBu)_6(HO_2C^tBu)_3]$ (1)	0.25	Fe_2CoO_4	2.34	0.66	0.24	0.56	0.46	0.84	1.04	S1
$[Fe_2CoO(O_2C^tBu)_6(HO_2C^tBu)_3]$ (1)	0.5	Fe_2CoO_4	2.03	0.97	0.11	0.73	0.2	0.86	0.97	S2
$[Co_4Fe_2O_2(O_2C^tBu)_{10}]$ (2)	0.25	Fe_2CoO_4	1.96	1.04	0.14	0.48	0.24	0.63	1.08	S3
$[Co_4Fe_2O_2(O_2C^tBu)_{10}]$ (2)	0.5	Fe_2CoO_4	1.99	1.01	0.19	0.72	0.32	0.83	0.84	S4
			Fe	**Mn**						
$[Fe_2MnO(O_2C^tBu)_6(HO_2C^tBu)_3]$ (3)	0.5	$Mn_{0.43}Fe_{2.57}O_4$	2.78	0.22	0.32	0.4	0.68	0.79	1.32	S6
			3	0	0.5	0.5	1	1	1	Magnetite

3.4.3 Zinc and nickel ferrite nanoparticles

The ferrite nanoparticles obtained from zinc iron precursor **(4)** and nickel iron precursor **(5)** were analysed by powder X-ray diffraction (p-XRD), TEM, ICP, EPMA, XMCD and SQUID.

3.4.3.1 Zinc and nickel ferrite nanoparticles obtained at different reaction times

The p-XRD pattern obtained from **(4)** showed that the intensity and crystallinity of the peaks increases with time (Fig. 3.18(a)). No product was formed at 5 minutes whilst the pattern obtained at 15 minutes was broad. The peaks begin to appear distinct at 30 minutes and were predominantly of hexagonal iron oxide (ICDD Card No: 04-013-3305). The peaks obtained at 1 hour were predominantly zinc iron oxide with traces of iron oxide whilst at 2 hours, all the peaks were corresponding to zinc iron oxide ($Zn_{0.93}Fe_2O_4$) (ICDD Card No: 04-006-1956). The diameter and crystallinity of the particles increases over time as observed in the images taken at 30 minutes (3.6 ± 0.4 nm, image at 1 hour which looks like an assembly (4.2 ± 0.8 nm) and at 2 hours (5.1 ± 0.7 nm) (Fig. 3.18(b)-(d)).

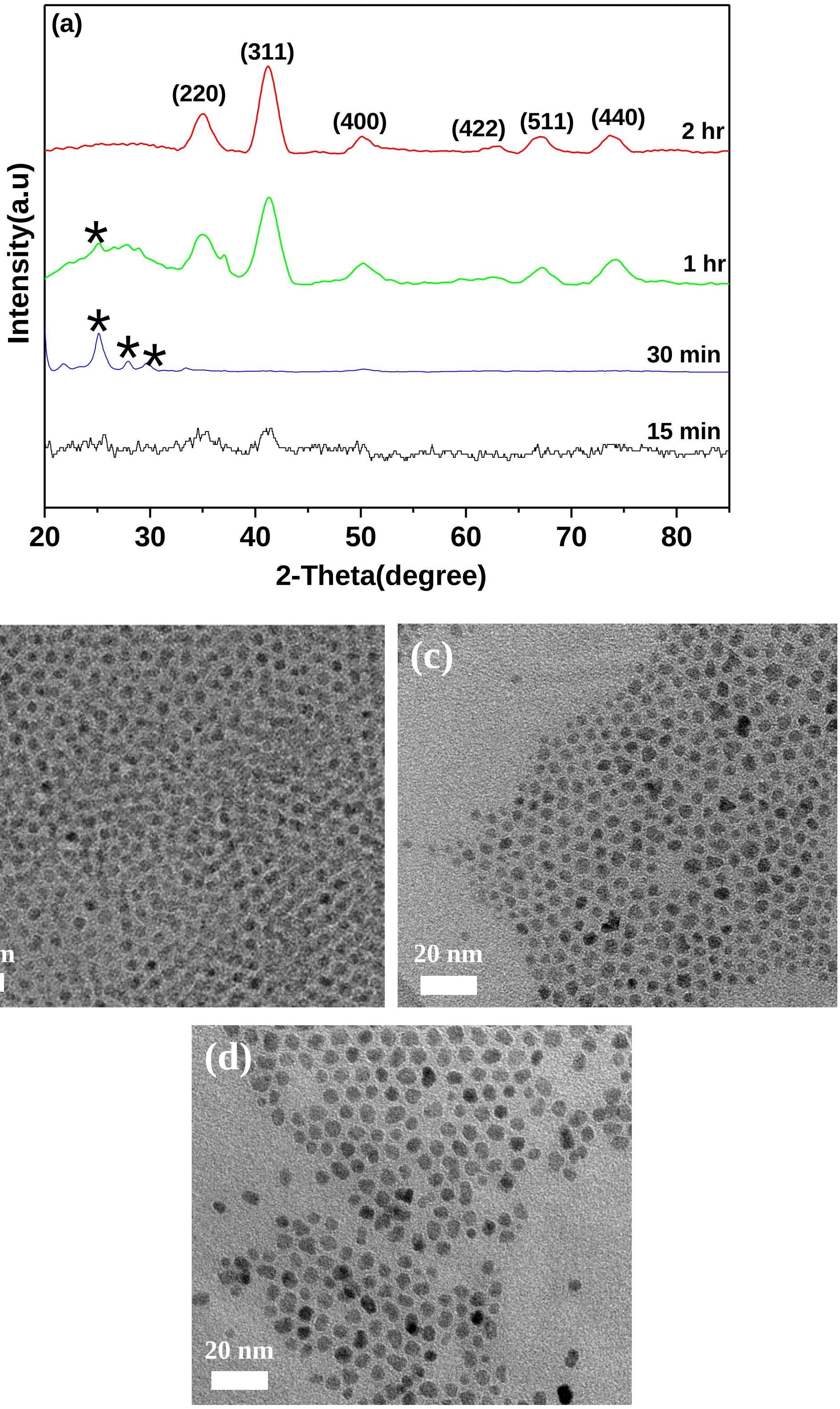

Fig. 3.18 (a) A series of p-XRD pattern for $Zn_{0.93}Fe_2O_4$ nanoparticles from **(4)** at different times. * corresponds to the Fe_2O_3 peaks. (b)- (d): TEM images of $Zn_{0.93}Fe_2O_4$ obtained from **(4)** at 30 minutes, 1 hour and 2 hours respectively.

The p-XRD of the nanoparticles obtained from **(5)** at different times exhibit the same behaviour as those from **(4)**. No product was obtained at 5 minutes. Products obtained at 15 minutes and 30 minutes contain hexagonal iron oxide peaks (ICDD card No: 04-013-3305) whilst the peaks obtained at 1 hour and two hours were of cubic nickel ferrite (ICDD Card No: 00-054-0964) (Fig. 3.19(a)).

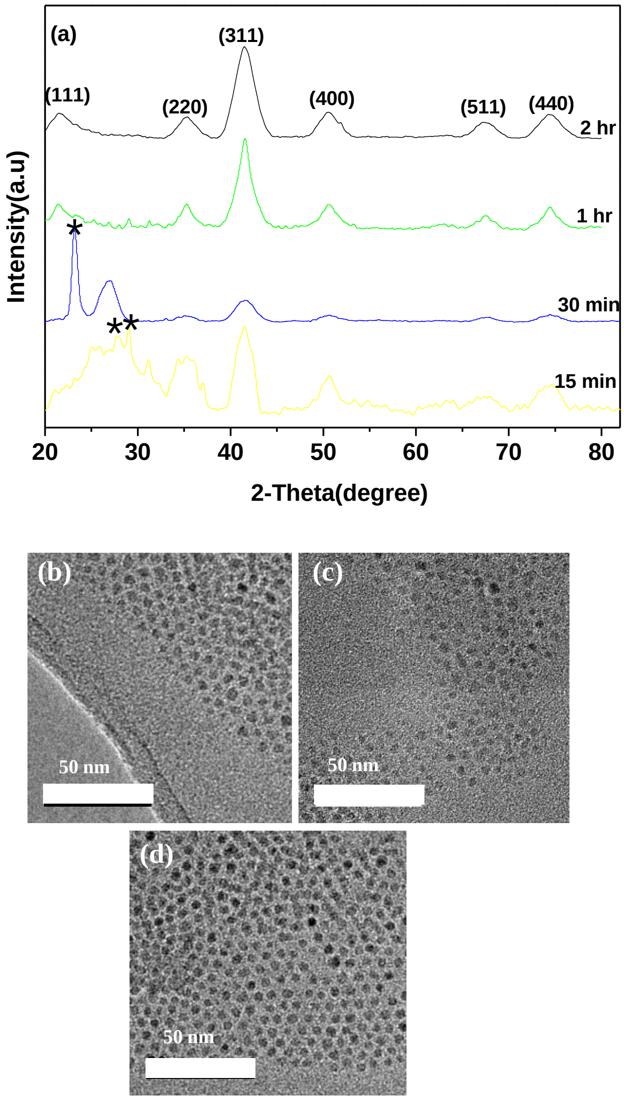

Fig. 3.19 (a) A series of p-XRD pattern for $NiFe_2O_4$ nanoparticles from **(5)** at different times.* corresponds to the Fe_2O_3 peaks. (b)- (d): TEM images of $NiFe_2O_4$ obtained from **(5)** at 30 minutes, 1 hour and 2 hours respectively.

The average diameters calculated from the TEM images taken for samples are 3.1 ± 0.7 nm at 30 minutes, 3.6 ± 0.6 nm at 1 hour and 4.4 ± 0.6 nm at 2 hours (Fig.3.19 (b)-(d)). The diameters of the nanoparticles obtained from **(4)** and **(5)** tend to increase over time. This same trend was observed for the cobalt and manganese ferrite nanoparticles prepared from **(1)**, **(2)** and **(3).**

3.4.3.2 Zinc and nickel ferrite nanoparticles obtained at different injection temperatures

The p-XRD pattern for nanoparticles obtained from the thermolysis of **(4)** at 260 and 300 °C correspond to cubic $Zn_{0.93}Fe_2O_4$ (ICDD card No: 04-006-1956) (Fig. 3.20(a)). The average particle size estimated by Scherrer equation are 4 nm for particles obtained at 260 ºC and 5 nm for those obtained at 300 ºC.

The thermolysis of **(5)** at 260 and 300 °C resulted in cubic nickel ferrite (ICDD Card No: 00-054-0964) (Fig 3.20 (b)). Using Scherrer equation, the average crystallite sizes were found to be 3.8 nm and 5 nm for nanoparticles obtained at 260 °C and 300 °C respectively.

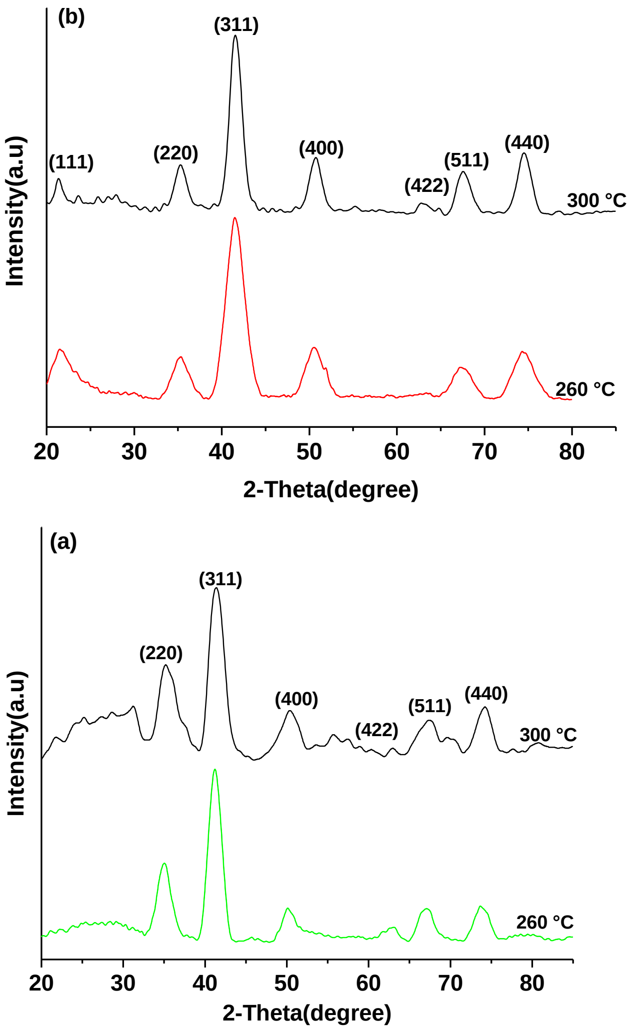

Fig. 3.20 The p-XRD pattern for nanoparticles obtained in different boiling point solvents of diphenyl ether (260 °C) or benzyl ether (300 °C). (a) cubic $Zn_{0.93}Fe_2O_4$ from (4) and (b) cubic $NiFe_2O_4$ from **(5).**

The TEM images for $Zn_{0.93}Fe_2O_4$ and $NiFe_2O_4$ revealed that an increase in diameters was observed for nanoparticles obtained at higher temperature with diameters 5.1 ± 0.7 nm at 260 °C and 5.6 ± 0.5 nm at 300 °C for $Zn_{0.93}Fe_2O_4$ whilst the corresponding $NiFe_2O_4$ are of diameters 4.4 ± 0.6 nm at 260 °C and 5 ± 0.6 nm at 300 °C (Fig. 3.21). This is also evident in their p-XRD peaks as broader peaks were obtained with the nanoparticles having smaller diameter (Fig. 3.20). The same trend was observed for the cobalt and manganese ferrites prepared from precursors **(1)** and **(3)** respectively.

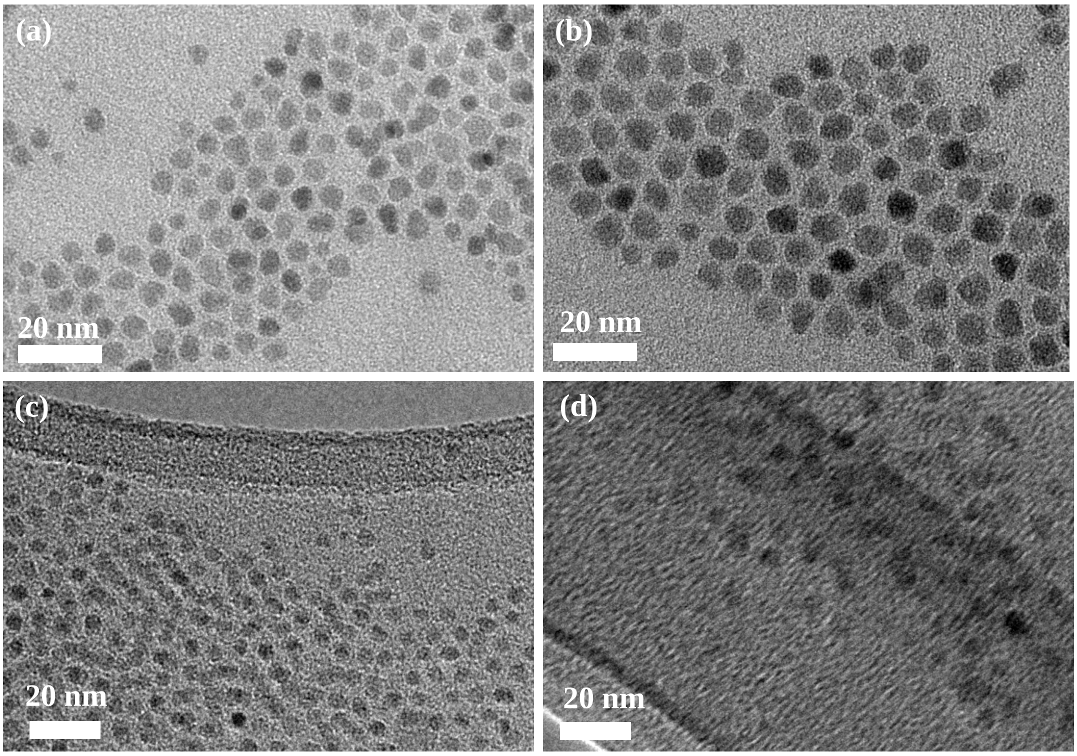

Fig. 3.21 (a) - (b) TEM images of $Zn_{0.93}Fe_2O_4$ from **(4)** at 260 °C and 300 °C. (c) - (d) TEM of $NiFe_2O_4$ from **(5)** at 260 and 300 °C respectively.

Table 3.3 Size of the ferrite nanoparticles obtained by thermolysis of **(4)** and **(5)** at different temperatures.

Precursor	Temp. (°C)	TEM (nm)	p-XRD(nm)
(4)	260	5.1 ± 0.7	4.0
(4)	300	5.6 ± 0.5	5.0
(5)	260	4.4 ± 0.6	3.8
(5)	300	5.0 ± 0.6	5.0

3.4.3.3 Zinc ferrite nanoparticles obtained from (4) at different concentrations

The p-XRD pattern for particles obtained from **(4)** with 0.25 mmol concentration were matched with cubic $Zn_{0.93}Fe_2O_4$ (ICDD card No: 04-006-1956) whilst those obtained with 0.50 mmol concentration were of Franklinite, $ZnFe_2O_4$ (ICDD card No: 01-070-6393) (Fig. 3.22) The average crystallite size calculated by the Scherrer equation are 3 and 4 nm for nanoparticles obtained from 0.50 and 0.25 mmol precursor concentrations respectively.

TEM images revealed that the particles obtained at 0.50 mmol precursor concentration are more monodispersed with an average diameter of 3.2 ± 0.2 nm whilst those obtained at 0.25 mmol precursor concentration have an average diameter of 5.1 ± 0.7 nm (Fig. 3.22(a)). These results showed that the TEM analysis is in good agreement with the calculated value obtained by the Scherrer's equation. The synthesised nanoparticles are crystalline as seen in the lattice fringes with a *d*-spacing of 2.98 Å which is very close to the (220) reflection of zinc iron oxide (ICDD Card No: 01-070-6393) (Fig. 3.22(a)).

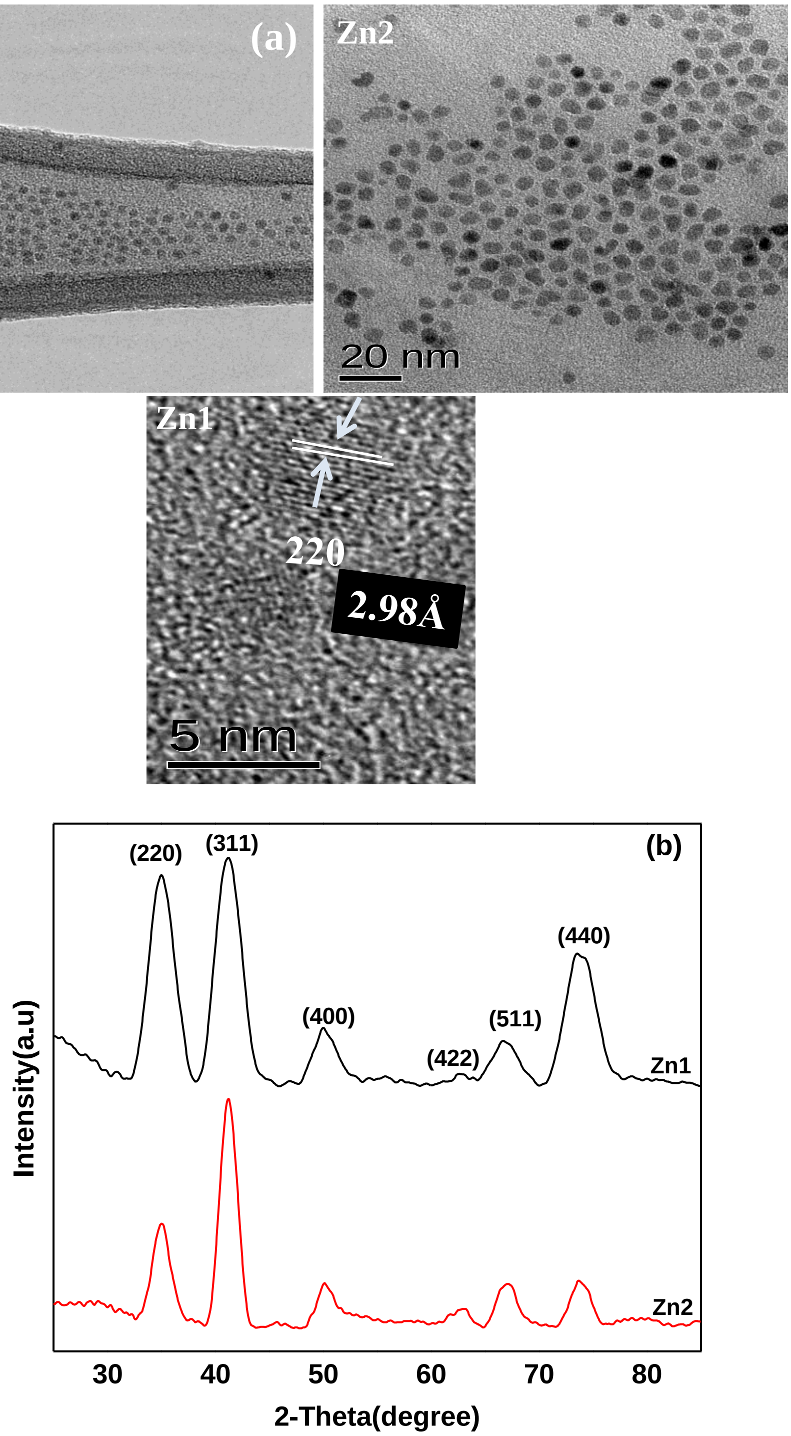

Fig. 3.22 (a) TEM and HRTEM images of $ZnFe_2O_4$ obtained from precursor **(4)** at different concentrations. Zn1 and Zn2 correspond to nanoparticles obtained from 0.50 mmol and 0.25 mmol precursor concentrations respectively, (b) The p-XRD patterns of cubic spinel $ZnFe_2O_4$ nanoparticles obtained from **(4)** at different precursor concentrations.

Magnetic measurements of $ZnFe_2O_4$ obtained from **(4)** revealed that the nanoparticles display superparamagnetic behaviour at room temperature. An estimate for the blocking temperature (T_B) of the samples were done and the data showed that T_B increases with increasing particle diameter, ranging from 10 K for zinc ferrite nanoparticles obtained from **(4)** at 0.50 mmol with an average diameter of 3.2 nm (Zn1) to 20 K for particles produced at 0.25 mmol with an average diameter of 5.1 nm (Zn2) (Fig. 3.23(a)).

Field dependent magnetisation studies performed at temperatures of 5 and 300 K on zinc ferrite nanoparticles obtained from **(1)** showed that the saturation magnetisation (M_s) increases with the average particle diameter at both temperatures (Fig. 3.23(b)). Zinc ferrite nanoparticles of average diameter 3.2 nm are characterised by M_s values of 59 (5 K) and 22 emu.g^{-1} (300 K) whilst those with average diameter of 5.3 nm exhibit M_S values of 87 (5 K) and 37 emu.g^{-1} (300 K).

The magnetisation *versus* field measurements at 5 K for zinc ferrite nanoparticles showed some hysteresis loop and coercivity (H_c) of *ca.* 0.14 kOe and 11.5 emu.g^{-1} for nanoparticles of average diameter 5.1 nm whilst the remanence and coercivity of zinc ferrite nanoparticles of average diameter 3 nm are negligible (inset of Fig. 3.23(b)).

Bulk zinc ferrite has a normal spinel structure with the absence of Fe^{3+} ions in the tetrahedral sites thus making zinc ferrite antiferromagnetic below 10 k. However, in our zinc ferrite nanoparticles, the saturation magnetisation values and corecivity are enhanced. This can be explained by the cation redistribution, involving migration of some Fe^{3+} ions to the tetrahedral sites thereby creating a stronger ferrimagnetic interaction between the Fe^{3+} ions in tetrahedral and octahedral sites. [53,55,100]

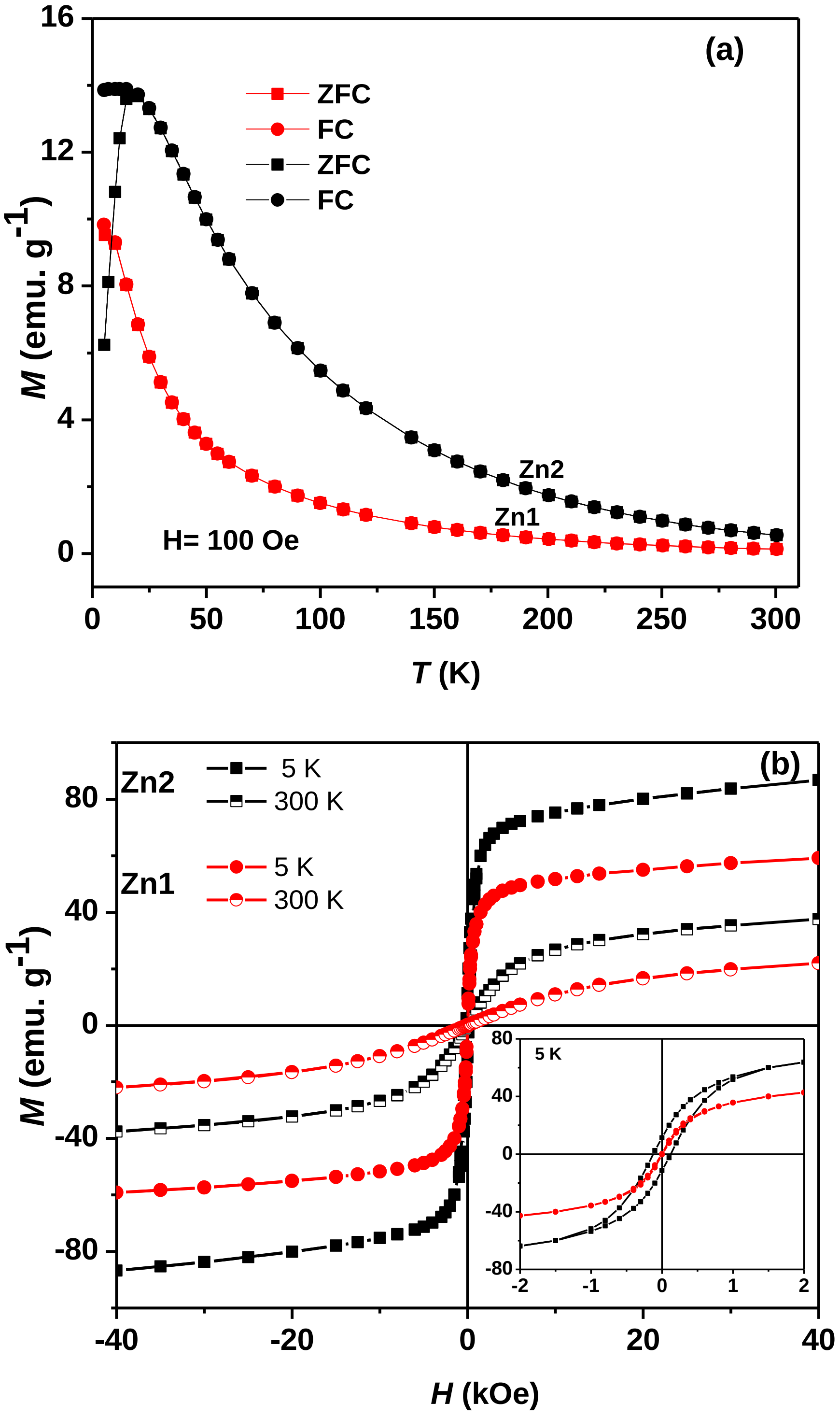

Fig. 3.23 (a) ZFC and FC magnetisation curves for Zn1 and Zn2 ($ZnFe_2O_4$) nanoparticles obtained from **(4)** of average diameter 3.2 ± 0.2 nm and 5.1 ± 0.7 nm respectively. (b) The hysteresis loops measured at 5 and 300 K for Zn1 and Zn2 nanoparticles.

3.4.3.4 Nickel ferrite nanoparticles obtained from (5) at different concentrations

The p-XRD pattern for particles obtained from **(5)** at both (0.25 and 0.50 mmol) concentrations were matched with cubic $NiFe_2O_4$ (ICDD card No: 00-054-0964) (Fig. 3.24). The average nanoparticles's sizes calculated by the Scherrer equation are: 3.3 and 3.8 nm respectively for nanoparticles obtained from 0.50 and 0.25 mmol precursor concentrations.

TEM images showed monodispersed nanoparticles were obtained from both precursor concentrations but with smaller sizes at higher concentration. The average diameter estimated from the TEM are 3.3 ± 0.2 nm and 4.4 ± 0.5 nm at 0.50 and 0.25 mmol precursor concentration respectively (Fig. 3.24(a)). The lattice fringes of the nanoparticles are distinct, indicating the highly crystallinity of the nickel ferrite nanoparticles. A *d*-spacing value of 2.512 Å was obtained which is the same as the (311) reflection of nickel iron oxide (ICDD Card No: 00-054-0964) (Fig. 3.24(a)).

Magnetic measurements were performed on $NiFe_2O_4$ nanoparticles obtained from **(5)** with average diameters 3.3 ± 0.2 nm (Ni1) and 4.4 ± 0.5 nm (Ni2). The blocking temperature of both Ni1 and Ni2 nanoparticles is about 11 K, both are well defined indicating a narrow distribution of particle diameters (Fig. 3.25(a)).

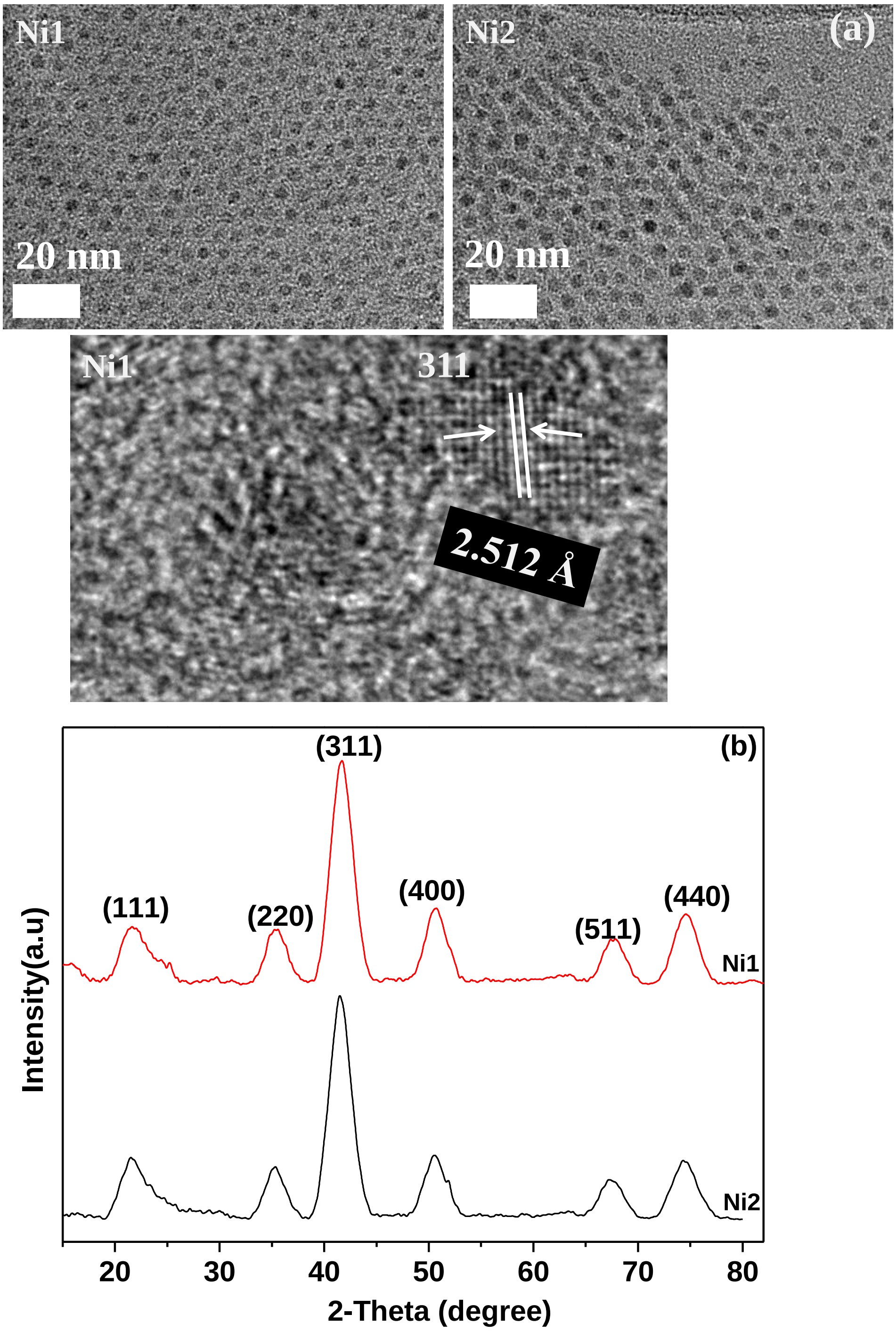

Fig. 3.24 (a) TEM and HRTEM images of $NiFe_2O_4$ obtained from precursor **(5)** at different concentrations. Ni1 and Ni2 correspond to nanoparticles obtained from 0.50 mmol and 0.25 mmol precursor concentrations respectively, (b) The p-XRD patterns of cubic spinel $NiFe_2O_4$ nanoparticles obtained from **(5)** at different precursor concentrations.

The saturation magnetisation values were measured for these nanoparticles at 5 K and 300 K, for Ni1 (average diameter 3.3 nm) 34 and 26.5 emu.g^{-1} were recorded, whilst for Ni2, (average diameter 4.4 nm) 42 and 29.3 emu.g^{-1} values were obtained (Fig. 3.25(b)).

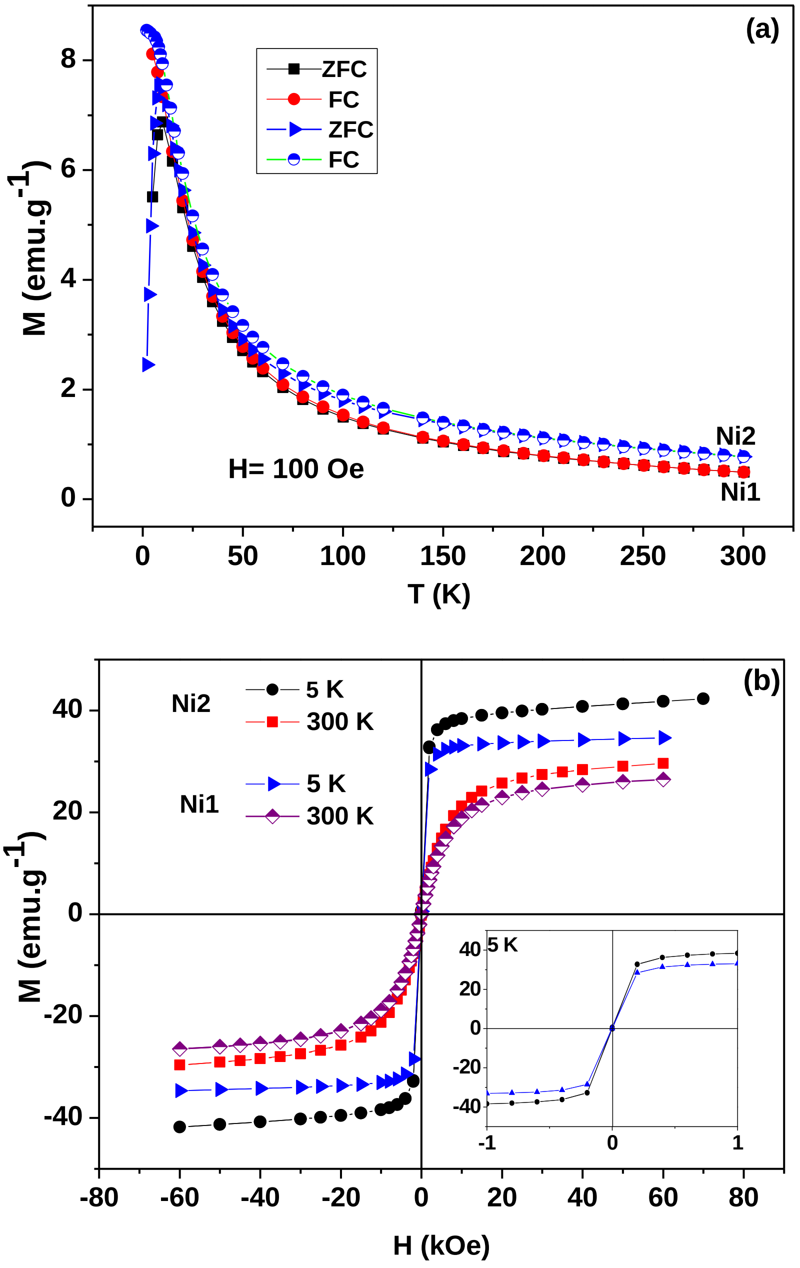

Fig. 3.25 (a) ZFC and FC magnetisation curves forNi1 and Ni2 ($NiFe_2O_4$) nanoparticles obtained from **(5)** of average diameters 3.3 ± 0.2 nm and 4.4 ± 0.5 respectively.((b) The hysteresis loops measured at 5 and 300 K for Ni1 and Ni2 nanoparticles.

The coercivity and remanence of these nanoparticles are negligible at both temperatures. Bulk nickel ferrite nanoparticles have a saturation magnetisation value of about 56 emu/g[100] which is higher than the values obtained for our nanoparticles.

3.4.3.5 ICP, EPMA and XMCD analysis of zinc ferrite and nickel ferrite nanoparticles.

ICP-OES analysis showed that the [Fe]: [Zn] is approximately 2.0: 1.0 for $ZnFe_2O_4$ particles obtained at 0.50 mmol precursor concentrations (Zn1). In addition, the cation (Fe, Zn) ratios of the nanoparticles were determined using EPMA, and this were found to be 2.2: 0.7 for Zn1, slightly less than was found from ICP-OES (2.0: 1.0).

ICP-OES analysis showed that the [Fe] : [Ni] is approximately 2: 1 for $NiFe_2O_4$ particles obtained at 0.50 mmol precursor concentration (Ni1) whilst EPMA revealed 2.12 : 0.88, a value slightly less than that obtained from ICP-OES.

Examination of the XMCD spectra (Fig. 3.26b) shows three peaks in the Fe L_3-edge characteristic of the three Fe environments within magnetite. These can be fitted using multiplet calculations for the three iron environments to give the quantitative data shown in Table 3.4. These data indicate that the magnetite is deficient in both $Fe^{2+}O_h$ and $Fe^{3+}T_d$, but has excess $Fe^{3+}O_h$. This suggests that there is partial oxidation of Fe^{2+} to Fe^{3+} within the structure but the amount of excess Fe^{3+} in O_h sites cannot account for all the ‘missing’ Fe^{2+} in O_h geometry. It can therefore be assumed that at least some of the sites that would normally be occupied by Fe^{2+} contain Zn as is supported by the magnetometry measurements.

Table 3.4 Fe site occupancies determined using Fe+cation ratios, XMCD spectra and atomic multiplet calculations.

Sample	Fe+(Ni or Zn) = 3 (from EPMA)		Fe occupancies (normalised)			Fe^{2+}/Fe^{3+} ratio	T_d/O_h ratio
	Fe	Ni or Zn	Fe^{2+} O_h	Fe^{3+} T_d	Fe^{3+} O_h		
Zn1	2.2	0.7	0.38	0.66	1.17	0.21	0.43
Ni1	2.12	0.88	0.37	1.03	1.07	0.18	0.72
Ni2			0.41	0.69	1.17	0.22	0.44
Magnetite			1.00	1.00	1.00	0.50	0.50

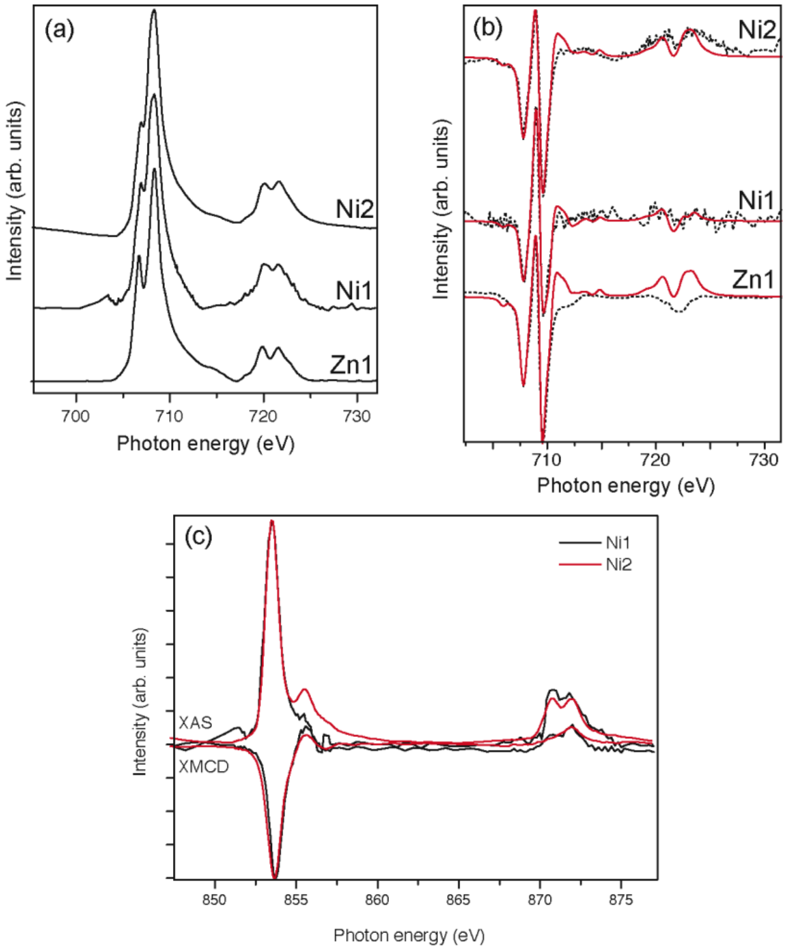

Fig. 3.26 Fe $L_{2,3}$-edge (a) isotropic XAS and corresponding (b) XMCD for samples Zn1, Ni1 and Ni2, data (black) and XMCD calculated fits (red). (c) Ni $L_{2,3}$-edge XAS and XMCD for Ni1 (black) and Ni2 (red). (Zn1 corresponds to zinc ferrite nanoparticles from **(4)** at 0.50 mmol; Ni1 and Ni2 correspond to nickel ferrite nanoparticles from **(5)** at 0.50 and 0.25 mmol respectively).

In addition, since Zn has a strong affinity for T_d sites[101] it is unsurprising that there is a deficit of Fe^{3+} in this site most likely due to Zn substitution. It should be noted that there is only space for 0.34 cations of Zn and there is double this quantity indicated by EPMA; this gives a second suggestion that some of the Zn resides in O_h geometry.

From integration of the area under the Fe L_3 and Ni L_3 XAS spectra the relative quantities of these two cations can be calculated in the samples (Table 3.4). Ni1 has 18% Ni compared to Fe and Ni2 has 24% Ni compared to Fe.

The Ni $L_{2,3}$-edge XAS spectra (Fig. 3.26(c)) are indicative of Ni^{2+} in an octahedral environment as it is similar to the spectral shape in Coker *et al.*[98] which agrees with calculations for this Ni environment in van der Laan and Kirkman.[95] Both samples are similar and the presence of XMCD at the Ni $L_{2,3}$-edge and therefore magnetic Ni shows that the Ni has been incorporated into the spinel structure in the expected coordination and geometry. This result is confirmed by quantitative fitting of the respective Fe $L_{2,3}$-edge XMCD spectra for each of the samples (Fig. 3.26b; Table 3.4), which show a deficit in Fe^{2+} in O_h geometry within the spinel, suggesting substitution by the Ni cation. The Fe L_3-edge XAS (Fig. 3.26a) has a shoulder feature on the low energy side as seen above in the Zn samples, with Ni2 having a more pronounced feature. Again this shows that the sample is oxidised compared to stoichiometric magnetite, which would be expected if Ni^{2+} is substituting for Fe^{2+} in the spinel structure.

3.4.4 Chromium cobalt ferrite nanoparticles

The ferrite nanoparticles obtained from the iron cobalt chromium precursor $[CrCoFeO(O_2C^tBu)_6(HO_2C^tBu)_3]$ **(6)** were analysed by p-XRD, TEM, ICP, EPMA, EDX, XMCD and SQUID. The physicochemical parameters (such as reaction time, temperature and concentration) affecting the morphology and phase of the nanoparticles are described as follows.

3.4.4.1 Chromium cobalt ferrite nanoparticles obtained at different reaction times

The p-XRD pattern obtained from **(6)** showed that the intensity and crystallinity of the peaks increases with time (Fig. 3.27(a)). No product was formed at 5 minutes whilst the pattern obtained at 15 minutes and 30 minutes and were predominantly of cubic magnetite (Fe_3O_4) (ICDD Card No: 01-079-0416) and iron oxide ($Fe_{2.67}O_4$) (ICDD Card No: 04-014-1682).

The peaks obtained at 1 hour were mostly chromium iron cobalt iron oxide with traces of iron oxide whilst at 2 hours, all the peaks were corresponding to chromium iron cobalt oxide ($CrFeCoO_4$) (ICDD Card No: 04-015-5178). The diameter and crystallinity of the particles increases over time as observed in the images taken at 30 minutes (4.6 ± 0.6 nm), 1 hour (5.0 ± 0.4 nm) and at 2 hours (5.7 ± 0.5 nm) (Fig. 3.27(b)-(d)).

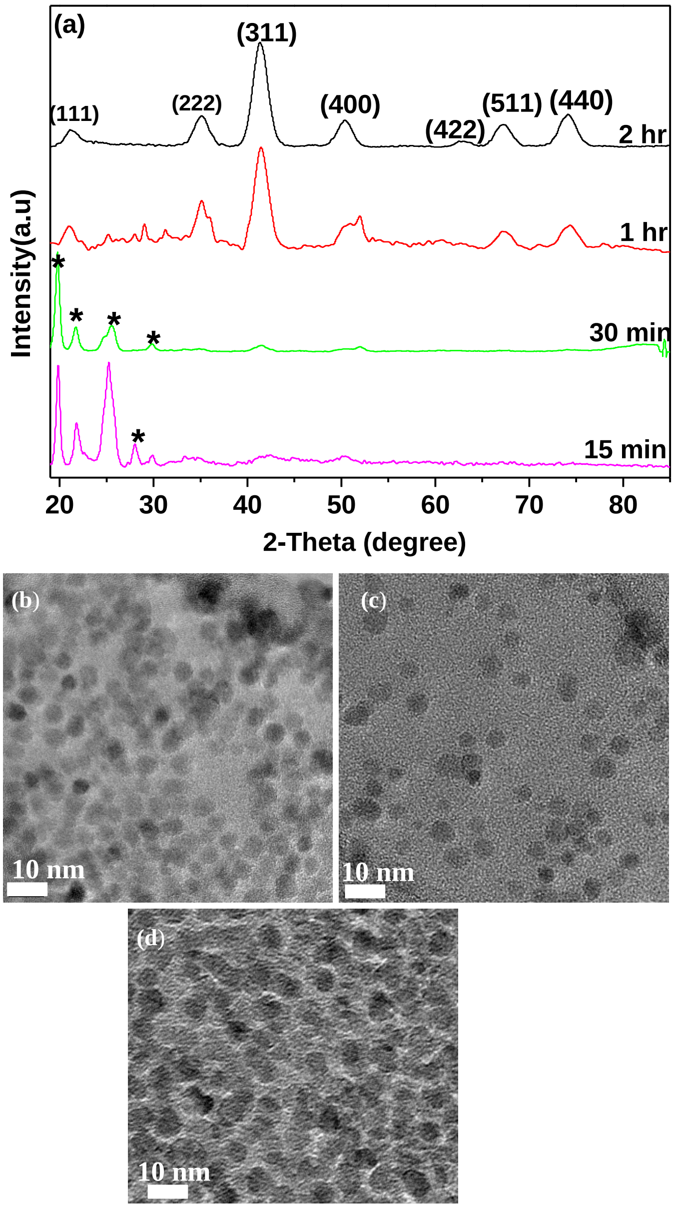

Fig. 3.27 (a) the p-XRD pattern for $CrCoFeO_4$ nanoparticles from **(6)** at different times.* corresponds to the iron oxide peaks. (b)- (d) are TEM images of $CrCoFeO_4$ obtained from **(6)** at 30 minutes, 1 hour and 2 hours respectively.

3.4.4.2 Chromium cobalt ferrite nanoparticles prepared in different solvent systems

The thermolysis of $[CrCoFeO(O_2C^tBu)_6(HO_2C^tBu)_3]$ **(6)** was carried out in three different solvents : diphenylether (260 °C), dibenzylether (300 °C) and octadecene

(300 °C). No product was obtained for the thermolysis in dibenzyl ether even after several hours of reaction time. The p-XRD pattern of the nanoparticles obtained with diphenyl ether as solvent correspond to $CrFeCoO_4$ (ICDD Card No: 04-015-5178) whilst the thermolysis in octadecene produced a mixture of $CrFeCoO_4$ (ICDD Card No: 04-015-5178), wurtsite (ICDD card No: 01-073-2144) and maghemite (ICDD card No: 00-039-1346) (Fig. 3.28).

Their average crystallite sizes estimated by the Scherrer formula were found to be 5.2 nm and 11.5 nm for nanoparticles at 260 °C and 300 °C respectively.

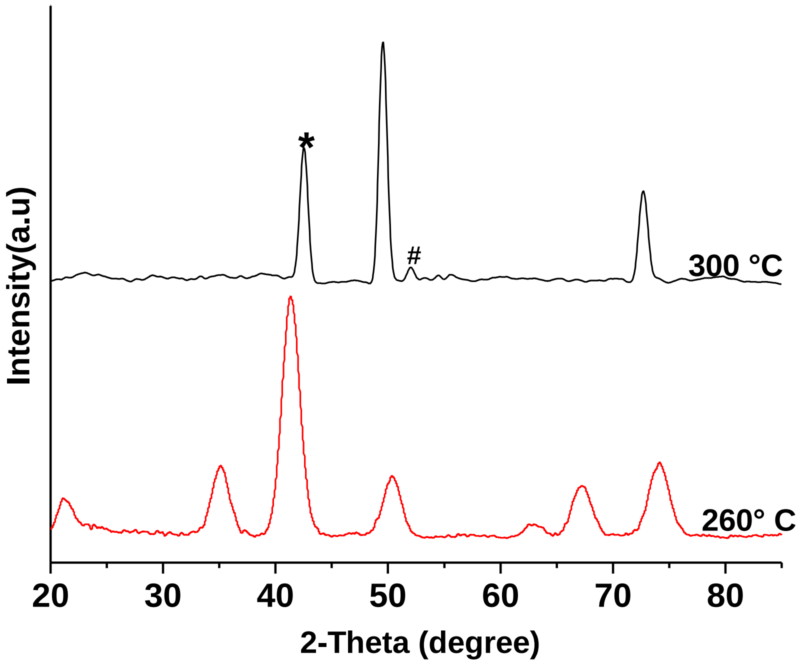

Fig. 3.28 The p-XRD pattern for $CrCoFeO_4$ nanoparticles obtained from **(6)** in different solvents of diphenyl ether (260 °C) or octadecene (300 °C). *corresponds to wustite and # was assigned to maghemite.

TEM images showed larger nanoparticles at higher temperature (300 °C) with average diameter 13.71 ± 1.08 nm whilst smaller particles of average diameter 5.7 ± 0.5 nm were obtained at 260 °C (Fig. 3.29). These results follow the same pattern observed for nanoparticles prepared from precursors **(1), (3)**, **(4)** and **(5).**

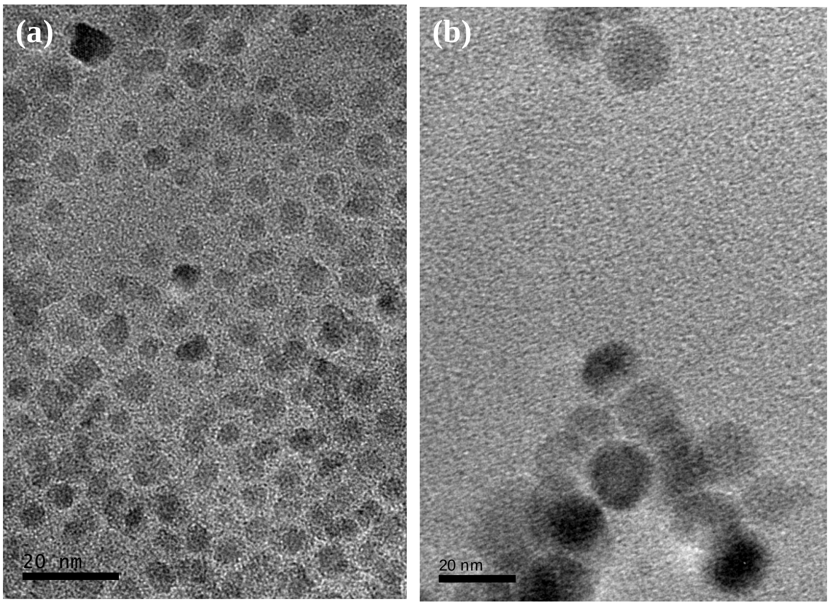

Fig. 3.29 TEM images of chromium cobalt ferrite from (6) at (a) 260 °C with diphenyl ether and (b) at 300 °C with octadecene.

3.4.4.3 Chromium cobalt ferrite nanoparticles obtained from (6) at different concentrations

The p-XRD patterns of nanoparticles obtained from **(6)** at 0.50 and 0.25 precursor concentrations correspond to cubic $CrFeCoO_4$ (ICDD card No: 04-015-5178) (Fig. 3.30). Their average crystallite sizes was estimated by Scherrer formula and were found to be 4.0 nm and 5.2 nm with 0.50 and 0.25 mmol precursor concentrations respectively. TEM images showed that smaller particles of average diameter 4.0 ± 0.4 nm (C1) were obtained using 0.50 mmol precursor concentrations whilst larger particles of diameter 5.7 ± 0.5 nm (C2) were produced with 0.25 mmol precursor concentration (Fig. 3.30(a)). The crystallinity of these nanoparticles is evident in their lattice fringes with a *d*-spacing value of 2.53 Å.

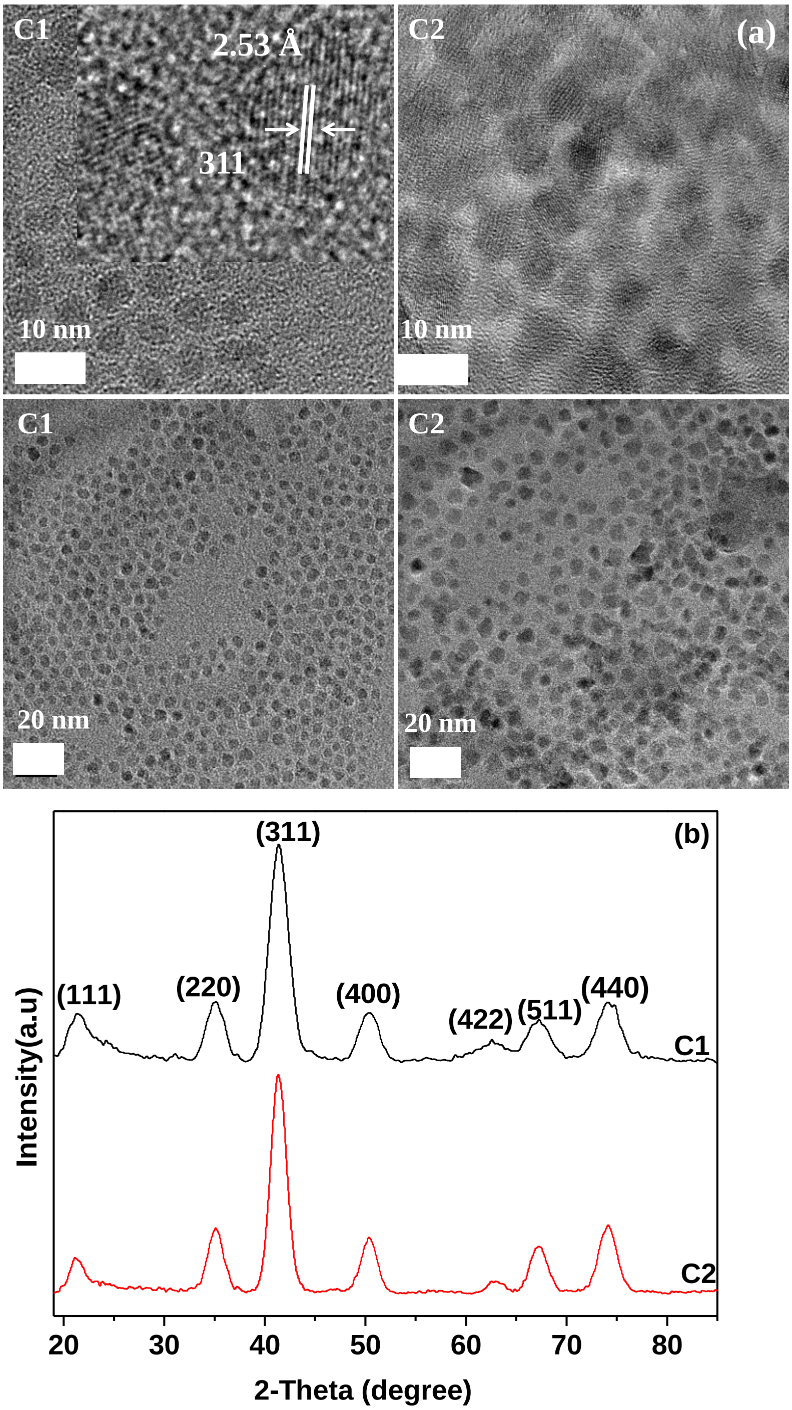

Fig. 3.30 (a) TEM and HRTEM images of chromium cobalt ferrite obtained from precursor **(6)** at different concentrations. C1 and C2 correspond to nanoparticles obtained from 0.50 mmol and 0.25 mmol precursor concentrations respectively, (b) The p-XRD patterns of cubic spinel chromium cobalt ferrite nanoparticles obtained from **(6)** at different precursor concentrations.

Magnetic measurements were performed on chromium cobalt ferrite nanoparticles obtained from **(6)** with average diameters 4.0 ± 0.4 nm (C1) and 5.7 ± 0.5 nm (C2). An estimate for the blocking temperature (T_B) of the samples were done and the data showed that T_B increases with increasing particle diameter, ranging from 130 K for chromium cobalt ferrite nanoparticles with an average diameter of 4.0 nm (C1) to 153K for particles with an average diameter 5.7 nm (C2) (Fig. 3.31(a)).

Field dependent magnetisation studies were performed at temperatures of 5 and 300 K. for C1 of average diameter 4.0 nm are characterised by M_s values of 53 (5 K) and 43 emu.g^{-1} (300 K) whilst C2 with average diameter of 5.7 nm exhibit M_S values of 51 emu.g^{-1} (5 K) and 40 emu.g^{-1}(300 K) (Fig. 3.31(b)). The magnetisation *versus* field measurements at 5 K for $CrFeCoO_4$ nanoparticles showed a high coercivity and remanence of about 9.8 kOe and 30.0 emu.g^{-1} for C1 whilst 10.0 kOe and 32 emu.g^{-1} were obtained for C2. Compared with Fe_2CoO_4 nanoparticles of about the same diameter, the M_S and M_R values of chromium cobalt ferrite nanoparticles of average diameter 5.7 nm (M_S = 53 emu.g^{-1} at 5K, M_R= 32 emu.g^{-1}) are higher than their corresponding Fe_2CoO_4 nanoparticles (M_S = 48 emu.g^{-1} at 5 K, M_R = 28.4 emu.g^{-1}). This is justified by the higher cobalt content of the Fe_2CoO_4.

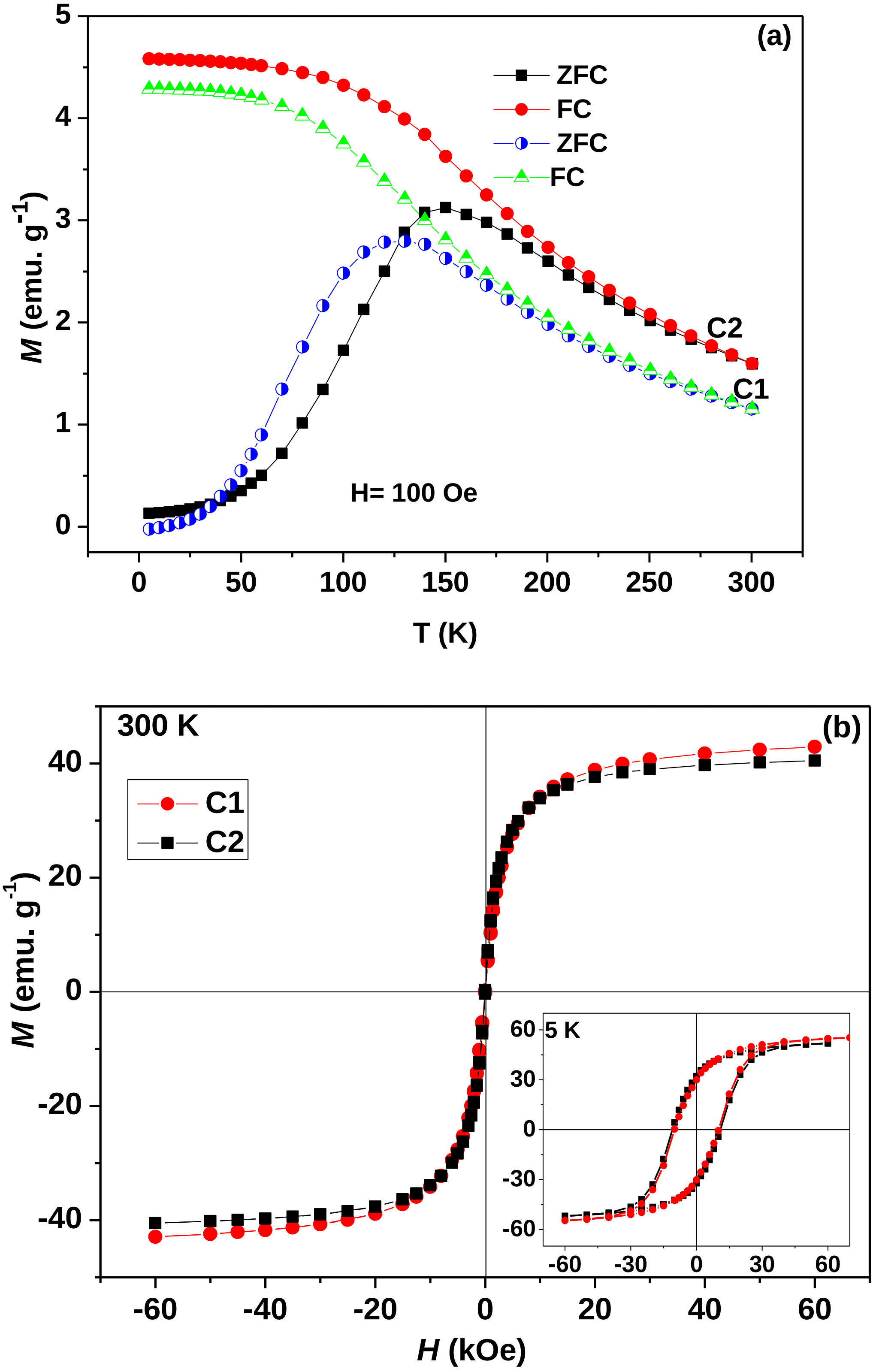

Fig. 3.31 (a) ZFC and FC magnetisation curves for C1 and C2 (CrCoFeO4) nanoparticles obtained from **(6)** of average diameters 4.0 ± 0.4 nm and 5.7 ± 0.5 nm respectively. (b) The hysteresis loops measured at 5 and 300 K for C1 and C2 nanoparticles.

3.4.4.4 ICP-OES, EPMA, EDX and XMCD analysis of chromium cobalt ferrite nanoparticles

The stoichiometry of the chromium cobalt ferrite nanoparticles was determined by ICP-OES and EPMA analysis and was found to be $Cr_{0.02}Co_{0.87}Fe_{2.11}O_4$ within measurement errors. EDX analysis also confirms the presence of Cr, Co and Fe in the sample (Fig. 3.32)

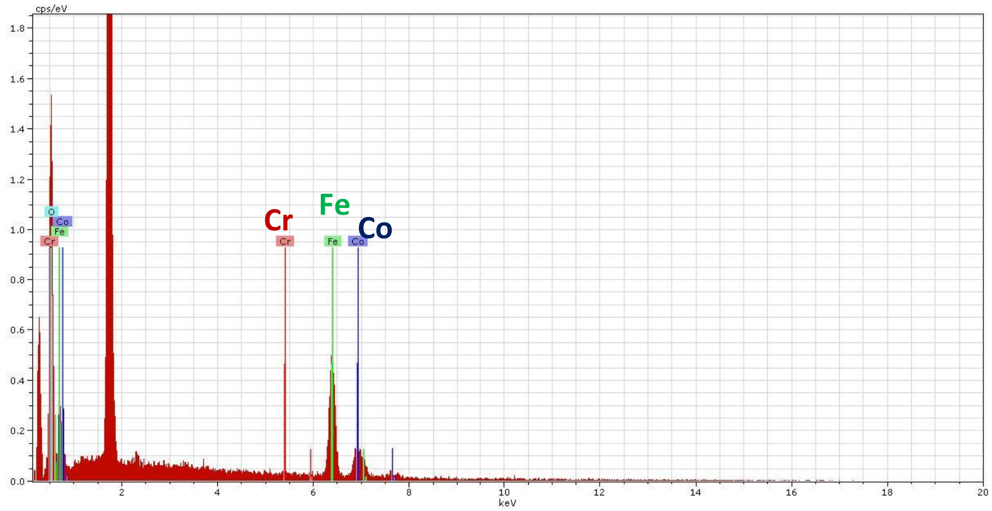

Fig. 3.32 EDX spectrum showing the elements present in the chromium cobalt ferrite nanoparticles.

The calculated lattice parameter for C1 ($Cr_{0.02}Co_{0.87}Fe_{2.11}O_4$) is 8.418 Å, a value intermediate between that of $CrCoFeO_4$ (8.374 Å), $CoFe_2O_4$ (8.40 Å) and Fe_3O_4 (8.396 Å). The observed increased in lattice cell for our sample (8.418 Å) compared with $CrCoFeO_4$ (8.374 Å) can be explained by the fact that smaller Cr is being replaced by Fe and Co.

Using X-ray absorption spectroscopy only the Fe and Co $L_{2,3}$-edge spectra were discernable, and no edge was measured over the energy region corresponding to Cr. This could be due to either the low concentration of Cr (from EPMA), or the Cr is buried in the nanoparticle beneath the detection depth of the TEY signal. The % of Co compared to Fe calculated from the relative peak areas of the Fe and Co L_3 XAS are 26 and 28% for samples C1 and C2 respectively.

Samples C1 and C2 show very similar characteristics in both the Fe and Co $L_{2,3}$-edge XAS and XMCD (Fig. 3.33).

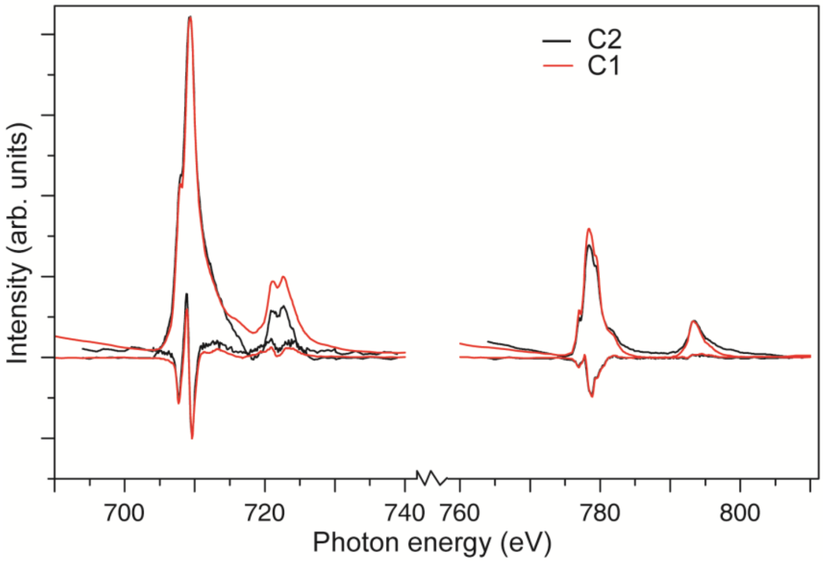

Fig. 3.33 Fe and Co $L_{2,3}$-edge X-ray absorption (XAS) and X-ray magnetic circular Dichroism (XMCD) spectra for chromium cobalt ferrite samples C1 and C2. (C1 and C2 correspond to chromium cobalt ferrite nanoparticles obtained from **(6)** at 0.50 mmol and 0.25 mmol respectively).

Both samples have a small shoulder feature on the low energy side of the Fe L_3-edge, this is similar to that seen in the XAS of oxidised Fe minerals such as goethite and ferrihydrite and as such indicates the presence of more Fe^{3+} than is present in stoichiometric magnetite. This could be due to either oxidation of the sample due to air exposure or due to the presence of a cation (such as Co) replacing some of the Fe^{2+} within the spinel structure, thus altering the ratio of Fe^{2+} :Fe^{3+} and giving a spectral shape dominated by oxidised Fe. Examination of the Fe L_3-edge XMCD spectra (Fig. 3.33) shows three peaks characteristic of the three Fe environments within magnetite. These can be fitted using multiplet calculations for the three Fe environments to give the quantitative data shown in Table 3.5. These data indicate that the magnetite is deficient in both $Fe^{2+}O_h$ and $Fe^{3+}T_d$, but has excess $Fe^{3+}O_h$.

Table 3.5 Fe site occupancies determined using Fe+Co ratios from XAS data, XMCD spectra and atomic multiplet calculations.

Sample	**Fe+Co = 3 (from XAS peak integration)**		**Fe occupancies (normalised)**			**Fe^{2+}/Fe^{3+} ratio**	**T_d/O_h ratio**
	Fe	**Co**	**Fe^{2+} O_h**	**Fe^{3+} T_d**	**Fe^{3+} O_h**		
C2	2.22	0.78	0.23	0.87	1.12	0.12	0.65
C1	2.16	0.84	0.30	0.75	1.12	0.16	0.53
Magnetite			1.00	1.00	1.00	0.50	0.50

This suggests that there is partial oxidation of Fe^{2+} to Fe^{3+} within the structure compared to stoichiometric magnetite, but the amount of excess Fe^{3+} in O_h sites cannot account for all the 'missing' Fe^{2+} in O_h geometry. Therefore it can be assumed that at least some of the sites that would otherwise be occupied by Fe^{2+} most likely contain Co. An examination of the Co $L_{2,3}$-edge XAS and XMCD confirms the presence of Co within a magnetic structure, due to the presence of the magnetic Co signal. From a comparison with calculated data in Coker *et al.*,[28] the XAS spectra for both samples suggests that not all the Co is Co^{2+} in O_h geometry, which would be the most likely situation for the Co cations The lack of a strong doublet feature on the peak of the Co L_3-edge XAS suggests either Co^{2+}, or perhaps Co^{3+}, in T_d geometry is also present within the mineral, however the majority of the Co is Co^{2+} in O_h geometry and this is also reflected in the Co $L_{2,3}$ edge XMCD.

Table 3.6 Summary of the results obtained from precursors **(1), (2)** and **(3)** at different reaction conditions.

Precursor	**conc**	**Phase**	**p-XRD (nm)**	**TEM (nm)**	***Ms*(5 K)**	***T_B***	***H_C* (5 K)kOe**	**Fe+Co = 3 (EPMA)**		**Ratios**		**Fe site occupancies**			**Sample**
		CUBIC						**Fe**	**Co**	**Fe^{2+}/Fe^{3+}**	**T_d/O_h**	**Fe^{2+} O_h**	**Fe^{3+} T_d**	**Fe^{3+} O_h**	
$[Fe_2CoO(O_2C^tBu)_6(HO_2C^tBu)_3]$ **(1)**	0.25	Fe_2CoO_4	5	5.3 ± 1	48	90	10	2.34	0.66	0.24	0.56	0.46	0.84	1.04	S1
$[Fe_2CoO(O_2C^tBu)_6(HO_2C^tBu)_3]$ **(1)**	0.5	Fe_2CoO_4	3	3.6 ± 0.2	47	67	11.3	2.03	0.97	0.11	0.73	0.2	0.86	0.97	S2
$[Co_4Fe_2O_2(O_2C^tBu)_{10}]$ **(2)**	0.25	Fe_2CoO_4	6	6.7 ± 1				1.96	1.04	0.14	0.48	0.24	0.63	1.08	S3
$[Co_4Fe_2O_2(O_2C^tBu)_{10}]$ **(2)**	0.5	Fe_2CoO_4	6	7.0 ± 1	61.4	180	9.8	1.99	1.01	0.19	0.72	0.32	0.83	0.84	S4
								Fe	**Mn**						
$[Fe_2MnO(O_2C^tBu)_6(HO_2C^tBu)_3]$ **(3)**	0.5	$Mn_{0.43}Fe_{2.57}O_4$	3	3.5 ± 0.2	54	9	0.02	2.78	0.22	0.32	0.4	0.68	0.79	1.32	S6
								3	0	0.5	0.5	1	1	1	Magnetite

Table 3.7 Summary of the results obtained from precursors **(4)**, **(5)** and **(6)** at different reaction conditions.

Precursor	**conc**	**Phase**	**p-XRD (nm)**	**TEM (nm)**	***Ms*(5 K)**	T_B	H_C **(5 K)kOe**	**Fe+Co = 3 (EPMA)**		**Ratios**		**Fe site occupancies**			**Sample**
		CUBIC						**Fe**	**Zn**	Fe^{2+}/Fe^{3+}	T_d/O_h	Fe^{2+} O_h	Fe^{3+} T_d	Fe^{3+} O_h	
$[Zn_4Fe_2O_2(O_2C^tBu)_{10}]$ **(4)**	0.50	$Zn_{0.93}Fe_2O_4$	3	3.2 ± 0.2	59	10		2.2	0.7	0.21	0.43	0.38	0.66	1.17	Zn1
$[Zn_4Fe_2O_2(O_2C^tBu)_{10}]$ **(4)**	0.25	$ZnFe_2O_4$	4	5.1 ± 0.7	87	20	0.14								Zn2
								Fe	**Ni**						
$[Fe_2NiO(O_2C^tBu)_6(HO_2C^tBu)_3]$ **(5)**	0.50	$NiFe_2O_4$	3.3	3.3 ± 0.2	34	11		2.12	0.88	0.18	0.72	0.37	1.03	1.07	Ni1
$[Fe_2NiO(O_2C^tBu)_6(HO_2C^tBu)_3]$ **(5)**	0.25	$NiFe_2O_4$	3.8	4.4 ± 0.5	42	11				0.22	0.44	0.41	0.69	1.17	Ni2
								Fe	**Co**						
$[CrCoFeO(O_2C^tBu)_6(HO_2C^tBu)_3]$ **(6)**	0.5	$CrFeCoO_4$	4	4.0 ± 0.4	53	130	9.8	2.22	0.78	0.12	0.65	0.23	0.87	1.12	C1
$[CrCoFeO(O_2C^tBu)_6(HO_2C^tBu)_3]$ **(6)**	0.25	$CrFeCoO_4$	5.2	5.7 ± 0.5	51	153	10	2.16	0.84	0.16	0.53	0.30	0.75	1.12	C2
								3	0	0.5	0.5	1	1	1	Magnetite

3.5 Conclusions

The single source precursors- [$Fe_2CoO(O_2C^tBu)_6(HO_2C^tBu)_3$] **(1),** [$Co_4Fe_2O_2(O_2C^tBu)_{10}$ **(2)**, [$Fe_2MnO(O_2C^tBu)_6(HO_2C^tBu)_3$] **(3),** [$Zn_4Fe_2O_2(O_2C^tBu)_{10}$ **(4)** and [$Fe_2NiO(O_2C^tBu)_6(HO_2C^tBu)_3$] **(5)** were used for the direct synthesis of cobalt, manganese, zinc and nickel ferrite nanoparticles. Highly monodispersed ferrite nanoparticles were obtained from precursors **(1)**, **(3), (4)** and **(5)** (0.50 mmol precursor) whilst cobalt ferrite nanoparticles from (**2**) were nearly monodispersed. The effect of decomposition temperature studied for the five precursors (0.25 mmol) revealed that larger nanoparticles of cobalt, manganese, zinc and nickel ferrites were obtained at 300 °C of **(1)**, **(3), (4)** and **(5)** respectively. Different results were obtained for cobalt ferrite from **(2)** with smaller particles at the higher temperature. We have established that shorter reaction times (less than 1 hour) at 0.25 mmol precursor concentration in all cases gave a mixture of iron oxide and bimetallic oxide whilst only the corresponding bimetallic oxide was obtained after 1 hour. The intensity of the p-XRD peaks increases as the time of reaction increases indicating the higher crystallinity of the nanoparticles. The ICP and the EPMA results are consistent and revealed that the stoichiometry of the cobalt ferrite depends upon the concentration of the precursor; only 0.50 mmol precursor concentration gave stoichiometric cobalt ferrite (Fe_2CoO_4). The stoichiometry of manganese ferrite however was independent of the concentration of precursor as manganese depleted ferrite was obtained using both 0.25 and 0.50 mmol concentration. XMCD analysis established that the majority of Co^{2+} is in octahedral sites in the cobalt ferrite nanoparticles, and this fact was supported by magnetic measurements, all the cobalt ferrite samples showed a large hysteresis. Both cobalt ferrite and manganese ferrite nanoparticles are superparamagnetic at room temperature with high saturation magnetisation values.

The EPMA and XMCD analysis of zinc ferrite nanoparticles obtained from **(4)** showed that despite the strong affinity of zinc ferrite for the tetrahedral sites, some of the zinc ferrite resides in the O_h geometry; this is further confirmed by the hysteresis observed in the magnetic measurements. They also exhibit a high saturation magnetisation values and are superparamagnetic at room temperature.

Nickel ferrite nanoparticles obtained from **(5)** showed a high preference for octahedral geometry as expected. They were also characterised by medium saturation magnetisation values and negligible coercivity at room temperature.

Quaternary oxide of the stoichiometry $Cr_{0.02}Co_{0.87}Fe_{2.11}O_4$ was obtained from the thermolysis of the single source precursor- $[CrCoFeO(O_2C^tBu)_6(HO_2C^tBu)_3$ **(6).** Concentration dependence studied for **(6)** revealed that smaller nanoparticles were obtained with higher precursor concentration (0.50 mmol) as compared with those produced from 0.25 mmol precursor. The thermolysis of **(6)** (0.25 mmol) in different boiling point solvents showed that larger nanoparticles were produced in higher boiling solvent (octadecene at 300 °C) whilst no products were obtained using dibenzyl ether. The effect of reaction time investigated using 0.25 mmol of **(6)** showed that traces of iron oxide was present for nanoparticles withdrawn at less than 1 hour whilst pure quaternary oxide of chromium cobalt ferrite was obtained after 1 hour.

XAS measurements carried out on the chromium cobalt ferrite nanoparticles showed only Fe and Co edge whilst the chromium edge was not discernable probably due to its low concentration. XMCD analysis suggests that most of the cobalt resides in the octahedral geometry.

3.6 References

1. Y. Kinemuchi, K. Ishizaka, H. Suematsu, W. Jiang, and K. Yatsui, *Thin Solid Films*, 2002, **407**, 109.
2. S. P. Gubin, Y. I. Spichkin, G. Y. Yurkov, and A. M. Tishin, *Russ. J. Inorg. Chem.*, 2002, **47**, 32.
3. S. Sun, H. Zeng, D. B. Robinson, S. Raoux, P. M. Rice, S. X. Wang, and G. Li, *J. Am. Chem. Soc.*, 2004, **126**, 273.
4. A. J. Rondinone, A. C. S. Samia, and Z. J. Zhang, *Appl. Phys. Lett.*, 2000, **76**, 3624.
5. A. J. Rondinone, C. Liu, and Z. J. Zhang, *J. Phys. Chem. B*, 2001, **105**, 7967.
6. M. Sugimoto, *J. Am. Ceram. Soc.*, 1999, **82**, 269.
7. C. W. Jung and P. Jacobs, *Magn. Reson. Imaging*, 1995, **13**, 661.
8. P. Majewski and B. Thierry, *Crit. Rev. Solid State Mater. Sci.*, 2007, **32**, 203.
9. C. V. G. Reddy, S. V Manorama, and V. J. Rao, *J. Mater. Sci. Lett.*, 2000, **9**, 775.
10. K. Maaz, A. Mumtaz, S. K. Hasanain, and A. Ceylan, *J. Magn. Magn. Mater.*, 2007, **308**, 289.
11. Y. Qi, Y. Yang, X. Zhao, X. Liu, P. Wu, F. Zhang, and S. Xu, *Particuology*, 2010, **8**, 207.
12. R. T. Olsson, G. Salazar-Alvarez, M. S. Hedenqvist, U. W. Gedde, F. Lindberg, and S. J. Savage, *Chem. Mater.*, 2005, **17**, 5109.
13. H. Zeng, P. M. Rice, S. X. Wang, and S. Sun, *J. Am. Chem. Soc.*, 2004, **126**, 11458.
14. K. P. Naidek, F. Bianconi, T. C. R. da Rocha, D. Zanchet, J. A. Bonacin, M. A. Novak, M. D. G. F. Vaz, and H. Winnischofer, *J. Colloid Interface Sci.*, 2011, **358**, 39.
15. Q. Song and Z. J. Zhang, *J. Am. Chem. Soc.*, 2004, **126**, 6164.
16. N. Bao, L. Shen, W. An, P. Padhan, C. Heath Turner, and A. Gupta, *Chem. Mater.*, 2009, **21**, 3458.
17. M. Moriya, M. Ito, W. Sakamoto, and T. Yogo, *Cryst. Growth Des.*, 2009, **9**, 1889.
18. S. W. Lee, S. Bae, Y. Takemura, I. B. Shim, T. M. Kim, J. Kim, H. J. Lee, S. Zurn, and C. S. Kim, *J. Magn. Magn. Mater.*, 2007, **310**, 2868.

19. S. Mohapatra, S. R. Rout, and A. B. Panda, *Colloids Surf., A*, 2011, **384**, 453.
20. A. D. Arelaro, E. Lima, L. M. Rossi, P. K. Kiyohara, and H. R. Rechenberg, *J. Magn. Magn. Mater.*, 2008, **320**, e335.
21. S. Verma and D. Pravarthana, *Langmuir*, 2011, **27**, 13189.
22. E. Kang, J. Park, Y. Hwang, M. Kang, J.-G. Park, and T. Hyeon, *J. Phys. Chem. B*, 2004, **108**, 13932.
23. L. Zhao, H. Zhang, Y. Xing, S. Song, S. Yu, W. Shi, X. Guo, J. Yang, Y. Lei, and F. Cao, *J. Solid State Chem.*, 2008, **181**, 245.
24. L. Chen, Y. Shen, and J. Bai, *Mater. Lett.*, 2009, **63**, 1099.
25. E. Manova, B. Kunev, D. Paneva, I. Mitov, L. Petrov, C. Estourne, D. Orle, J. Rehspringer, and I. P. C. M. S. G. Mate, *Chem. Mater.*, 2004, **16**, 5689.
26. C. Liu, B. Zou, A. J. Rondinone, and Z. J. Zhang, *J. Phys. Chem. B*, 2000, **104**, 1141.
27. C. R. Vestal and Z. J. Zhang, *Nano Lett.*, 2003, **3**, 1739.
28. V. S. Coker, N. D. Telling, G. van der Laan, R. A. D. Pattrick, C. I. Pearce, E. Arenholz, F. Tuna, R. E. P. Winpenny, and J. R. Lloyd, *ACS Nano*, 2009, **3**, 1922.
29. A. Cabañas and M. Poliakoff, *J. Mater. Chem.*, 2001, **11**, 1408.
30. T. Sato, K. Sue, W. Suzuki, M. Suzuki, K. Matsui, Y. Hakuta, H. Hayashi, K. Arai, S. Kawasaki, A. Kawai-Nakamura, and T. Hiaki, *Ind. Eng. Chem. Res.*, 2008, **47**, 1855.
31. L. J. Cote, A. S. Teja, A. P. Wilkinson, and Z. J. Zhang, *Fluid Phase Equilib.*, 2003, **210**, 307.
32. X. Li, G. Tan, W. Chen, B. Zhou, D. Xue, Y. Peng, F. Li, and N. J. Mellors, *J. Nanopart. Res.*, 2012, **14**, 751.
33. D. S. Mathew and R.-S. Juang, *Chem. Eng. J.*, 2007, **129**, 51.
34. J. Wang, *Mater. Sci. Eng., B*, 2006, **127**, 81.
35. H. Kobayashi, A. Hirukawa, A. Tomitaka, T. Yamada, M. Jeun, S. Bae, and Y. Takemura, *J. Appl. Phys.*, 2010, **107**, 09B322.
36. Y. Jun, J.-H. Lee, and J. Cheon, *Angew. Chem. Int. Ed.*, 2008, **47**, 5122.
37. L. Satyanarayana, K. M. Reddy, and S. V. Manorama, *Mater. Chem. Phys.*, 2003, **82**, 21.
38. P. Lavela and J. L. Tirado, *J. Phys. Chem. C*, 2010, **114**, 12828.

39. M. M. Rashad and O. A. Fouad, *Mater. Chem. Phys.*, 2005, **94**, 365.
40. P. Sivakumar, R. Ramesh, A. Ramanand, S. Ponnusamy, and C. Muthamizhchelvan, *J. Mater. Sci- Mater. Electron.*, 2011, **23**, 1041.
41. K. Maaz, S. Karim, A. Mumtaz, S. K. Hasanain, J. Liu, and J. L. Duan, *J. Magn. Magn. Mater.*, 2009, **321**, 1838.
42. W. Cheng, K. Tang, and J. Sheng, *Chem. Euro. J.*, 2010, **16**, 3608.
43. K. Nejati and R. Zabihi, *Chem. Cent. J.*, 2012, **6**, 23.
44. Y. Cheng, Y. Zheng, Y. Wang, F. Bao, and Y. Qin, *J. Solid State Chem.*, 2005, **178**, 2394.
45. J. Huo and M. Wei, *Mater. Lett.*, 2009, **63**, 1183.
46. A. Baykal, N. Kasapoğlu, Y. Köseoğlu, M. S. Toprak, and H. Bayrakdar, *J. Alloys Compd.*, 2008, **464**, 514.
47. S. Yáñez-Vilar, M. Sánchez-Andújar, C. Gómez-Aguirre, J. Mira, M. A. Señarís-Rodríguez, and S. Castro-García, *J. Solid State Chem.*, 2009, **182**, 2685.
48. P. Sivakumar, R. Ramesh, A. Ramanand, S. Ponnusamy, and C. Muthamizhchelvan, *Mater. Res. Bull.*, 2011, **46**, 2204.
49. M. Srivastava, A. K. Ojha, S. Chaubey, and A. Materny, *J. Alloys Compd.*, 2009, **481**, 515.
50. N. Bao, L. Shen, Y. Wang, P. Padhan, and A. Gupta, *J. Am. Chem. Soc.*, 2007, **129**, 12374.
51. H. Ehrhardt, S. J. Campbell, and M. Hofmann, *Scr. Mater.*, 2003, **48**, 1141.
52. S. Bid and S. K. Pradhan, *Mater. Chem. Phys.*, 2003, **82**, 27.
53. Y. Xu, Y. Liang, L. Jiang, H. Wu, H. Zhao, and D. Xue, *J. Nanomaterials*, 2011, **2011**, 1.
54. C. Bárcena, A. K. Sra, G. S. Chaubey, C. Khemtong, J. P. Liu, and J. Gao, *Chem. Commun.*, 2008, 2224.
55. R. Sai, S. D. Kulkarni, K. J. Vinoy, N. Bhat, and S. A. Shivashankar, *J. Mater. Chem.*, 2012, **22**, 2149.
56. R. Zhang, J. Huang, J. Zhao, Z. Sun, and Y. Wang, *Energy Fuels*, 2007, **21**, 2682.
57. F. Gao, X. Y. Chen, K. B. Yin, S. Dong, Z. F. Ren, F. Yuan, T. Yu, Z. G. Zou, and J. M. Liu, *Adv. Mater.*, 2007, **19**, 2889.

58. M. Milanović, E. G. Moshopoulou, D. Stamopoulos, E. Devlin, K. P. Giannakopoulos, A. G. Kontos, K. Eleftheriadis, M. I. Gini, and L. M. Nikolić, *Ceram. Int.*, 2013, **39**, 3235.
59. C. A. Ladole, *Int. J. Chem. Sc.*, 2012, **10**, 1230.
60. M. Veith, M. Haas, and V. Huch, *Chem. Mater.*, 2005, **17**, 95.
61. J. W. Moon, Y. Roh, R. J. Lauf, H. Vali, L. W. Yeary, and T. J. Phelps, *J. Microbiol. Methods*, 2007, **70**, 150.
62. L. W. Yeary, J. W. Moon, C. J. Rawn, L. J. Love, A. J. Rondinone, J. R. Thompson, B. C. Chakoumakos, and T. J. Phelps, *J. Magn. Magn. Mater.*, 2011, **323**, 3043.
63. F. Grasset, N. Labhsetwar, D. Li, D. C. Park, N. Saito, H. Haneda, O. Cador, T. Roisnel, S. Mornet, E. Duguet, J. Portier, and J. Etourneau, *Langmuir*, 2002, **18**, 8209.
64. J. Wan, X. Jiang, H. Li, and K. Chen, *J. Mater. Chem.*, 2012, **22**, 13500.
65. Y. Köseoğlu, M. I. Oleiwi Oleiwi, R. Yilgin, and A. N. Koçbay, *Ceram. Int.*, 2012, **38**, 6671.
66. M. Sajjia, M. Oubaha, T. Prescott, and A. G. Olabi, *J. Alloys Compd.*, 2010, **506**, 400.
67. S. Singhal, S. Jauhar, J. Singh, K. Chandra, and S. Bansal, *J. Mol. Struct.*, 2012, **1012**, 182.
68. M. A. Gabal, Y. M. Al Angari, and F. A. Al-Agel, *J. Mol. Struct.*, 2013, **1035**, 341.
69. B. G. Toksha, S. E. Shirsath, M. L. Mane, S. M. Patange, S. S. Jadhav, and K. M. Jadhav, *J. Phys. Chem. C*, 2011, **115**, 20905.
70. M. Han, C. R. Vestal, and Z. J. Zhang, *J. Phys. Chem. B*, 2004, **108**, 583.
71. A. M. Cojocariu, M. Soroceanu, L. Hrib, V. Nica, and O. F. Caltun, *Mater. Chem. Phys.*, 2012, **135**, 728.
72. C. R. Vestal and Z. J. Zhang, *Chem. Mater.*, 2002, **14**, 3817.
73. P. P. Hankare, U. B. Sankpal, R. P. Patil, I. S. Mulla, P. D. Lokhande, and N. S. Gajbhiye, *J. Alloys Compd.*, 2009, **485**, 798.
74. M. J. Iqbal and M. R. Siddiquah, *J. Alloys Compd.*, 2008, **453**, 513.
75. E. Pervaiz and I. H. Gul, *J. Magn. Magn. Mater.*, 2012, **324**, 3695.

76. J. A. Paulsen, A. P. Ring, C. C. H. Lo, J. E. Snyder, and D. C. Jiles, *J. Appl. Phys.*, 2005, **97**, 044502.
77. C. Burda, X. Chen, R. Narayanan, and M. A. El-Sayed, *Chem. Rev.*, 2005, **105**, 1025.
78. S. G. Kwon and T. Hyeon, *Small*, 2011, **7**, 2685.
79. J. Park, J. Joo, S. G. Kwon, Y. Jang, and T. Hyeon, *Angew. Chem. Int. Ed.*, 2007, **46**, 4630.
80. J. Park, K. An, Y. Hwang, J.-G. Park, H.-J. Noh, J.-Y. Kim, J.-H. Park, N.-M. Hwang, and T. Hyeon, *Nat. Mater.*, 2004, **3**, 891.
81. W. W. Yu, J. C. Falkner, C. T. Yavuz, and V. L. Colvin, *Chem. Commun.*, 2004, 2306.
82. K. Abdulwahab, M. A. Malik, P. O'Brien, K. Govender, C. A. Muryn, G. A. Timco, F. Tuna, and R. E. P. Winpenny, *Dalton Trans.*, 2013, **42**, 196.
83. A. G. Roca, M. P. Morales, K. O'Grady, and C. J. Serna, *Nanotechnology,* 2006, **17**, 2783.
84. E. V Shevchenko, D. V Talapin, H. Schnablegger, A. Kornowski, O. Festin, P. Svedlindh, M. Haase, and H. Weller, *J. Am. Chem. Soc.*, 2003, **125**, 9090.
85. M. F. Casula, Y. Jun, D. J. Zaziski, E. M. Chan, A. Corrias, A. P. Alivisatos, M. Science, and L. Berkeley, *J. Am. Chem. Soc.*, 2006, **128**, 1675.
86. C. A. Crouse and A. R. Barron, *J. Mater. Chem.*, 2008, **18**, 4146.
87. J. M. Byrne, N. D. Telling, V. S. Coker, R. A. D. Pattrick, G. van der Laan, E. Arenholz, F. Tuna, and J. R. Lloyd, *Nanotechnology*, 2011, **22**, 455709.
88. A. H. Lu, E. L. Salabas, and F. Schüth, *Angew. Chem. Int. Ed.*, 2007, **46**, 1222.
89. B. Martinez, X. Obradors, L. Balcells, A. Rouanet, and C. Monty, *Phys. Rev. Lett.*, 1998, **80**, 181.
90. S. Verma and P. A. Joy, *J. Appl. Phys.*, 2005, **98**, 124312.
91. S. Verma, H. M. Joshi, T. Jagadale, A. Chawla, R. Chandra, and S. Ogale, *J. Phys. Chem. C*, 2008, **112**, 15106.
92. C. Liu, B. Zou, A. J. Rondinone, and Z. J. Zhang, *J. Am. Chem. Soc.*, 2000, **122**, 6263.
93. M. Ghosh, E. V. Sampathkumaran, and C.N.R. Rao, *Chem. Mater.*, 2005, **17**, 2348.

94. G. van der Laan and B. T. Thole, *Phys. Rev., B*, 1991, **43**, 13401.
95. G. van der Laan and I. W. Kirkman, *J. Phys. Condens. Matter* 1992, **4**, 4189.
96. R. A. D. Pattrick, G. van der Laan, C. M. B. Henderson, P. Kuiper, E. Dudzik, and D. J. Vaughan, *Eur. J. Mineral.*, 2002, **14**, 1095.
97. C. I. Pearce, C. M. B. Henderson, R. A. D. Pattrick, G. van der Laan, and D. J. Vaughan, *Am. Mineral.*, 2006, **91**, 880.
98. V. S. Coker, C. I. Pearce, R. A. D. Pattrick, G. van der Laan, N. D. Telling, J. M. Charnock, E. Arenholz, and J. R. Lloyd, *Am. Mineral.*, 2008, **93**, 1119.
99. V. S. Coker, J. M. Byrne, N. D. Telling, G. van der Laan, J. R. Lloyd, A. P. Hitchcock, J. Wang, and R. A. D. Pattrick, *Geobiology*, 2012, **10**, 347.
100. A. Kundu, C. Upadhyay, and H. C. Verma, *Phys. Lett. A*, 2003, **311**, 410.
101. V. G. Harris, N. C. Koon, C. M. Williams, Q. Zhang, M. Abe, and J. P. Kirkland, *Appl. Phys. Lett.*, 1996, **68**, 2082.

Chapter 4

Water-Dispersible Ferrite Nanoparticles

4.1 Summary

This chapter describes the synthesis of water-dispersible magnetite (Fe_3O_4) and ferrite (MFe_2O_4 where M = Co, Ni, Zn, Mn) nanoparticles by a one pot synthesis. The magnetite nanoparticles were synthesised by both co-precipitation method (dual-source) and by hot injection thermal decomposition of iron pivalate clusters (single source). The ferrite nanoparticles were synthesised by hot injection thermolysis of heterometallic pivalate clusters in a mixture of polyvinylpyrrolidone (PVP) (capping agent) and triethylene glycol (TREG) (solvent). The magnetite nanoparticles produced from the thermolysis of the single source precursor were more monodispersed (4.1 ± 0.3 nm) compared to those obtained from co-precipitation (7.0 ± 1.0 nm). All the ternary ferrites nanoparticles produced are monodispersed without a further size selection process. The nanoparticles are directly dispersible in water without any further post synthesis procedure. The nanoparticles were characterised by powder X-ray diffraction (p-XRD), transmission electron microscopy (TEM), high resolution transmission electron microscopy (HRTEM), energy dispersive spectroscopy (EDS) and selected area electron diffraction (SAED).

4.2. Introduction

Ferrite nanoparticles have attracted a lot of attention recently due to their wide range of applications including drug delivery,[1,2] magnetic resonance imaging,[1,3-5] hyperthermia treatment,[1,4,6] data storage,[7] ferrofluids,[8] environmental remediation[9,10] and catalysis.[11,12] Ferrite nanoparticles are well suited for biomedical applications because their sizes can be manipulated and also their surface can be functionalised with appropriate molecules to make them highly selective towards their targets.[13,14] In addition, their superparamagnetic properties make it possible for controlling their movement under the influence of an external magnetic field.

Various synthetic and functionalisation methods have been employed to synthesise ferrite nanoparticles suitable for such applications. The co-precipitation method is commonly used for the synthesis of magnetite and other ferrite nanoparticles because it is easy to use and scalable.[9,10,15–29] However, nanoparticles obtained from this method tend to have a broad size distribution and poor crystallinity. As such, other non-hydrolytic methods have been employed to synthesise these nanoparticles including solvothermal methods and thermal decomposition of iron- based complexes.

The biological methods have been used to synthesise water soluble ferrite nanoparticles including iron,[30–40] cobalt,[41–43] manganese,[43] nickel[42,43] and zinc.[43,44] Although this approach could be exploited for industrial scale, the success of getting monodispersed nanoparticles depends on environmental parameters such as temperature, redox potential and pH.[45]

Thermal decomposition methods have been proven to produce monodispersed crystalline nanoparticles[46,47] but the shortcoming of this method is that the capping agents usually employed are hydrophobic and thus not dispersible in aqueous medium. This in turn has hampered its applications in producing nanoparticles for biomedical and environmental applications. In view of this, there has been ongoing research into preparing water dispersible ferrite nanoparticles with desirable properties. Methods proposed to achieve this goal are either direct synthesis or post synthesis by ligand exchange to obtain the desired surface modification.

To disperse the highly crystalline nanoparticles obtained from thermolysis in aqueous medium, various post synthesis surface modification/ ligand exchange techniques have been employed including surface exchange of amine modified poly(acrylic acid),[48] glucosaminic acid,[49] α-cyclodextrin,[50] dimercaptosuccinic acid[51,52] silesquioxane ligands[53] modified polyethylene glycol,[54,55] modified polymaleic anhydride,[56,57] citrate,[58] hydroxamic acid[59] and tetramethylammonium 11-aminoundecanoate.[60]

A major shortcoming of post-synthesis surface modification is incomplete replacements of ligand that reduces stability in aqueous solution; also often the ligand exchange procedures are often tedious, requiring prolonged reaction times and excess of the new ligand to disrupt the established surface coat and as such may require further purification after ligand exchange. Consequently, the direct synthesis of highly-crystalline ferrite nanoparticles that can be dispersed in water is a preferable alternative.

A direct synthesis of water dispersible ferrite nanoparticles has been investigated by different synthetic routes. A hydrothermal / solvothermal method has been used to produce a hydrophilic magnetite and cobalt ferrite nanoparticles using polyethylene glycol as surfactant.[61] Using the same method, Guan *et al* produced amine functionalised magnetite nanoparticles with a narrow size distribution which can be dispersed in aqueous media.[62] Single-crystal hollow spheres magnetite of average diameter 200-300 nm were synthesised by Zhu and co-workers using ethylenediamine as surfactant in the presence of ethylene glycol by the solvothermal route.[63] Ferrite colloidal spheres of high saturation magnetisation and dispersibility in water have been synthesised by hydrothermal treatments of chloride salts, urea and polyacryl-amide (PAM) as stabilisers.[64]

The thermal decomposition method has been further developed to produce water dispersible ferrite nanoparticles by using strong polar capping agents. Li *et al.* synthesised magnetite nanoparticles *via* the thermal decomposition of iron(III) acetylacetonates [Fe(acac)$_3$] in the presence of 2-pyrrolidone as the capping agents and obtained a 5 nm diameter nanoparticles which were further used as seeds to grow larger particles.[65] Similarly, Li *et al.* produced magnetite nanoparticles using the same precursor and capping agent and in addition to that carboxyl- terminated poly(ethylene glycol) were used to coat the nanoparticles.[66,67,68] The size of the obtained magnetite nanoparticles could be varied by varying the ratio between MPEG-COOH and [Fe(acac)$_3$], as smaller particles were obtained when the ratio of MPEG-COOH to [Fe(acac)$_3$] was set to 3:1.[66] This same group further developed their method by using the same precursor but with N-vinyl-2-pyrrolidone (NVP) to achieve PVP coated magnetite nanoparticles.[69]

Glycol and its derivatives have been used as capping agents for the direct synthesis of water soluble ferrite nanoparticles. Yang *et al.* used tetraethylene glycol as a stabiliser to produce water soluble manganese ferrite nanoparticles by the thermal decomposition of manganese(III)acetylacetonate and [Fe(acac)$_3$].[70] Caruntu and his team employed the hydrothermal method to synthesise magnetite nanoparticles in the presence of diethylene glycol and *N*-methyl ethanolamine as surfactants.[71] Using iron pentacarbonyl as the precursor, magnetite nanoparticles have been produced with 4-methylcatechol (4-MC) as the surfactant.[72] The 4-MC coated magnetite nanoparticles were then further functionalised with a peptide, making the particles stable in a physiological environment.

In this chapter, we explore the use of pivalate clusters as single source precursors for the synthesis of water soluble ferrite nanoparticles by a hot injection thermolysis method. Co-precipitation has also been used to produce magnetite nanoparticles.

4.3 Experimental

4.3.1 Synthesis of Precursors:

Synthesis of $[Fe_3O(O_2C^tBu)_6(H_2O)_3](O_2C^tBu).HO_2C^tBu$**(1)** $[Fe_2MnO(O_2C^tBu)_6(HO_2C^tBu)_3]$ **(2),** $[Fe_2CoO(O_2C^tBu)_6(HO_2C^tBu)_3]$ **(3)**, $[Zn_4Fe_2O_2(O_2C^tBu)_{10}]$ **(4),** and $[Fe_2NiO(O_2C^tBu)_6(HO_2C^tBu)_3]$ **(5)** was carried out by the methods described in chapters 2 and 3.

4.3.2 Synthesis of nanoparticles

4.3.2.1 Magnetite nanoparticles

The magnetite nanoparticles were synthesised by two different methods: co-precipitation and hot injection thermolysis.

4.3.2.1.1 Co-precipitation method

In a typical reaction, a mixture of $FeCl_3.6H_2O$ (0.2703 g, 1 mmol) and $FeCl_2.4H_2O$ (0.099 g, 0.5 mmol) was added slowly into ammonium hydroxide (0.05 M, 50 mL) at room temperature and stirred vigorously for 30 minutes under nitrogen. The black precipitate was collected with a magnetic stirrer and washed with deionised water. This was followed by the addition of polyallylamine hydrochloride (PAH) and ultrasonication for 15 minutes.

PAH was prepared as follows: Polyallyl amine (M_w 17,000, 20% solution, 10 mg) was diluted with 10 mL deionised and adjusted to pH 3 with Hydrochloric acid (HCl). 1 mL of this solution was further diluted 5 times and added to 0.1 mL suspension of the magnetite nanoparticles.

4.3.2.1.2 Thermal decomposition method

In a typical reaction, polyvinylpyrrolidone PVP (M_w 40,000 0.25 g) and triethylene glycol (TREG) (15 mL) was degassed at 100 ºC under vacuum for 30 minutes and then heated to the boiling point of the solvent (TREG) under nitrogen. The precursor, $[Fe_3O(O_2C^tBu)_6(H_2O)_3](O_2C^tBu).HO_2C^tBu$ (0.275 g, 0.25 mmol) was dispersed in TREG (10 mL) and injected into the solution of the hot mixture. The reaction was maintained at 230 ºC for 2 hours. The dark mixture was allowed to cool and acetone was added to precipitate the nanoparticles which were then isolated by centrifugation. The residue was washed with acetone three times and then re-dispersed in deionised water.

4.3.2.2 Manganese, cobalt, zinc and nickel ferrite nanoparticles

All the nanoparticles were synthesised by a hot injection thermolysis. Reactions were carried out using 0.25 mmol of each precursor following the same method as described for the synthesis of magnetite nanoparticles in section 4.3.2.1.2.

4.4 Results and discussion

4.4.1 Magnetite nanoparticles

Nanoparticles produced were analysed by p-XRD, TEM, HRTEM and SAED. The p-XRD nanoparticles obtained from both methods were matched with cubic magnetite (Fe_3O_4) (ICDD Card No: 00-019-0629) (Fig. 4.1). Their average particle diameters were estimated using the Scherrer equation and also from their TEM images. Nanoparticles obtained from the thermal decomposition method have an average diameter of 5 nm (XRD) and 4.1 ± 0.3 nm (TEM) whilst 6.5 nm (XRD) and 7.0 ± 1.0 nm (TEM) were obtained for nanoparticles synthesised by the co-precipitation method. From these results, it was observed that the nanoparticles synthesised from the thermal decomposition method have a narrow size distribution compared with nanoparticles obtained from co-precipitation. Also the nanoparticles obtained from thermal decomposition are spherical and highly crystalline as observed in the lattice fringes and the diffraction pattern (Fig. 4.2(a) and (c)). The *d*-spacing measured from the lattice fringes of the nanocrystallite correspond to a value of 2.54 Å which can be indexed to the (311) reflection plane of magnetite (ICDD Card No: 00-019-0629). The SAED pattern (Fig. 4.2(c)) contains information from a large number of magnetite nanoparticles and the observed strong diffraction rings can be indexed to (220), (311) and (400) planes.

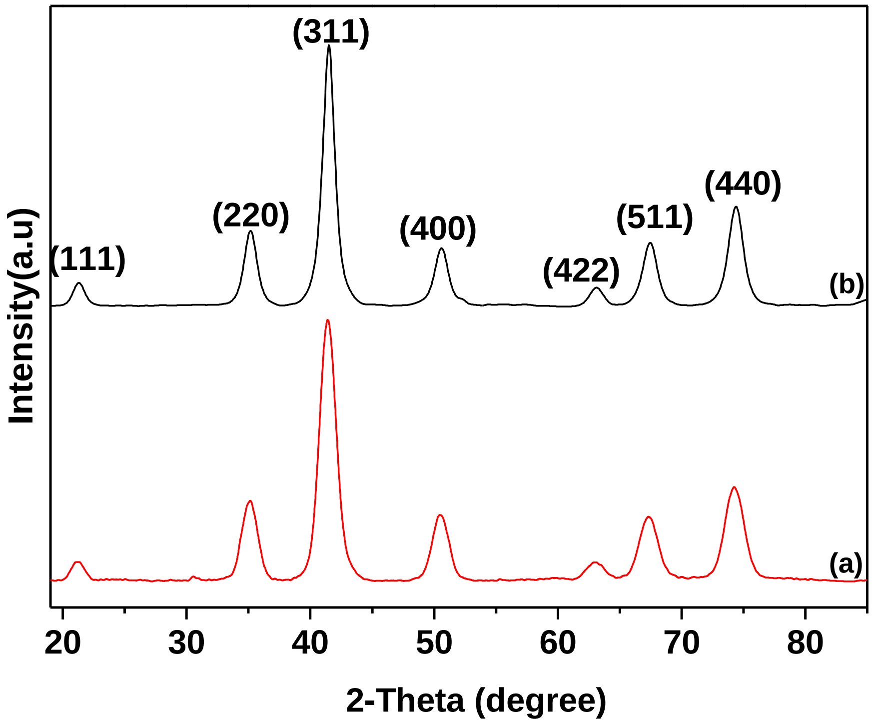

Fig. 4.1 The p-XRD pattern for magnetite (Fe_3O_4) nanoparticles obtained from (a) the thermolysis of (**1**) in PVP and TREG, (b) co-precipitation of Fe^{2+} and Fe^{3+} with PAH as stabiliser.

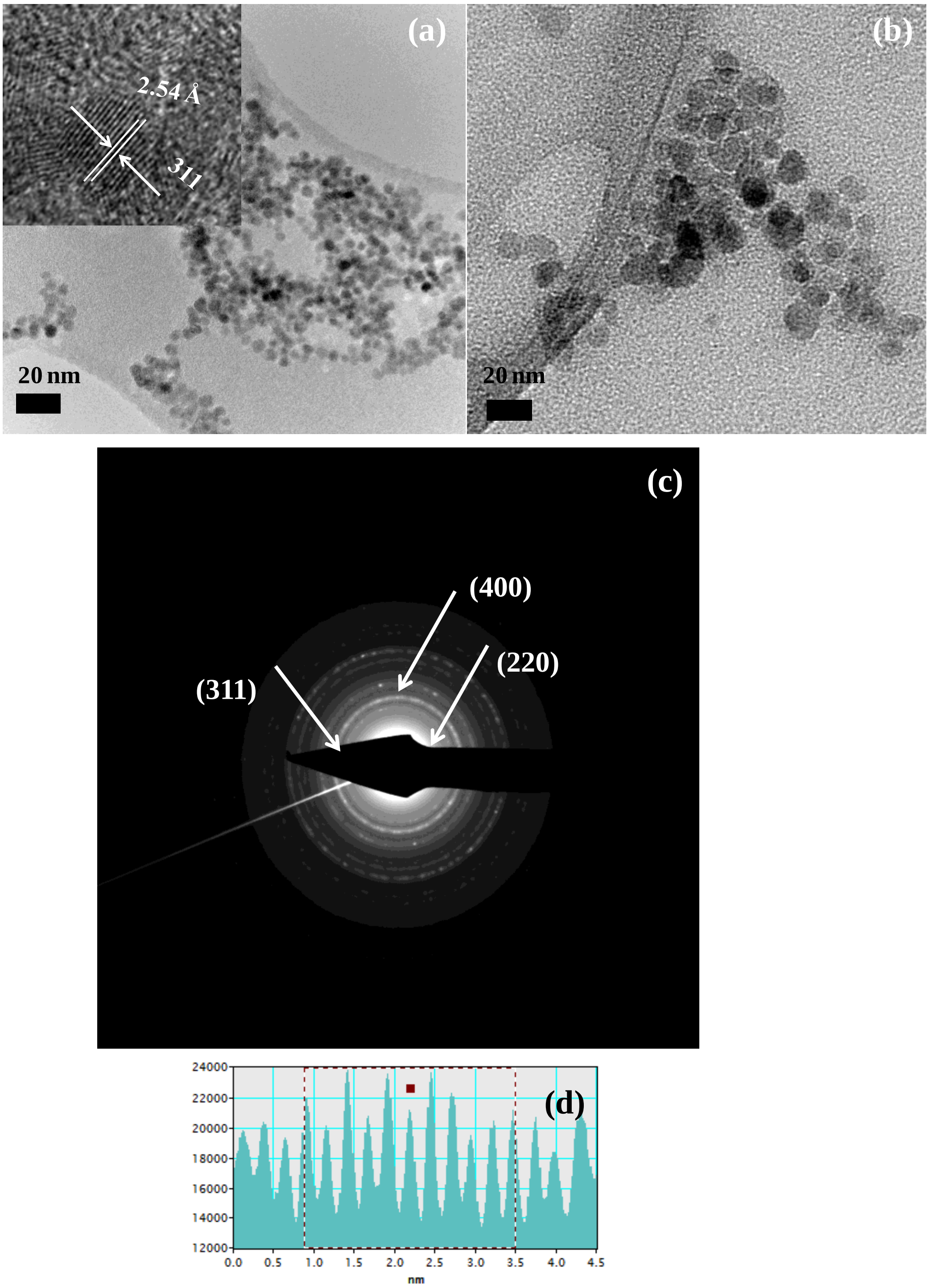

Fig. 4.2 (a) and (b) are TEM images obtained for magnetite (Fe_3O_4) nanoparticles obtained from thermal decomposition and co-precipitation respectively. (c) SAED of (a). (d) Line profile obtained by drawing a perpendicular line across the fringes in (a) from which the *d* -spacing is estimated.

4.4.2 Manganese ferrite nanoparticles

The p-XRD patterns of the nanoparticles are broad indicating the nanocrystallinity of the material obtained from **(2)** and correspond to cubic phase of manganese iron oxide ($Mn_{0.43}Fe_{2.57}O_4$) (ICDD Card No: 01-089-2807) (Fig. 4.3(a)). The average crystallite size estimated by the Scherrer equation is 6.0 nm whilst average diameters calculated from the TEM images is 6.3 ± 0.7 nm. The size and shape of these nanoparticles agrees with that described in previous reports .[70,73]

The HRTEM images showed that spherical nanoparticles were obtained and the lattice fringes observed also supports the high crystallinity of the manganese ferrite nanoparticles. The *d*- spacing value of 3.00 Å (Fig. 4.3(c)) was calculated which can be indexed to the (220) reflection plane of $Mn_{0.43}Fe_{2.57}O_4$ within measurement errors. It is worth mentioning that the average *d*-spacing of the nanoparticles were calculated from a number of lattice fringes by drawing a perpendicular line across the fringes which produced a line profile from which the spacing is estimated (Fig. 4.3 (d)).

The SAED of $Mn_{0.43}Fe_{2.57}O_4$ nanoparticles also confirms the formation of cubic $Mn_{0.43}Fe_{2.57}O_4$ with the strong diffraction rings matching the (220) and (311) planes (Fig. 4.3 (e)).

The elemental composition of these nanoparticles was also confirmed by the EDX analysis showed that both manganese and iron are present in the ratio Fe: Mn is 1.0: 0.1 (Fig. 4.3(f)). The EDX quantitative measurement is low as compared to the initial precursor ratio (Fe: Mn = 2.0:1.0). The manganese deficient ferrite nanoparticles obtained is also indicated in the p-XRD pattern phase corresponding to $Mn_{0.43}Fe_{2.57}O_4$.

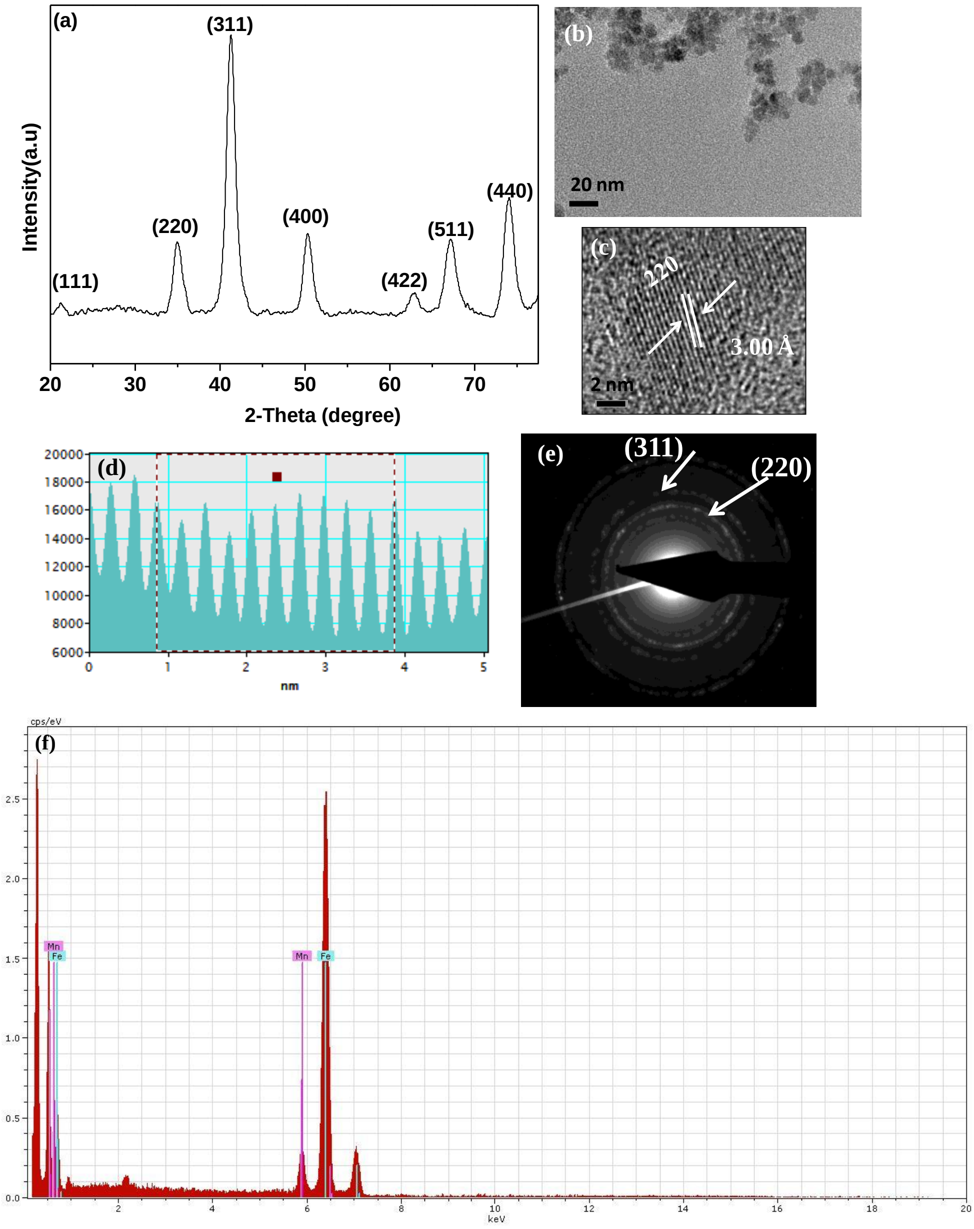

Fig. 4.3 (a) p-XRD pattern for cubic manganese iron oxide nanoparticles ($Mn_{0.43}Fe_{2.57}O_4$), (b)-(c) TEM images, HRTEM obtained for these particles. (d) Line profile used for calculating the *d*-spacing from (c). (e) The diffraction rings obtained from (b). (f) EDX spectrum.

4.4.3 Cobalt ferrite nanoparticles

The p-XRD patterns of the nanoparticles obtained from **(3)** were of single phase with no traces of impurities which correspond to cubic cobalt iron oxide ($CoFe_2O_4$) (ICDD Card No: 04-005-7078) (Fig. 4.4(a)).

Scherrer analysis of the XRD peaks gave a crystallite size of 6.5 nm which is in close proximity to with those estimated from the TEM images (6.7 ± 0.7 nm). The spherical shape of the nanoparticles was clearly evident in the HRTEM images and from the lattice fringes, a *d*-spacing value of 2.11 Å was calculated (Fig. 4.4(c)) which correspond to the (400) plane of cubic cobalt iron oxide. The line profile was used to estimate the *d*-spacing by counting ten spaces which correspond to the value in Å. Similar results have been reported with PVP as the capping agent using dual source precursors.[74,75] A good size distribution and uniform shape was attained with this method compared to those obtained by Moon *et al.* using microbial method.[43]

SAED also confirmed the purity and crystallinity of the cobalt ferrite nanoparticles with diffraction rings matching the (200) and (400) planes of the cubic phase.

EDX analysis was performed which confirmed the presence of both iron and cobalt in the ratio of 1.0: 0.4 (Fig. 4.4 (f)).

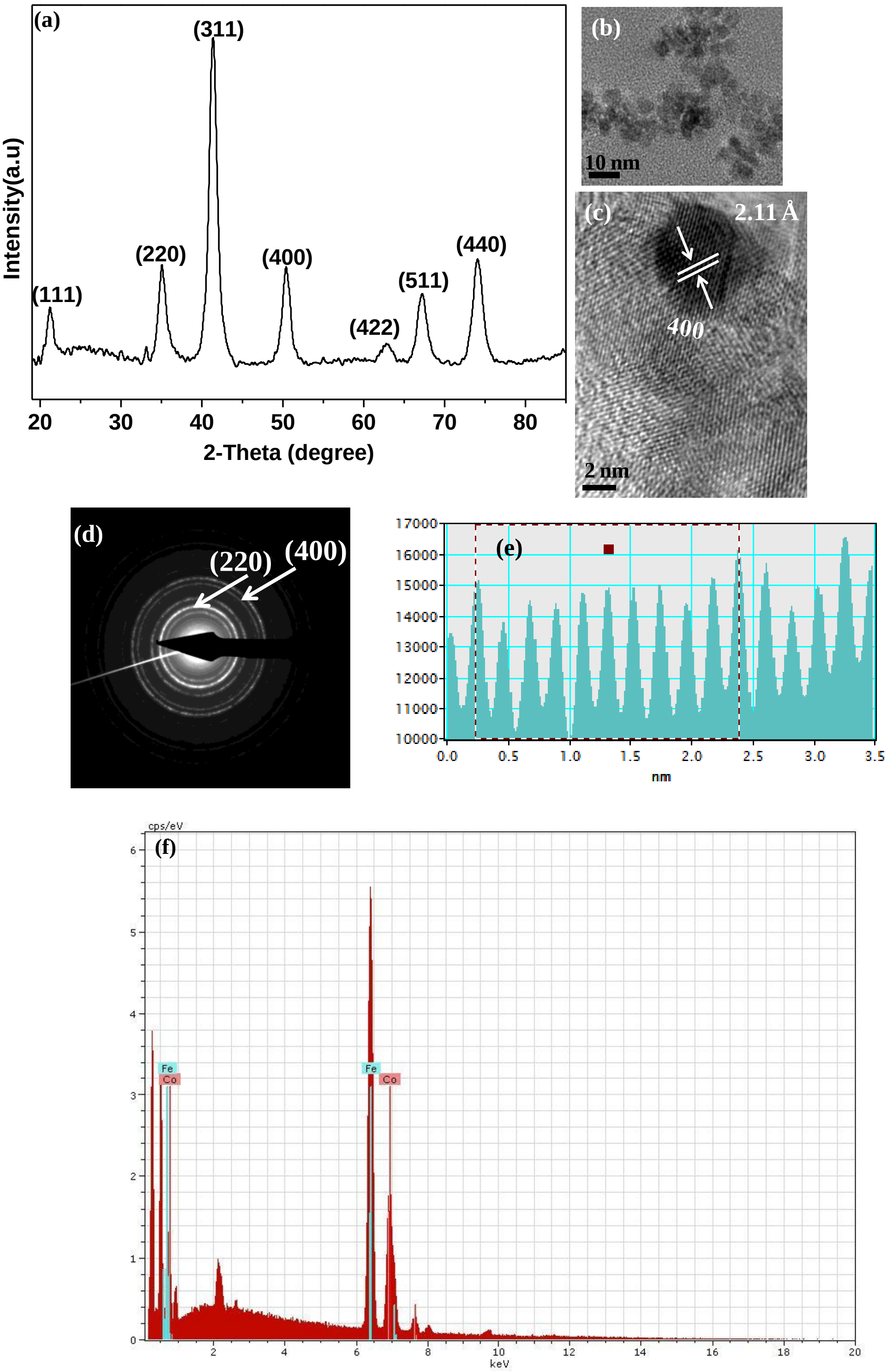

Fig. 4.4 (a) p-XRD pattern for cubic cobalt iron oxide nanoparticles ($CoFe_2O_4$). (b)-(c) TEM images, HRTEM obtained for these particles. (d) The diffraction rings obtained from (b). (e) Line profile used for calculating the *d*-spacing from (c). (f) EDX spectrum.

4.4.4 Zinc ferrite nanoparticles

The p-XRD patterns of the nanoparticles obtained from **(4)** correspond to cubic zinc iron oxide ($Zn_{0.35}Fe_{2.65}O_4$) (ICDD Card No: 01-086-0510) (Fig. 4.5(a)). The average particle size determined from the full width at the half maximum (FWHM) using the well-known Scherrer equation was found to be 5.3 nm. The average diameter calculated from the TEM images (5.5 ± 0.6 nm) are in good agreement with the XRD. As observed from the TEM images, spherical zinc ferrite nanoparticles produced were of high crystallinity as is evident in their lattice fringes (Fig. 4.5(b)). This good size distribution was obtained without any post synthesis size selectivity. A *d*-spacing value of 2.54 Å was calculated using the line profile by counting ten spaces (Fig. 4.5(d)), which correspond to the (311) reflection of the cubic zinc ferrite. Strong lattice rings in SAED image can be indexed to (220) and (311) planes of the zinc ferrite confirming the purity of the nanoparticles (Fig. 4.5(c)).

The zinc ferrite nanoparticles are well dispersed in water without traces of aggregation and this has been attributed to the role played by PVP.[76,77] Zinc ferrite microspheres of average diameter 200 nm have been reported using ethylene glycol by the solvothermal method.[61]

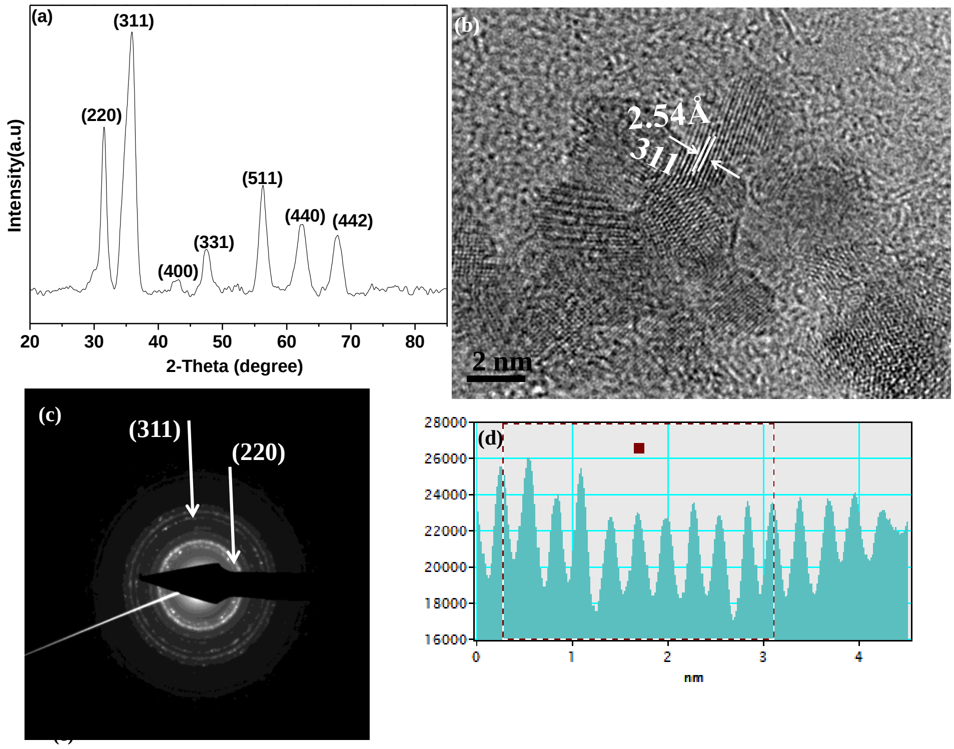

Fig. 4.5 (a) p-XRD pattern for cubic zinc iron oxide nanoparticles ($Zn_{0.35}Fe_{2.65}O_4$). (b) TEM images (c). The diffraction rings obtained from (b). (d) Line profile used for calculating the *d*-spacing from (b).

4.4.5 Nickel ferrite nanoparticles

A mixture of nickel ferrite and iron oxide was obtained after 2 hours and the reaction was left for an additional one hour to obtain a pure single phase. The p-XRD patterns were matched with cubic trevorite- nickel iron oxide ($NiFe_2O_4$) (ICDD Card No: 00-054-0964) (Fig. 4.6(a)). The average crystallite size calculated by the Scherrer formula is 6.5 nm whilst 7 ± 0.7 nm was obtained from TEM images which show they are in good agreement. The formation of monodispersed nickel ferrite nanoparticles has been attributed to the stabilisation provided by the PVP which is achieved by controlling the growth and preventing aggregation of nanoparticles.[78,79]

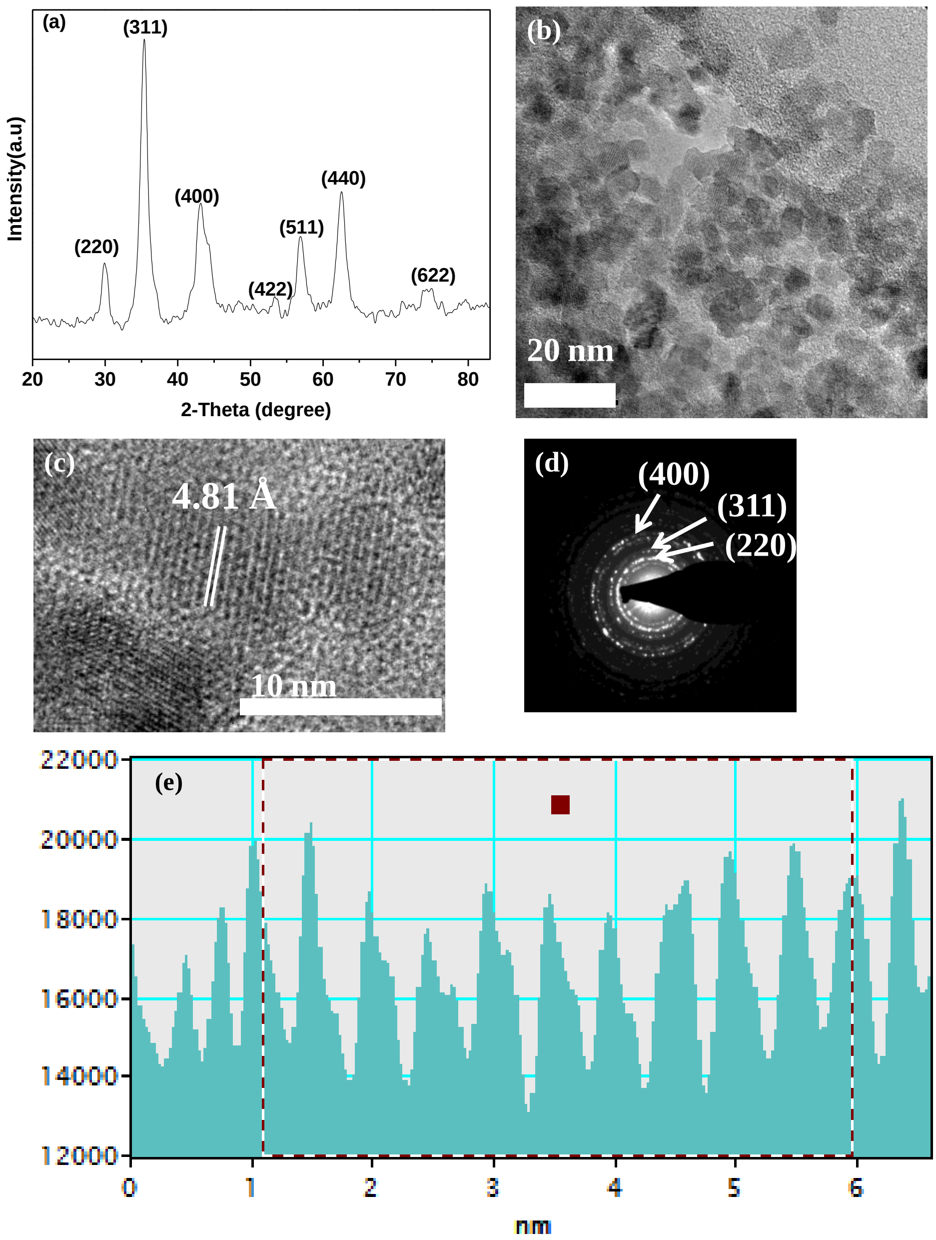

Fig. 4.6 (a) p-XRD pattern for cubic nickel iron oxide nanoparticles ($NiFe_2O_4$). (b) TEM images (c) HRTEM showing lattice fringes. (d) Diffraction rings obtained from (b). (e) Line profile used for calculating the *d*-spacing from (c).

The crystallinity of the sample is evident in their lattice fringes with *d*-spacing value of 4.81 Å (Fig 4.6(c)) which corresponds to the (111) reflection plane. The diffraction patterns also confirmed the purity of the trevorite nanoparticles with strong diffraction rings matching the (220), (311) and (400) planes of the cubic phase (Fig 4.6(d)).

EDX analysis confirmed the presence of both nickel and iron in the ratio of 1: 0.5 (Fig. 4.7).

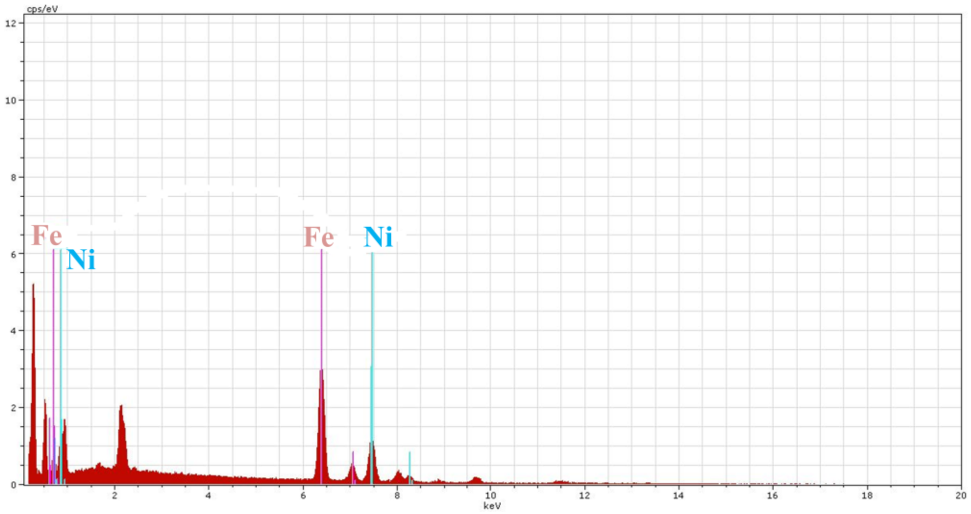

Fig. 4.7 EDX spectrum of nickel ferrite nanoparticles.

4.5 Conclusion

Water-dispersible ferrite nanoparticles of manganese, cobalt, zinc and nickel have been synthesised by hot injection thermolysis of heterometallic pivalate clusters. The magnetite nanoparticles obtained from the thermal decomposition method have a better size distribution than those obtained from co-precipitation. A good size distribution was obtained in all cases without any post synthesis size selective precipitation. All the nanoparticles produced were of pure single phase as evident in their p-XRD, SAED and HRTEM images. The nanoparticles dispersion was stable for several months at room temperature. Hot injection thermolysis of pivalate clusters in PVP and TREG have proven to be a good route for the synthesis of water soluble ferrite nanoparticles.

4.6 References

1. P. Majewski and B. Thierry, *Crit. Rev. Solid State Mater. Sci.*, 2007, **32**, 203.
2. R. Mout, D. F. Moyano, S. Rana, and V. M. Rotello, *Chem. Soc. Rev.*, 2012, **41**, 2539.
3. R. Qiao, C. Yang, and M. Gao, *J. Mater. Chem.*, 2009, **19**, 6274.
4. J. Jang, H. Nah, J. H. Lee, S. H. Moon, M. G. Kim, and J. Cheon, *Angew. Chem. Int. Ed.*, 2009, **48**, 1234.
5. H. J. Lee, K. S. Jang, S. Jang, J. W. Kim, H. M. Yang, Y. Y. Jeong, and J. D. Kim, *Chem. Commun.*, 2010, **46**, 3559.
6. S. W. Lee, S. Bae, Y. Takemura, I. B. Shim, T. M. Kim, J. Kim, H. J. Lee, S. Zurn, and C. S. Kim, *J. Magn. Magn. Mater.*, 2007, **310**, 2868.
7. R. F. Ziolo, E. P. Giannelis, B. A. Weinstein, M. P. O’horo, B. N. Ganguly, V. Mehrotra, M. W. Russell, and D. R. Huffman, *Science*, 1992, **257**, 219.
8. K. Raj, B. Moskowitz, and R. Casciari, *J. Magn. Magn. Mater.*, 1995, **149**, 174.
9. Y. G. Li, H. S. Gao, W. L. Li, J. M. Xing, and H. Z. Liu, *Bioresour. Technol.*, 2009, **100**, 5092.
10. I. Safarik, L. F. T. Rego, M. Borovska, E. Mosiniewicz-Szablewska, F. Weyda, and M. Safarikova, *Enzyme Microb. Technol.*, 2007, **40**, 1551.
11. A. Hu, G. T. Yee, and W. Lin, *J. Am. Chem. Soc.*, 2005, **127**, 12486.
12. A. H. Lu, W. C. Li, A. Kiefer, W. Schmidt, E. Bill, G. Fink, and F. Schüth, *J. Am. Chem. Soc.*, 2004, **126**, 8616.
13. D. L. Leslie-Pelecky and R. D. Rieke, *Chem. Mater.*, 1996, **8**, 1770.
14. T. Suzuki, M. Shinkai, M. Kamihira, and M. Kobayashi, *Biotechnol. Appl. Biochem.*, 1995, **21**, 335.
15. J. Mürbe, A. Rechtenbach, and J. Töpfer, *Mater. Chem. Phys.*, 2008, **110**, 426.
16. P. Sivakumar, R. Ramesh, A. Ramanand, S. Ponnusamy, and C. Muthamizhchelvan, *Mater. Lett.*, 2011, **65**, 483.
17. R. T. Olsson, G. Salazar-Alvarez, M. S. Hedenqvist, U. W. Gedde, F. Lindberg, and S. J. Savage, *Chem. Mater.*, 2005, **17**, 5109.
18. I. Martínez-Mera, M. E. Espinosa-Pesqueira, R. Pérez-Hernández, and J. Arenas-Alatorre, *Mater. Lett.*, 2007, **61**, 4447.

19. K. Maaz, A. Mumtaz, S. K. Hasanain, and A. Ceylan, *J. Magn. Magn. Mater.*, 2007, **308**, 289.
20. F. Dang, N. Enomoto, J. Hojo, and K. Enpuku, *J. Cryst. Growth*, 2010, **312**, 1736.
21. C. Yang and H. Yan, *Mater. Lett.*, 2012, **73**, 129.
22. Y. Qi, Y. Yang, X. Zhao, X. Liu, P. Wu, F. Zhang, and S. Xu, *Particuology*, 2010, **8**, 207.
23. Y. Sahoo, A. Goodarzi, M. T. Swihart, T. Y. Ohulchanskyy, N. Kaur, E. P. Furlani, and P. N. Prasad, *J. Phys. Chem. B*, 2005, **109**, 3879.
24. R. F. Fakhrullin, J. García-Alonso, and V. N. Paunov, *Soft Matter*, 2010, **6**, 391.
25. X. M. Guo, B. Guo, Q. Zhang, and X. Sun, *Dalton Trans.*, 2011, **40**, 3039.
26. C. Wilhelm, C. Billotey, J. Roger, J. N. Pons, J. C. Bacri, and F. Gazeau, *Biomaterials*, 2003, **24**, 1001.
27. Z. Lu, G. Wang, J. Zhuang, and W. Yang, *Colloids Surf., A*, 2006, **278**, 140.
28. X. Liu, M. D. Kaminski, Y. Guan, H. Chen, H. Liu, and A. J. Rosengart, *J. Magn. Magn. Mater.*, 2006, **306**, 248.
29. M. M. Lin, S. Li, H. H. Kim, H. Kim, H. B. Lee, M. Muhammed, and D. K. Kim, *J. Mater. Chem.*, 2010, **20**, 444.
30. W. Li, L. Yu, P. Zhou, and M. Zhu, *World J. Microbiol. Biotechnol.*, 2007, **23**, 1489.
31. C. T. Lefèvre, F. Abreu, M. L. Schmidt, U. Lins, R. B. Frankel, B. P. Hedlund, and D. A. Bazylinski, *Appl. Environ. Microbiol.*, 2010, **76**, 3740.
32. W. Zhou, W. He, S. Zhong, Y. Wang, H. Zhao, Z. Li, and S. Yan, *J. Magn. Magn. Mater.*, 2009, **321**, 1025.
33. T. Perez-Gonzalez, C. Jimenez-Lopez, A. L. Neal, F. Rull-Perez, A. Rodriguez-Navarro, A. Fernandez-Vivas, and E. Iañez-Pareja, *Geochim. Cosmochim. Acta*, 2010, **74**, 967.
34. Y. Amemiya, A. Arakaki, S. S. Staniland, T. Tanaka, and T. Matsunaga, *Biomaterials*, 2007, **28**, 5381.
35. L. W. Yeary, L. J. Love, J. R. Thompson, C. J. Rawn, and T. J. Phelps, *IEEE Trans. Magn.*, 2005, **41**, 4384.

36. A. Bharde, D. Rautaray, V. Bansal, A. Ahmad, I. Sarkar, S. M. Yusuf, M. Sanyal, and M. Sastry, *Small*, 2006, **2**, 135.
37. V. S. Coker, C. I. Pearce, C. Lang, G. van der Laan, R. A. D. Pattrick, N. D. Telling, D. Schüler, E. Arenholz, and J. R. Lloyd, *Eur. J. Mineral.*, 2007, **19**, 707.
38. A. P. Philipse and D. Maas, *Langmuir*, 2002, **18**, 9977.
39. D. A. Bazylinski, R. B. Frankel, and H. W. Jannasch, *Nature*, 1988, **334**, 518.
40. V. S. Coker, J. A. Bennett, N. D. Telling, T. Henkel, J. M. Charnock, G. van der Laan, R. A. D. Pattrick, C. I. Pearce, R. S. Cutting, I. J. Shannon, J. Wood, E. Arenholz, I. C. Lyon, and J. R. Lloyd, *ACS Nano*, 2010, **4**, 2577.
41. V. S. Coker, N. D. Telling, G. van der Laan, R. A. D. Pattrick, C. I. Pearce, E. Arenholz, F. Tuna, R. E. P. Winpenny, and J. R. Lloyd, *ACS Nano*, 2009, **3**, 1922.
42. Y. Roh, R. J. Lauf, A. D. McMillan, C. Zhang, C. J. Rawn, J. Bai, and T. J. Phelps, *Solid State Commun.*, 2001, **118**, 529.
43. J. W. Moon, Y. Roh, R. J. Lauf, H. Vali, L. W. Yeary, and T. J. Phelps, *J. Microbiol. Methods*, 2007, **70**, 150.
44. L. W. Yeary, J. W. Moon, C. J. Rawn, L. J. Love, A. J. Rondinone, J. R. Thompson, B. C. Chakoumakos, and T. J. Phelps, *J. Magn. Magn. Mater.*, 2011, **323**, 3043.
45. Abhilash, K. Revati, and B. D. Pandey, *Bull. Mater. Sci.*, 2011, **34**, 191.
46. T. Hyeon, S. S. Lee, J. Park, Y. Chung, and H. B. Na, *J. Am. Chem. Soc.*, 2001, **123**, 12798.
47. S. Sun and H. Zeng, *J. Am. Chem. Soc.*, 2002, **124**, 8204.
48. Y. Li, M. Afzaal, and P. O'Brien, *J. Mater. Chem.*, 2006, **16**, 2175.
49. C. Yu, J. Zhao, Y. Guo, C. Lu, X. Ma, and Z. Gu, *J. Biomedical Mater. Res.*, 2008, **87**, 364.
50. Y. Wang, J. F. Wong, X. Teng, X. Z. Lin, and H. Yang, *Nano Lett.*, 2003, **3**, 1555.
51. Y. W. Jun, Y. M. Huh, J. S. Choi, J. H. Lee, H. T. Song, S. Kim, S. Yoon, K. S. Kim, J. S. Shin, J. S. Suh, and J. Cheon, *J. Am. Chem. Soc.*, 2005, **127**, 5732.

52. Y. M. Huh, Y. Jun, H. T. Song, S. Kim, J. Choi, J. H. Lee, S. Yoon, K. Kim, J. S. Shin, J.-S. Suh, and J. Cheon, *J. Am. Chem. Soc.*, 2005, **127**, 12387.
53. B. L. Frankamp, N. O. Fischer, R. Hong, S. Srivastava, and V. M. Rotello, *Chem. Mater.*, 2006, **18**, 956.
54. N. Kohler, G. E. Fryxell, and M. Zhang, *J. Am. Chem. Soc.*, 2004, **126**, 7206.
55. M. Kim, Y. Chen, Y. Liu, and X. Peng, *Adv. Mater.*, 2005, **17**, 1429.
56. T. Pellegrino, L. Manna, S. Kudera, T. Liedl, D. Koktysh, A. L. Rogach, S. Keller, J. Ra, G. Natile, and W. J. Parak, *Nano Lett.*, 2004, **4**, 703.
57. T. Kikuchi, R. Kasuya, S. Endo, A. Nakamura, T. Takai, N. Metzler-Nolte, K. Tohji, and J. Balachandran, *J. Magn. Magn. Mater.*, 2011, **323**, 1216.
58. M. Hatakeyama, H. Kishi, Y. Kita, K. Imai, K. Nishio, S. Karasawa, Y. Masaike, S. Sakamoto, A. Sandhu, A. Tanimoto, T. Gomi, E. Kohda, M. Abe, and H. Handa, *J. Mater. Chem.*, 2011, **21**, 5959.
59. A. Hofmann, S. Thierbach, A. Semisch, A. Hartwig, M. Taupitz, E. Rühl, and C. Graf, *J. Mater. Chem.*, 2010, **20**, 7842.
60. S. Sun, H. Zeng, D. B. Robinson, S. Raoux, P. M. Rice, S. X. Wang, and G. Li, *J. Am. Chem. Soc.*, 2004, **126**, 273.
61. H. Deng, X. Li, Q. Peng, X. Wang, J. Chen, and Y. Li, *Angew. Chem. Int. Ed.*, 2005, **44**, 2782.
62. N. Guan, J. Xu, L. Wang, and D. Sun, *Colloids Surf., A*, 2009, **346**, 221.
63. L. Zhu, H. Xiao, W. Zhang, G. Yang, and S. Fu, *Cryst. Growth Des.*, 2008, **8**, 957.
64. W. Cheng, K. Tang, and J. Sheng, *Chem. Euro. J.*, 2010, **16**, 3608.
65. Z. Li, H. Chen, H. Bao, and M. Gao, *Chem. Mater.*, 2004, **16**, 1391.
66. Z. Li, L. Wei, M. Y. Gao, and H. Lei, *Adv. Mater.*, 2005, **17**, 1001.
67. F. Q. Hu, L. Wei, Z. Zhou, Y. L. Ran, Z. Li, and M. Y. Gao, *Adv. Mater.*, 2006, **18**, 2553.
68. F. Hu, Z. Li, C. Tu, and M. Gao, *J. Colloid Interface Sci.*, 2007, **311**, 469.
69. X. Lu, M. Niu, R. Qiao, and M. Gao, *J. Phys. Chem. B*, 2008, **112**, 14390.
70. H. Yang, C. Zhang, X. Shi, H. Hu, X. Du, Y. Fang, Y. Ma, H. Wu, and S. Yang, *Biomaterials*, 2010, **31**, 3667.
71. D. Caruntu, G. Caruntu, Y. Chen, C. J. O. Connor, G. Goloverda, and V. L. Kolesnichenko, *Chem. Mater.*, 2004, **16**, 5527.

72. J. Xie, K. Chen, H. Y. Lee, C. Xu, A. R. Hsu, S. Peng, X. Chen, and S. Sun, *J. Am. Chem. Soc.*, 2008, **130**, 7542.
73. K. Vamvakidis, D. Sakellari, M. Angelakeris, and C. Dendrinou-Samara, *J. Nanopart. Res.*, 2013, **15**, 1743.
74. M. Goodarz Naseri, E. B. Saion, H. A. Ahangar, A. Shaari, and M. Hashim, *J. Nanomater.*, 2010, **2010**, 1.
75. S. Pauline and A. P. Amaliya, *Arch. Phy. Res.*, 2012, **3**, 78.
76. M. G. Naseri and E. B. Saion, *Crystallization in Spinel Ferrite Nanoparticles, Advances in Crystalization Processes*, Intech, Croatia, Europe, 2012.
77. M. Goodarz Naseri, E. B. Saion, and A. Kamali, *ISRN Nanotechnology*, 2012, **2012**, 1.
78. M. G. Naseri, E. B. Saion, H. A. Ahangar, M. Hashim, and A. H. Shaari, *Powder Technol.*, 2011, **212**, 80.
79. M. Goodarz Naseri, E. Saion, and N. Khalil Zadeh, *Int. Nano Letters*, 2013, **3**, 19.

Chapter 5

General Experimental

5.1 Chemicals

Oleylamine and octadecene were purchased from Acros Organics. Triethylene glycol was purchased from Alfa Aesar. Oleic acid was purchased from Fisher scientific. Diphenyl ether, dibenzyl ether, methanol, acetone, dioctyl ether, dodecanol, hexadecanol, polyvinylpyrrolidone (PVP), toluene, iron(III) chloride, iron(II) chloride, ammonia, polyallyl amine, hexane, acetonitrile, potassium hydroxide, pivalic acid, 4-phenylphenol, iron nitrate nonahydrate, cobalt(II) nitrate hexahydrate, petroleum ether, cobalt(II) acetate tetrahydrate, manganese(II) nitrate tetrahydrate, zinc acetate dihydrate, nickel(II) nitrate hexahydrate, pyridine, diethyl ether, trichloroethylene, chromium nitrate nonahydrate, tetrahydrofuran and ethanol were purchased from Sigma-Aldrich chemical company and used as received. Solvents were distilled prior to use.

5.2 Powder X-Ray diffraction (p-XRD)

p-XRD studies were performed on a Bruker Discover 8 diffractometer using Co-Kα radiation. The samples were mounted flat and scanned between 10 to 85° in a step size of 0.02 and a count rate of 4 sec. The samples were prepared by dropping dispersion of the nanoparticles on a glass slide until a thick film is formed.

5.3 Transmission electron microscopy (TEM), high resolution TEM (HRTEM) and selected area electron diffraction (SAED)

TEM, HRTEM and SAED were performed using Tecnai F30 FEG TEM instrument operating at 300 kV. TEM samples were prepared by placing 1 or 2 drops of the nanoparticles dispersion (in toluene) on a lacey carbon-coated copper grid, after which the grids were left to dry at room temperature.

5.4 Energy dispersive X-ray spectroscopy (EDAX)

EDAX was performed using a SEM Philips XL 30FEG and a DX4 instrument.

5.5 Thermogravimetric analysis (TGA)

TGA were performed using a Mettler Toledo/DSC 1 STAR^e instrument with a heating rate of 10 °C/ min under nitrogen. TGA was performed by the microanalysis team of the School of Chemistry.

5.6 Elemental analysis

CHN analysis was carried out using Thermo Flash 2000 organic elemental analyzers. A weighed sample is placed in a tin container and put in a furnace to burn. The products of combustion typically carbon dioxide (C), water vapour (H) and nitrogen (N) were analysed in a gas chromatography (GC) column to determine the amount of each element present in the sample.

Metal analysis were performed on Thermo iCAP 6000 series ICP-OES by digesting a weighed sample in acid and then made up with water to form a solution. Elemental analysis was performed by the microanalysis section of the School of Chemistry.

5.7 Magnetic measurements

Magnetic measurements were performed on polycrystalline samples restrained in eicosane using a Quantum Design MPMS-XL SQUID magnetometer equipped with a 7 T magnet. Zero-field cooled (ZFC) and Field-cooled (FC) magnetizations were recorded over 5-300 K temperature range with an applied magnetic field of 100 Oe. The diamagnetism of the sample holder and eicosane was measured and extracted from the raw magnetic data. Magnetic measurements were performed by Dr. Floriana Tuna.

5.8 X-ray Magnetic Circular Dichroism (XMCD) and Electron probe Microanalysis (EPMA)

XMCD data were acquired at beamline 4.0.2 at the Advanced Light Source, LBNL, Berkeley.[1] Ferrite nanoparticle samples were mounted on carbon tape attached to a copper sample probe and X-ray absorption spectroscopy (XAS) was used to measure the Fe, Co and Mn $L_{3,2}$-edges in vacuum in total electron yield (TEY) mode. XMCD spectra are obtained as the difference between two XAS spectra recorded in two opposite applied magnetic fields of ± 0.6 T (parallel and antiparallel to the beam direction). At energies of 710 eV (the Fe L_3 edge energy) the effective probing depth is ~3-4 nm. EPMA to determine Co, Fe and Mn ratios was undertaken using a Cameca Camebax SX100 with a beam size of 2 µm, a beam current of 20 na and an accelerating voltage of 15 KeV, using pure metal standards. Samples of the nanoparticles were pressed into carbon tape for analysis. XMCD and EPMA were performed by Prof. Richard Patrick of the School of environmental sciences.

5.9 Inductively coupled plasma optical electron microscopy (ICP-OES)

The ICP-OES was measured on a Perkin-Elmer Optima 5300 dual view ICP-OES. The sample was prepared by digesting 1 mg nanoparticle in 2 % nitric acid solution (10 ml). The measurements were performed by the analytical geochemistry unit in the School of environmental sciences.

5.10 Reference

1. V. S. Coker, N. D. Telling, G. van der Laan, R. A. D. Pattrick, C. I. Pearce, E. Arenholz, F. Tuna, R. E. P. Winpenny, and J. R. Lloyd, *ACS Nano*, 2009, **3**, 1922.

Chapter 6

Conclusion and Future Work

6.1 Conclusion

Ferrite nanoparticles are important and interesting class of nanomaterials which have found applications in drug delivery, contrast agents in MRI, hyperthermia treatment, information storage, gas sensors, environmental remediation and catalysis. The thermal decomposition method has been exploited as a major synthetic route for ferrite nanoparticles with different shapes and sizes. The work described in this thesis deals with the investigations of iron based pivalate clusters as novel single source precursors for the synthesis of monodispersed ferrite nanoparticles using hot injection thermolysis.

Iron pivalate clusters were used as single source precursors for the first time to synthesise iron oxide nanoparticles by thermolysis in different solvent/capping agent combinations. The diameter of the spherical nanoparticles can be controlled by manipulating the ratios of capping agents, varying the injection temperature or reaction time. The structure of the product (maghemite or magnetite) depended on the time of reaction. Magnetic studies showed that blocking temperature and saturation magnetisation values vary with size of the nanoparticles. All the nanoparticles exhibit superparamagnetism at room temperature.

The heterometallic pivalate complexes were used to synthesise ternary ferrites of cobalt, manganese, zinc, nickel and quaternary oxide of chromium cobalt ferrites. These complexes were thermolysed in different solvents with different precursor concentrations. The diameters of the nanoparticles obtained in all cases can be controlled by manipulating the precursor concentration, injection temperature and reaction time. The structure (iron oxide or the corresponding ferrite) was highly depended on the reaction time and the stoichiometry of the ferrite in most cases depends on the precursor concentration. The cobalt and nickel ferrite are found to be inverse spinel structure as confirmed by the XMCD analysis with majority of Co and Ni cations in the octahedral geometry. Zinc ferrite nanoparticles also exhibit some form of cation inversion as some Zn cations occupied the octahedral geometry. This is evident in their magnetic studies and XMCD measurements. All the ferrite nanoparticles are superparamagnetic at room temperature but at 5 K, cobalt ferrite and chromium cobalt ferrite showed large hysteresis.

Water soluble ferrite nanoparticles were also synthesised from the thermolysis of pivalate clusters in PVP with TREG as solvent. Monodispersed water dispersible iron oxide, nickel, cobalt, zinc and manganese ferrites were obtained directly without any further post synthesis procedure. SAED also confirmed the crystallinity of the ferrites nanoparticles obtained with strong diffraction patterns observed in all cases. The elemental compositions of the ferrites were confirmed by EDX analysis.

6.2 Future Work

Homo/ Heterometallic pivalate clusters could be explored further to synthesise one and two dimensional nanocrystals including cubes, rods and wires using both hot injection thermolysis and the heating up methods.

These clusters could also be used to deposit thin films by Aerosol Assisted Chemical Vapour Deposition (AACVD) and Low Pressure Chemical Vapour Deposition (LPCVD) methods as these precursors are volatile. These ferrite thin films have potential applications in magnetic sensors and magnetic recording.

Heterometallic pivalate clusters could be used as single source precursors to synthesise quaternary ferrite nanoparticles including $FeCrCoO_{4,}$ $FeCrNiO_{4.}$ The effect of different reaction parameters (temperature, time, solvent, concentration) should be investigated with emphasis on getting good stoichiometry.

The water soluble ferrite nanoparticles could be functionalised with different groups such as antibodies, proteins to make them target specific for use in biomedical fields and environmental remediation.

Table A1 Crystal data and structural refinement parameters for compounds $[Fe_2CoO(O_2C^tBu)_6(HO_2C^tBu)_3]$ **(1),** $[Co_4Fe_2O_2(O_2C^tBu)_{10}(MeCN)_2]$ **(2),** $[Fe_2MnO(O_2C^tBu)_6(HO_2C^tBu)_3]$ **(3)** and $[Fe_8(OH)_4(O_2C^tBu)_{12}(OC_6H_4C_6H_5)_8]$ **(4).**

Compound	**1**	**2**	**3**	**4**
Formula	$C_{45}CoH_{84}Fe_2O_{19}$	$C_{54}Co_4H_{96}Fe_2N_2O_{22}$	$C_{45}H_{84}Fe_2MnO_{19}$	$C_{164}H_{190}Fe_8O_{37}$
M_r	1099.75	1472.75	1092.74	3198.07
Crystal system	Orthorhombic	Monoclinic	Orthorhombic	Tetragonal
Space group	$Cmc2_1$	$C2/c$	$Cmc2_1$	$P4/n$;
a [Å]	18.4388(15)	14.1994(7)	18.3946(10)	20.1880(3)
b [Å]	20.3317(14)	22.4866(6)	20.3034(16)	20.1880(3)
c [Å]	17.1858(14)	22.0322(7)	17.1311(11)	21.5726(7)
V [Å^3]	6442.8(9)	7026.1(5)	6398.0(7)	8792.0(3)
R_1 (obs),wR_2 (all)^b	0.0776, 0.2452	0.0895, 0.2424	0.0883, 0.2835	0.0572, 0.1692
Goodness of fit	1.011	1.026	1.030	1.096

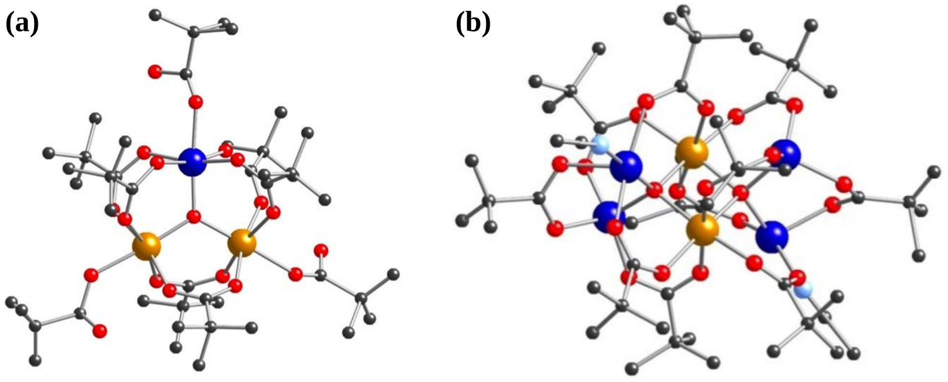

Fig. A1 (a) The structure of $[Fe_2CoO(O_2C^tBu)_6(HO_2C^tBu)_3]$ **(1)** and $[Fe_2MnO(O_2C^tBu)_6(HO_2C^tBu)_3]$ **(3)** in the crystal. (b) The structure of $[Co_4Fe_2O_2(O_2C^tBu)_{10}(MeCN)_2]$ **(2)** in the crystal. Colors: Co- blue, Fe- orange, O- red, C- black. Hydrogens removed for clarity.

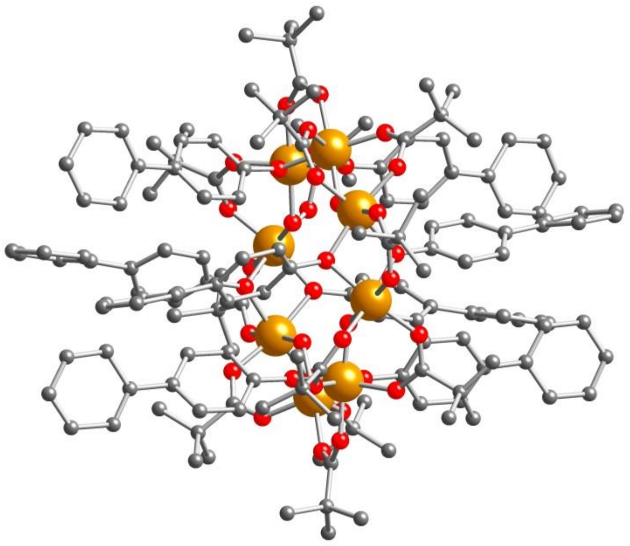

Fig. A2 The crystal structure of $[Fe_8(OH)_4(O_2C^tBu)_{12}(OC_6H_4C_6H_5)_8]$ **(4).** Colours: Fe- orange, O- red, C- black. Hydrogens removed for clarity.

List of Publications

- **Khadijat Abdulwahab,** Mohammad A. Malik, Kuveshni Govender, Christopher A. Muryn Grigore A. Timco, Richard E. P. Winpenny, Floriana Tuna and Paul O'Brien, "Synthesis of Monodispersed Magnetite Nanoparticles from Iron Pivalate Clusters", *Dalton Trans*., 2013**, 42**, 196.
- **Khadijat O. Abdulwahab,** Mohammad A. Malik, Christopher A. Muryn, Grigore A. Timco, Richard E. P. Winpenny, Floriana Tuna, Victoria S. Coker, Richard A.D. Pattrick, Elke Arenholz and Paul O'Brien, "A one pot synthesis of monodispersed cobalt and manganese ferrite nanoparticles from bimetallic pivalate clusters", *Chem. Mater*., (manuscript accepted).
- **Khadijat O. Abdulwahab,** Mohammad A. Malik, Christopher A. Muryn, Grigore A. Timco, Richard E. P. Winpenny, Floriana Tuna, Victoria S. Coker, Richard A.D. Pattrick, Elke Arenholz and Paul O'Brien, "Hot injection thermolysis of heterometallic pivalate clusters for the synthesis of monodisperse zinc and nickel ferrite nanoparticles" (Ready for submission).

List of Presentation

- Synthesis of monodispersed ferrite nanoparticles from iron pivalate clusters by thermal decomposition methods. **Khadijat O. Abdulwahab,** Mohammad A. Malik and Paul O'Brien, SO-8.4, International Conference on Nanoscience+ Technology (ICN+T), Paris, Sorbonne, 23-27 July 2012.